Developing multiparametric and novel magnetic resonance imaging biomarkers for prostate cancer

Edward William Johnston

Ph.D. Thesis,

Submitted for the degree of Doctor of Philosophy,

University College London,

December 2017

DECLARATION

I, Edward Johnston, confirm that the work presented in this thesis is my own. Where information has been derived from other sources, I confirm that this has been indicated in the thesis.

Dr. Edward W. Johnston, FRCR

ABSTRACT

Whilst biomarker research is gaining momentum within the cancer sciences, disappointingly few biomarkers are successfully translated into clinical practice, which is partly due to lack of rigorous methodology. In this thesis, I aim to systematically study several quantitative magnetic resonance imaging (MRI) biomarkers (QIBs), at various stages of biomarker development for use as tools in the assessment of local and metastatic prostate cancer according to clinical need.

I initially focus on QIBs derived from conventional multiparametric (mp) prostate MRI sequences, namely T2 weighted (T2W), apparent diffusion coefficient (ADC) and dynamic contrast enhanced (DCE). Firstly, by optimising analytical methods used throughout the thesis, deciding which approach is more reliable between single-slice region-of-interest vs. contouring the whole tumour volume using two different software packages. I then consider whether metric reproducibility can be improved by normalisation to different anatomical structures, and assess whether it is preferable to use statistics derived from imaging histograms rather than the current convention of using mean values.

I combine multiple QIBs in a logistic regression model to predict a Gleason 4 component in known prostate cancer, which represents an unmet clinical need, as non-invasive tools to distinguish these more aggressive tumours do not currently exist. I subsequently 'technically validate' a novel microstructural diffusion-weighted MRI technique called VERDICT (Vascular, Extracellular and Restricted Diffusion for Cytometry in Tumours) to detect aggressive prostate cancer as part of a prospective cohort study. I assess the image quality, contrast-to-noise ratio, repeatability and performance of quantitative parametric VERDICT maps to discriminate between Gleason grades vs. the current best performing, but still imperfect tool of ADC.

In the final two results chapters, motivated by the limited diagnostic accuracy of the prostate cancer staging modalities in current clinical use, I investigate the ability of mp-whole body (WB) MRI to stage aggressive cancer outside the prostate in patients with a high risk of metastases at primary diagnosis, and in biochemical failure following prostatectomy.

IMPACT STATEMENT

In addition to the knowledge dissemination that have occurred at meetings and in published/proposed peer reviewed articles; my research could be put to beneficial use in multiple ways inside and out of academia.

Within academia, the improved analytical methods I have developed for quantitative multiparametric (mp)-prostate MRI could be used to standardise research methodology, which should help address the 'reproducibility crisis' that is agreed to exist within the medical sciences. More robust assays would also lead to more robust conclusions, stronger effect sizes and better classification of patients. My finding that open source (rather than commercial) DICOM viewers lead to more reliable measurements will also help reduce the costs associated with quantitative imaging trials. As a result of this research, other members of my group have already begun to use my suggested analytical methods in combination with the plugins I have co-developed with collaborators at CMIC.

My logistic regression model has demonstrated an ability to classify peripheral zone (PZ) tumours, which is beneficial knowledge to other groups who work in metabolic imaging whereby their techniques are likely to hold greater potential for classifying transition zone (TZ) tumours. My work spent developing VERDICT maps as quantitative imaging biomarkers is a natural progression from this model, since both techniques aim to improve our ability to estimate Gleason grade non-invasively. Whilst I strive to be as rigorous as possible in the development of these novel putative biomarkers, prior to widespread application, further development should occur in collaborations outside of UCL. Indeed, we are already in discussion with the University of Toronto with a view towards multicentre validation.

My work on WB-MRI could also initiate further research. In the case of primary staging, multicentre and statistically powered collaborations now are urgently required prior to clinical adoption, which should include engagement with health economists. The use of the technique in biochemical failure could promote development of techniques which have potentially greater sensitivity e.g. mp-MRI for local recurrence and Prostate Specific Membrane Antigen (PSMA) PET/CT or PET/MRI for distant disease.

Outside of academia, I hope to see aspects of my work being used in routine clinical practice within the NHS. Whilst mp-MRI looks poised to be introduced into the prostate cancer management pathway by NICE relatively soon, it is still hampered by a lack of

biological specificity, as evidenced by the 40% of indeterminate scans. Patients who have an mp-MRI positive prostate lesion could attend for an MRI 'virtual biopsy' examination comprising quantitative mp-MRI with VERIDCT, whereby a logistic regression models (or more sophisticated machine learning algorithms) could classify lesion(s) in combination with clinical data such as fluidic biomarkers to estimate Gleason grade, avoid biopsy, prognosticate and reduce biopsies. Similarly, patients deemed to be at high risk of metastatic spread could contemporaneously undergo WB-MRI and avoid the requirement for multiple visits or investigations including BS, mp-MRI, and PET/CT. To achieve this, the public should be informed of important developments arising from this work and non-academic radiologists would need to be trained regarding how to report these emerging investigations.

CONTENTS

LIST OF FIGURES

LIST OF TABLES

LIST OF ABBREVIATIONS

ADC	Apparent Diffusion Coefficient
ADT	Androgen Depravation Therapy
AIC	Akaike Information Criterion
AIF	Arterial Input Function
AJCC	American Joint Committee on Cancer
AUC	Area Under the Curve
B-A	Bland-Altman
BI-RADS	Breast Imaging Reporting and Data System
BIC	Bayesian Information Criterion
BPH	Benign Prostatic Hyperplasia
BS	Bone Scintigraphy
CABI	Centre for Advanced Biomedical Imaging
CI	Confidence Interval
CMI	Centre for Medical Imaging
CMIC	Centre for Medical Image Computing
CoV	Coefficient of Variation
CRF	Case Report Form
CRUK	Cancer Research UK
CT	Computed Tomography
CZ	Central Zone
DCE	Dynamic Contrast Enhanced
DICOM	Digital Imaging and Communications in Medicine
DKI	Diffusion Kurtosis Imaging
DRE	Digital Rectal Examination
DTI	Diffusion tensor imaging
DUS	Distal urethral sphincter
DWI	Diffusion Weighted Imaging
EE	Early Enhancement
EES	Extravascular, Extracellular Space
EORTC	European Organisation for Research and Treatment of Cancer
EPI	Echo Planar Imaging
ePLND	Extended Pelvic Lymph Node Dissection
EQUATOR	Enhancing the QUAlity and Transparency Of health Research
FDA	Food and Drug Administration
FDG	Fludeoxyglucose
FID	Free Induction Decay
FN	False Negative
FP	False Positive
GBCA	Gadolinium Based Contrast Agent
GE	Gradient Echo
GV	Gland Volume
H&E	Haematoxylin and Eosin
ICC	Intraclass Correlation Coefficient
INNOVATE	CombIning advaNces in imagiNg with biOmarkers for improVed diagnosis of Aggressive prosTate cancEr
IQR	Interquartile Range

IRAS	Integrated Research Approval System
IRB	Institutional Review Board
ISMRM	International Society for Magnetic Resonance in Medicine
IVC	Inferior Vena Cava
IVIM	Intravoxel Incoherent Motion
LOO	Leave One Out
LR	Logistic Regression
MASTER	MRI Accuracy in Staging and Evaluation of Treatment Response in Cancer
MDC	Model Derivation Cohort
mDixon	Multiecho Dixon
MDT	Multidisciplinary Team
ME	Maximum Enhancement
mp	Multiparametric
MR	Magnetic resonance
MRI	Magnetic Resonance Imaging
NHS	National Health Service
NICE	The National Institute for Health and Care Excellence
NIH	National Institutes of Health
NMR	Nuclear magnetic resonance
OI	Obturator Internus
PACS	Picture Archiving and Communication System
PCUK	Prostate Cancer UK
PET	Positron Emission Tomography
PGSE	Pulsed Gradient Spin Echo
PI-RADS	Prostate Imaging Reporting and Data System
PICTURE	Prostate Imaging (multi-parametric MRI and Prostate HistoScanning™) Compared to Transperineal Ultrasound guided biopsy for significant prostate cancer Risk Evaluation
PLND	Pelvic Lymph Node Dissection
PROPS	PET /MRI pre-Radiotherapy for Post-Prostatectomy Salvage
PSA	Prostate Specific Antigen
PSAd	Prostate Specific Antigen Density
PSAdt	Prostate Specific Antigen Doubling Time
PSMA	Prostate Specific Membrane Antigen
PZ	Peripheral Zone
QIB	Quantitative Imaging Biomarker
QIBA	Quantitative Imaging Biomarkers Alliance
QIN	Quantiative Imaging Network
RARE	Rapid Acquisition with Relaxation Enhancement;
REC	NHS Research and Ethics Committee
RECIST	Response Evaluation Criteria In Solid Tumors
REMARK	REporting recommendations for tumor MARKer prognostic studies (REMARK)
RF	Radiofrequency
ROC	Receiver Operating Characteristic
ROI	Region of Interest
SD	Standard Deviation
SE	Spin Echo
SI	Signal Intensity
SMOTE	Synthetic Minority Oversampling Technique

SNR	Signal-to-noise ratio
SV	Seminal vesicle
T2nSI	T2 normalised Signal Intensity
T2W	T2-weighted
TE	Time to Echo
TN	True Negative
TNM	Tumor, Nodes, Metastases
TP	True Positive
TPM	Transperineal Template Mapping Biopsy
TR	Time to Repeat
TRUS	Transrectal Ultrasound
TSC	Temporally Separated Cohort
TSE	Turbo Spin Echo
TV	Tumour Volume
TZ	Transition Zone
UCL	University College London
UCLH	University College London Hospital
VERDICT	Vascular, Extracellular and Restricted Diffusion for Cytometry in Tumours
VOI	Volume of Interest
WB	Whole Body

ACKNOWLEDGEMENTS

I would like to acknowledge the many people without whom this thesis would not have been possible. First and foremost, I would like to extend my deepest gratitude to Dr. Shonit Punwani for taking me on as a PhD candidate. He has been an exemplary supervisor and provided me with everything I required to succeed throughout my work and always with good humour. As a result, I believe I have matured considerably as both a scientist and clinician and also feel inspired to pursue an academic career (although perhaps without the 7 a.m. meetings!).

Similarly, I would like to thank my secondary supervisor, Professor Daniel Alexander with whom it was also a privilege to work. Given my clinical background, collaborating with such a technical group was always going to be challenging, but I am pleased to have found the experience extremely rewarding. I also greatly value the contributions of the other members of his group including Laura Panagiotaki and Elisenda Bonet-Carné for developing VERDICT in the first place and for agreeing to work with our group to refine their technique. Further acknowledgments go to Ben Yvernault, Michela Antonelli and Dr David Atkinson for making my research much more effective with their technical wizardry.

I would like to recognise other junior members within our group including Arash Latifoltojar, Nikos Dikaios and James O'Callaghan whereby the net flow of knowledge in research methods and MRI physics was overwhelmingly towards me at the early stages of my work! The discussions we have had in the office over the past three years have kept me sane and quite often amused throughout.

I am also grateful to the radiologists who read the multiparametric and whole body MRIs for this thesis, namely Shonit Punwani, Navin Ramachandran, Harbir Sidhu, Mrishta Brizmohun and Nina Tunariu.

Thank you also to those who helped me run the clinical aspects of our projects, including Teresita Beeston, Joey Clememte, Wivijin Piga, Hayley Pye and all of the radiographers. I would also like to sincerely thank each and every patient (624 in total) for the altruism they have shown in agreeing to take part in this research.

Lastly, and most importantly, I would like to thank my wife Rebecca Johnston and my son Sidney Arthur Johnston for their continued support throughout this work - I could not ask for a better family. I hope that your patience has been worthwhile and I dedicate this thesis to you both.

WORK ARISING FROM THIS THESIS

Peer reviewed publications:

1. Bourne R, Bailey C, **Johnston E**, Pye H, Heavey S, Whitaker H, Siow B, Freeman A, Shaw G, Sridhar A, Mertzanidou T, Hawkes D, Alexander D, Punwani S, Panagiotaki E. Apparatus for histological validation of in vivo and ex vivo magnetic resonance imaging of the human prostate. Frontiers in Oncology. 47: 7, 2017.

2. **Johnston E,** Pye H, Bonet-Carne E, Panagiotaki E, Patel D, Galazi M, Heavey S, Carmona L, Freeman A, Trevisan G, Allen C, Kirkham A, Burling K, Stevens N, Hawkes D, Emberton M, Moore C, Ahmed H, Atkinson D, Rodriguez-Justo M, Ng T, Alexander D, Whitaker H, Punwani S. INNOVATE: A prospective cohort study combining serum and urinary biomarkers with novel diffusion-weighted magnetic resonance imaging for the prediction and characterization of prostate cancer. BMC Cancer. 2016 Oct 21;16(1):816.

3. **Johnston E,** Punwani S. Can We Improve the Reproducibility of Quantitative Multiparametric Prostate MR Imaging Metrics? Radiology. 2016 Nov; 281(2): 652-653.

4. Sidhu H, Benigno S, Ganeshan B, Dikaios N, **Johnston E,** Allen C, Kirkham A, Groves A, Ahmed H, Emberton M, Taylor S, Halligan S, Punwani S. Textural analysis of multiparametric MRI detects transition zone prostate cancer. Eur Radiol. 2017. Jun;27(6):2348-2358.

5. Appayya M, **Johnston E**, Punwani S. The role of multi-parametric MRI in loco-regional staging of men diagnosed with early prostate cancer. Curr Opin Urol. 2015 Nov; 25(6):510-7.

6. Linch M, Goh G, Hiley C, Shanmugabavan Y, McGranahan N, Rowan A, Wong Y, King H, Furness A, Freeman A, Linares J, Akarca A, Herrero J, Rosenthal R, Harder N, Schmidt G, Wilson G, Birkbak N, Mitter R, Dentro S, Cathcart P, Arya M, **Johnston E**, Scott R, Hung M, Emberton M, Attard G, Szallasi Z, Punwani S, Quezada S, Marafioti T, Gerlinger M, Ahmed H, Swanton C. Intratumoural evolutionary landscape of high-risk prostate cancer: the PROGENY study of genomic and immune parameters. Annals of Oncology 2017 Oct 1;28(10):2472-

2480.

Conference abstracts

Oral presentations:

2017 Carmona C, **Johnston E**, Hu Y, Gerlinger M, Ayra M, Emberton M, Freeman F, Punwani S, Barrett D, Whitaker H, Ahmed H. Prostate cancer intratumoural heterogeneity: correlation between clinical parameters, mpMRI and biomarkers. European Association of Urology, London

2017 Bailey C, Bourne R, Siow B, **Johnston E**, Heavey S, Pye H, Mertzanidou T, Whitaker H, Freeman A, Patel D, Shaw G, Hawkes D, Alexander D, Panagiotaki E. Validation of VERDICT MRI using fresh and fixed prostate specimens with aligned histological slices. The International Society for Magnetic Resonance in Medicine, Honolulu, Hawai'i

2017 **Johnston E**, Bonet-Carne E, Pye H, Clemente J, Yvernault B, Patel D, Heavey S, Appayya M, Saborowska A, Sridhar A, Shaw G, Ourselin S, Hawkes D, Moore C, Whitaker H, Rodriguez-Justo M, Freeman A, Panagiotaki E, Alexander D, Punwani S. Microstructural Diffusion-Weighted (VERDICT) MRI Metrics are Repeatable and Show Potential at Characterising Gleason 7 Prostate Cancer Non-Invasively. The International Society for Magnetic Resonance in Medicine, Honolulu, Hawai'i

Awarded Magna Cum Laude

2017 Dikaios N, **Johnston E**, Sidhu H, Appayya M, Freeman A, Ahmed H, Atkinson D, Punwani S. Deep learning to improve prostate cancer diagnosis. The International Society for Magnetic Resonance in Medicine, Honolulu, Hawai'i

Awarded Summa Cum Laude

2016 Bonet-Carne E, Daducci A, Panagiotaki E, **Johnston E**, Stevens N, Atkinson D, Punwani S, Alexander D, Alexander, D. AMICO-VERDICT: Ultrafast fitting algorithm for cancer microstructure characterization, a prostate cancer application. In Young Researchers' Futures Meeting (YRFM). London

2016 Bonet-Carne E, Daducci A, **Johnston E**, Panagiotaki E, Atkinson D, Punwani S, Alexander D. VERDICT, non-invasive quantification of prostate cancer, repeatability experiment. In Prosense. Bath, UK

2016 **Johnston E**, Latifoltojar A, Sidhu H, Ramachandran N, Sokolska M, Bainbridge A, Moore C, Ahmed H, Punwani S. Multiparametric Whole-body MRI vs. ^{18}FCH-PET-CT for the Primary Staging of Intermediate and High-Risk Prostate Cancer. The International Society for Magnetic Resonance in Medicine, Singapore

Awarded Magna Cum Laude

2016 **Johnston E**, Bonet-Carné E, Panagiotaki E, Stevens N, Atkinson D, Alexander D, Punwani S. Short term repeatability of microstructural (VERDICT) MRI vs. ADC in prostate cancer The International Society for Magnetic Resonance in Medicine, Singapore

Awarded Magna Cum Laude

Poster Presentations:

2017 **Johnston E**, Linch M, Goh G, Hiley C, Shanmugabavan Y, Antonelli M, Gerlinger M, Rowan A, Wong S, King H, Furness A, Freeman A, Linares L, Akarca A, Herrero J, Dentro S, Harder N, Schmidt G, Gareth G, McGranahan N, Birkbak N, Mitter R, Cathcart P, Scott R, Hung M, Emberton M, Attard G, Szallasi Z, Quezada S, Marafioti T, Ourselin S, Ahmed H, Swanton C, Punwani S. Lower Normalised T2 Signal Intensity is Associated with Higher Intratumoral Heterogeneity: A Radiogenomic Study in High-Risk Prostate Cancer. The International Society for

Magnetic Resonance in Medicine, Honolulu, Hawai'i

2017 **Johnston E**, Antonelli M, Dikaios N, Ourselin S, Atkinson D, Punwani S. Improving the Reproducibility of Quantitative Imaging Metrics for Multicentre Multiparametric Prostate MRI Trials. The International Society for Magnetic Resonance in Medicine, Honolulu, Hawai'i

2017 **Johnston E**, Appayya M, Allen C, Antonelli M, Dikaios N, Ourselin S, Punwani S. Single Slice (ROI) vs. Volumetric Analysis of Multiparametric Prostate MRI Metrics. The International Society for Magnetic Resonance in Medicine, Honolulu, Hawai'i

2017 **Johnston E**, Bailey C, Bonet-Carne E, Pye H, Heavey S, Patel D, Sridhar A, Siow B, Mertzanidou T, Devine W, Kalasthry J, Clemente J, Hawkes D, Whitaker H, Rodriguez-Justo M, Shaw G, Alexander D, Freeman A, Bourne R, Panagiotaki E, Punwani S. Why is the Peripheral Zone of the Normal Human Prostate High in ADC Value and T2-Weighted Signal Intensity? The International Society for Magnetic Resonance in Medicine, Honolulu, Hawai'i

2017 O'Callaghan J, **Johnston E**, Latifoltojar A, Sidhu H, Ramachandran N, Sokolska M, Bainbridge A, Punwani S. Improved lymph node staging using MRI mDixon fat fraction measurements in patients with intermediate and high-risk prostate cancer. The International Society for Magnetic Resonance in Medicine, Honolulu, Hawai'i

2017 Antonelli M, **Johnston E,** Cardoso M, Punwani S, Ourselin S. An mpMRI derived Logistic Regression Model for Gleason 4 Pattern Prediction in Peripheral Zone Prostate Cancer. The International Society for Magnetic Resonance in Medicine, Honolulu, Hawai'i

2017 Antonelli M, **Johnston E**, Cardoso M, Punwani S, Ourselin S. A New Multi-atlas Selection Strategy for Zone Segmentation of Prostate. The International Society for Magnetic Resonance in Medicine, Honolulu, Hawai'i

2017 Devine W, **Johnston E**, Bonet-Carne E, Punwani S, Alexander D, Atkinson D. Linking a multi-compartment T2 model to diffusion microstructure in prostate cancer. The International Society for Magnetic Resonance in Medicine, Honolulu, Hawai'i

2016 Devine W, **Johnston E**, Bonet-Carne E, Punwani S, Alexander D, Atkinson D. Microstructure prostate cancer heterogeneity using diffusivity distributions. In British Chapter of ISMRM, Leeds

2016 Panagiotaki E, Jacobs J, **Johnston E**, Freeman A, Patel D, Rodriguez-Justo M, Atkinson D, Punwani S, Brostow G, Alexander D. Histological validation of the VERDICT cellularity map. Comprehensive Imaging Cancer Centre First National Trainee Workshop, Fitzwilliam College, Cambridge

2016 Yvernault B, Antonelli M, **Johnston E**, Laitifolojar A, Punwani S, Ourselin S. Enabling large scale, robust data managrement and processing using cutting edge analysis for cancer imaging. Comprehensive Imaging Cancer Centre Conference, London

2016 **Johnston E**, Dikaios N, Sidhu H, Bonet-Carne E, Punwani S. Use of logistic regression models for the non-invasive characterisation of prostate cancer. Comprehensive Imaging Cancer Centre Conference, London

2016 Sidhu H, Benigno S, Ganeshan B, Dikaios N, **Johnston E**, Allen C, Kirkham A, Groves A, Ahmed H, Emberton M, Taylor S, Halligan S, Punwani S. Textural analysis of multiparametric MRI detects transition zone prostate cancer. International Society for Magnetic Resonance in Medicine, Singapore

2016 **Johnston E**, Cheung K, Dikaios N, Sidhu H, Appayya M, Simmons L, Freeman A, Ahmed H, Atkinson D, Punwani S. Logistic regression models may predict Gleason grade of prostate cancer in the peripheral zone but not the transition zone. International Society for Magnetic Resonance in Medicine, Singapore

2016 Jacobs J, **Johnston E**, Freeman A, Patel D, Rodriguez-Justo M, Atkinson D, Punwani S, Brostow G, Alexander D, Panagiotaki E. Histological validation of VERDICT cellularity map in a prostatectomy case. The International Society for Magnetic Resonance in Medicine, Singapore

2016 Bonet-Carne E, Daducci A, Panagiotaki E, **Johnston E**, Stevens N, Atkinson D, Punwani S, Alexander D. Non-invasive quantification of prostate cancer using AMICO framework for VERDICT MRI. The International Society for Magnetic Resonance in Medicine, Singapore

2016 Appayya M, Sidhu H, Dikaios N, **Johnston E**, Simmons L, Freeman A, Kirkham A, Ahmed H, Punwani S. Characterising Indeterminate Lesions (Likert 3/5) in the Peripheral Zone of the Prostate on Multi-parametric MRI. The International Society for Magnetic Resonance in Medicine, Singapore

2015 Panagiotaki E, Chan R, **Johnston E**, Ahmed H, Atkinson D, Punwani S, Hawkes D, Alexander D. Optimised VERDICT MRI protocol for prostate cancer characterisation. International society for magnetic resonance in medicine, Toronto, Canada.

1 INTRODUCTION

1.1 Thesis overview

Multiparametric (mp) MRI appears poised to revolutionise the prostate cancer management pathway, but nevertheless it is still falling short of its full potential due to limitations including subjective interpretation, the lack of standardization of analytical methods and an inability to adequately distinguish between Gleason grades. For example, whilst mp-MRI in clinical practice currently relies upon rudimentary analytical methods (visual inspection) and pulse sequences (T2W, ADC and DCE), more sophisticated quantitative analytical methods and biologically specific pulse sequences are available, which could potentially used to increase its performance. In addition, the ability of mp whole-body (WB) MRI to stage prostate cancer remains essentially unproven. The overall aim of this body of work is to develop quantitative and semiquantitative magnetic resonance prostate cancer imaging biomarkers to address some of these shortcomings.

This thesis is comprised of 10 chapters and is structured as follows:

Chapter 1 forms the introduction to the thesis. I provide an overview that outlines the content of each chapter, and then conduct a background literature review to justify my research aims. The background comprises section A, which considers the prostate itself, and section B, which focuses on extraprostatic disease. Section A provides an overview of prostate biology including its anatomy, development, physiology and histology with a particular emphasis on Gleason grading. Mp-MRI is then introduced, along with its current role and limitations, which form the problem statements for chapters 3 - 7. The biomarker development roadmap is introduced and will provide a framework to validate or devalidate imaging biomarkers throughout the thesis. Section B reviews the mechanisms of prostate cancer metastases, introduces the AJCC 'TNM' staging system (Tumor, Nodes, Metastases), justifies the importance of accurate cancer staging and then describes the limitations in current imaging staging methods to be addressed in chapters 8 and 9.

Chapter 2 details the MRI physics relevant to the contents of the thesis. Section A introduces the fundamentals of MRI physics including precession, excitation, relaxation, pulse sequences and diffusion. Section B focuses on the biophysical basis of T2-weighted (T2W) imaging, dynamic contrast enhanced (DCE) and diffusion modelling. Current limitations in biophysical modelling are discussed and serve as a

rationale for the use of quantitative mp and VERDICT (Vascular, Extracellular and Restricted Diffusion for Cytometry in Tumours) MRI as biomarkers in prostate cancer characterisation.

Chapter 3 states the research aims, objectives and hypotheses to be addressed in the thesis.

In **Chapter 4,** I consider how current analytical methods in quantitative imaging could be improved to reduce the heterogeneity between subsequent studies, as there is a lack of consensus in the literature regarding what constitutes optimal analysis. In section A, I investigate the agreement between single slice and volumetric analysis of prostate tumours using two different DICOM (Digital Imaging and Communications in Medicine) viewers and study the intra and interobserver precision of each method. In section B, I will investigate whether the scan-rescan reproducibility of simple quantitative imaging metrics (T2W, ADC and DCE) can be improved by normalizing to different anatomical structures, and assess whether it is preferable to use statistics derived from imaging histograms rather than the current convention of using mean values. The findings from these studies will thereby influence analytical methods throughout the thesis.

In **Chapter 5**, I use imaging data from the PICTURE (Prostate Imaging [multi-parametric MRI and Prostate HistoScanning™] Compared to Transperineal Ultrasound guided biopsy for significant prostate cancer Risk Evaluation) study to combine multiple Quantiative Imaging Biomarkers (QIBs) with prostate specific antigen (PSA) density in a logistic regression (LR) model for use as a potential tool to help classify a Gleason 4 component in prostate tumours non-invasively. This piece of work therefore seeks to combine the elements of the mp-MRI that are currently performed as part of routine clinical practice.

Chapter 6 introduces the INNOVATE (combining advances in imaging with biomarkers for improved diagnosis of aggressive prostate cancer) trial and the associated ethics application, which provides the framework in which I subsequently develop VERDICT as an imaging biomarker for prostate cancer characterization.

Chapter 7 uses a systematic approach to assess the clinical value of VERDICT MRI parameters as putative quantitative imaging biomarkers for non-invasive Gleason grade estimation, as per the imaging biomarker roadmap for cancer studies. I assess image quality, repeatability and the performance of quantitative parametric maps in

discriminating between Gleason grades vs. the current best performing, but still imperfect tool of ADC. This chapter therefore seeks to validate a new tool for Gleason grade prediction, which could supplement conventional mp-MRI.

Having worked towards the technical validation of new imaging biomarkers for the detection of aggressive prostate cancer within the prostate, I then aim to develop further tools which can detect nodal and osseous involvement in patients at high risk of metastatic disease.

Chapter 8 reports the findings of the MASTER (MRI Accuracy in Staging and Evaluation of Treatment Response in Cancer) study, whereby the diagnostic accuracy of WB-MRI will be compared with ^{99m}Tc bone scintigraphy (BS) and ^{18}F choline Positron Emission Tomography (PET)/Computed Tomography (CT), which are currently used as part of clinical care in our hospital. I am particularly interested in the optimal combination of pulse sequences that can achieve reasonable diagnostic accuracy within a clinically acceptable scan slot.

Chapter 9 presents the findings from the PROPS (PET/MRI pre-Radiotherapy for Post-Prostatectomy Salvage) study, which is a multicentre, multivendor, multinational trial whereby the image quality, interobserver agreement and diagnostic accuracy of WB-MRI will be considered in patients with biochemical failure following radical prostatectomy vs. ^{99m}Tc BS, conventional CT and ^{18}F-choline PET/CT.

Finally, **Chapter 10** summarises the thesis, provides a discussion, and makes recommendations for future research.

I have carried out all work myself unless otherwise stated in the declaration section at the beginning of each chapter.

1.2 Background

Section A: The Prostate

Anatomy

The adult prostate is a male composite sex organ located in the pelvis, which has an inverted pyramidal shape and a volume of around 30cc in health.

The modern understanding of the anatomy of the glandular prostate was provided by McNeal who introduced the concept of 'zones' in a 1981 paper (1), which replaced the older descriptions of lobes. These zones are best appreciated on T2-weighted (T2W) magnetic resonance imaging (MRI) and were first demonstrated in 1987 (2). The peripheral zone (PZ) has a longer T2 relaxation time and surrounds the lower signal central zone (CZ) and transition zone (TZ), which in turn surround the ejaculatory ducts and prostatic urethra respectively. The TZ tends to enlarge with age under the influence of testosterone in a process called benign prostatic hyperplasia (BPH), which can cause the gland to exceed 300ml in volume and gives rise to considerable anatomical variation.

The prostate is incompletely covered by nonglandular elements comprising the anterior fibromuscular stroma (AFS) which is continuous with the prostate 'capsule' (3), which surrounds the prostate. The *base* is related to the bladder superiorly and tapers inferiorly towards its *apex,* which is continuous with the distal urethral sphincter (DUS). The two seminal vesicles (SV) sit on either side of the gland base and open as ejaculatory ducts into the prostatic urethra, which runs vertically through the gland.

The aforementioned structures are demonstrated in Figures 1 – 3 (base to apex).

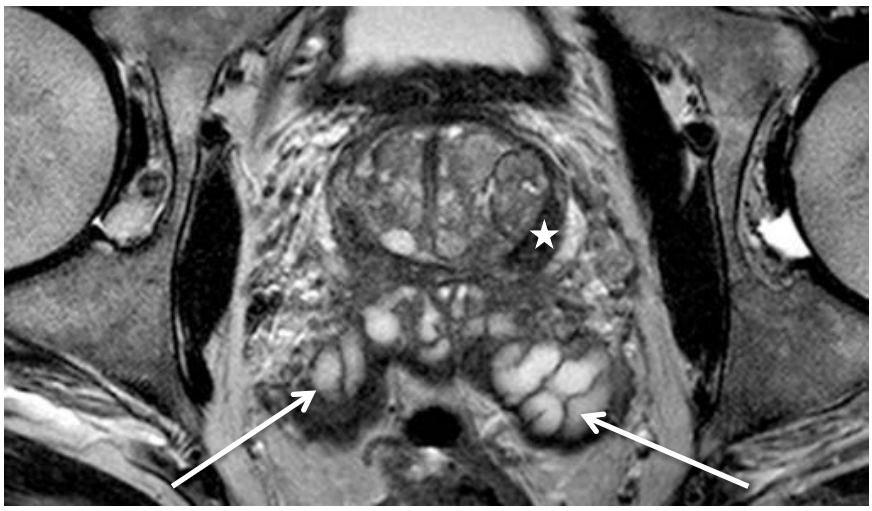

Figure 1: T2W turbo spin echo (TSE) at the gland base showing the SV (arrows) and CZ (star)

Figure 2: T2W TSE at the mid gland level showing the TZ (arrow) and PZ (stars)

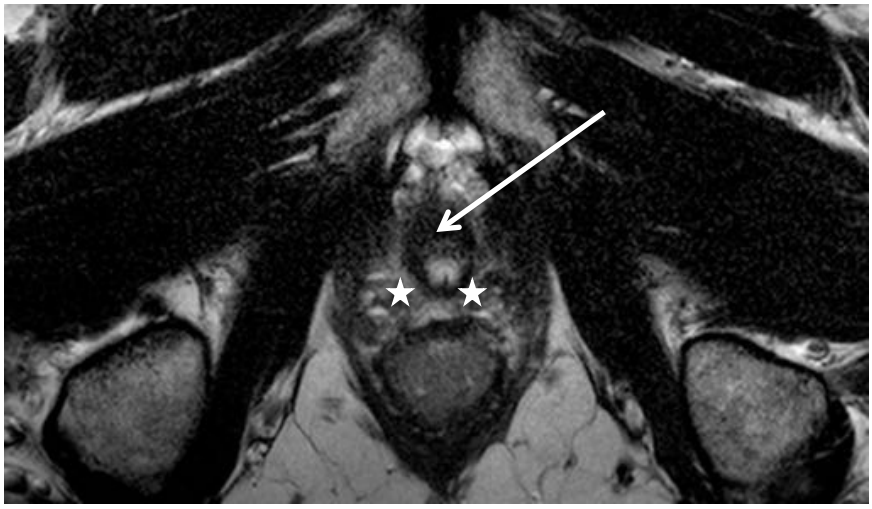

Figure 3: T2W TSE showing the apex (stars) and DUS (arrow)

The arterial supply is derived from multiple arteries, mainly the inferior vesical artery, which is a branch of the internal iliac artery, and to a lesser extent the middle rectal and internal pudendal arteries, all of which terminate as prostatic arteries and are distributed evenly throughout the prostate (4). Venous and lymphatic drainage will be considered in section B.

Development

The primordial prostatic buds develop from the urogenital sinus at about 10 weeks of life. Testicular androgens stimulate the endoderm and mesoderm to proliferate and differentiate into ductal structures prenatally, and remain similar until puberty when the adult phenotype develops. The CZ appears to derive from the mesonephric (Wolffian) ducts, which arise from the mesoderm whereas the TZ and PZ develop from the pelvic part of the urogenital sinus, which is derived from the endoderm (5).

Physiology and function

The main function of the prostate is to produce and release a thin citrate and acid phosphatase rich fluid for liquefaction of semen that contributes 30% of the ejaculatory volume and provides a favourable environment for fertilization. The smooth muscle cells are innervated by the inferior hypogastric plexus, which maintains both parasympathetic control of glandular secretion and sympathetic innervation to facilitate occasional but rapid muscular contraction during ejaculation. The prostate also has a mechanical role in preventing urinary incontinence (6).

Histology (microstructure)

30 - 50 tubuloalveolar glands are composed of pseudostratified columnar epithelium, which function as exocrine cells that secrete their products into a central lumen and empty into the prostatic urethra via tubules during ejaculation. Beneath the epithelial cells are basal cells, which rest on the basement membrane and regenerate the epithelium. The epithelium is in turn surrounded by connective tissue and smooth muscle to form the stroma within which the vascular, venous and lymphatic vessels are embedded (7). A photomicrograph of these normal histological appearances is provided in Figure 4.

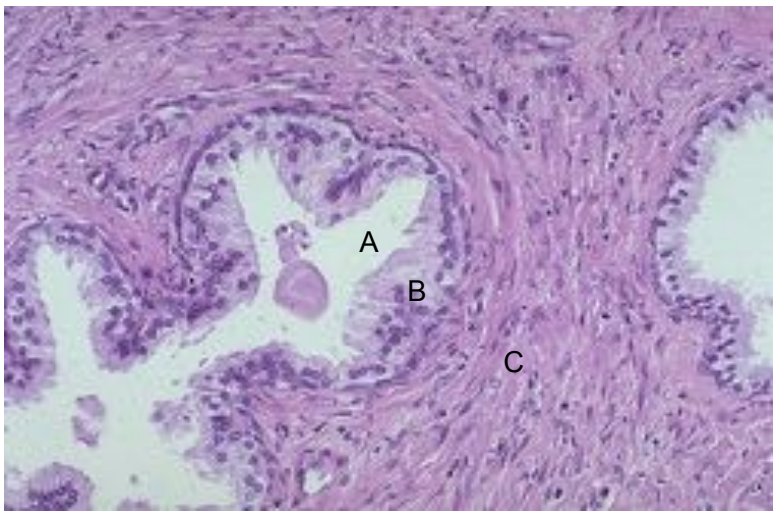

Figure 4: Photomicrograph of normal human prostate (H&E stain)

A: lumen, B: epithelium, C: stroma. Permission to reproduce this image has been granted by Dr Edward Klatt MD.

Histologically the TZ and PZ have similar glandular structure, although the PZ has a looser stroma with a higher proportion of ground substance, less collagen and elastin and fewer stromal elements to potentially proliferate into nodules. The CZ is easy to distinguish from the TZ and PZ as it is composed of more interleaving smooth muscle and complex, large polygonal glands (8). The TZ, PZ and CZ are demonstrated in figures 5 – 7 below.

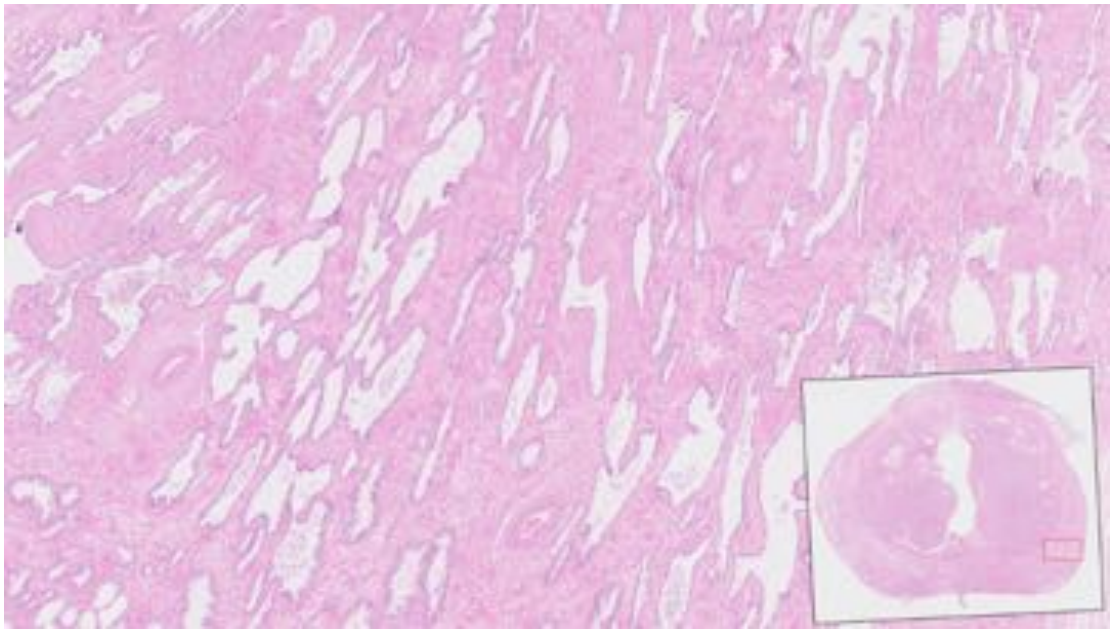

Figure 5: Photomicrograph of the PZ (H&E stain)

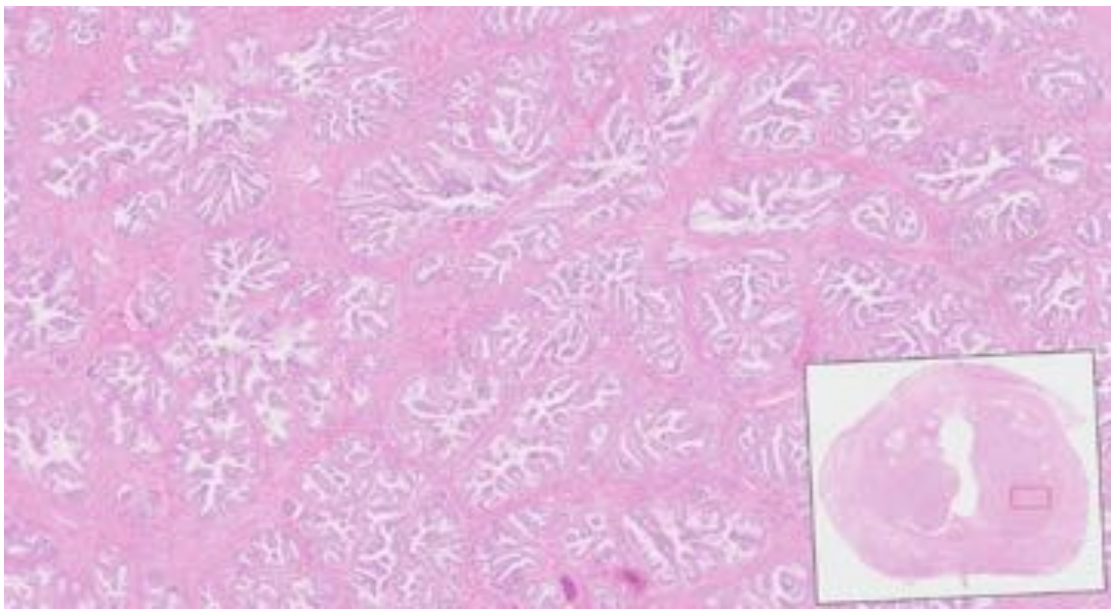

Figure 6: Photomicrograph of the TZ (H&E stain)

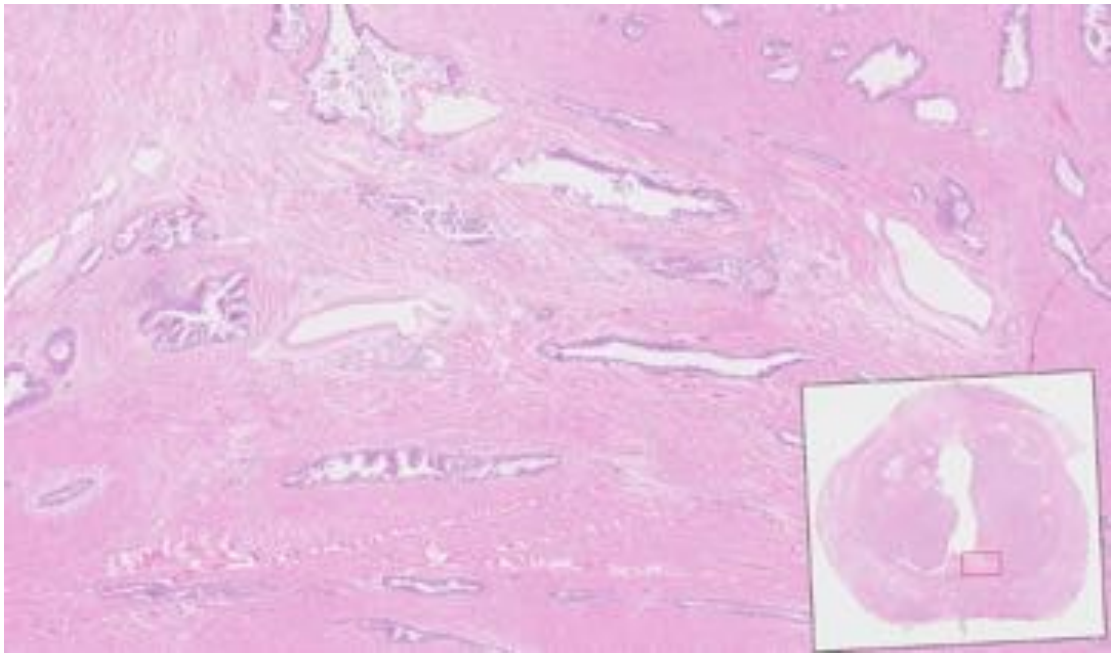

Figure 7: Photomicrograph of the CZ (H&E stain)

BPH

BPH is caused by an altered oestrogen:testosterone ratio, whereby the dihydrotestosterone (DHT) secreted by stromal cells causes increased growth factor (GF) transcription, bringing about an increase in cell number and stromal content with papillary buds, infoldings and cysts with a tendency towards squamous metaplasia and infarction (5). The stromal-to-epithelial ratio has been shown to change from 2:1 in the healthy prostate to 5:1 in men with BPH (9). T2W MRI appearances of the normal transition zone vs. BPH are shown in figure 8.

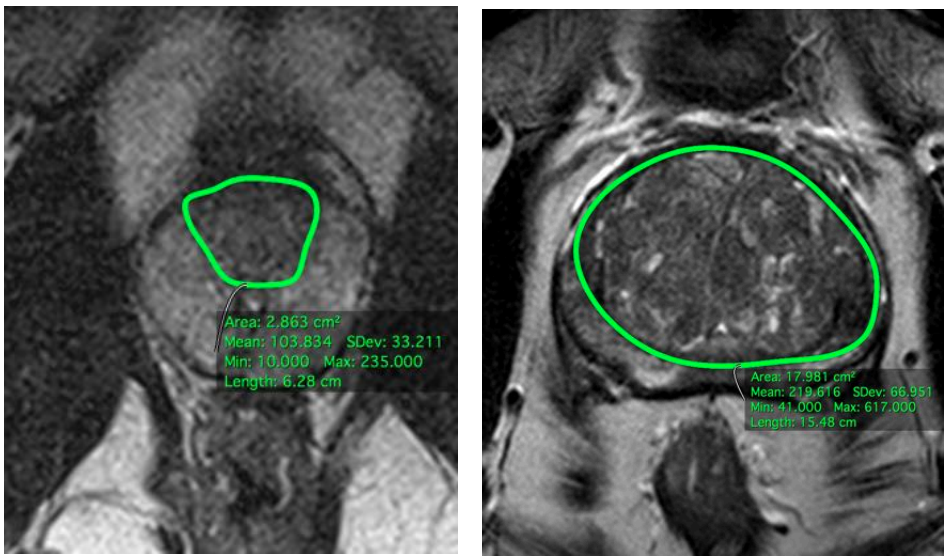

Figure 8: T2W TSE showing a segmented normal TZ (left) and a TZ affected by BPH (right)

Note the difference in the size of the TZ in both prostates (2.9 vs. 18.0 cm^2).

Prostate cancer

Epidemiology

Prostate cancer is the most common cancer in Western males with more than 40 000 new cases diagnosed per year in England and Wales (10). The incidence of prostate cancer is increasing, in part due to the impact of prostate specific antigen (PSA) screening and triple assessment (covered later).

The three well established risk factors associated with prostate cancer are increasing age, ethnic origin (with higher rates in Afro-Caribbean men) and family history. It has also been observed that higher levels of insulin-like growth factor I (IGF-1) are encountered in men with prostate cancer, which may explain its association with the sedentary western lifestyle, which increases its production (11).

Whilst prostate cancer poses a significant economic and health burden to healthcare systems, most cancers will remain clinically occult and will not reduce life expectancy, even if left untreated. For example, an autopsy series of 249 cases showed incidental small prostate carcinomas in up to 20% men aged 30 to 40 and 64% men aged 60 to 70 (12). This raises some difficult questions regarding an optimal strategy for screening, diagnosis, management and follow-up of disease and is why prostate cancer remains one of the most controversial topics in the medical literature.

Histopathology

Adenocarcinoma is by far the most common histological cancer subtype (95%), and arises from acinar or ductal epithelium, likely from a precursor of prostatic intraepithelial neoplasia (13). Other cancer subtypes include transitional cell carcinoma, sarcoma and neuroendocrine tumours. 70% of adenocarcinomas arise in the PZ, 24% in the TZ and 8% in the CZ (14). As cancers progress, malignant cells breach the basement membrane and invade into the lumen and stroma.

In 1966, Dr. Donald F Gleason (a Minnesotan pathologist) published a unique grading system for prostate cancer based on architectural features at low-to-medium magnification, using Haematoxylin and Eosin (H&E) stain (15) which stains the nuclear chromatin and cytoplasmic material purple and orange-pink respectively. Appearances were classified into five 'Gleason grades' based on the extent of glandular differentiation and stromal invasion. The original diagram drawn by Dr. Gleason is shown in figure 9 below.

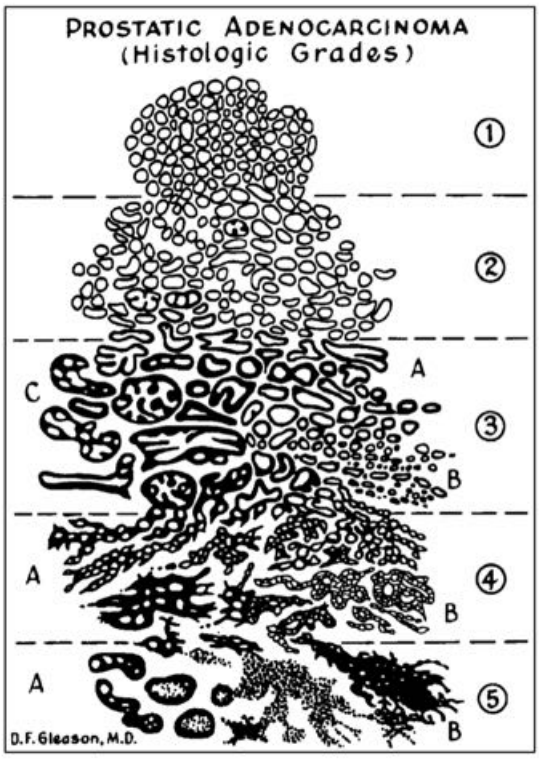

Figure 9: Original drawing of proposed Gleason grading system by Dr. Donald Gleason

Permission to reproduce this image has been granted by the Nature Publishing group.

The Gleason score is the sum of the two most prevalent patterns seen (primary and secondary) and may therefore range from 2 to 10. If only a single pattern is present, the two patterns are assigned the same grade. A considerable strength of the Gleason

grading system is that it has been prospectively validated in cohorts totalling around 5000 patients, with overall and cancer-specific survival as end points (16). Typical examples of each Gleason grade are provided in figures 10 – 14 below, whereby permission to reproduce these images has been granted by the Nature Publishing Group (16).

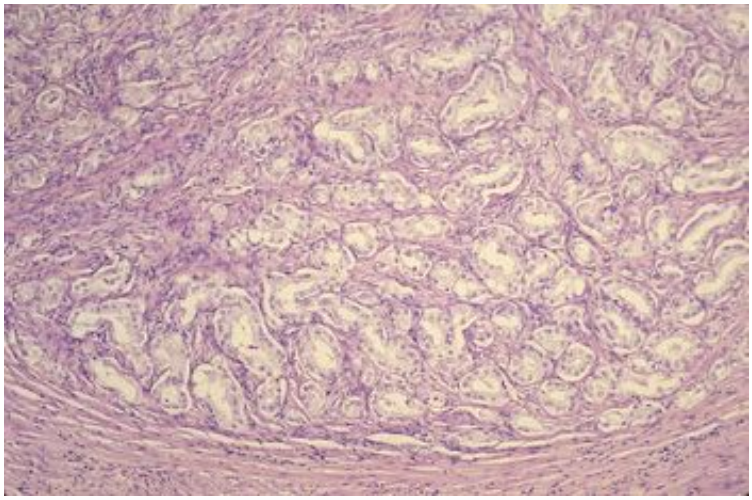

Figure 10: Photomicrograph showing Gleason grade 1 (H&E stain)

Gleason 1 closely resembles the normal prostate and has small, rounded, uniform, closely packed and well-circumscribed glands without evidence of stromal infiltration.

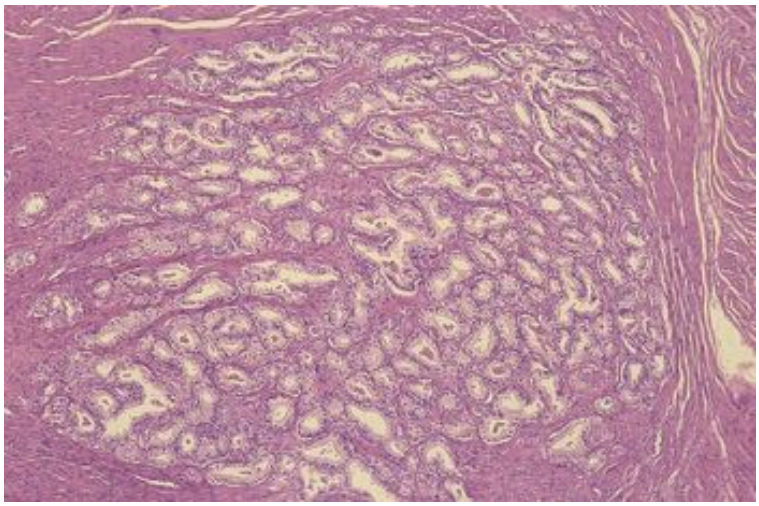

Figure 11: Photomicrograph showing Gleason grade 2 (H&E stain)

Gleason 2 also closely resembles normal prostate, although has greater variability in gland size and shape with a higher proportion of stroma separating the glands than Gleason 1. However, glands are larger than in pattern Gleason 3. Both Gleason patterns 1 and 2 are rare entities and are not reported clinically due to poor reproducibility, often with incorrect grading of higher-grade cancer (17).

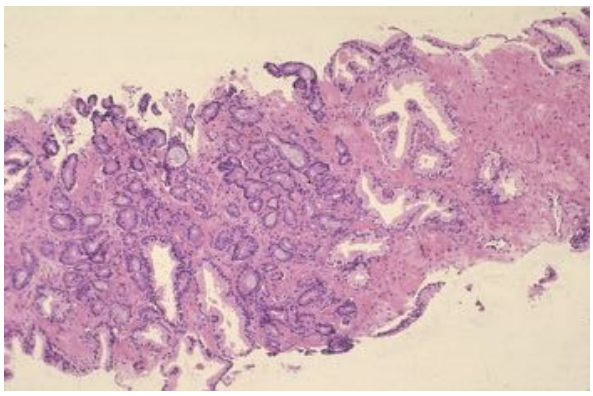

Figure 12: Photomicrograph showing Gleason grade 3 (H&E stain)

Gleason 3 is the most common score, and shows more variability in glandular distribution than in Gleason pattern 2. Glands are less well formed with irregular separation, ragged and poorly defined and slightly infiltrative edges. On the whole, glands are smaller with a lower proportion of stroma than in Gleason 1 and 2.

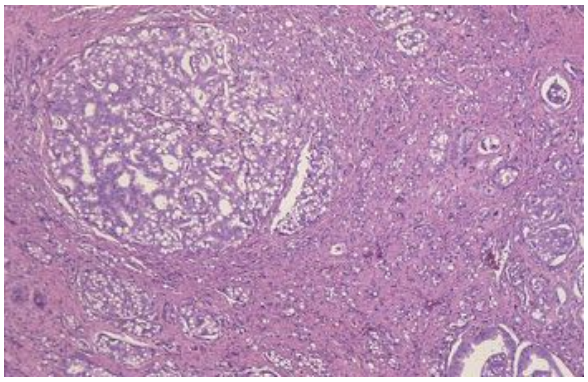

Figure 13: Photomicrograph showing Gleason grade 4 (H&E stain)

Gleason 4 tumours have pseudoacinar or cribriform glands that are coalescent, fused and poorly defined without intervening stroma and high degrees of infiltration.

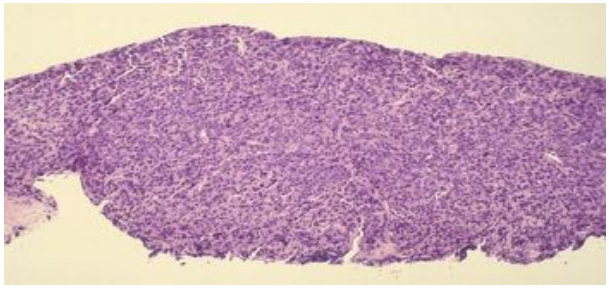

Figure 14: Photomicrograph showing Gleason grade 5 (H&E stain)

Gleason 5 cancer has no discernible glandular lumen, with necrotic sheets of epithelial cells.

Ancillary features used to diagnose and grade prostate cancer include increased nuclear-to-cytoplasmic ratio, nuclear atypia and intraluminal features including loss of corpora amylacea and deposition of crystalloids.

Whilst Gleason scoring in clinical practice is formed by the subjective opinion of a trained uropathologist analysing multiple complex features, digital pathology methods offer the potential for objective and quantitative measurements of some of these features. Groups have shown that segmented percentages of lumen, stroma and epithelium differ significantly between benign and cancerous regions, and also change significantly with increasing Gleason grade, whereby the percentage of lumen and stroma decrease as epithelium increases (18,19).

Clinical significance of Gleason grade

In a landmark paper, Albertsen *et al.,* (20) reported upon the natural progression of prostate cancer for each Gleason grade whereby 767 men were treated with observation or delayed androgen depravation therapy (ADT) alone, with 20 year follow up. Mortality rates per 1000 person years were 6, 12, 30, 65 and 121 for Gleason grades 2-4, 5, 6, 7, and 8-10 respectively. Fifty years after its initial description, Gleason grade remains the single most important predictor of survival in prostate cancer (21), and it is therefore imperative that assays of cancer grade are as accurate as possible.

In addition, there is growing evidence that making a distinction between Gleason 3 and Gleason 4 cancer is particularly important, due to their different genomic signatures (22,23) and natural histories (24,25). Indeed, some authors have questioned whether Gleason 3 should be labelled cancer, as it fails to meet the hallmarks of cancer on multiple counts (26), occurs normally with age (27,28) and doesn't metastasize (29).

The traditional prostate cancer diagnostic pathway

The management of prostate cancer was revolutionized by the introduction of triple assessment in the 1990s, which combines digital rectal examination (DRE) and serum PSA level with transrectal ultrasound (TRUS) guided biopsy. The National Institute of Health and Clinical Excellence (NICE) have recommended triple assessment as the standard of care ever since this approach was first proposed (30) but even when used in combination each of these tests have inherent flaws, which will be outlined

subsequently.

DRE

DRE is used to detect cancers adjacent to the rectum, which are harder than the normal prostate on palpation. Despite the fact that most cancers being located in the PZ (near the rectal wall), tumour detection is dependent upon clinical experience and subject to substantial interobserver error (κ=0.63) amongst experienced urologists (31). Furthermore, its sensitivity is poor at 37% (with a 91% specificity) meaning nearly 2/3 of tumours will be missed by DRE, even in experienced hands (32).

PSA screening

PSA is a glycoprotein enzyme produced by normal prostate epithelium, which liquefies seminal fluid coagulum and plays an important role in fertility. Whilst the highest concentration of PSA is found in the seminal fluid, a small quantity escapes the prostate and enters the bloodstream (33) which causes a rise in serum PSA levels. Whilst increased serum PSA is observed in prostate adenocarcinoma, BPH and prostatitis may also cause false positive results. False negative results may be found in tumours which do not secrete PSA e.g. neuroendocrine tumours – a rare but lethal cancer subtype (34).

PSA testing consequently has a fairly flat receiver operating characteristic (ROC) curve with an AUC of 0.7 i.e. it is relatively poor at predicting or excluding significant prostate cancer at all diagnostic levels (35). Whilst PSA density levels (PSA level/gland volume), act to normalize the gland volume effect from BPH (36), its performance characteristics appear to yield only slight improvement (37), which drives the need for more specific circulating biomarkers in the diagnosis of prostate cancer. Circulating biomarkers in serum, plasma, urine, and prostatic fluid have all been explored, but thus far remain invalidated in large cohorts collected under standardised conditions.

TRUS biopsy

TRUS guided biopsy involves sampling the prostate with core biopsies under TRUS guidance using a semi-systematic approach. However, TRUS systematically misses the anterior prostate and the extreme apex, posterior midline tumours, CZ and extreme basal tumours are also commonly under sampled (38). TRUS also has a false negative rate of up to 40% (39), may detect clinically unimportant tumours (40) and localises disease poorly due to tangential needle deployment.

Multiparametric prostate MRI at University College London Hospital (UCLH)

Multiparametric (mp) prostate MRI employs a combination of different pulse sequences in a single examination, due to the advantages and limitations of each sequence. Scanning protocols have been established on 1.5 and 3 Tesla (T) machines at our institution and are compliant with UK (41) and European (42) guidelines. We administer 0.2 mg/kg (maximum 20 mg) of spasmolytic (Buscopan; Boehringer Ingelheim, Ingelheim, Germany) intravenously prior to scanning to reduce rectal peristalsis and 0.2ml/kg intravenous macrocyclic gadolinium based contrast agent (GBCA) (Prohance, Bracco, Milan, IT) at the beginning of the 6th acquisition at 3ml/s followed by a saline flush of 20 ml for dynamic contrast enhanced (DCE) imaging. Notably, we maintain spatial resolution at a cost of temporal resolution for DCE images using a ≥12s sampling time between frames. Alongside the b=0, b=150, b=500 and b=1000s/mm^2 used to generate the Apparent Diffusion Coefficient (ADC) map which use 16 signal averages, we acquire a separate high b-value DWI acquisition (b=1400 and 2000s/mm^2 at 1.5 and 3T respectively) with 32 signal averages to increase the sensitivity for small and TZ tumours (43).

Examination protocols at 1.5 and 3T are provided in tables 1 and 2 respectively. We have 3 machines at 1.5T, all of which are Siemens Avanto (Siemens Healthcare, Erlangen, Germany) scanners and have the same scanning protocol. The 3T scanner is a Philips Achieva (Philips Healthcare, Eindhoven, NL).

Sequence	TR	TE	FA degrees	BW Hz/Px	FoV mm	ST mm	Gap	ETL	Phasing direction	FS	Matrix base
T2 TSE Coronal	5240	104	150	190	180	3	0.3	24	R>L	No	256
T2 axial TSE 3mm	5170	92	180	191	180	3	0.3	22	A>P	No	256
ep2d Diffusion b0 150 500 1000	2100	96	0	968	260	5	0	172	A>P	Yes	172
ep2d Diffusion b1400	2200	98	0	968	320	5	0	172	A>P	Yes	172
T1 VIBE 5degrees	5.61	2.5	5	300	260	3	0.6	0	A>P	Yes	192
T1 VIBE 20degrees	5.61	2.5	20	300	260	3	0.6	0	A>P	Yes	192
T1 VIBE 10degrees	5.61	2.5	10	300	260	3	0.6	0	A>P	Yes	192
T1 VIBE 15degrees	5.61	2.5	15	300	260	3	0.6	0	A>P	Yes	192
T1 VIBE 25degrees	5.61	2.5	25	300	260	3	0.6	0	A>P	Yes	192
T1 Flash 3d match VIBE	10.4	4.78	15	130	260	3	0.6	0	A>P	Yes	256

Table 1: UCLH prostate MRI acquisition protocol at 1.5T

VIBE = Volumetric Interpolated Breath-hold Examination, TR = repetition time, TE = echo time, FA = flip angle, ST = slice thickness, ETL = echo train length, BW = bandwidth, FS = fat saturation

Sequence	TR	TE	FA degrees	BW Hz/Px	FoV mm	ST mm	Gap	TSE factor	Phasing direction	FS	ACQ matrix	Total scan duration
T2 sag REF	1579	100	90	217.3	240	5	5	20	A>P	No	120 x 89	00:18.9
T2 TSE coronal	6128	100	90	160.7	180	3	3	16	R>L	No	300 x 290	05:55.4
T2 TSE axial	5407	100	90	160.7	180	3	0	16	R>L	No	300 x 290	05:13.6
DWI 0 150 500 1000	2753	80	90	10.8	220	5	0	-	A>P	SPAIR	168 x 169	05:16.5
DWI b2000	2000	78	90	9.9	220	5	0	-	A>P	SPIR	168 x 169	03:40.0
DCE 20 dyn mod SENSE	5.8	2.8	10	246.1	180	3	0	-	R>L	SPAIR	140 x 162	04:14.1

Table 2: UCLH prostate MRI acquisition protocol at 3T

Applications

The use of mp-MRI, performed prior to targeted biopsy has brought about a revolution prostate cancer care at UCLH, where we perform >3000 examinations annually. Sensitivities and specificities of 70%–90% and 61%–89% respectively have been reported for the detection of clinically significant cancer (44–46), which make it the most sensitive and specific imaging technique available for this purpose (47). Of particular importance is the recently published multicentre UK-based PROMIS study (48) in which 576 men underwent both mp-MRI performed at 1.5T and TRUS biopsy, using 5mm template mapping biopsy (TPM) as the reference standard. The study showed sensitivities and specificities of 93% and 41% for mp-MRI, compared with 48% and 96% for TRUS biopsy for the detection of clinically significant cancer. The authors concluded that if mp-MRI is used as a triage test in cases of suspected cancer, a quarter of TRUS biopsies could be avoided. An example of a typical positive prostate detection mp-MRI is provided in figure 15 below.

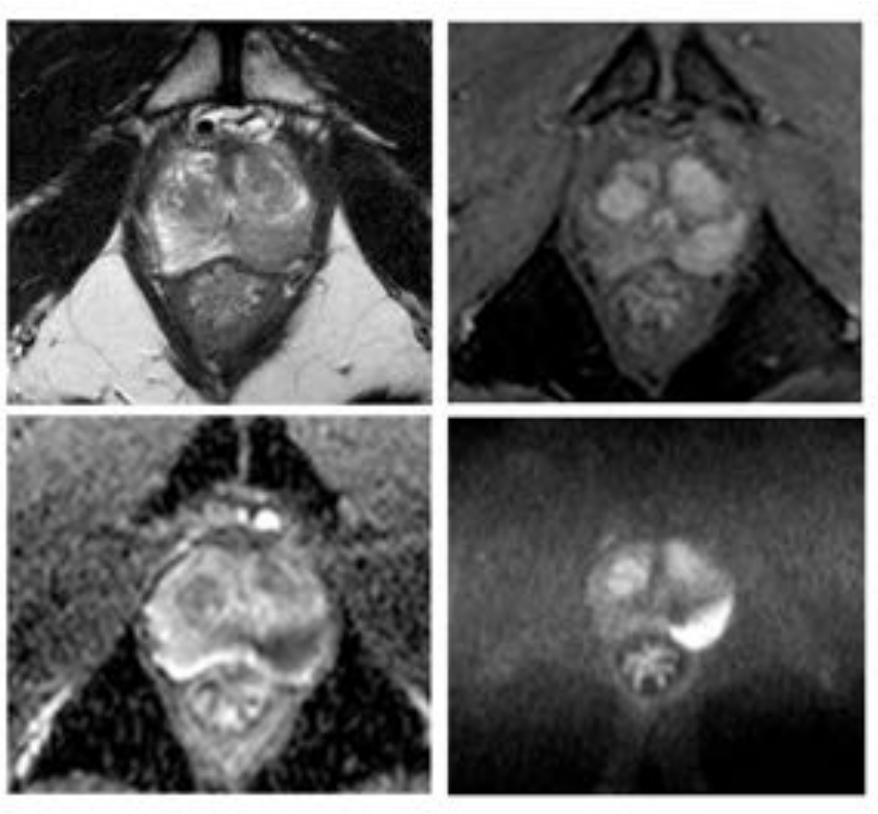

Figure 15: mp-MRI showing a typical Likert 5 lesion

Top left: T2W TSE showing a region of low T2 signal in the left PZ at midgland level extending from 3 to 6 o'clock. Top right: DCE images showing lesional enhancement. Bottom left: ADC map showing restricted diffusion within the lesion. Bottom right: b= 2000 s/mm^2 showing high lesional signal intensity.

In addition to cancer detection and avoidance of biopsy, mp-MRI can localize and stage tumours (49), guide biopsy (50), increase the detection of high-risk lesions and reduce unnecessary detection of low-risk lesions vs. TRUS (51). Other emerging applications include the facilitation of focal therapies (52), monitoring in active surveillance programs (53) and for detecting recurrence following treatment (54). In this way, mp-MRI can help inform decisions at almost every stage of the prostate cancer management pathway. However, there are still a number of limitations with mp-MRI, which will now be considered.

Limitations

Human observers interpret medical images in a complex, subjective, but educated mental process that is poorly understood (55), whereby each of the available sequences is interpreted in combination and an opinion given as to the suspicion of cancer. Whilst reports were initially constructed in a disparate and unstructured manner (56), ordinal scoring systems have since been adopted, influenced by their success in Breast Radiology. Here, impressive reduction in inter and intra-observer variability was shown (57) with subsequent integration into standard clinical practice (58).

The Likert scale is the simplest of the scoring systems, and was first proposed in 2011 (59). The overall impression of cancer likelihood is provided using a 1- 5 scale (42) 1: highly unlikely, 2: unlikely, 3: equivocal, 4: likely and 5: highly likely for the presence of clinically significant tumour, rather than a the traditional binary present/absent system. This scale may also incorporate clinical suspicion (considering clinical history, PSA etc.) in addition to imaging appearances. In 2012, ESUR proposed the Prostate Imaging Data and Report System (PI-RADS) score which also uses a five-point scale, but scored lesions on each individual sequence and provides clear definitions as to what constitutes a 1 – 5 score (60) based on consensus opinion and literature review. PI-RADS™ version 2 was published with updated guidelines in 2015, in consensus with the American College of Radiology (61). PI-RADS v2 introduced a common lexicon for reporting and introduced the concept of 'dominant sequences' (62) which simplified PI-RADS and gave a greater bearing on the final score, namely T2 for the TZ and DWI for the PZ.

However, such scoring systems are still imperfect. For example, interobserver agreement for all scoring systems (as measured by Cohen's κ) is around 0.4 – 0.7 (63–66), and require prospective validation which takes several years to perform and must be repeated each time guidelines are changed.

Quantitative MRI

Whilst MRI emerged from nuclear magnetic resonance (NMR) – developed for the quantitative analysis of chemical substances, its quantitative origins were all but abandoned by the clinical community following spatial encoding. However, MRI still affords the opportunity to objectively measure tumoural biophysics (considered in detail in the next chapter) which could reduce inter and intra observer variability and support clinical decision making e.g. in the contexts of avoiding, triggering and targeting biopsy for MR-positive lesions, monitoring patients for change in status whilst on active surveillance and when making decisions regarding treatment.

The ability of quantitative MRI to make a non-invasive, *in vivo,* whole lesion assessment of disease status is particularly appealing because biopsies are subject to sampling error (67–69) and as invasive procedures confer multiple theoretical risks. Specifically, the National Institute for Health and Care Excellence (NICE) special advisers committee recognise septicaemia, bleeding, urinary tract infection and haematuria as potential adverse events (70). Not only does e*x-vivo* tissue lose physiological information, registering each core to its true *in vivo* location remains an

issue, as does tissue shrinkage, breakage and distortion during slide preparation. In addition, intraobserver and interobserver agreement of κ =0.66 and κ=0.54 have been demonstrated amongst consultant UK pathologists (71).

Whilst 'virtual biopsy' using quantitative MRI could potentially address some of these shortcomings, we face a number of challenges before imaging biomarkers can be used to inform clinical decision-making.

Definitions

Quantitative imaging is a metrological discipline, and a common lexicon has been set out in consensus documents (72–77). Key definitions and considerations will be provided, using direct quotations where necessary to accurately preserve their meaning.

Quantitative imaging is defined as *"the extraction of quantifiable features from medical images for the assessment of normal [findings] or the severity, degree of change, or status of a disease, injury, or chronic condition relative to normal [findings]"* (72). Characteristics that are measured to reflect structure or function of normal or pathological processes are called biomarkers, and have been defined by the Food and Drug Administration (FDA)-National Institutes of Health (NIH) Biomarker Working Group as an: *"Indicator of normal biological processes, pathogenic processes, or responses to an exposure or intervention, including therapeutic interventions"*(78). Biomarkers may be used to detect whether disease is present or absent (diagnostic biomarker), identify a clinical endpoint (prognostic biomarker), or identify those likely to respond to a treatment (predictive biomarker)(78).

These notions have been combined to produce a definition for a **quantitative imaging biomarker (QIB):** *"…an objective characteristic derived from an in vivo image measured on a ratio or interval scale as an indicator of normal biological processes, pathogenic processes or a response to a therapeutic intervention."* (72).

Bias concerns the absence of systematic error from the true value of the measurand (the measurement in question), whereas **precision** represents the agreement between quantitative values obtained by replicate measurements (absence of random error). Precision may be tested under the same experimental conditions; **repeatability**, or different experimental conditions; **reproducibility**.

Limitations of quantitative imaging biomarker research

Despite a mounting body of literature concerning quantitative imaging biomarker research (as evidenced by the PubMed search result in figure 16), only a handful of magnetic resonance imaging biomarkers have been translated to clinical practice (79), and usually characterize tumour burden (such as 'TNM' staging or RECIST (Response Evaluation Criteria in Solid Tumors)) rather than physiology or microstructure. The reasons behind this are multifactorial and largely due to lack of standardization of the multiple variables that are required to form and analyse an MR image. For example, clinical workflows favour high throughput anatomical images rather than reliable quantitative measurements, meaning there is a lack of competition between vendors to develop better-calibrated machines. This leads to considerable heterogeneity in study methods, inconsistent results and adds to the 'reproducibility crisis' which is being experienced throughout science (80).

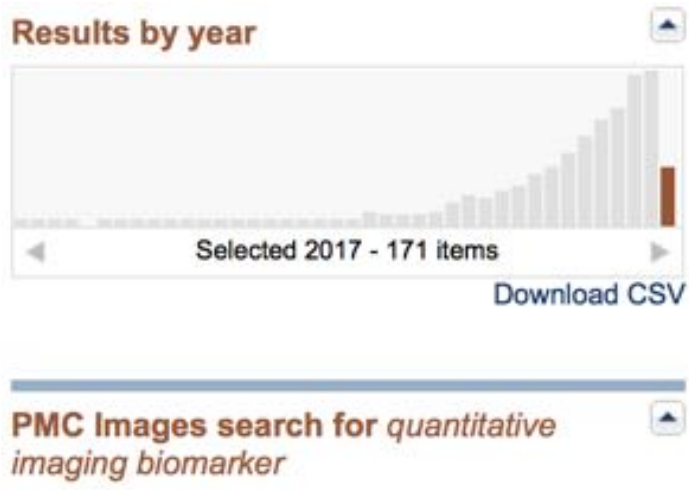

Figure 16: Results from a PubMed search for 'quantitative imaging biomarker'

Carried out 6/5/2017

One of the objectives of a quantitative imaging researcher should be to assess and minimize sources of unwanted variation in the measuring system to expose the true biological variation within or between subjects. A summary of the sources of this variation provided in table 3 (constructed with the assistance of (79,81)).

Image data collection:	**Image analysis:**
Room temperature	Image viewing conditions:
Hardware:	*Display window, image magnification, viewing*
Vendor, field strength, coil architecture, institutional	*distance, ambient lighting*
maintenance	Artefacts
Scanner software platform/version	Analytic software
Acquisition parameters	Changes in analysis software over time
Shim quality	Inter observer error
Signal/contrast to noise ratio	Intra observer error
Radiographer technique/experience	
Image artefacts	
Post processing techniques	
PACS storage	
Vendor competition	
Scanners poorly established for quantitative imaging	
Patient factors:	***True differences in biophysical properties***
Patient size/shape/cooperativeness	
Repositioning between examinations	
Movement artefact	
Bowel gas artefact	

Table 3: Causes of variation within an MRI measuring system

Improving quantitative imaging biomarkers

The imaging community has assembled a number of organisations to reduce this variation, including the Quantitative Imaging Biomarkers Alliance (QIBA, from the RSNA), the Quantitative Imaging Network (QIN, from the National Cancer Institute), and the International Society for Magnetic Resonance in Medicine (ISMRM) *ad hoc* committee on standards for quantitative MRI. Indeed, the mission statement of QIBA is to: *'Improve the value and practicality of quantitative imaging biomarkers by reducing variability across devices, patients and time'* (72).

A **'qualified'** imaging biomarker must possess the following characteristics in prospective, adequately powered patient cohorts (73,79,82):

1. Technical validation: precision and absence of bias
2. Biological validation: relationship of the biomarker to the disease process in question
3. Clinical validation: Diagnostic performance characteristics with the disease process in question (sensitivity, specificity, predictive values). N.B. this is not equivalent to forecasting clinical outcome, which defines a *surrogate* biomarker, or clinical *utility* whereby contributions to patient management are considered.

Additional considerations include cost effectiveness, availability and tolerance of the biomarker.

In order to facilitate the process of imaging biomarker qualification, a Biomarker Roadmap was produced as a consensus document with the backing of Cancer Research UK (CRUK) and the European Organisation for Research and Treatment of Cancer (EORTC) (79). Here, a stepwise development pipeline is recommended, whereby biomarkers are discovered, assessed in terms of repeatability early on, combined with biological validation as summarized in figure 17.

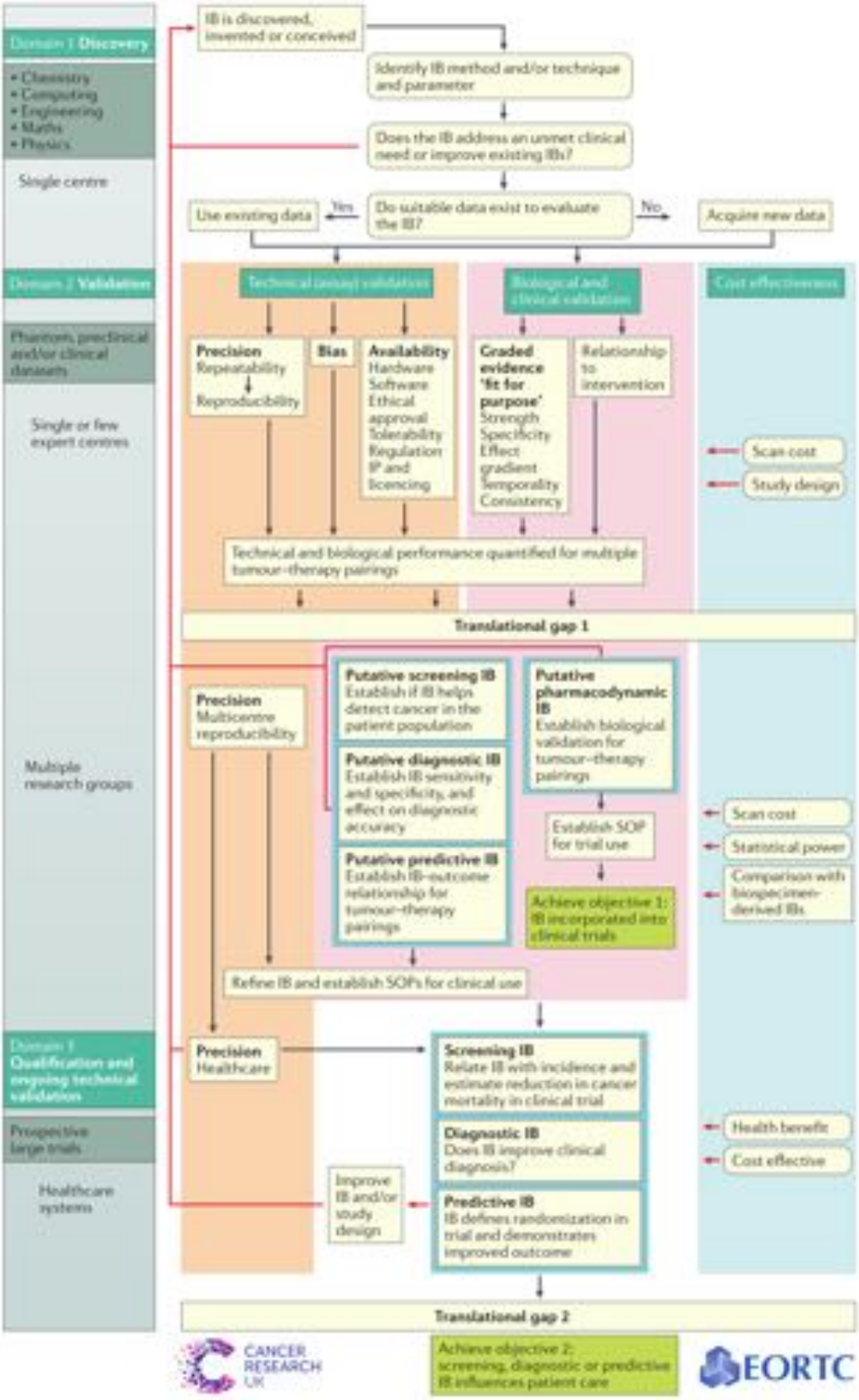

Figure 17: The imaging biomarker roadmap for cancer studies

This image is distributed under a creative commons license.

On the whole, research should therefore progress from simple to more complex methods, measuring and reducing bias and precision at each stage where possible. A number of experimental frameworks are available at UCL to test the value of emerging biomarkers. Their advantages and disadvantages are considered in table 4 below, along with the research groups that have the facilities to perform them.

	Advantages	**Disadvantages**
Computer simulation	Cheap Convenience No ethics required	Least realistic
Phantom	Need temperature control Convenience Stability Can know 'truth value' No ethics or recruitment required Can scan at higher field strengths	Unrealistic: no anatomy, physiology or pathology
Biophantom	Need temperature control Relative convenience Can know 'truth value' No ethics or recruitment required Can scan at higher field strengths	Can be difficult to make Not very realistic No anatomy Little physiology or pathology
Animal	Homeostasis controls temperature No recruitment required Can scan at higher field strengths High throughput *In* and *ex vivo* experiments Can mimic pathology in a controlled way Physiology and pathology Can control therapies	Project and personal license No human anatomy/physiology or pathology
Healthy human volunteer	Homeostasis controls temperature Human anatomy and physiology Can control for age and gender etc. Generally compliant	Requires ethics Less convenient No pathology No therapy response Often unethical to give contrast
Patient with disease	Homeostasis controls temperature Ideal: human anatomy, physiology and pathology Can study therapy response	Inconvenient: Ethics, difficult to recruit to

Table 4: Experimental frameworks for biomarker validation

CMIC; the Centre for Medical Image Computing, CABI; the Centre for Advanced Biomedical Imaging; CMI; the Centre for Medical Imaging.

No different from other areas of research, biomarker development studies have

historically been incompletely reported which has motivated the EQUATOR (Enhancing the QUAlity and Transparency Of health Research) network to produce the REMARK (REporting Recommendations for Tumor MARKer Prognostic Studies) guidelines (83), which provide a checklist for reporting biomarker studies, albeit with a focus on non-imaging tumour markers. Others have advocated the prospective registration of trial protocols on clinicaltrials.gov (84), and/or publication of research protocols prior to data collection (85) to hold the research team to account (e.g. avoiding multiple *post hoc* comparisons) and to promote reproducible research.

Extracting quantitative imaging metrics

Quantitative features are usually extracted by manually placing a region/volume of interest (ROI/VOI) around a region of pathological tissue in a process also called segmentation, which requires *a priori* knowledge of anatomy and pathology.

Since every image pixel is a greyscale representation of a quantitative value of signal intensity or measured biophysical behaviour, ROIs are in fact a matrix of numbers, which can be represented as a frequency histogram. Multiple statistical descriptors can be extracted from the histogram, but by far the most widely used is the mean value. Other histographic descriptors, which negate spatial information but provide measures of imaging heterogeneity include SD, entropy, skewness and kurtosis. However, their repeatability and reproducibility are uncertain (86,87) and thus are at an earlier stage of biomarker development than typical mean values. Since ROI/VOI placement is also subjective, measurements are subject to inter and intra observer error, and optimal analytical methods remain essentially uncertain.

Section A summary and future directions

In summary, Gleason grade is the most important predictor of prostate cancer survival and QIBs that could help predict Gleason grade would have multiple potential clinical applications.

In order to achieve this, the precision of potential biomarkers must be considered in terms of their repeatability, reproducibility, intra and interobserver error and developed in a systematic way, adhering to the biomarker development pipeline. Prospective imaging biomarker development trials should also be registered on an appropriate trial database, and reported according to REMARK guidelines.

1.2 Background

Section B: Nodal and metastatic prostate cancer

Prostate cancer cells must overcome multiple steps in order to spread to other sites. Whilst still at the primary site, cells lose their cell adhesion molecules, invade and degrade the local stroma, with distant spread subsequently occurring via two possible routes; the lymphatic system or (neo)vasculature.

Lymphatic system

The lymphatic system is composed of blind ending capillaries lined by endothelial cells, which collect and drain macromolecules and interstitial fluid to lymph nodes, where lymphocytes and antigen presenting cells mediate the immune system. Lymph is transported from the nodes, along the thoracic duct (in addition to chyle from the digestive system) and then returned to the circulation at the confluence of the left brachiocephalic vein. This pathway is generally preferred to the vascular alternative because lymph vessels are larger in calibre than smaller capillaries, lack a basement membrane and flow velocities are an order of magnitude slower than in the systemic circulation and have a closer chemistry to interstitial fluid than blood, which promotes cell viability(88). The initial route of spread in prostate cancer tends to be via the pelvic lymph nodes, which forms the basis for pelvic lymph node dissection (PLND) as a treatment strategy(89).

Nodal anatomy

The regional nodes in prostate cancer consist of the internal and external iliac lymph nodes, along with perivisceral lymph nodes. The external iliac group is located adjacent to the external iliac vessels, between the inguinal ligament and the iliac bifurcation and subdivided into the medial and lateral chains. A commonly involved sentinel node is located in the medial chain, referred to as the ‘obturator node’ due to its close proximity with obturator internus (OI) muscle. The internal iliac nodes are located deeper in the pelvis, adjacent to the internal iliac vessels and named according to the many subdivisions of these vessels. Notably, this group includes the junctional node at the iliac bifurcation. Perivisceral nodes are located around the rectum, bladder and prostate and are less commonly involved than the iliac nodes(88).

Metastatic groups comprise the common iliac, paraaortic and inguinal lymph nodes. The common iliac nodes are adjacent to the vessels, superior to the iliac bifurcation and can be subdivided into the lateral, middle and medial chains. The paraaortic lymph

nodes are located adjacent to the aorta and inferior vena cava (IVC), and are subdivided into seven groups, each named according to their relationship with these vessels. Those related to the IVC are the laterocaval; precaval and retrocaval groups, those related to the aorta are the lateroaortic; preaortic and retroaortic groups, with the aortocaval nodes between the two main vessels. The inguinal nodes are also split into superficial and deep groups, according to their relationship with the inferior epigastric vessels.

Nodal pathways

Whilst there is some controversy as to the exact course the lymphatic vessels and nodes take, the strongest data arises from large series of PLND whereby positive common iliac nodes are always accompanied by positive pelvic nodes, and positive paraaortic nodes are always accompanied by positive common iliac nodes(90,91), which suggests sequential progression towards the diaphragm.

Vascular system

In 1889, Stephen Paget (the son of James) observed that whilst embolic abscess in septic patients were equally likely to arise in the liver and the spleen, breast cancer metastases overwhelmingly favoured the liver which led to the ‘soil and seed hypothesis’, whereby tumours (seeds) could have affinity for certain ‘fertile’ organs (soil)(92). This hypothesis was temporarily superseded by the work of James Ewing who proposed that tumour cells are guided towards their sites by the lymphatic and blood vessels(93). However, pioneering work from Joseph Fidler suggested that these two theories are not mutually exclusive(94).

Prostate cancer cells that spread via the (neo)vascular system must survive the forces imparted on them by the bloodstream and evade immune system defences. Once near the site of a potential secondary, they extravasate through the vascular wall, effect changes in the local microenvironment and establish deposits which may continue proliferating(95). The venous (rather than arterial) system is preferred in prostate cancer due to thinner vascular walls, the distal location of the prostate and as evidenced by the distribution of metastatic disease.

Compelling and complimentary work by carried out by Batson(96) and Bubendorf and colleagues(97) informed the understanding of haematogenous dissemination in prostate cancer, whereby two separate systems are thought to channel metastases,

namely the IVC and the vertebral venous plexus (of Batson). In his seminal paper, Oscar Batson cannulated the dorsal vein of the penis in cadavers and showed that injection of a thick radiopaque contrast agent led to opacification of the iliac veins and IVC. With a thin agent, the IVC was not demonstrated and plexiform veins were opacified in an ascending fashion throughout the spine to connect with the intercostal veins and the cerebral venous sinuses. This axial skeletal drainage is thought to be a portal system and is similar to the main disease distribution in prostate cancer as confirmed by Bubendorf. In this highly cited autopsy study of 19,316 cases carried out between 1967 and 1995, of whom 1,589 had prostate cancer(97), the prevalence of skeletal metastases was 90% for the spine (97% lumbar, 57% thoracic and 38% cervical), with a clear ascending distribution and skip lesions occurring in only 1 – 2% of cases. The second route (via the IVC) is thought to give rise to appendicular and soft tissue metastases much later in the disease(97), which are relatively rare in the PSA screening era. However, most common sites in this pathway include lungs and pleura, liver and adrenal glands(98). The independence of these two systems was suggested by an inverse relationship between spine and lung metastases ($p < .0001$).

Whilst there is a lack of large cohort studies performed in the PSA screening era, a single paper reported disease distribution in nearly 75 000 patients with prostate cancer with 84% bone involvement, 10.6% metastatic lymph nodes, 10.2% liver metastases and 9.1% thoracic disease(99). However, their reference standard was not stated.

Clinical staging of prostate cancer

By far the most widely used staging method for this purpose is the American Joint Committee on Cancer (AJCC) staging system, which was introduced in 1977 and now is in its seventh edition (with the 8th to be adopted on January 1st 2018). Here, the tumour stage is classified by way of TNM: Tumour (extent of the primary), Nodes (nodal invasion) and Metastases (presence or absence)(100).

Staging can be assessed using a variety of means including physical examination, imaging, pathology, and autopsy results and decisions regarding how best to do this should consider the accuracy, invasiveness and cost effectiveness of each diagnostic test. Staging or restaging can take place in a number of potential clinical situations including primary staging of disease at diagnosis, following focal or whole gland therapies, for response assessment following treatment and to assess for suspected recurrence following treatments.

The clinical staging system for prostate cancer that should be used for diagnostic imaging tests is stated below(101):

Primary tumour (T)

TX	Primary tumour cannot be assessed
T0	No evidence of primary tumour
T1	Clinically inapparent tumour not palpable or visible by imaging
T1a	Tumour incidental histologic finding in ≤5% of tissue resected
T1b	Tumour incidental histologic finding in >5% of tissue resected
T1c	Tumour identified by needle biopsy (because of elevated prostate specific antigen [PSA] level)
T2	Tumour confined within prostate; tumours found in 1 or both lobes by needle biopsy but not palpable or reliably visible by imaging
T2a	Tumour involves one-half of 1 lobe or less
T2b	Tumour involves more than one-half of 1 lobe but not both lobes
T2c	Tumour involves both lobes
T3	Tumour extends through the prostatic capsule; invasion into the prostatic apex, or the prostatic capsule is classified not as T3 but as T2
T3a	Extracapsular extension (unilateral or bilateral)
T3b	Tumour invading seminal vesicle(s)
T4	Tumour fixed or invades adjacent structures other than seminal vesicles (e.g. bladder, levator muscles, and/or pelvic wall)

Regional lymph nodes (N)

NX	Regional lymph nodes were not assessed
N0	No regional lymph node metastasis
N1	Metastasis in regional lymph node(s)

Distant metastasis (M)

M0	No distant metastasis
M1	Distant metastasis
M1a	Nonregional lymph nodes(s)
M1b	Bone(s)
M1c	Other site(s) with or without bone disease

Clinical significance of cancer stage

Since patient survival depends heavily on disease stage, accurate staging underpins prognostication and management decisions.

Organ confined prostate cancer

When organ confined, the cancer-specific mortality for prostate malignancy is low compared with other cancers. Large cohort studies in Sweden with follow-up >20 years report 16% cancer-specific mortality in one study(102) and 29% in another study(20) for patients with early stage disease (T1-3). Similarly, ten-year follow-up studies of active surveillance vs. prostatectomy report cancer-specific mortality rates of 15% in the watchful waiting arm of the Scandinavian prostate cancer group 4(103) and 8.4% for the PIVOT study.

Lymph node positive prostate cancer

There are no studies in the literature that follow up untreated node-positive prostate cancer due to ethical reasons, which in itself illustrates a different natural history to organ-confined disease. However, the EORTC reported an 18-month median time to progression with untreated node positive disease(104).

Metastatic prostate cancer

Although a heterogeneous population in terms of age, fitness, disease distribution and burden, metastatic prostate cancer remains an incurable disease with a poor prognosis which is comparable with other disseminated malignancies, and has a median overall survival of 42 months in the recently published STAMPEDE trial, despite ADT (105).

Staging of metastatic prostate cancer: challenges with imaging studies

Since diagnostic yield is affected by the PSA level, Gleason grade and cancer stage(106), studies concerning metastatic prostate staging are heterogeneous due to variations in the i) cancer risk categories (D'Amico/UCSF CAPRA etc), ii) guidelines concerning indications for imaging and iii) inconsistent reference standards.

Where possible, use of a histopathological reference standard by way of PLND is usually preferable. This can be done in multiple ways, with conventional PLND solely dissecting the obturator fossa, extended PLND (ePLND) also removing internal and external iliac nodes and superextended PLND removing common iliac and presacral nodes in addition(107). Some groups have also removed paraaortic nodes(91). However, this balance can be difficult as there is proportional relationship between yield and complication rates (107) and once PLND is performed, the registration of resected nodes to images can present further difficulties. Furthermore, ethical approval for invasive procedures will usually only be granted whereby prostatectomy is being performed, which leads to spectrum bias. Whilst imaging-based reference standards may provide alternatives, studies are limited by the performance characteristics of each test and also suffer from incorporation bias.

Reference standards are even more difficult for skeletal disease as histology does not form part of routine care, research biopsies are difficult to secure ethical approval for and autopsies are declining (108,109), and often miss disease(97,110). Composite or follow-up based imaging reference standards are therefore often used, although depend on the performance of the reference test.

Imaging tools for staging prostate cancer

There are at least eight separate international guidelines which provide recommendations on when to stage prostate cancer (111), leading to confusion amongst clinicians and researchers alike. However, all guidelines currently recommend BS +/- pelvic CT as staging modalities.

Technitium-99m bone scan

BS uses intravenously injected technetium radiotracer, often labelled to methylene diphosphonate (MDP), which adsorbs onto hydroxyapatite and images osteoblastic bone mineralisation. BS is widely available, low cost and as a small series of images, are relatively quick to report. However, their performance characteristics are limited since false negative (FN) findings commonly occur due to low spatial resolution or lack of osteoblastic activity. False positive findings may be caused by benign conditions such as joint disease, healing fractures and benign bone neoplasms. A recent meta-analysis provided pooled sensitivities and specificities of 0.59 (95%CI: 0.55–0.63) and 0.82 (95%CI: 0.78–0.85) respectively(112).

(Abdomino)pelvic CT

The detection of positive lymph nodes in computerized tomography (CT) is heavily dependent on short axis diameter measurements combined with assessment of morphological features such as a rounded shape or the loss of the normal fatty hilum. Due to relatively flat ROC curves, performance is limited at all cut-offs for size with the largest meta-analysis to date of 1024 patients in 24 studies giving a pooled sensitivity of 0.42 (0.26 - 0.56 95% CI) and specificity of 0.82 (0.80 - 0.83 95% CI)(113).

This limited performance in staging modalities currently recommended by international guidelines has acted as the main driver for further research into more accurate techniques.

Choline PET/CT

^{18}F-choline-PET/CT techniques combine anatomical imaging using CT with functional radiopharmacological information to stage both the lymph nodes and bones in a single examination. Whilst the glucose analogue Fludexoyglucose (FDG) is the most widely used PET tracer, tracer uptake and avidity tend to be poor as prostate cancer generally progresses slowly and has limited glycolytic metabolism. Techniques concerning

choline were therefore developed and have improved performance. Choline is an essential component of the cell membrane, which depends on the production of phosphatidyl-choline, which is elevated in cancer cells(114). Two main techniques have been described, namely ^{11}C and ^{18}F with the latter having a longer half-life, permitting distribution without a cyclotron.

Clinical trials regarding the use of ^{18}F-choline-PET/CT generally show superior performance over routine imaging. For primary lymph node staging, studies report a relatively low, often variable sensitivity with high specificity. A 441 patient meta-analysis carried out by Evangelista *et al.* reported an I^2 index of 71.7 for sensitivity and 22.7 specificity, showing that studies are heterogeneous, with a pooled sensitivity of 49.2% (95% confidence interval (CI), 39.9–58.4) and a specificity of 95% (95% CI, 92.0–97.1)(115).

For bone metastases, a meta-analysis of 1102 patients gave a pooled sensitivity and specificity of 0.91 (95 % CI 0.83–0.96) and 0.99 (95%CI: 0.93–1.00) respectively, with I^2 heterogeneity statistics of 0.0 and 2.8. In this way, ^{18}F-choline-PET/CT studies demonstrate high diagnostic accuracy for bone metastases with impressive consensus between studies. Furthermore, this additional improvement in diagnostic performance has been shown to be clinically valuable by Beheshti *et al*. who found that management was changed in 15% of cases when patients were staged with ^{18}F-choline-PET/CT(116). In the context of biochemical failure following prostatectomy or radiotherapy, the predictive value of PET/CT is dependent on clinical features such as PSA level, PSA doubling time and PSA velocity(117). A meta-analysis of 19 studies in 1555 patients showed a pooled sensitivity and specificity for lymph nodes of 100% (95% CI: 90.5% -100%) and 81.8% (95% CI: 48.2% - 97.7%) respectively. The performance for bone metastases was not reported in this study, but another study concerning biochemical failure reported sensitivities and specificities of 88 and 99% respectively(118).

However, PET/CT is not without its limitations. Firstly, the radiation associated with both PET and CT confer a substantial radiation dose and potential cancer risk (119,120). Tracer availability is limited and financial and logistical difficulties mean it can be difficult to implement on a large scale. The spatial resolution of PET is also limited to 5mm (121), whereby the 45% of positive nodes <4mm(122) could account for its poor sensitivity. Finally, the contrast resolution of CT is relatively poor, especially with unenhanced scans. Despite this these limitations, ^{11}C-choline PET CT has been recommended by the European Association of Urology guidelines 2015 for patients

with an equivocal bone scan and for biochemical failure following prostatectomy(107).

Whole-Body MRI

The concept of whole-body MRI (WB-MRI) was first proposed as early as 1969(123) but has only recently been implemented as a result of advances in magnet design, receiver coil and moving table technology, post-processing equipment and viewing software. WB-MRI has shown success in other tumour types including breast (124), colorectal(125), myeloma (126), lymphoma(127) and paediatric tumours(128), with the International Myeloma Working Group recommending its use as part of the clinical management pathway(129). The first report of WB-MRI with diffusion in prostate cancer was in 2004(130).

Theoretical advantages of WB-MRI over the aforementioned cancer staging modalities include absence of ionizing radiation, widespread availability without the need for specialist equipment, delivering a 'one-stop' staging modality (131), relatively low cost(132) and superior contrast resolution to CT.

Using anatomical sequences alone, MRI has equivalent sensitivity and specificity to CT(113) for lymph node detection, and is superior to bone scan at detecting bone metastases(133–135). The addition of newer sequences such as multiecho Dixon (mDixon) which images fat and water, diffusion which can probe microstructure and post contrast imaging which reflects tumoural vascularity, may further improve its performance and could be combined in mp imaging protocols.

For the primary staging of nodal disease, studies which incorporate diffusion into scanning protocols report a highly variable sensitivity ranging from 17%(136) to 73%(137). Whilst both of these studies used ePLND as the reference standard, the lower sensitivity of the first study by Pinaquay and colleagues used b-values of 0 and 100s/mm^2, and failed on multiple counts to meet the international recommendations for using diffusion as a cancer biomarker(138), which emphasizes the need for optimised scanning technique. The specificity for nodal detection is generally thought to be high, with a limited number of studies ranging from 86%(137) to 98%(139).

A meta-analysis concerning WB-MRI for the detection of bone metastases reported pooled sensitivity and specificity of 0.97 (95 % CI: 0.91–0.99) and 0.95 (95%CI: 0.90–0.97) respectively(112), confirming substantial promise for the detection of bone metastases. However, MRI studies have higher levels of heterogeneity than PET/CT,

as evidenced by I^2 indices of 67.1 and 57.6 for sensitivity and specificity of MRI vs. 0.0 and 2.8 for choline PET/CT respectively. Heterogeneity in WB-MRI studies may arise from differences in scanning protocols, and somewhat 'impure' studies which do not report nodal accuracy and group together multiple tumour types (often with breast cancer) for bone metastases(140–143).

Consideration of what represents an optimal protocol of WB-MRI in primary staging is an area of uncertainty. Perhaps partially due to uncertainty in disease distribution during the PSA screening era, complete coverage has been both suggested (144) and deemed unnecessary (145), and no studies have been reported which consider the individual contribution of each pulse sequence to diagnostic accuracy. The subjective nature of clinical reporting also raises similar issues to those experienced with mp-prostate MRI, whereby it may be preferable to use an ordinal scale to score the suspicion of cancer.

Further potential limitations of WB-MRI include scan duration and the presence of artefacts including susceptibility, motion, distortion, fat swapping with mDixon images, poor fat saturation with diffusion images and stitching artefacts at station boundaries. This is particularly pertinent in multicentre studies where heterogeneity can arise due to differences in scanning technique (see table 3). Additionally, the literature to date has focused on use of the technique in primary staging, with a single study focusing on use in biochemical relapse following prostatectomy whereby the diagnostic accuracy (in terms of sensitivity and specificity) was not reported, nor was interobserver agreement considered.

Section B summary and future directions

In summary, accurate staging of prostate cancer is of paramount importance when making clinical decisions, yet currently hinges upon inaccurate techniques. WB-MRI holds significant potential for disease staging prostate cancer, although requires further validation before it is introduced into routine clinical practice.

Specifically, studies comparing choline-PET/CT and bone scan +/- CT in the same cohort would be welcome whereby utility of each sequence could be considered. Diagnostic accuracy should also be reported using the best possible reference standard and multicentre studies are required to produce generalizable data with high patient numbers, although would require consideration regarding image quality. Trials that use the technique in situations other than primary staging are also lacking, and

should consider the interobserver agreement vs. PET/CT. Finally, reporting practices may be harmonised by the use of scoring systems, much like mp-prostate MRI.

2 MAGNETIC RESONANCE IMAGING THEORY: ACQUISITION AND ANALYSIS

Section A: from proton to pulse sequence

The following texts were used extensively throughout this section:

1. Gadian, David G. *NMR and its applications to living systems*. Vol. 7. Oxford: Oxford University Press, 1995.

2. McRobbie, Donald W., et al. *MRI from Picture to Proton*. Cambridge university press, 2006.

3. Johansen-Berg, Heidi, and Timothy EJ Behrens, eds. *Diffusion MRI: from quantitative measurement to in vivo neuroanatomy*. Academic Press, 2013.

4. Quantitative MRI in Cancer, Thomas E. Yankeelov, David R. Pickens, Ronald R. Price, September 13, 2011 by CRC Press

Hardware

Modern MRI scanners are comprised of a cylindrical static superconducting electromagnet (typically 1.5 Tesla (T) or 3T), radiofrequency (RF) coils, gradient coils and shim coils. A liquid helium cryogen is used to achieve zero resistance in the coils and is maintained at around 4 Kelvin (K) (figure 18). The static field polarizes nuclear spins within a patient and shim coils keep the static field as homogeneous as possible, adjusting for the magnetic field variations produced by the body. RF coils act as transmitters of an RF pulse and receivers of the nuclear magnetic resonance (NMR) signal. Three gradient coils are arranged orthogonally and spatially encode the NMR signal by making the spins precess at frequencies unique to their location using linear magnetic field variations, superimposed on B_0. These coils are named G_{SS} for slice selection, G_{Φ} for phase encoding and G_v for frequency encoding. High power amplifiers drive the gradient coils which have high slew rates, and the timings of RF pulses and gradients are manipulated by a computer as part of a ‘pulse sequence’, which is a predefined set of instructions which determine the characteristics of MR images. Other computer systems reconstruct and display images, and act as an interface with Picture Archiving and Communications systems (PACS) for the storage and retrieval of imaging data.

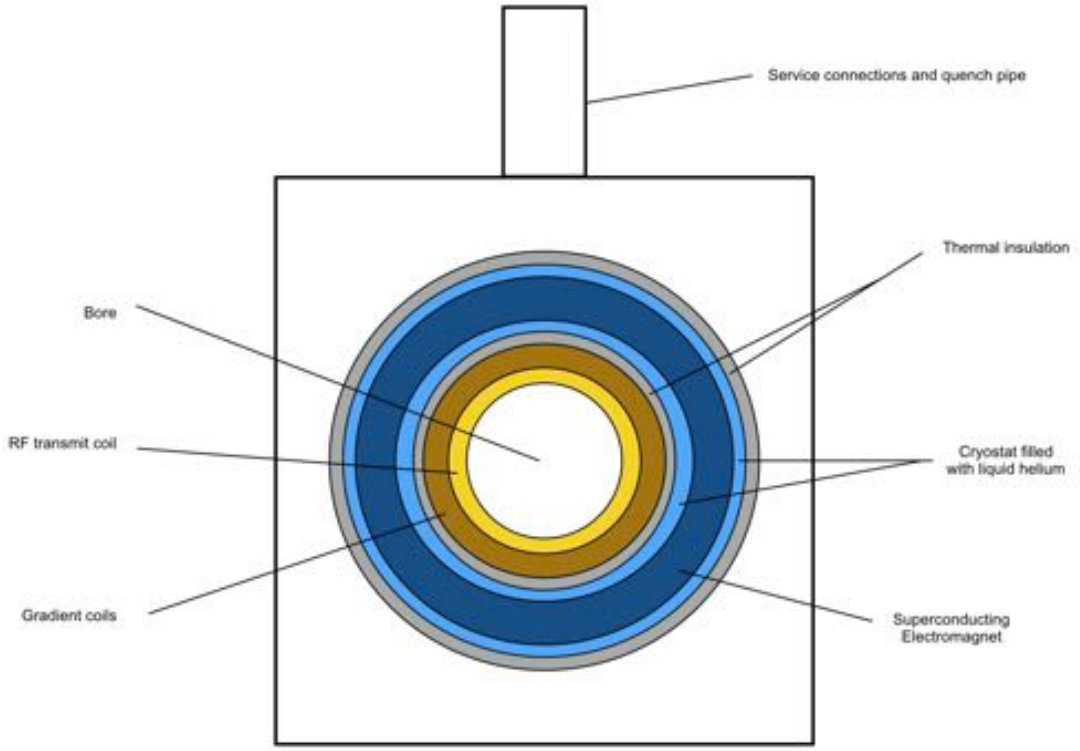

Figure 18: Cross section of an MRI scanner

Proton spins in an external magnetic field

The ^{1}H nucleus, along with other nuclei such as ^{3}He, ^{13}C and ^{23}Na are found to exhibit a property called 'spin' and in the presence of an external magnetic field, 'precess' around this magnetic field (figure 19). The gyromagnetic ratio (γ) determines the precessional frequency, and is unique for each elemental nucleus.

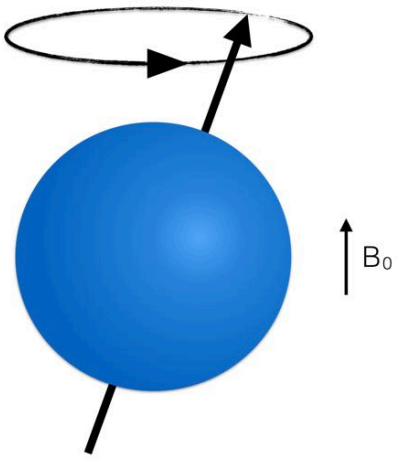

Figure 19: A precessing proton

In the absence of an external magnetic field, the net magnetization vector within a body is nulled due to the cancelling of randomly orientated nuclear spins. However, once the

external static magnetic field (B_0) is applied, spins may assume one of two possible discrete energy states: parallel or antiparallel (called spin-up and spin-down) to B_0, with slightly more spins (approximately 9 for every 1 million for ^1H at 1.5T) assuming the parallel position, as it is a lower energy state. The proportion of spin up to spin down energy states is governed by the Boltzmann distribution, which is a quantum mechanical description given by:

Equation 1

$$\frac{N_{up}}{N_{down}} = e^{\left(\frac{-\gamma \hbar B_0}{kT}\right)}$$

Where N_{up} is the number of spin up protons, N_{down} is the number of spin down protons, ħ is Plank's constant, k is the Boltzmann constant and T is temperature in Kelvin.

This unequal distribution generates a net magnetization vector (M_0) (summed across all spins) aligned to B_0.

The precessional frequency of nuclei or Larmor frequency (*ω)*, in an external magnetic field (*B_0*) is given by:

Equation 2

$$\omega = B_0 \gamma$$

Excitation

NMR signal develops from perturbing M_0 with a RF pulse (B_1), transmitted orthogonally to B_0 and oscillating at the Larmor frequency of precessing protons. In the quantum mechanical model, the B_1 pulse excites spins to higher energy states, and once switched off, photons with are released with an energy level equal to the difference between the two states (the Larmor frequency). However, it is often more helpful to consider the bulk properties of spin populations (rather than individual nuclei), which is why the classical mechanical model is used in preference for the rest of this chapter. In this model, the B_1 pulse causes the net magnetization vector to rotate away from its initial alignment in a process called excitation (figure 20). The angle the vector assumes following excitation is called the 'flip angle', which is commonly 90° whereby the longitudinal magnetisation (M_z, long the z-axis) is converted to transverse magnetisation (M_{xy} – in the XY plane, perpendicular to Z) meaning M_z is 0. However, other flip angles less than 90° can also be used in certain circumstances (such as 'gradient echo' experiments - considered later in this chapter). A degree of M_{xy}

magnetisation is necessary for signal detection as this produces much higher recordable levels of signal intensity.

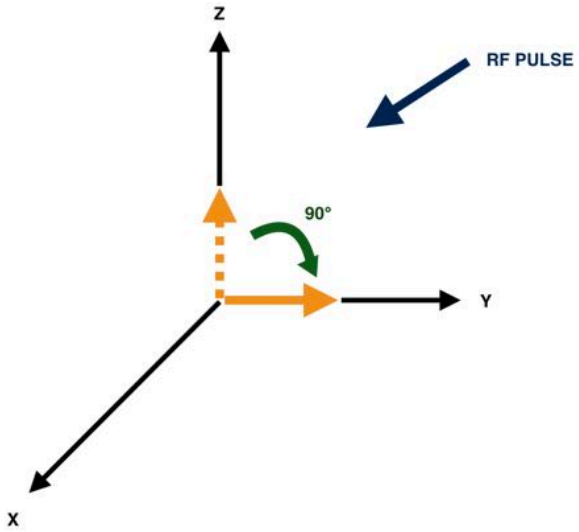

Figure 20: Excitation depicted within the rotating frame of reference

Relaxation

After the RF pulse is switched off, spins return to their original state in a process called relaxation whereby M_z recovers to the original M_0 value and M_{xy} decays to zero, which are defined by time constants T1 and T2* respectively. The changing magnetic fields that occur during relaxation induce a measurable electrical current ('signal') oscillating at the Larmor frequency within a receiver coil according to Faraday's law; called free induction decay (FID, figure 21).

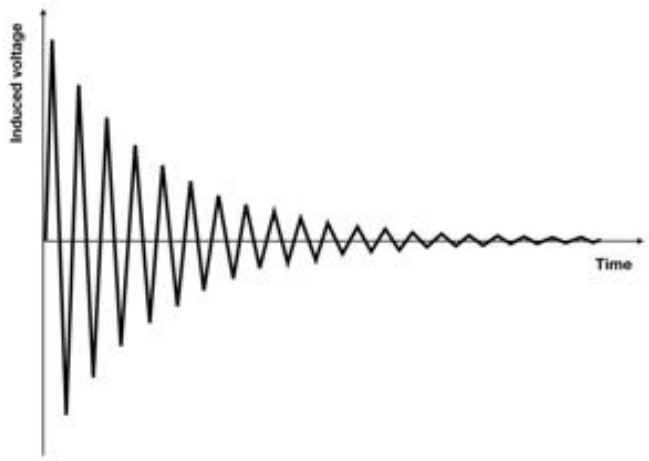

Figure** 21**: Free induction decay

Spin-Lattice (T1) Relaxation

The recovery of M_z occurs through 'spin-lattice relaxation' whereby the net magnetisation vector returns to thermodynamic equilibrium with its surroundings longitudinally. This requires an energy exchange process, whereby the energy absorbed through RF excitation is dissipated to by nuclei to their surroundings (the "lattice"). It can be modelled as a simple first order exponential growth and ranges from tenths of seconds to seconds in normal biological tissue.

T1 relaxation occurs when molecules in higher energy states encounter the magnetic moment of another nearby nucleus rotating at, or near the Larmor frequency. T1 relaxation times are therefore dependent on field strength, temperature, the mobility of the spins, the presence of macromolecules and paramagnetic influences. It is given by the formula:

Equation 3

$$M_z(t) = M_0(1 - e^{-t/T1})$$

Where t = time and *T1* = time for magnetisation to recover to ($1\text{-}e^{-1}$) of M_0, or 63.2% (figure 22).

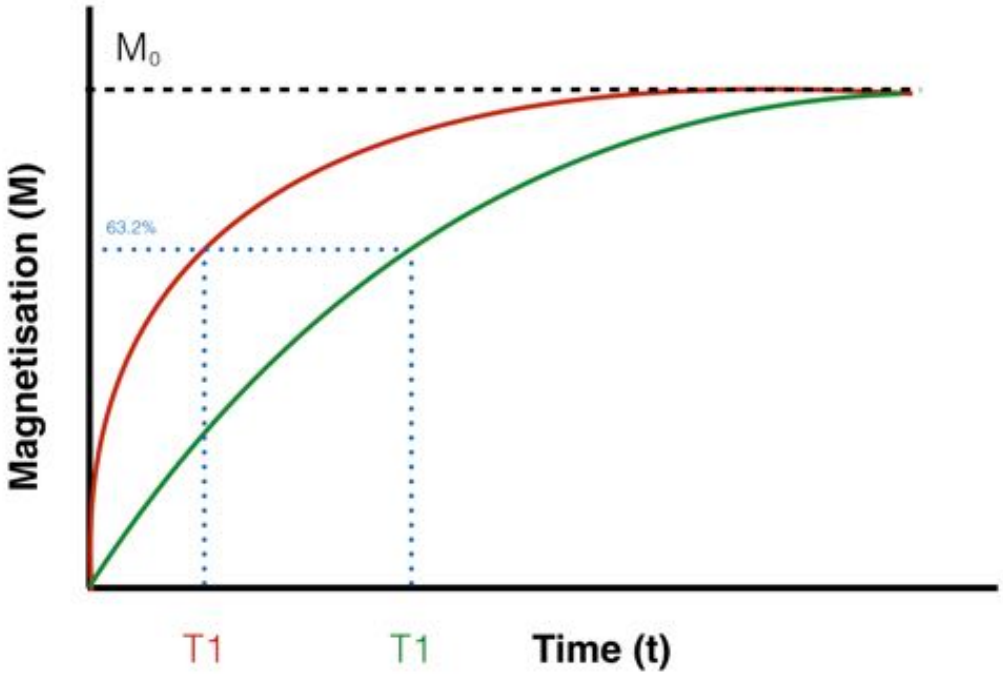

Figure 22: T1 relaxation

According to figure 22, voxels with different measured T1 relaxation times (as a consequence of their biophysical properties) will have different values of signal intensity at certain times, which is exploited for image contrast. However, native T1 relaxation is unused in current clinical detection and characterization protocols for prostate cancer, other than to demonstrate T1-hyperintense post-biopsy haemorrhage. However, DCE imaging forms a key part of the prostate mp-MRI examination and utilizes the T1 shortening effect of intravenously injected chelated Gadolinium to probe regional differences in vascularity (a combination of vascular density, blood flow, permeability and interstitial volume). DCE imaging in prostate cancer will be considered in further detail in section B of this chapter.

Spin-spin (T2) relaxation:

T2 relaxation occurs when spins interact with one another (spin-spin interaction), causing a change in precessional frequency and decay in M_{xy} as a consequence of loss in phase coherence in the XY plane, and occurs without energy transfer (figure 23).

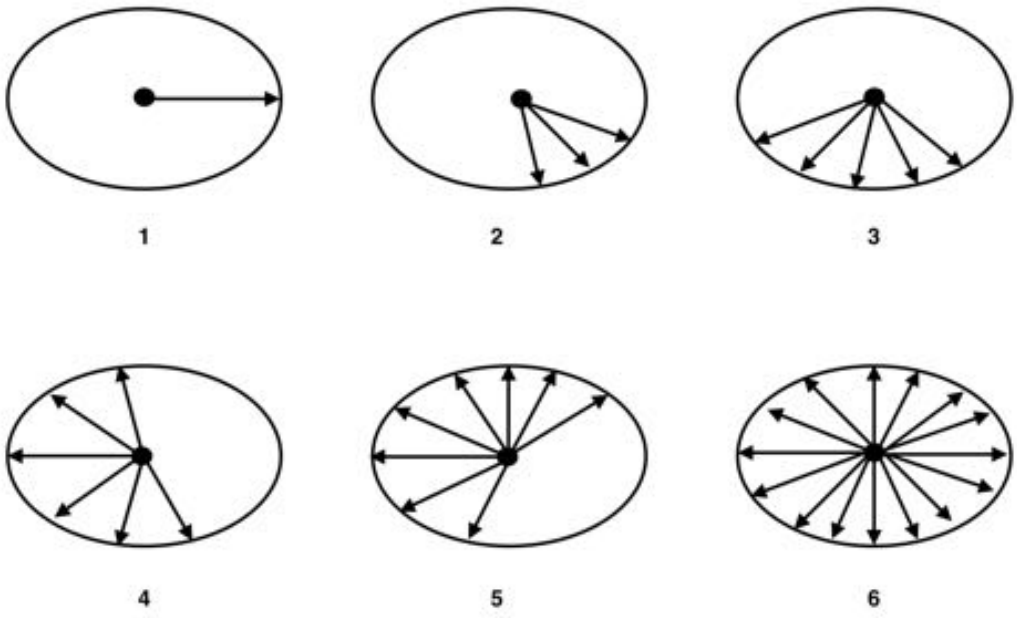

Figure 23: Loss in phase coherence

Rotational and tumbling motion of nuclei causes spatially and temporally varying magnetic fields. Hence, the magnetic field experienced by any given nucleus over time becomes slightly different to other nuclei. As the precessional frequency of a nucleus is dependent on the external magnetic field it experiences (equation 2), these differences

result in a dephasing effect across all nuclei that increases with time following the 90 degree RF pulse.

T2 relaxation can in its simplistic form be modelled as monoexponential decay, and is in the order of milliseconds in biological tissues:

Equation 4

$$M_{xy}(t) = M_{xy}(0)e^{-t/T2}$$

Where T2 is the time taken for the signal to decay to 36.8% (e^{-1}) of its initial value of M_{xy} (figure 24).

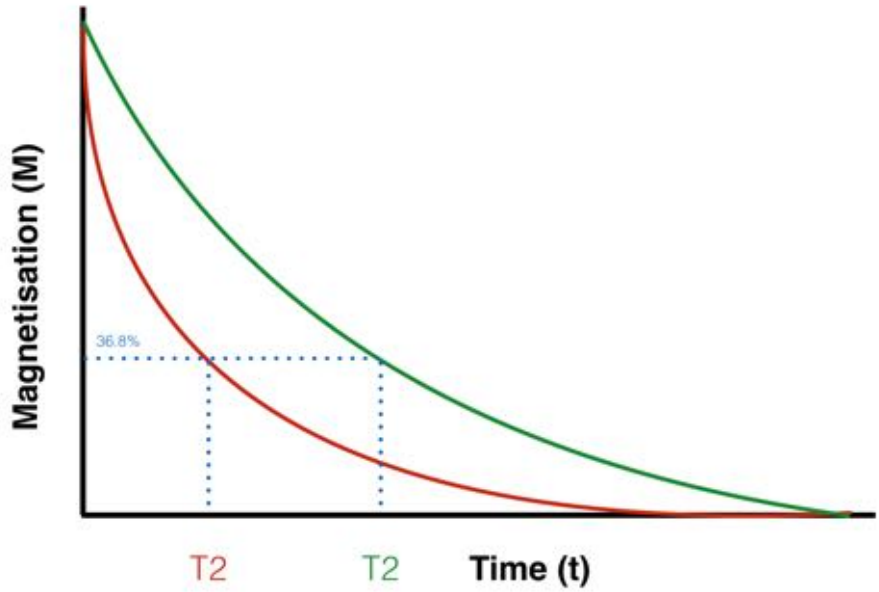

Figure 24: T2 relaxation

Similar to T1 relaxation, figure 24 shows that voxels with different measured T2 relaxation times (driven by differing biophysical properties) can have different values of signal intensity at certain times, which is again exploited for image contrast. However, pure T2 relaxation only occurs when the static external field is entirely homogenous, which in practical terms is never the case. Additional dephasing effects occur from static inhomogenieities in B_0 due to induced magnet imperfections and susceptibility gradients generated within the body which speed up dephasing, termed T2'. When these effects are not corrected the dephasing is termed T2* (equation 5).

Equation 5

$$\frac{1}{T2^*} = \frac{1}{T2} + \frac{1}{T2'}$$

T2* decay occurs gradient echo (GE) experiments but can be minimized by spin echo (SE) experiments (giving approximate T2 contrast), and will be considered later.

Unlike native T1, native T2 contrast mechanisms are important for prostate cancer detection, due to different relaxation times in cancerous and non-cancerous tissue. The biophysical basis of T2 signal in prostate cancer will also be considered in more detail in section B of this chapter.

MRI contrast agents

MRI contrast agents cause T1 and T2 shortening by generating oscillating local magnetic fields. The agents in widespread clinical use are based around gadolinium (Gd^{3+}) ions, which are strongly paramagnetic due to 7 unpaired electrons, and have a magnetic moment 1000 more than that of a hydrogen nucleus (146). The degree of T1 and T2 shortening per millimole of substance is defined as the *relaxivity* ($1/\Delta T1$ or T2). T1-weighted images (see later) are usually preferred over T2W images due to more pronounced effects (T1>> T2) whereby tissues with high gadolinium concentrations will appear bright. Since elemental Gd is toxic to multiple organ systems (147), it is chelated to large stable complexes as gadolinium based contrast agents (GBCAs) where it is bound until excretion, predominantly by the kidneys. GBCAs are generally considered to be amongst the safest compounds that are administered to patients in the short and medium term with adverse incidences occurring in less than 2 per cent of cases. However, there is growing concern regarding long term accumulation in soft tissues, and nephrogenic systemic fibrosis can occur with severe renal impariment (148).

Echo formation and pulse sequences

Rather than sampling the FID directly, it is more common to further manipulate the spins to form a so-called ‘echo’ (since the powerful B1 pulse still has effects on the receiver coil). The two main families of echoes are produced in ‘spin echo’ and ‘gradient echo’ experiments.

Spin echo (SE)

To form a SE, when spins dephase in the transverse plane, a ‘refocusing RF pulse’, typically 180° is applied at a time equal to half the time to echo (TE/2) such that the phase differences (and field inhomogeneity) are reversed, and a SE signal is formed by

signal regrowth with maximum amplitude at TE (when the spins are back in phase). The sequence is repeated with a time between excitations known as the repetition time (TR), which controls the amount of signal in the longitudinal plane (figure 25) since it determines how long the magnetisation vector has to recover between excitations.

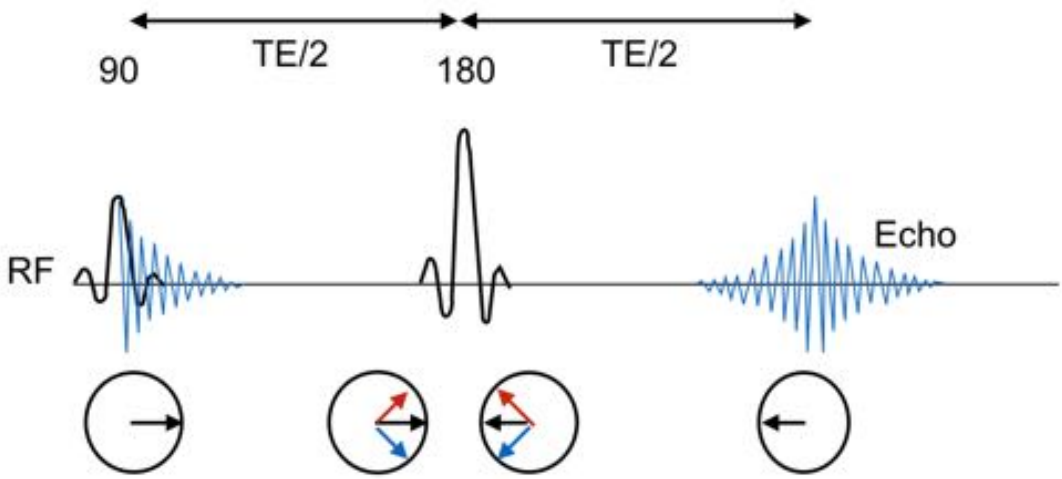

Figure 25: SE pulse sequence.

Rapid acquisition with relaxation enhancement (RARE)

To reduce imaging time, multiple 180° pulses may be applied before each TR (provided there is sufficient residual transverse magnetisation), to create multiple echoes in an 'echo train' as part of a RARE sequence (figure 26). Whilst repeated 180° pulses result in high energy deposition (which has encouraged the development of other sequences with reduced flip angles), RARE sequences remain the clinical workhorse for T2W imaging of the prostate as SNR is comparable to conventional SE sequences but with significantly reduced scanning time. RARE has been assigned the proprietorial name 'TSE' by Philips, which is used in preference throughout this thesis.

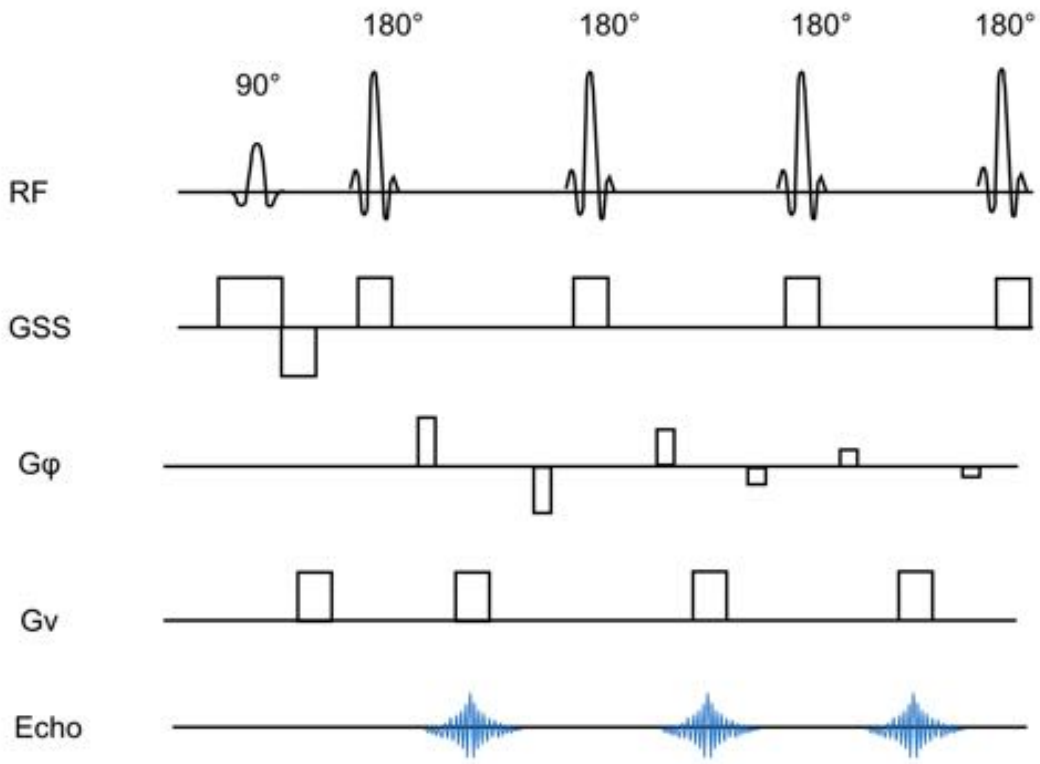

Figure 26: RARE pulse sequence

GE

GE experiments use a short TR and do not apply a 180° refocusing pulse, meaning the decay of transverse magnetisation is governed by T2*. Instead, bipolar magnetic field gradients are applied after the initial excitation pulse to dephase and rephase the spins and create an echo. Here, smaller repeated RF excitations are applied that convert only a fraction of M_z to M_{xy}, meaning more signal is available for the next excitation. In this context, flip angles that produce the highest signal intensity (called the 'Ernst angle') are <90°, M_z recovery is more rapid and imaging times are shorter (figure 27). However, the compromise of low flip angle techniques is the smaller amount of transverse magnetisation, which results in less SI than spin echo experiments. N.B. flip angles other than the Ernst angle are often intentionally selected to optimise image contrast. In addition, a 'spoiler' gradient may be applied at the end of data acquisition, or the frequency-encoding gradient extended to remove residual unnecessary transverse magnetisation that can cause artefacts (figure 27).

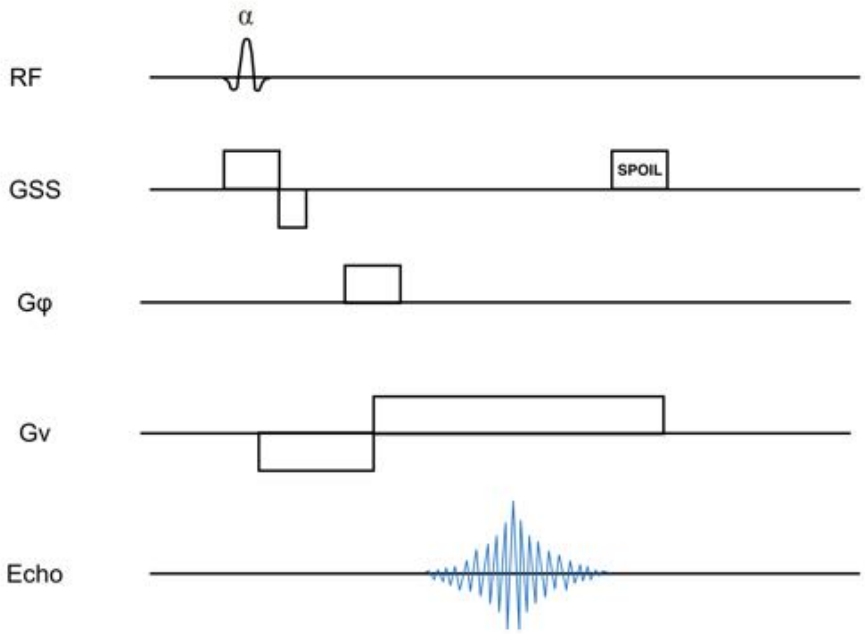

Figure 27: GE pulse sequence

GE pulse sequences are preferred for DCE prostate imaging due to their short acquisition time, which permits sufficient multiframe time resolution although their governing T2* decay makes them susceptible to artefacts and short acquisition time generally trades spatial resolution and signal-to-noise ratio (SNR). DCE images used as part of the prostate mp MRI protocol are often fat saturated to maximize contrast between enhancing tumour and surrounding peri-prostatic fat.

Fat-water imaging: the Dixon method

Water and fat have markedly different chemical structures, whereby water is a small polar molecule with an electronegative oxygen atom, which pulls the shielding electron cloud away from the hydrogen nuclei and exposes them to a relatively stronger magnetic field which results in a high rotational frequency. In comparison, fat molecules are much larger and have better-shielded protons with a lower rotational frequency that is more efficient for T1 relaxation. As a result, T1 relaxation times are lower for fat than water and the resonant frequency of water molecules is slightly higher than fat, referred to as ‘chemical shift’.

The different rotational frequency of water and fat protons mean their spins cycle in and out of phase with each other every 1.1ms after the original RF pulse at 3.0T (149) as seen in figure 28.

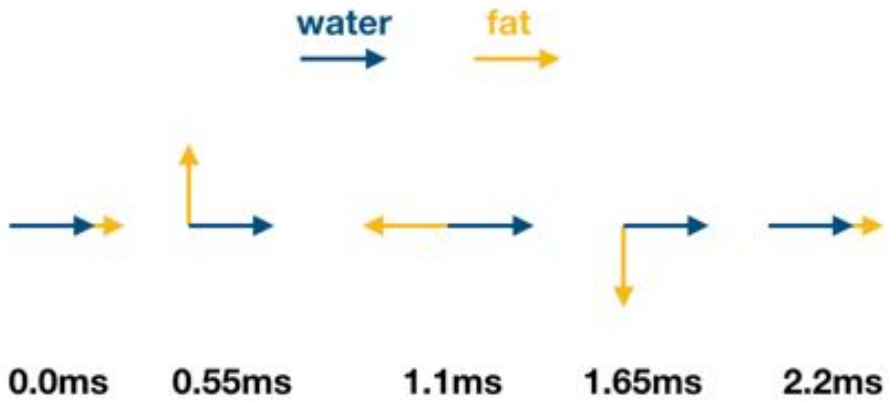

Figure 28. Phase cycling of water and fat.

Spins are in phase at 0.0 and 2.2ms, and out-of-phase at 1.1ms.

Since the human body consists mainly of water and fat, these differences can be exploited by MR techniques and give rise to different T1 weightings. Multiecho (m) Dixon imaging was first proposed by Thomas Dixon in 1984 (150) and acquires a set of two images with different echo times; one where fat and water spins are in phase and another where they are out-of-phase. From these images, water and fat only images can be calculated and reconstructed as shown in figure 29.

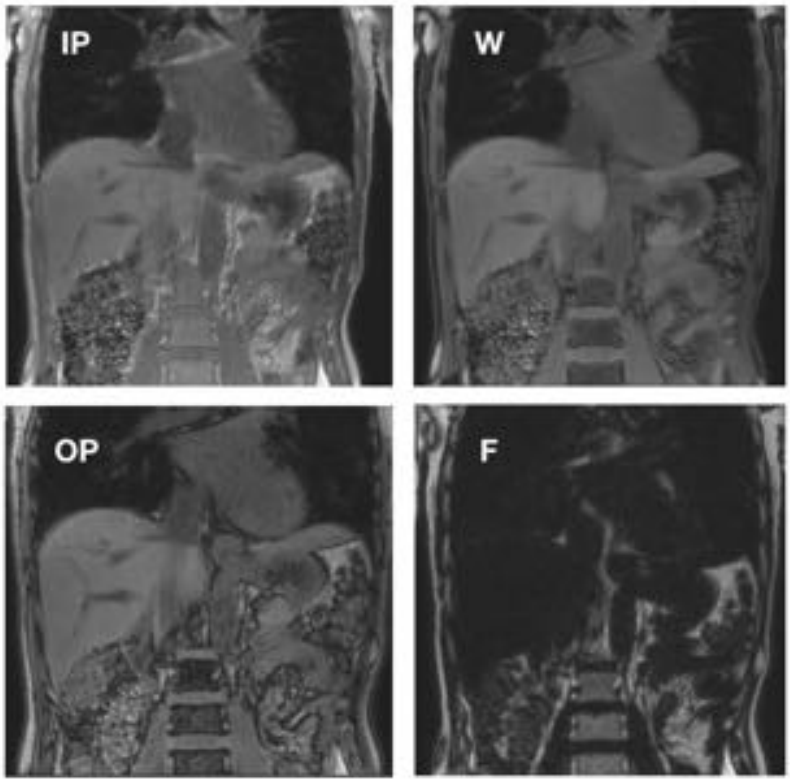

Figure 29. Example of mDixon Images

IP= in phase, OOP= out-of-phase, F=fat only W=water only

Spatial encoding, MR signal collection, storage and image generation

To spatially encode an image and determine spin location, G_{ss} is initially applied (often in the z-direction), which causes spins to precess at different frequencies. A block of spins is chosen using a resonance RF pulse with the same range of resonant frequencies (bandwidth) as the desired slice. Within this slice, G_v is applied across one dimension during the signal read out to give each pixel a unique value of precessional frequency from which their spatial position can be deduced in this dimension. G_ϕ is applied orthogonally to G_v and G_{ss} prior to read out, whereby its magnitude is increased for each repetition to give each pixel in the G_ϕ direction a different value of rate of precessional phase change, from which spatial position can be deduced in this dimension.

Echoes are sampled and digitised by an analog-to-digital converter and stored in 'k-space', which is the spatial frequency domain of digitised MR signals. Here, a 'line' of k-space represents a sampled echo at a particular value of G_ϕ. 2D Fourier transforms are then used to reconstruct an MR image from k-space within echoes (in the frequency encoding direction and between echoes (in the phase encoding direction) (figure 30).

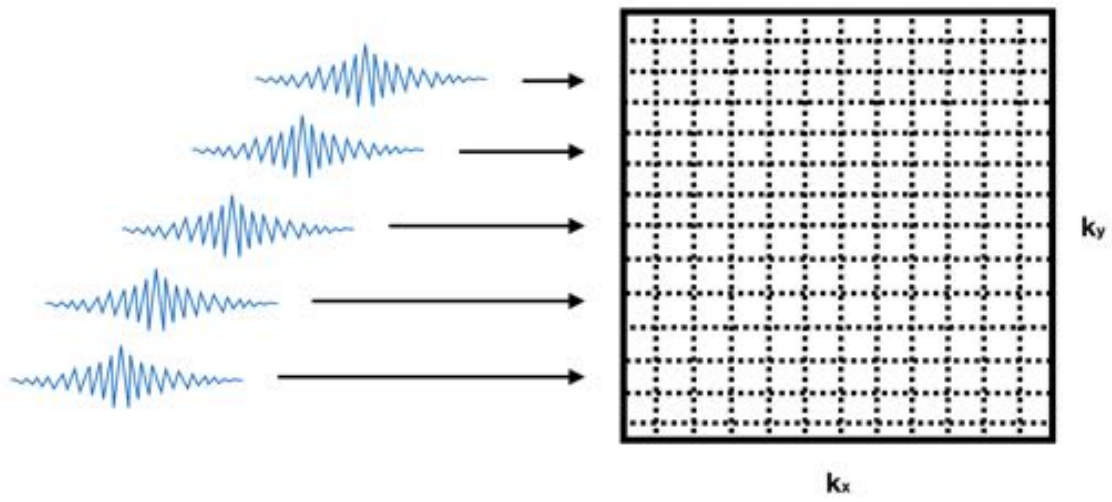

Figure 30. Filling of k-space.

Diffusion MRI: basic principles

Diffusion is the process whereby molecules naturally disperse. The speed at which this occurs is influenced by temperature, viscosity, particle size and the presence of a physical barrier. Whilst the path taken for a given molecule is truly random, when a large population of molecules are studied in homogeneous media e.g. pure water, a Gaussian displacement distribution is encountered, which resembles a ball in 3 dimensions (figure 31) since spins placed at the centre of the ball will diffuse towards its surface with equal probability in all directions. Situations that potentially violate these Gaussian assumptions will be considered later in this thesis.

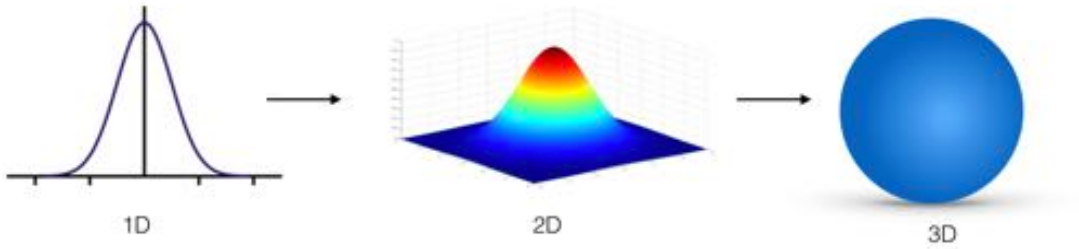

Figure 31: Gaussian displacement distributions

Albert Einstein showed that:

Equation 6

$$< r^2 > = 6D\Delta t$$

Where $<r^2>$ is the root mean squared displacement, D is the diffusion coefficient ≈ 3 x 10^{-3} mm^2/s for water at 37°C and Δt is the diffusion time (151).

For example, if Δt were 50ms (a typical measurement time in a diffusion MRI pulse sequence), mean displacement would be around 30μm. Whilst water molecules in the luminal space would be freely diffusing under such conditions, water molecules in other environments may not be. For example, in the case of *intracellular* water, 30μm is larger than the mean distance to prostate cancer cell membranes, which have a typical radius of 10μm (152), which physically restricts water motion and violates free isotropic Gaussian displacement. In this way, microstructural configuration can change diffusion behaviour. Diffusion-weighted imaging (DWI) sequences are sensitive to the displacement of water molecules and are achieved by the addition of 'diffusion gradients' to a standard pulse sequence.

Pulse Gradient Spin Echo (PGSE) sequence

The simplest, and most commonly used diffusion-weighted MRI sequence is the PGSE, which is a modified form of the spin-echo sequence. The sequence uses two identical diffusion-sensitising gradients either side of the 180° pulse to dephase and rephase spins. If there is no change in position of spins relative to the applied gradient at TE, the phase shifts will cancel and signal will be unchanged. However, there is displacement in the direction of the gradient, phase shifts will not cancel and the returned signal will have been attenuated (figure 32). The sensitivity of diffusion-weighted sequences have to restricted water motion can be altered by varying:

G: Gradient strength
δ: Gradient duration
Δ: Timing between diffusion gradients

Higher values for each of these parameters give rise to greater diffusion weighting. Overall diffusion weighting can be represented as a single 'b-value', calculated as:

Equation 7

$$b = \gamma^2 . G^2 . \delta^2 . (\Delta - \frac{\delta}{3})$$

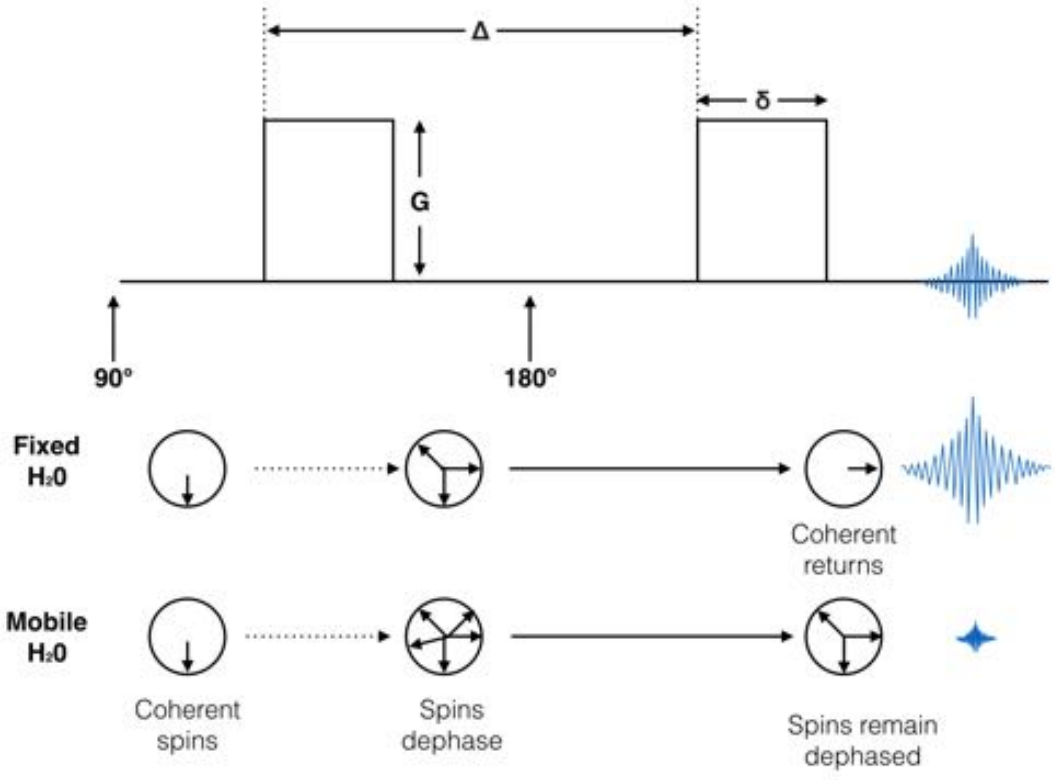

Figure 32: Diffusion-weighted pulse sequence

Echo planar imaging

Most diffusion-weighted acquisitions use a technique called echo-planar imaging (EPI) as a means of obtaining a whole image within a single excitation, which substantially reduces acquisition time for fast imaging. EPI is achieved by oscillating the frequency encoding gradient from positive to negative amplitudes, and 'blipping' the phase encoding gradient (figure 33) to traverse k-space in a zigzag fashion within a single excitation. Specifically, the frequency encoding polarity is oscillated from positive to negative to dephase and rephase spins in a sinusoidal fashion. In k-space this means sweeping from right to left, then left to right in the K_x direction with the blipped phase encoding gradient acting as to move up the k_y axis at the end of each line. The disadvantages of echo-planar techniques generally arise from susceptibility and ghosting artefacts arising as a result of these rapidly changing magnetic field gradients.

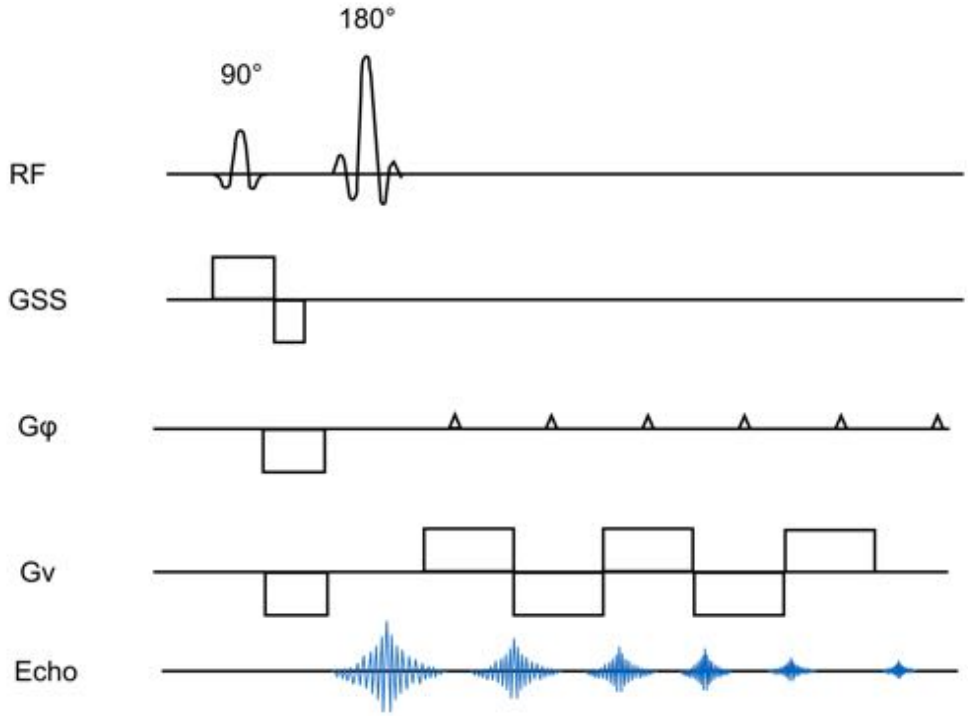

Figure 33: EPI pulse sequence

Section B: The biophysical basis of MRI techniques

To detect prostate cancer, MR pulse sequences exploit the different biophysical properties of benign and cancerous tissues to generate image contrast. When discriminating between individual Gleason grades however, even slighter differences in biophysical properties must be probed. I considered the biological differences in each Gleason grade in chapter 1, and will focus on their behaviour under the conditions of pulse sequences. T2W, DCE and DWI will be reviewed in turn, with particular emphasis on recent developments in DWI with a view to improved microstructural characterisation.

T2

Mechanisms of T2 relaxation in perfectly homogeneous media were described by Felix Bloch in 1946(153) and were covered in part A of this chapter. Throughout the 1950s, NMR research was unravelling behaviour in more complex materials, such as different liquids and crystals. Even in the simplest of substances, T2 relaxation times are governed by multiple complex physical processes, meaning the biophysical basis of T2 signal in prostate cancer remains poorly understood.

T2 and water

Despite its simple chemical formula, water is a complex substance with remarkable physical properties. Under physiological conditions, water protons have long relaxation times relative to fat and other macromolecules and thus generate the majority of MR signal in most tissues, with higher water content generally causing higher T2W signal intensity (SI) (154). However, the biochemical environment alters fluid dynamics via the cohesive and adhesive forces exerted by macromolecules, which act as to reduce T2 relaxation time. Important theory regarding these effects was introduced in a landmark paper written by Bloembergen, Purcell and Pound in 1948; often referred to as the BPP paper(155). In order to understand this theory, the concept of the *correlation time* (T_c) must be understood.

Molecular (rather than nuclear) rotation may generate local magnetic fields that induce T2 relaxation. This rotation can be represented as T_c, which is defined as the time taken for a molecule to rotate by 1 radian (≈57°). T_c depends on molecular size and is unsurprisingly lower for smaller molecules (e.g. water) than for macromolecules (e.g. proteins and fat). Molecules with low T_c have magnetic field fluctuations so rapid that

their average effect upon nearby molecules (called “motional averaging”) is negligible as it rotates very rapidly. Conversely, the slowly varying fields induced by macromolecules cause more sustained local magnetic field inhomogeneities, which significantly increases local dephasing effects and causes more rapid loss in transverse magnetisation, reducing the T2 relaxation time. In this way, water molecules closer to macromolecules will experience more rapid dephasing and reduced T2 relaxation times. Three differing ‘hydration layers’ around macromolecules can be considered, with increasing influence of dephasing effects, and reduced T2 the closer water spins are to macromolecules, namely ‘free’, ‘structured’ and ‘bound’ layers (figure 34) (156).

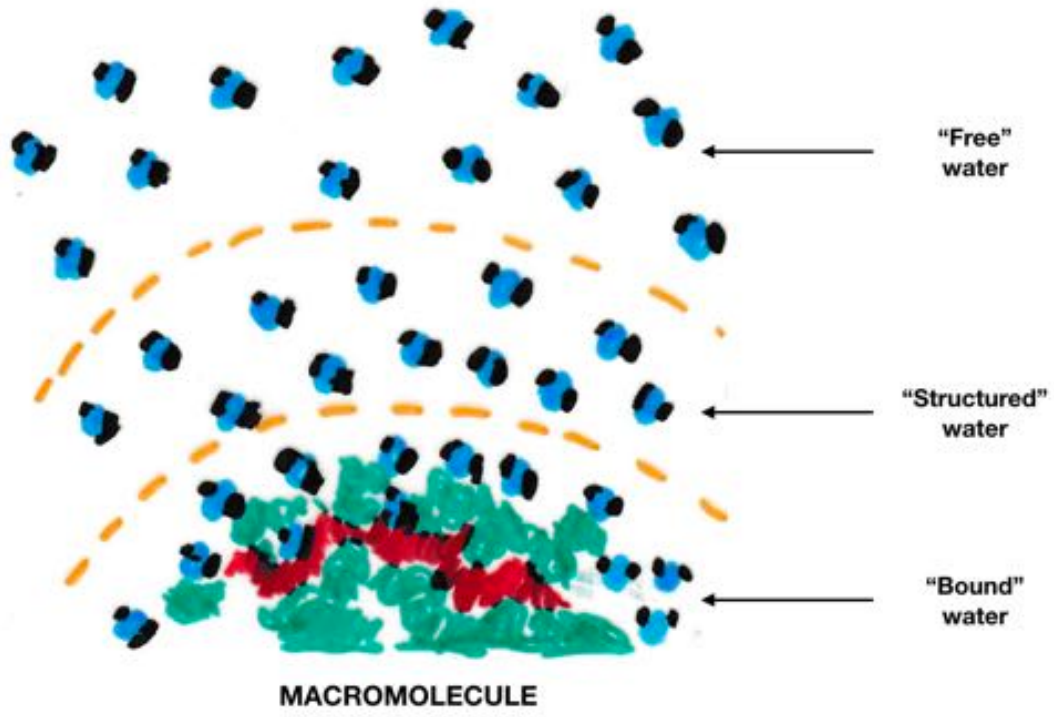

Figure 34: Hydration layers around a macromolecule

Macromolecules are loosely defined as molecules with > 1000 atoms(157), and have correlation times so short that pronounced dephasing causes them to be practically invisible at echo times used in clinical imaging. However, macromolecules do produce *indirect* effects on water as a consequence of their strong local magnetic field fluctuations, which causes more rapid T2 decay. Therefore, the longer water molecules spend in the vicinity of macromolecules, the shorter T2. The ‘**bound**’ pool immediately surrounds macromolecules and therefore has the shortest T2. As a consequence, proteinaceous fluid often has an intermediate T2. The ‘**free**’ pool is relatively unaffected by macromolecules and therefore has the longest T2 and the ‘**structured**’ pool lies between the free and bound pools, with an intermediate T2.

T2 relaxation in prostate cancer

Whilst the concepts outlined above are useful descriptors of T2 relaxation in relatively simple lattices, the situation *in vivo* is vastly more complex and further considerations need to be made. For example, unlike ADC which is almost universally low in viable tumour tissue relative to the surrounding healthy tissue, T2 relaxation times vary between tumours, and can be of high signal intensity (e.g. glioblastomas and hepatic metastases), intermediate signal intensity (e.g. breast and renal tumours - depending on the histological subtype) or low signal intensity, as is the case in prostate cancer. Furthermore, there is substantial evidence for bi- or multiexponential T2 decay(158–161) in prostate cancer.

Regional differences of water *amount* within the tumour microenvironment may provide some understanding into multiexponential behaviour, although this probably only provides an partial explanation because the relationship between amount of water and T2 relaxation time is found to be weak (156,157). Other possible contributors include different oxidation states of haemoglobin(164) and pH levels(165) have also been implicated, as has tissue compartmentalisation (luminal, stromal, intracellular) (159–161,163,166). Langer et al(19) correlated parametric T2 values with segmented regions of prostatectomy specimens and found that nuclear (mean slope -0.42, $p=0.001$), cytoplasmic (-0.39, $p=0.01$) and luminal (0.52, $p<0.001$), but not stromal (0.01, $p=0.92$) proportions correlated with T2 signal. It has also been shown that T2 of the normal PZ decreases significantly (by 14%) immediately after ejaculation(167) which could be due to loss in this luminal fluid. Consequently, the lower T2 signal encountered in aggressive tumours may be (partially) explained by loss in tubuloacinar structures as Gleason grade increases.

Indeed, a study in 74 patients confirmed decreasing T2W SI, normalized to the OI muscle with increasing Gleason grade ($p<0.001$)(168), suggesting potential clinical utility for T2 normalised signal intensity (T2nSI) in differentiating between Gleason grades. However, further evidence is required, because this is an isolated study to the best of my knowledge.

DCE

Since contrast in DCE imaging exploits altered haemodynamic and vascular permeability in tumours, it is important to review vascular biology.

Tumour vascular biology

Cancer cells are defined by unlimited replicative potential, resistance to apoptosis and are insensitive to antigrowth signals and self-sufficient in growth signals(169). Whilst early cancers with a few cells can rely upon nutrient diffusion to sustain cellular function, once cancers exceed a certain size (around 1mm), cellular hypoxia ensues and a complex proangiogenic signalling pathway commences to recruit vessels and exceed these size limitations (170). This transition to a vascularized state is called the 'angiogenic switch', which was first proposed by Judah Folkman in 1971 (171) and relies heavily upon vascular endothelial derived growth factor (VEGF) expression, a signalling protein which promotes endothelial cell migration and proliferation combined with factors such as fibroblast growth factors (FGFs)(172) and matrix metallopeptidases (MMPs) (173). The vascular bed within tumours is also denser than normal tissues, poorly constructed, spatially heterogeneous, immature and often incomplete with vascular pseudochannels, arteriovenous shunting(174) and increased porosity to macromolecules (including GBCAs)(175).

Microvessel density (MVD) is often used as a quantitative marker of angiogenesis and has been linked with survival in breast(176) and colorectal(177) cancers. However, MVD remains a controversial issue in prostate cancer because its relationship with outcome is disputed. Furthermore, whilst many investigators have shown an increase in MVD of prostate cancer vs. normal tissue(178,179), others have found no such relationship(179) with overlapping values in BPH(180) and conflicting evidence regarding changes with Gleason grade(181,182). Part of the reason for this heterogeneity between studies could be attributed to different methods by which it is measured (183) ranging from the maximal vascular density within a specimen (184), to the use modern digital segmentation techniques to count all vessels within a region of interest (179).

Acquisition protocols for DCE

DCE imaging involves acquiring serial volumetric images though the prostate at regular intervals before, during and after administration of a GBCA. Effective fat saturation is recommended (61) to null the signal from periprostatic fat which has high T1W SI which can mask enhancement if left unsaturated. In this way, fat saturation in DCE prostate protocols allow for more accurate assessment of extracapsular extension and therefore tumour staging (185).

At our institution, fat saturation is achieved using SPAIR (Spectral Attenuated Inversion Recovery) (186), which provides optimal fat saturation when compared with other fat saturation techniques (187). The requirement for a time series means T1-weighted 3D spoiled GE sequences with a low flip angle are also used.

Despite the existence of international guidelines, institutional practice in DCE technique can vary substantially, largely because there is a trade-off between temporal resolution - preferable for quantitative curve fitting due to an increased number of data points to capture the signal intensity changes as precisely as possible, and spatial resolution - preferable to define prostate anatomy. Rapid image acquisition also necessitates larger voxels to maintain SNR, meaning spatial resolution is usually less than T2W sequences.

GBCAs

GBCAs are used to probe the aforementioned changes in vascular biology, and have an intravascular biodistribution with rapid passage into the interstitial (but supposedly not intracellular) space. Contrast agent then passes back into the plasma (down a concentration gradient) and is eliminated by glomerular filtration with an effective half-life of around 2h. The only intended effect is T1 shortening, whereby regions of high Gadolinium concentration have high T1W SI.

Time-intensity curves

When an ROI is placed on each frame of a DCE acquisition (figure 35) and the SI plotted as a function of time a, 'time-intensity curve' is generated (figure 36) which reflects the pharmacokinetic handling of contrast medium in that region.

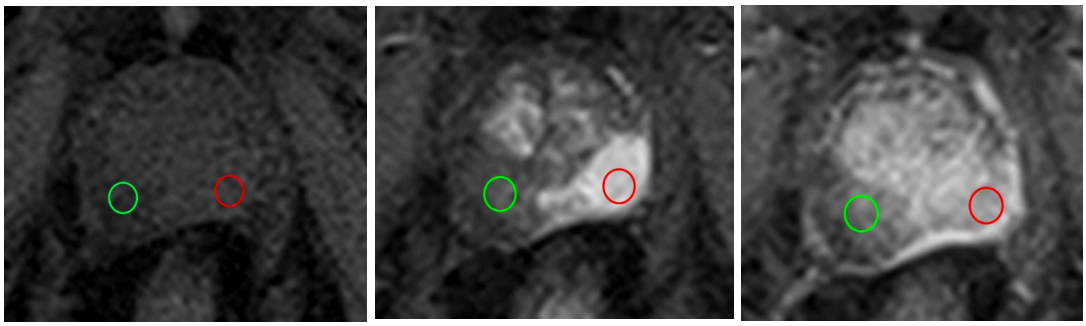

Figure 35: DCE images showing enhancing tumour

Left: precontrast ROIs on normal (green) and cancerous (red) prostate, time point 1 in figure 33 below. Middle: early postcontrast ROIs on normal and cancerous prostate, showing excellent contrast resolution between cancerous and non-cancerous regions, time point 2 in figure 33 below. Right: late postcontrast ROIs on normal and cancerous prostate, showing poor contrast resolution between cancerous and non-cancerous regions, time point 3 in figure 33 below.

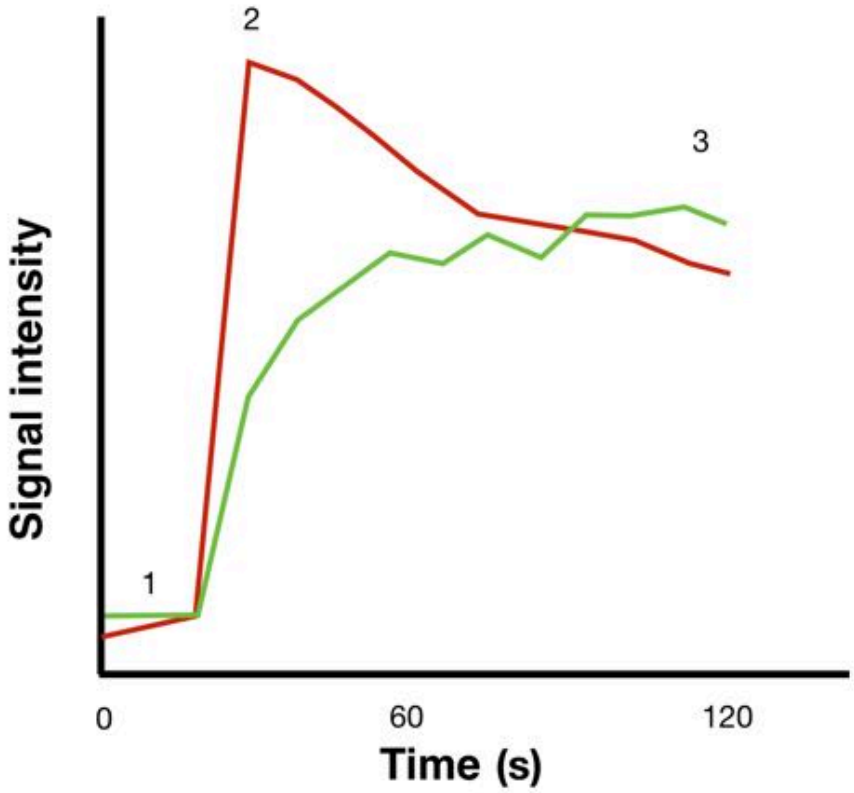

Figure 36: Time intensity curves from cancerous and non-cancerous regions of the prostate

Typical time-intensity curves of the normal and cancerous prostate are shown in figure 33 above, with the green curve representing normal tissue and the red curve cancerous tissue. As a consequence of increased angiogenesis, prostate cancer tends to demonstrate increased early enhancement with and rapid washout (which may relate to AV shunting)(171). Hence, early-enhanced images provide optimal contrast resolution between tumour and normal tissue.

Data analysis

There are three methods for analysing DCE images in current use, which, in order of increasing biological specificity but also technical difficulty are: qualitative, semi-quantitative, and quantitative.

Qualitative analysis

Qualitative assessment involves visual inspection of early-enhanced DCE images (and sometimes time-intensity curves), whereby tumours appear as a region of hyperenhancement. Qualitative assessment of images is the mainstay of DCE in clinical practice and is all that is recommended in both PI-RADS(60) and UK(188)

guidelines. However, central limitations to DCE comprise a lack of microstructural specificity and substantial overlap between hyperplastic TZ, prostatitis and tumour. Two further assessments can be made from qualitative images. Firstly, the early-enhanced DCE metric (EE) can be calculated, defined as the SI of the second enhancing image, normalized to the precontrast SI (189). Secondly, curve type can be assessed, which considers whether the washout phase continuously increases (type I), plateaus (type II), or washes out (type III). Whilst there is evidence behind use of such analyses for Breast Imaging Reporting and Data System (BI-RADS) assessment in breast MRI(58), evidence for its use in prostate MRI is lacking(190), and was therefore removed when PI-RADS was revised for version 2.

Semiquantitative analysis

Semiquantitative assessment of DCE data concerns the model-free assessment of time-intensity curve shape ('curveology'). Parameters are commonly extracted from time-intensity curves are shown in figure 37 and table 5 and have been defined previously (189,191).

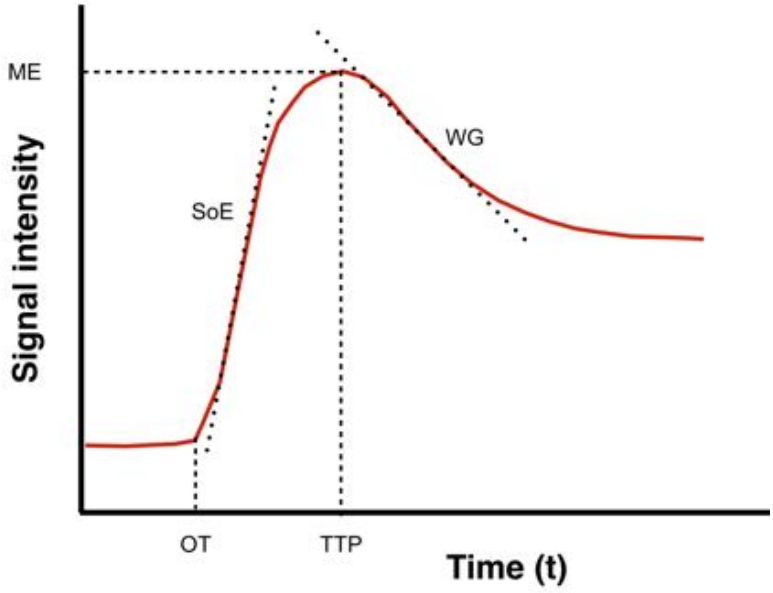

Figure 37: Semiquantitative enhancement characteristics of a time-intensity curve

Parameter	Abbreviation	Definition
Area under the curve	AUC	Area under the time intensity curve
Enhancement slope	SoE	Gradient of the enhancement slope
Maximum enhancement	ME	SI of maximum enhancement
Onset time	OT	Time to from first image to curve inflection
Time to peak	TTP	Time from first image to peak enhancement
Washout slope	WG	Gradient of the washout slope

Table 5: Definitions of semiquantitative enhancement characteristics

The advantage of semiquantitative metrics are that they are relatively simple to calculate, tend to be more reproducible than modelling-based parameters(192) and do not require such stringent limitations in time resolution as pharmacokinetic modelling. The disadvantage is that differences in temporal resolution and injection rates make absolute values meaningless (and therefore should be normalized) and there is a lack understanding as to the physiological meaning of parameters.

Quantitative analysis

True quantitative analysis uses pharmacokinetic models to convert SI measurements to gadolinium concentration, since ΔR1 is ∝[Gd]. In order to do this accurately, the native T1 contrast of the tissue (T_{10}) should be measured, and the haematocrit should also be taken into account (since GBCA does not pass into red blood cells).

The most popular pharmacokinetic model for cancer imaging is the 'Extended Toft's Model', which also requires 'arterial input function' (AIF) to be provided, which represents the GBCA bolus within the arterial system supplying the prostate. The model assumes passive diffusion from the vasculature into the EES and 4 main pharmacokinetic parameters may be estimated, namely K^{trans}, K_{ep}, V_e and V_p (figure 38)(193,194).

- K^{trans} is the 'forward mass transfer constant' i.e. the rate of transfer of gadolinium from the plasma into the EES, which depends on a combination of 3 factors: blood flow (F), the vascular surface area (S) and the vascular permeability (P).
- K_{ep} is the 'reflux rate constant' i.e. rate of transfer from the EES back into the vasculature
- V_e is the volume of gadolinium in the extracellular space, and can be calculated from K^{trans}/K_{ep}

- V_p is the volume of gadolinium in the blood plasma

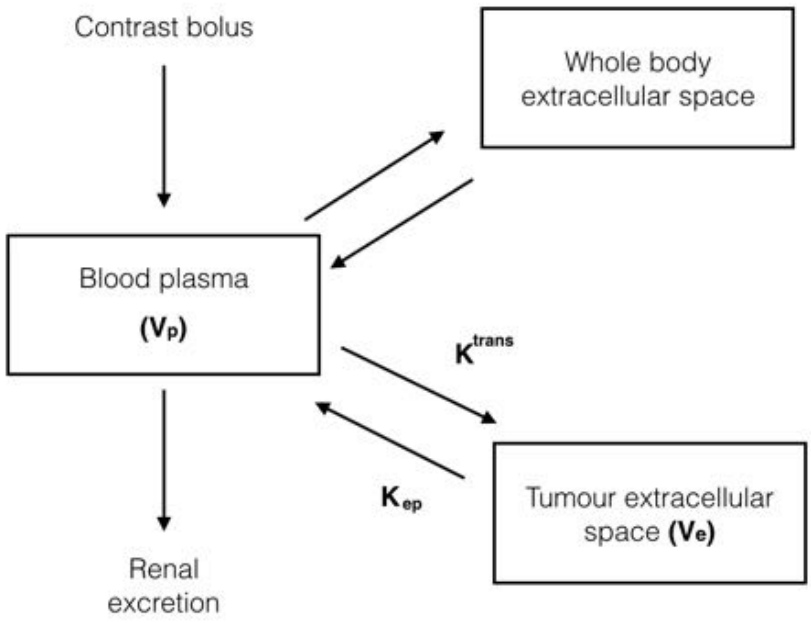

Figure 38: Schematic representation of Tofts' pharmacokinetic model

Pharmacokinetic modelling is potentially advantageous because it theoretically extracts parameters with physiological meaning. Where cancer has increased blood flow and volumes, K^{trans}, K_{ep} and V_p would all increase, whereas V_e would decrease with decreasing stromal proportion. However, in order to perform accurate measurements (e.g. capture the AIF peak), temporal resolution should be as high as possible, which compromises the spatial resolution of clinical images. In addition, the reproducibility of extended Toft's parameters has been questioned(195).

DCE analysis and Gleason grade estimation

Overall, the evidence of quantitative DCE analysis in Gleason grade assessment is fairly weak and probably obscured by heterogeneity in acquisition protocols. The most encouraging study was performed by Vos and colleagues who showed statistically significant correlations with Gleason grade for both quantitative and semiquantitative parameters, with similar performance for both types of metric with Spearman's ρ of 0.33 - 0.43(196). Engelbrecht et al. showed weak correlations between multiple semiquantitative DCE parameters and Gleason score (Pearson's r between -0.34 and +0.21), with the strongest correlations with onset time and time to peak enhancement (197). Interestingly, Chen and colleagues (198) found a relationship between washout gradient and Gleason score, where K^{trans} and K_{ep} failed to achieve significance, despite

use of a T_{10} map and a 2s time resolution, giving credence to the possibility that 'simplest is best' for DCE analysis. Finally, no discriminatory value was found for semiquantitative(199) and Tofts' parameters for Gleason grade(200) estimation in two other studies, meaning the use of DCE parameters in Gleason grade prediction remains an area of debate.

DWI

This section discusses the different mathematical models that can be used to describe the diffusion MRI signal in prostate cancer. Their evidence base and shortcomings will also be considered.

Introduction to diffusion modelling

If a perfectly homogeneous material with free Gaussian diffusion (*e.g. water)* is scanned at increasing b-values, the measured SI is found to fall with monoexponential decay, as shown in figure 39 below.

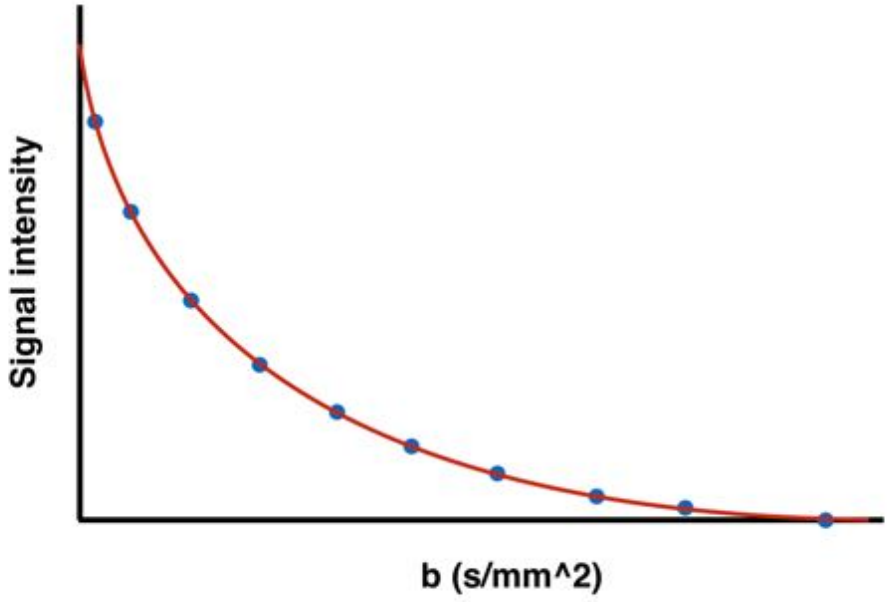

Figure 39: Signal decay curve

Blue dots: measured signal, red line: monoexponential fit to measured data

However, normal and cancerous prostate tissue are heterogeneous and compartmentalized, with a wide range of diffusion behaviours in each voxel meaning

decay curves *in vivo* are consistently found to be multiexponential(138), whereby monoexponential models are found to underestimate SI at low b-values and high b-values (figure 40), due to 'IVIM' and 'Kurtosis' effects, which will be considered subsequently.

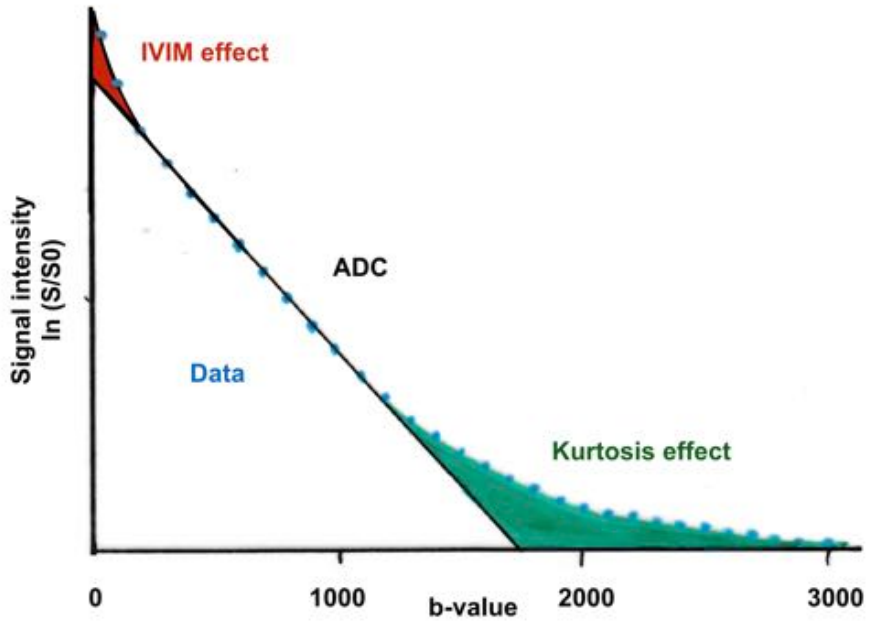

Figure 40: Signal decay curve of in-vivo tissue showing IVIM and Kurtosis effects

Diffusion models attempt to best describe the observed decay in SI and can provide quantitative information regarding tissue integrity. Models can be broadly categorized into 'signal models', which aim to describe the shape of the decay curve in mathematical terms, and 'microstructural models', which aim to assign the overall diffusion behaviour in each voxel into individual histological components.

Isotropic signal models

ADC

ADC is the simplest diffusion model and describes the diffusion curve as a monoexponential decay function, assuming a Gaussian displacement distribution and requires at least 2 b-values. The model takes the form:

Equation 8

$$S = S_0 \, e^{-b.ADC}$$

Where S = signal intensity, S_0= signal intensity at b=0, where b is the diffusion weighted factor also known as b-value, and ADC = apparent diffusion coefficient.

Intravoxel Incoherent Motion (IVIM)

Denis Le Bihan proposed that signal loss at low b-values was due an additional effect of randomly orientated capillaries, with fast flowing blood mimicking diffusion (perfusion, or 'pseudodiffusion')(201). Such effects are only detectable at b-values <150 mm/s^2 (138), after which conventional diffusion effects predominate. Therefore, acquisitions which include b-values <150 mm/s^2 can potentially capture this information and split diffusion and perfusion effects into separate pools. The formula for the IVIM model is given by:

Equation 9

$$S = S_0 (1 - f) e^{-bD} + f e^{-bD*}$$

Where f is the perfusion fraction – the intravascular volume, D is the real diffusion coefficient and D is the perfusion coefficient.*

Diffusion Kurtosis and Stretched Exponential

However, IVIM still underestimate SI at high b-values (>2000 mm/s^2) (202–205). Diffusion Kurtosis imaging (DKI) and stretched exponential (SE) both attempt to describe this additional non-Gaussian phenomenon, which is thought to arise due to the restriction to diffusion imparted by obstacles such as cell membranes and fibres(206). Both necessitate acquisitions with b-values >2000 mm/s^2. DKI includes a Kurtosis index (*K*) in the model, which is a description of the deviation from Gaussian behaviour, with higher values thought to reflect more deviation and therefore microstructural complexity (207).

Equation 10

$$\boldsymbol{S = S_0 e^{-(D_K b - \frac{K}{6} D_K^2 b^2)}}$$

The stretched exponential takes the form:

Equation 11

$$S = S_0 e^{-(D_s b)^{\alpha}}$$

Where α is the stretching parameter (or heterogeneity index), whereby a value closer to 1 indicates greater similarity to the monoexponential situation. D_s is the distributed diffusion coefficient, which is the stretch-adjusted diffusivity.

Anisotropy and diffusion tensor imaging

Where there is diffusion anisotropy caused by diffusion preference or hindrance in a particular direction (governed by tissue microstructure), diffusivities are unsurprisingly found to be different in each direction. Diffusion tensor imaging (DTI) can represent this anisotropy whereby 'diffusion tensor' is a 3 x 3 matrix used to describe 3D displacements, with three principal diffusion directions (eigenvectors) and their diffusivities (eigenvalues $\lambda_1 > \lambda_2 > \lambda_3$):

Equation 12

$$\boldsymbol{D} = \begin{bmatrix} \boldsymbol{D_{xx}} & \boldsymbol{D_{xy}} & \boldsymbol{D_{xz}} \\ \boldsymbol{D_{yx}} & \boldsymbol{D_{yy}} & \boldsymbol{D_{yz}} \\ \boldsymbol{D_{zx}} & \boldsymbol{D_{zy}} & \boldsymbol{D_{zz}} \end{bmatrix}$$

The diagonal elements (D_{xx}, D_{yy} and D_{zz}) represent diffusivities along each principle axis, and the rest of the elements represent the correlation between them. Since $D_{xy}=D_{yx}$, $D_{xz}=D_{zx}$ and $D_{yz}=D_{zy}$, there are six unknowns which can solved using multivariable linear regression to estimate the eigenvectors and eigenvalues in each voxel, provided the acquisition uses at least six gradient directions and a b=0 (since the diffusion tensor is symmetrical i.e. $D_{zx}=D_{xz}$), using multivariable linear regression (208). The diffusion tensor can also be graphically represented as an ellipsoid, with the principle axes representing principal eigenvectors, and the diffusion distances their eigenvalues (figure 41).

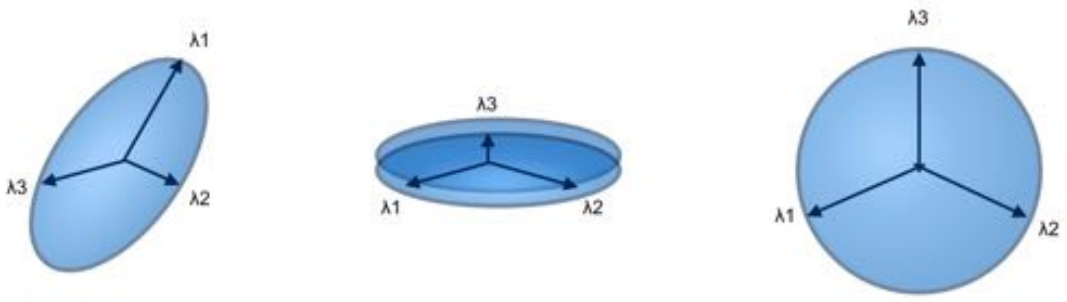

Figure 41: Diffusion ellipsoids; L: prolate, middle: oblate, R: isotropic ball

For example, the ellipsoid may be:
A ball, (isotropic) where $\lambda_1 \approx \lambda_2 \approx \lambda_3$
Prolate (cigar shaped), where $\lambda_1 >> \lambda_2 \approx \lambda_3$
Oblate (disc-like), where $\lambda_1 \approx \lambda_2 >> \lambda_3$

The fractional anisotropy (*FA*), can be calculated to provide a measure of diffusion

asymmetry within each voxel, using the eigenvalues:

Equation 13

$$FA = \sqrt{\frac{(\lambda_1 - \lambda_2)^2 + (\lambda_2 - \lambda_3)^2 + (\lambda_1 - \lambda_3)^2}{2(\lambda_1^2 + \lambda_2^2 + \lambda_3^2)}}$$

Diffusion models for prostate cancer

Various studies have investigated the relationship between model estimates and Gleason score. At least ten studies have shown a consistent and fairly strong negative relationship between increasing Gleason grade and ADC score (209–220), which make it the most robust tool for non-invasive estimation of Gleason grade. However, all studies demonstrate overlapping ADC values between each Gleason grade meaning ADC, when used alone, fails to accurately predict Gleason grade in an individual patient.

The tendency for cancerous tissues to demonstrate low ADC values is often attributed to 'cellularity'. However, whilst authors have demonstrated some correlation between decreasing ADC and nuclear count, correlation is only moderate(221,222) and ADC seems to be more closely related with the percentage of individual components of prostate cancer tissue (lumen, epithelium and stroma)(18). Notably, pathologists also make assessments of Gleason grade by assessing tissue architecture rather than cell density, and the proportion of these components also changes with Gleason grade (as has been considered in chapter 1). Therefore, it would be very useful if a validated imaging biomarker could explain the contribution to the diffusion signal for each of these components so their relative fractions can be determined.

The IVIM model was an important development because it offers subvoxel information and was the first model to have a hypothesized relationship with tissue microstructure. Whilst IVIM has been shown to provide a better fit to data than ADC(203), its usefulness in prostate cancer detection and characterization is uncertain as the evidence is conflicting(223,224), and is a relatively new technique in the prostate(225). Furthermore, the relevance of vascularity in the grading of prostate cancer is questionable. Whilst both stretched exponential and DKI have been shown to fit the signal better than ADC(203,205), evidence for their use in prostate cancer is again insufficient with fewer studies in the literature than IVIM. DTI studies have been inconsistent in the prostate, which may relate to the sensitivity of FA measurements to noise and the relatively large voxel volumes of in vivo scans(202,226–232).

In conclusion, whilst a range of signal models exist and can provide a relatively good fit of *in vivo* diffusion data, they lack biological specificity and microstructural correlates at histology. This makes accurate biological validation very difficult to achieve, and motivates the development of microstructural models.

Microstructural models

"If one knows what to look for, it is much easier to find it (206)*"*

Microstructural models relate the contributions to MR signal from each tissue compartment directly to histological features. A number of models have been gaining interest due to their ability to estimate histology non-invasively, and have yielded impressive results in high field strength ex-vivo neuroimaging studies(233).

VERDICT

VERDICT (Vascular, Extracellular and Restricted Diffusion for Cytometry in Tumours) is a framework which models diffusion signal in three distinct environments(234), and can be mathematically represented by the equation:

Equation 14

$$\boldsymbol{S = \sum_{i=1}^{3} f_i S_i}$$

Which can also be expressed as:

$$S = f_1 S_1 + f_2 S_2 + f_3 S_3$$

Where: f= fraction, S1 is the signal from the intracellular water, S2 is the signal from the extravascular, extracellular space and S3 is the signal from the blood vessels.

Intracellular water has the lowest diffusivity of all compartments, with water diffusion being 'restricted' by cell membranes(235). This compartment also has a high viscosity due to macromolecules(236) with higher nuclear: cytoplasmic ratios, (which increase with Gleason grade) causing further diffusion restriction(237). In this way, VERDICT also provides a measure of the amount of non-Gaussian behaviour experienced at higher b-values.

In the Extracellular, extravascular space (EES) we are likely to encounter two pools of

water molecules with distinct behaviours:

i. Free Gaussian diffusion within luminal spaces with monoexponential decay.
ii. Hindered diffusion of molecules travelling in the fibrous and muscular stroma and navigating around epithelial cells.

16T *ex-vivo* microimaging with isotropic voxels of 40μm has confirmed that the diffusivities in both of these components differ substantially (2.1 and 0.7 x $10^{-3}mm^2/s$ respectively) but are both higher than in epithelial cells (0.4 x $10^{-3}mm^2/s$)(235). It has also been suggested that the greater the tortuosity (λ) of EES, which in turn is affected by cell size, density and organisation, the greater the slowing of water motion(238). Diffusion behaviour in the vascular compartment is the fast-flowing intravascular pseudodiffusion previously considered in IVIM.

Following model selection using Akaike Information Criterion (AIC) and Bayesian Information Criterion (BIC) ranking, the optimal components for the compartments (after Panagiotaki et al(239)) in prostate cancer were shown to be:

i) 'Spheres' for the intracellular compartment, which have impermeable boundaries, a non-zero radius and isotropic diffusion.
ii) 'Balls' for the EES, which are isotropic tensors with Gaussian diffusion.
iii) Astrosticks for the vascular compartment, which are multiple uniformly distributed cylinders of zero diameter. Whilst pseudodiffusion in each stick is anisotropic, the overall sum means each voxel is isotropic.

Fitting the model to each voxel produces parametric maps for the whole organ, with three maps produced for each acquisition, namely f_{IC} – the intracellular volume fraction, f_{EES} – the extravascular extracellular volume fraction, and f_{vasc} – the vascular volume fraction. Typical examples are shown in figure 42, alongside the conventional mp-MRI.

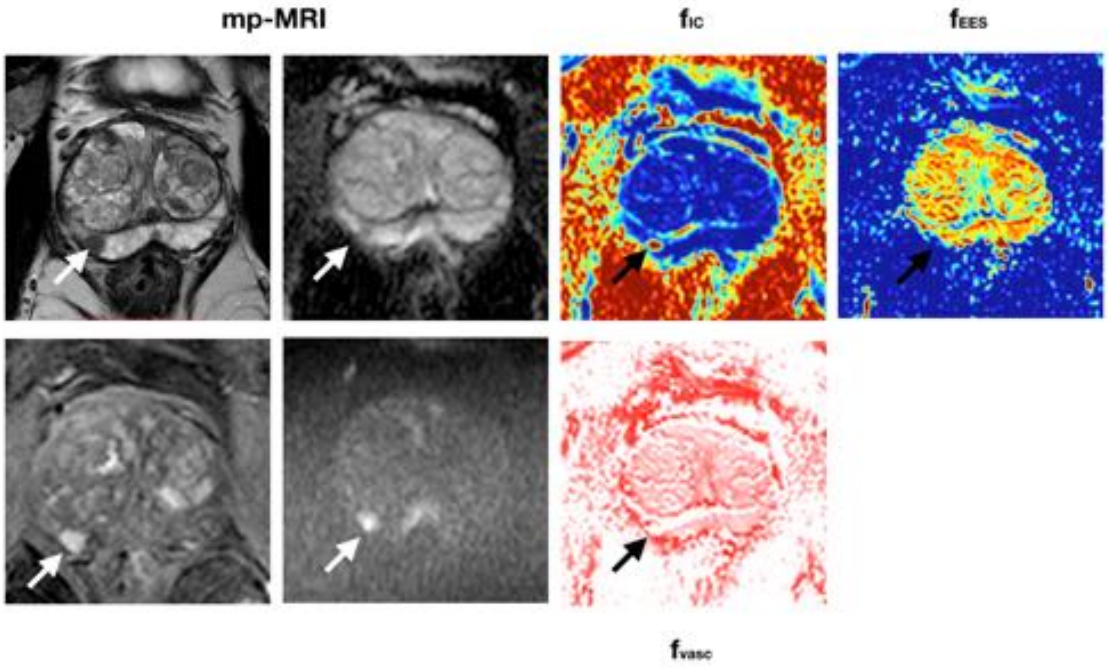

Figure 42: mp-MRI (leftmost 4 images) and VERDICT MRI (rightmost 3 images).

Left: Mp-MRI shows a right PZ lesion between 7 – 8 o'clock (arrows) which has a high T2W SI (top L), low ADC value (top right), lesional enhancement (lower left) and high signal on high b-value images (lower right). Right: VERDICT images show elevated f_{IC}, reduced f_{EES} and equivocal f_{vasc}.

The VERDICT prostate model assumes no exchange between the compartments and does not account for fluid viscosity, variations in cell size, shape or membrane porosity. The lumen and stroma are also considered as a single isotropic compartment as part of the EES.

VERDICT and the biomarker development pipeline

After proof-of-concept using computer simulations, proof-of-principle studies were carried out at 9.4T in two murine colorectal cancer models with known differences in histology, whereby these differences were successfully measured using VERDICT, as were changes following administration of gemcitabine, where ADC and IVIM failed to detect significant differences(205). An *in-vivo* study of VERDICT in human prostate cancer was then performed at 3T, and showed discrimination of benign and cancerous tissue, with AIC confirming that VERDICT was the most appropriate model over ADC, IVIM and DKI. The scanning protocol was then optimized to reduce the scan time from 40 minutes to 10 minutes using an optimization procedure(240), whereby VERDICT can now supplement conventional detection mp-prostate MRI. In this way, investigation in domain 1 of the biomarker roadmap has been completed and, after 'lock-down' of acquisition and analytical methods, we strive to validate the putative clinical value of

VERDICT maps for the non-invasive estimation of Gleason grade. This will include technical validation, by way of image quality, repeatability and biological validation, by examining the values of the VERDICT parameters in each Gleason grade.

In summary, there are multiple diffusion models that have demonstrated potential for the non-invasive estimation of Gleason grade, which could be developed as surrogate markers of survival outcomes to help inform management decisions in the prostate cancer pathway. In particular, whilst each component of the mp-MRI (T2W, ADC, DCE) has shown some potential at classifying Gleason grade, predictive models which combine each of these parameters may have better value than each single predictor. Whilst VERDICT also harbours potential for improved biological specificity vs. ADC, it currently remains in the discovery domain of the biomarker roadmap, and therefore needs translation and validation in order to assess its putative value as a predictor of Gleason grade.

3 AIMS, OBJECTIVES AND HYPOTHESES

In this chapter I define the problem statements, aims, objectives and hypotheses of each of the results chapters (namely chapters 4, 5, 7, 8 &9) in order to emphasize how each chapter builds upon the work of the previous, and to act as a concise reference for the body of my work.

Chapter 4

Problem statement:

Analytical methods for quantitative mp-prostate MRI have not been standardised.

Aim

To standardise methods for quantitative mp-MRI analysis throughout this thesis.

Objectives:

i. To assess the intermethod, intraobserver and interobserver agreement of quantitative mp-MRI tumour measurements using single slice (ROI) vs. volumetric (VOI) analysis with two different DICOM viewers.
ii. To assess whether normalisation of T2W SI can be improved the reproducibility by normalising to regions other than the current standard practice of using OI.
iii. To determine whether histographic metrics are more reproducible than mean parameters.

Null hypotheses:

i. There is no significant difference between ROI and VOI analysis in terms of intermethod, intraobserver and interobserver agreement.
ii. The reproducibility of T2nSI will be the same, regardless of the region selected as a normalization reference.
iii. The reproducibility of histographic metrics such as standard deviation (SD), entropy, skewness and kurtosis are equivalent to mean values.

Chapter 5

Problem statement:

Non-invasive tools that can predict a Gleason 4 component in patients undergoing active surveillance do not currently exist. Whilst each component of the MRI has been shown to predict Gleason grade individually, their use in combination may be superior but is less well established.

Aim

To combine components of mp-MRI with clinical parameters in zone-specific predictive models that best predict a Gleason 4 component in known prostate cancers.

Objectives:

i. Develop logistic regression (LR) models for the prediction of a Gleason 4 component in known prostate tumours
ii. Test the model performance following leave-one-out (LOO) internal validation and a prospective test cohort
iii. Assess model performance vs. the opinion of experienced radiologists

Null hypotheses

i. LR models cannot predict a Gleason 4 component in prostate cancer
ii. Models do not maintain their performance at internal and external validation
iii. Models cannot outperform radiologist opinion

Chapter 7

Problem statement

The ability of current components of the mp-MRI to distinguish between Gleason grades non-invasively is limited. VERDICT MRI (a microstructural diffusion-weighted technique) holds theoretical potential for this purpose, although requires technical and biological validation prior to clinical validation and utility studies.

Aim

To technically validate, and perform early biological validation regarding the use of VERDICT parametric maps as quantitative imaging biomarkers in prostate cancer, according to the imaging biomarker roadmap.

Objectives

To test VERDICT maps in terms of:

i. Image quality
ii. Repeatability
iii. Their ability to distinguish between Gleason grades

Null hypotheses

i. ADC maps are superior to VERDICT MRI maps (f_{IC}, f_{EES} and f_{vasc}) in terms of image quality
ii. ADC metric repeatability is superior to that of VERDICT estimates
iii. ADC is superior to VERDICT estimates (f_{IC}, f_{EES} and f_{vasc}) in terms of ability to discriminate between Gleason grades

Chapter 8

Problem statement:

Accurate staging of aggressive primary prostate cancer is of paramount importance when making clinical decisions, yet currently hinges upon bone scan (BS) +/- CT, which are inaccurate techniques. WB-MRI holds significant promise for this purpose, but requires further development before it can be introduced into clinical practice.

Aim:

To develop WB-MRI using semiquantitative scoring systems for use in the primary 'TNM' staging of aggressive prostate cancer.

Objectives:

i. To use a semiquantitative scoring system in conjunction with mp-WB-MRI
ii. To determine agreement between WB-MRI and PET/CT and BS
iii. To determine the interobserver agreement of mp-WB-MRI
iv. To compare the diagnostic accuracy of mp-WB-MRI with BS and ^{18}F-choline PET/CT for both nodal and metastatic disease
v. To establish whether there is an additional value of T2W and post contrast mDixon above precontrast mDixon and DWI sequences alone

Null hypotheses:

i. Intermodality agreement is equivalent for WB-MRI, PET/CT and BS
ii. Interobserver agreement in WB-MRI is low
iii. The diagnostic accuracy of WB-MRI is low
iv. There is no additional value of T2 and postcontrast mDixon sequences vs. precontrast mDixon and DWI alone

Chapter 9

Problem statement:

The image quality, interobserver agreement and diagnostic accuracy of WB-MRI remain unknown in the context of biochemical failure post prostatectomy due to a lack of studies reported in the literature.

Aim:

To assess the value of WB-MRI vs. ^{18}F-choline PET/CT in combination with a semiquantitative scoring system for staging patients with biochemical failure following radical prostatectomy in a multicentre, multivendor, multinational study.

Objectives:

i. To use WB-MRI in conjunction with a semiquantitative scoring system to classify disease status in patients with biochemical failure following radical prostatectomy.
ii. To determine the image quality of WB-MRI in a multicentre study
iii. To determine the interobserver agreement of WB-MRI
iv. To determine the diagnostic accuracy of WB-MRI and ^{18}F-choline PET/CT

Null hypotheses:

i. The image quality of WB-MRI is the same between each centre
ii. Interobserver agreement in WB-MRI is low
iii. The diagnostic accuracy of WB-MRI is low

4 IMPROVING THE RELIABILITY OF QUANTIATIVE MP-PROSTATE MRI METRICS

Section A: Single slice ROI vs. VOI analysis of mp-prostate MRI metrics using two different DICOM viewers

Author declaration

All of the work in this chapter was conceived, analysed and written by me personally, under the supervision of Dr. Shonit Punwani. Patients were recruited to the PICTURE study (241) by the Academic Urology team at UCLH for section A. A second Radiologist, Mrishta Brizmohun Appayya also contoured lesions in section A, to gauge intermethod agreement. Extraction of time-intensity curves and imaging histogram values in section B were performed using an Osirix plugin developed alongside, and written by, Michela Antonelli.

Introduction

A range of DICOM viewers have been developed for the analysis of quantitative imaging data, and each has their advantages and disadvantages. As I previously discussed in chapter 1, analytical methods in quantitative MRI trials have not been standardised, which increases the heterogeneity between studies and can thereby reduce their repeatability and reproducibility. Whilst consensus guidelines have, for example, advised volumetric analysis of tumours over single slice region-of-interest (ROI) analysis(138), presumably to standardise analytical methods and reduce some of this heterogeneity, to the best of my knowledge, there is no data in the prostate literature to confirm that VOI methods have higher levels of interobserver and interobserver agreement.

In this study, I compare the quantitative values obtained from ROI and VOI measurements in 20 patients with biopsy-confirmed prostate cancer using a different DICOM viewer for each method (Osirix for ROI, and MIM for VOI). Three fundamental metrics from mp-prostate MRI will be assessed, namely T2W SI, ADC and early-enhanced (EE) DCE. Their intermethod agreement will be compared, as will intraobserver repeatability and interobserver reproducibility. The results of the present study will be used to inform the analytical methods used throughout the rest of the thesis.

Materials and methods

Our Institutional Review Board (IRB) approved the study and waived the requirement for individual consent for retrospective analysis of patient data collected as part of clinical trials/routine care (R&D No: 12/0195, 16 July 2012). 330 patients were consecutively recruited for the main study, which has been reported previously (241). In brief, inclusion criteria were (i) men who underwent previous TRUS biopsy whereby suspicion remained that cancer was either missed or misclassified and (ii) men suitable for further characterisation using Transperineal Template Prostate Mapping (TPM) biopsy. Exclusion criteria were (i) previous history of prostate cancer treatment and (ii) men in whom TPM was inadequate for analysis due to lack of complete gland sampling or inadequate sampling density.

A subset of these men were analysed for the present study, imaged between February 2013 and January 2014. 20 men were chosen in total; 11 with PZ tumours and 9 with transition zone (TZ) tumours, as confirmed with cognitive MRI targeted biopsy(242). Tumours were selected to have Likert score ≥4, measure ≥ 0.5cc and be present on at least 3 contiguous ADC slices (Median 2.1cm^3, IQR 0.8 – 3.0). 4 tumours were Gleason 3+3, 14 were Gleason 3+4 and 2 were Gleason 4+4. Only index lesions were included in the analysis.

The 3T Achieva acquisition protocol was carried out in all patients (as defined in chapter 1).

Image analysis

Quantitative MRI parameters were extracted using i) open source Osirix software (v7.0 Bernex, Switzerland) to draw ROIs on single tumour slices, at the epicentre of lesions (ROI), and ii) MIM proprietorial software (Cleveland, USA) to draw the entire volume (VOI), whereby MIM software uses semiautomatic rigid translational co-registration of T2W, ADC and DCE images. VOIs were therefore placed on all registered sequences contemporaneously using a single VOI, unlike Osirix where separate placement of ROIs is necessitated (figure 43).

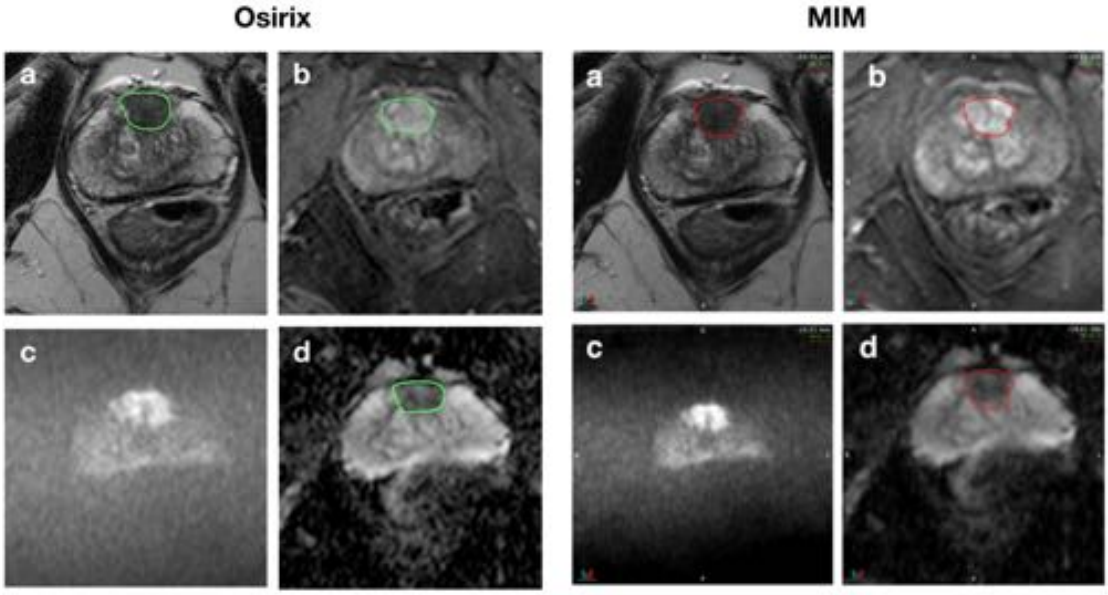

Figure 43. Lesion contouring of the same patient using both DICOM viewers.

Left fourmost images using Osirix, right fourmost images using MIM. For both viewers, a=T2, b=DCE, c=high B, d=ADC map.

For each case, the radiologist (EJ) was made aware of the location of the index lesion as defined by diagrams produced for the trial MRI reporting proforma. ROIs were drawn with a washout period of 1 week between single slice and volumetric measurements (to prevent the radiologist performing the analysis recalling the precise location of the previous ROIs drawn, in order to minimise bias) and gauge intermethod agreement. The analysis was then repeated following a washout period of 3 months to gauge intraobserver repeatability. A second board certified radiologist (MB) also performed the analysis to gauge interobserver reproducibility.

The mean SI of each ROI/VOI on T2W, ADC and DCE images at all time points was recorded. The EE DCE metric was defined as the second image following enhancement of the lesion, normalized to the precontrast ROI/VOI.

Statistical analysis

Statistical analysis was performed using GraphPad Prism v6.0 (La Jolla, California, USA) and using SPSS version 22 (IBM, New York, USA).

For intermethod comparison, paired t-tests were performed to assess constant differences between ROI and VOI methods. Lin's concordance correlation coefficients (ρ_c) and Bland-Altman (B-A) analyses were performed to assess agreement between methods.

For intraobserver agreement, paired t-tests, Intraclass Correlation coefficient (ICC) (3,1 with absolute agreement) and B-A analyses were performed. Mean values of the two metrics were also calculated for intermethod comparison, as described previously.

For interobserver agreement, paired t-tests, Lin's concordance correlation coefficients (ρ_c) and B-A analyses were performed. B-A plots are expressed as a percentage of the mean value, to facilitate comparison between methods and quantitative parameters. Where two measurements were taken during the intraobserver read, their mean value was used.

Scatterplots will also be presented. Levels of agreement for ICCs and ρ_c will be interpreted according to Landis and Koch(243): 0.0–0.20 no to slight agreement, 0.21–0.40 fair agreement, 0.41–0.60 moderate agreement, 0.61–0.80 substantial agreement, and 0.81–1 almost perfect agreement.

Results

Intermethod agreement

Results of intermethod agreement are presented in table 6 and figure 44. Whilst high levels of concordance are shown between both methods, as evidenced by narrow B-A limits of agreement and values of $\rho_c > 0.9$, single slice measurements gave lower T2 values and higher EE DCE than volumetric analysis, which reached statistical significance.

Method	Mean +/- SD	Paired t-test p-value	B-A 95% limits of agreement (%)	ρ_c
Single slice T2W	144.5 ± 56.5	0.03*	-15.2, 9.4	0.98 (0.96 – 0.99)
Volume T2W	150.1 ± 63.0			
Single Slice ADC	665.7±113.0	0.19	-16.7, 12.3	0.90 (0.76 – 0.96)
Volume ADC	681.3±120.5			
Single slice EE DCE	1.8 ± 0.26	0.005**	-6.8, 14.6	0.90 (0.78 – 0.96)
Volume EE DCE	1.7 ± 0.3			

Table 6: Agreement between ROI and VOI methods

95% CI (lower - upper) are provided in parentheses.

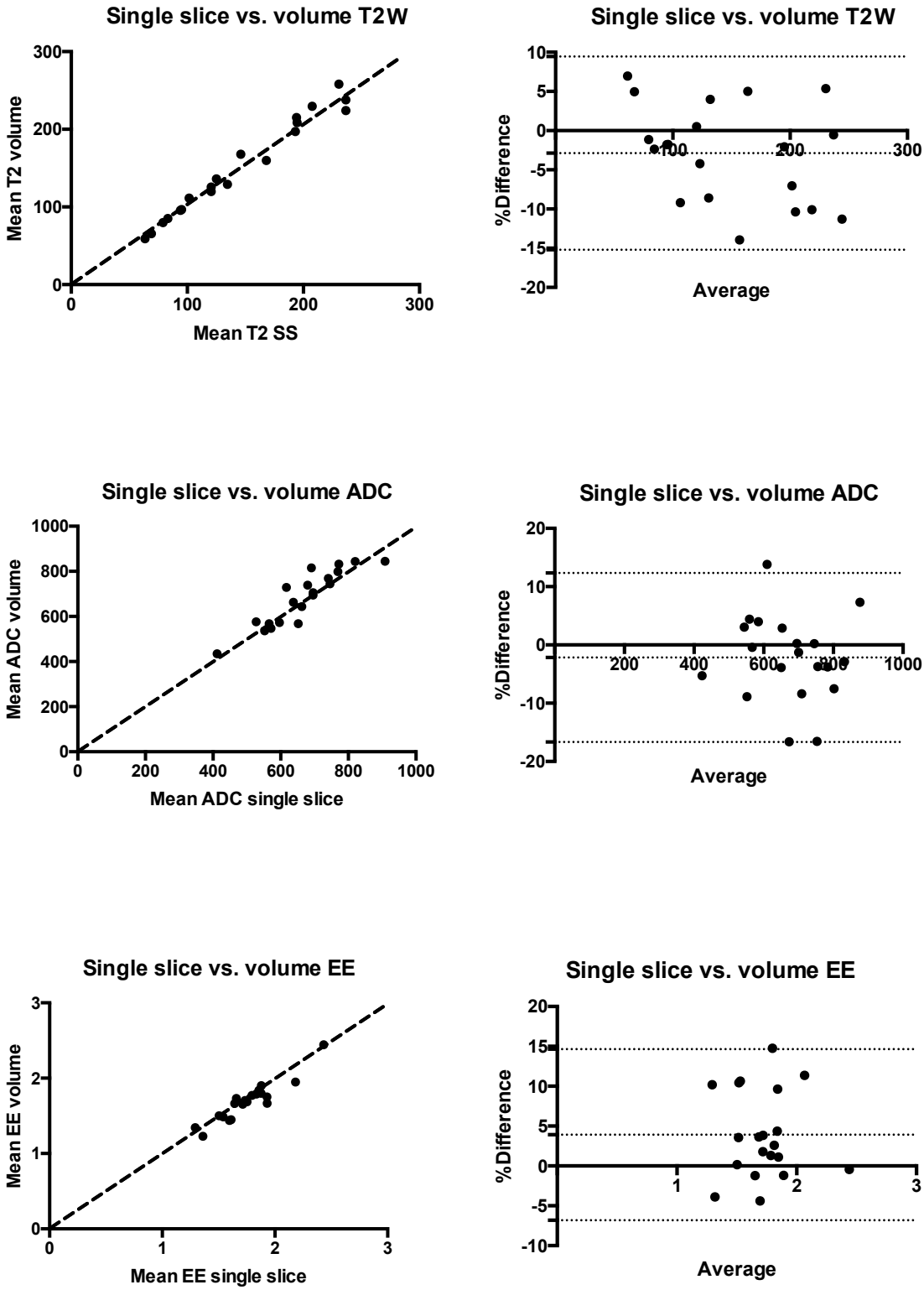

Figure 44: Graphical representation of intermethod reproducibility

Left column: scatterplots with a line of identity, Right column: B-A plots.

Intraobserver agreement

Results from assessment of intraobserver reproducibility are presented in table 7 and figures 45 and 46. Here, high levels of agreement were again obtained with B-A limits of agreement to within +/- 20% and ICC ≥0.86 with the exception of volumetric ADC analysis, whereby the second set measurements were significantly lower than the first.

Method	Mean +/-SD	Paired t-test p-value	B-A 95% limits of agreement	ICC
Single slice T2W				
Measurement 1	144.4±60.7	0.92	-18.6, 16.9	0.96 (0.91, 0.99)
Measurement 2	144.8±57.3			
Volume T2W				
Measurement 1	149.4±63.8	0.61	-15.9, 13.8	0.98 (0.95 – 0.99)
Measurement 2	150.9±62.9			
Single Slice ADC				
Measurement 1	662.5±114.9	0.56	15.9, 13.3	0.92 (0.80 – 0.96)
Measurement 2	668.9±116.2			
Volume ADC				
Measurement 1	705.0±124.8	0.005**	-11.5, 25.8	0.80 (0.43 – 0.93)
Measurement 2	657.6±125.4			
Single slice EE DCE				
Measurement 1	1.75±0.25	0.13	-16.5, 11.7	0.86 (0.68 – 0.94)
Measurement 2	1.79±0.26			
Volume EE DCE				
Measurement 1	1.70±0.24	0.94	-15.5, 16.5	0.86 (0.68 – 0.94)
Measurement 2	1.70±0.28			

Table 7: Intraobserver agreement

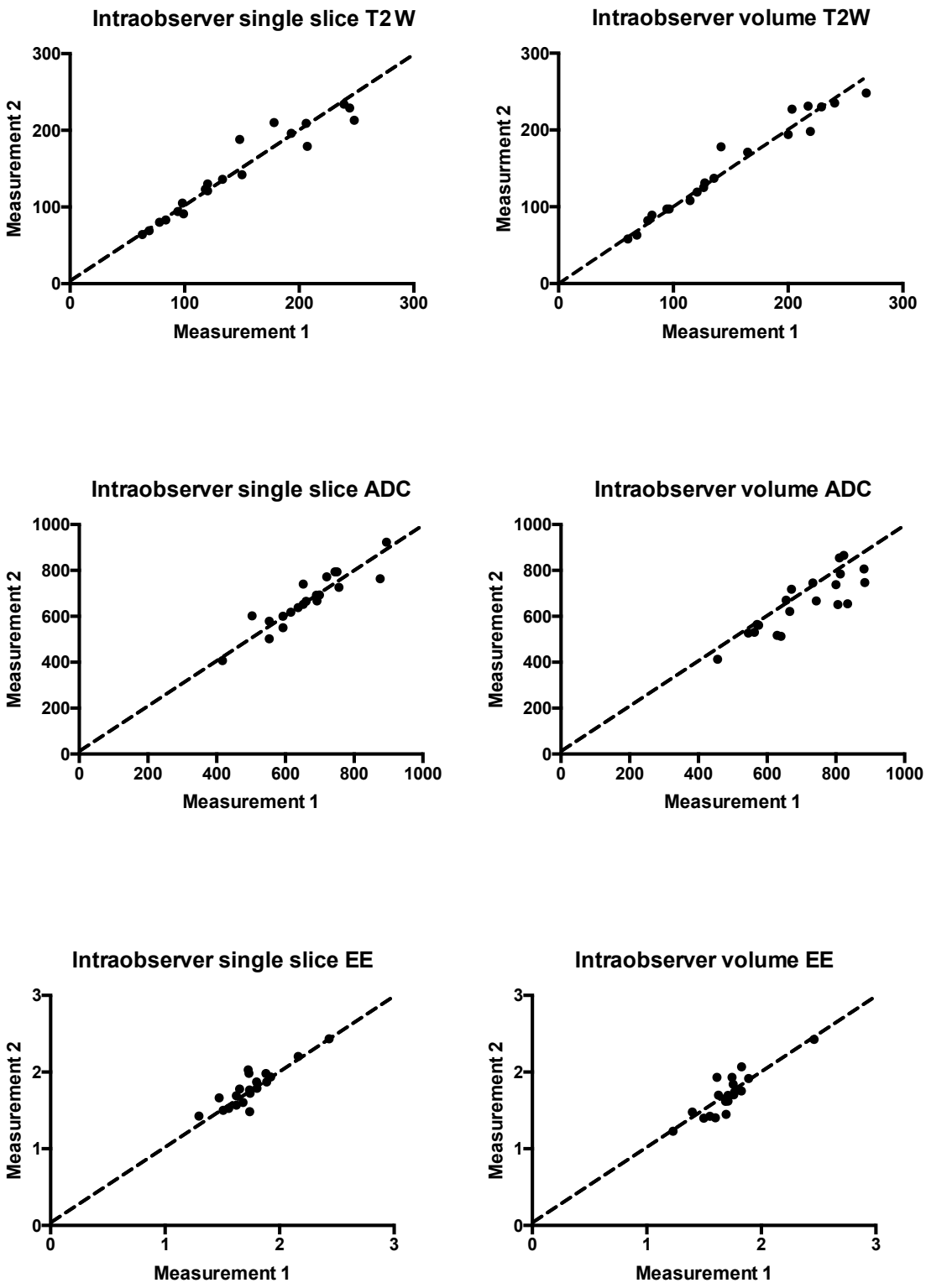

Figure 45: Scatterplots of intraobserver agreement

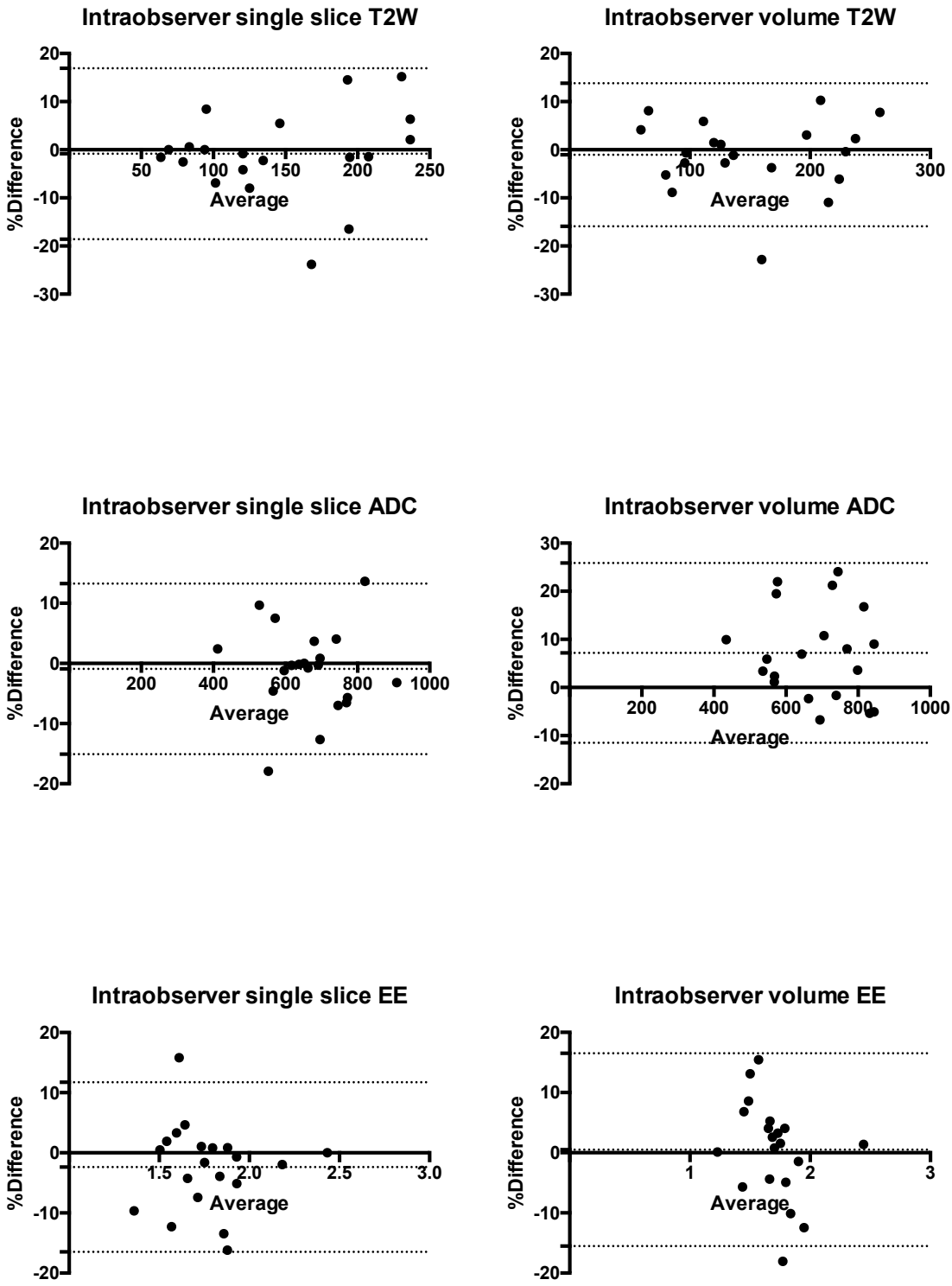

Figure 46: B-A plots of intraobserver agreement

SS; single slice

Interobserver agreement

Results of interobserver agreement are presented in table 8 and figures 47 and 48. Interoberver agreement was lower for EE DCE measurements than T2W and ADC, which achieved high levels of agreement ($\rho_c \geq 0.84$). In addition, the first reader obtained statistically significantly lower values of T2W SI than the second.

Method	Mean +/-SD	Paired t-test p-value	B-A 95% limits of agreement (%)	ρ_c
Single slice T2W				
Reader 1	144.6±58.5	0.03*	-13.1, 7.7	0.99 (0.98, 1.00)
Reader 2	148.4±59.5			
Volume T2W				
Reader 1	150.1±63.0	0.28	-21.6, 17.2	0.96 (0.91, 0.99)
Reader 2	154.3±66.0			
Single Slice ADC				
Reader 1	665.7±113.0	0.56	-15.0, 17.5	0.89 (0.74, 0.95)
Reader 2	658.5±116.6			
Volume ADC				
Reader 1	681.3±120.5	0.45	-17.8, 21.7	0.84 (0.65, 0.93)
Reader 2	669.6±125.0			
Single slice EE DCE				
Reader 1	1.77±0.24	0.86	-17.9, 18.7	0.80 (0.56, 0.91)
Reader 2	1.76±0.24			
Volume EE DCE				
Reader 1	1.70±0.25	0.13	-18.1, 27.9	0.70 (0.41, 0.86)
Reader 2	1.63±0.30			

Table 8: Interobserver agreement

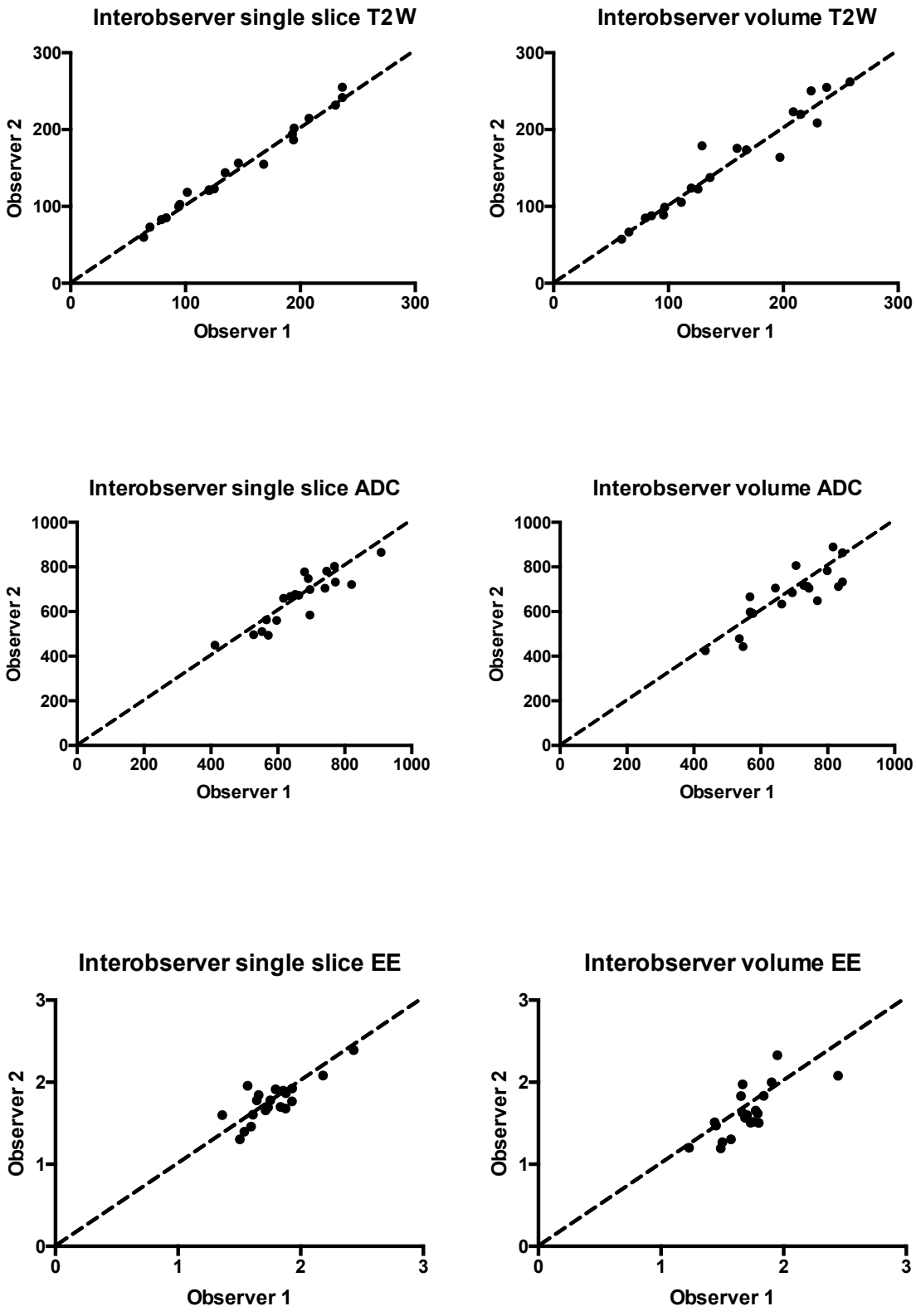

Figure 47: Scatterplots of interobserver agreement

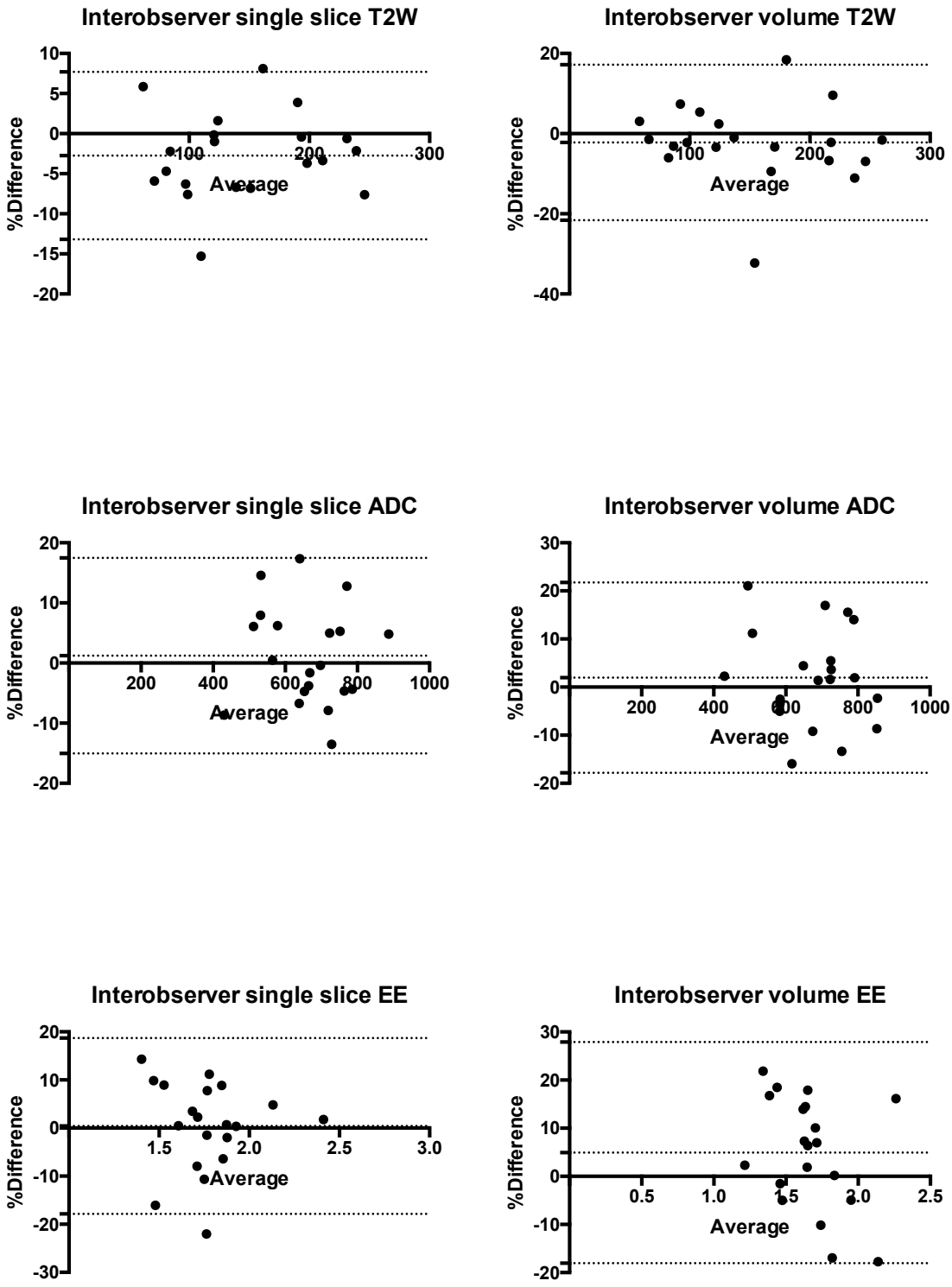

Figure 48: B-A plots of interobserver agreement

Discussion

A range of DICOM viewers are available for the analysis of quantitative imaging data, and each has their advantages and disadvantages. Of the open source packages, Osirix was chosen because is the most commonly used DICOM viewer in the world(244) and an open access version (Osirix Lite) is available to download for free. In this way, other researchers can easily reproduce analytical methods without the need for expenditure and in the spirit of open access technology; plugins may be developed and shared to further customize analysis. However, without plugins, Osirix is currently positioned for single slice ROI analysis, as VOIs are not summated. As a consequence, compliance with recommendations for volumetric analysis as suggested by Padhani et al. (138) is difficult using this software package. Furthermore, the lack of an automatic export function of quantitative imaging data into analytical spreadsheets risks transcription errors.

Fuelled by such shortcomings, companies like MIM have strived to develop further functionality within proprietorial packages. Of these packages, MIM was chosen because it has workflows that have been developed specifically for mp- prostate MRI, and UCLH has a close working relationship with the company meaning our group has experience with its use and training and technical support also readily available. However, other proprietorial DICOM viewers including ProFuse (Vision Medical, Australia) and OleaSphere (Olea Medical, France) are also available. Particular advantages of MIM include the ability to place a single VOI to extract all quantitative imaging metrics as a consequence of image registration. This makes extraction of values over a '4D' time series (e.g. DCE images) possible without placement of multiple ROIs, which speeds up workflow considerably. Furthermore, metrics may be easily 'copy and pasted' into an excel spreadsheet. However, since MIM is a private company, use of its software requires regular payments, which reduces its popularity and reproducibility. In addition, plugins cannot be developed for MIM without permission of the company, and may be commercialized, leading to lower levels of flexibility.

In terms of intermethod agreement, the results from this study show 'almost perfect' agreement between both Osirix ROI and MIM VOI methods for all components of the mp-MRI, with around +/- 10 - 15% precision for all maps and highest concordance for T2W imaging. ADC and EE DCE have slightly lower levels of agreement, which could be due to smaller numbers of pixels per lesion giving rise to higher variability. Single slice ROI measurements also produced significantly higher values of EE than VOI,

which could be due to the anecdotal observation that the epicentre of prostate tumours enhance more than the periphery. However, T2W and ADC values were not significantly different for both ROI and VOI techniques.

'Almost perfect' intraobserver agreement was also found for all quantitative parameters. Specifically, whilst intraobserver measurement precision was again in the order of +/- 10 - 15%, the lowest values of agreement were found for volumetric ADC measurements, whereby ADC values extracted during the second session were around 8% lower than the first. This may represent a training effect, whereby I became more familiar with the software by the time of the second session, and highlights another potential disadvantage of MIM.

In terms of interobserver agreement, values were similar for both radiologists, although agreement was lower for volumetric methods than single slice ROI analysis (by as much as 10%), which may be due to the nature of MIM software whereby the radiologist's judgment of successful registration could introduce further variation.

Whilst there is no data in the prostate literature comparing single slice ROI vs. volumetric techniques, there is one study comparing analytical methods in liver CT (245), which showed that volumetric measurements of tumour attenuation were more reproducible than single slice comparators (+/-23% and 7% respectively). However, the different modality and disease behaviour (e.g. larger lesions, with minimum 20mm in cross section) means these results are unlikely to conflict with my findings.

The main limitation of this study was the relatively small cohort of patients, which arose due to selecting patients with tumours large enough for volumetric analysis, but not so large as to make the dataset poorly representative of typical prostate tumours to be encountered during the rest of this thesis. Confidence intervals were also narrow enough to give a reasonable degree of certainty.

As a result of this work, Osirix was used in preference to MIM throughout this thesis. In order to expedite analysis using Osirix and address one of its shortcomings, I have worked with a computer engineer at CMIC to develop a plugin which enables the semiautomatic export of mean SI values to an excel spreadsheet, including values from a 4D series. In this way, it can produce a time-intensity curve from DCE data, without the need to place multiple ROIs. In addition, we have developed a plugin that can export quantitative metrics from tumour volumes in Osirix, which may be essential in certain situations e.g. assessment of intratumoural heterogeneity.

Further work could include investigation of ROIs vs. VOIs using a single platform i.e. Osirix to gauge which metrics are preferable, without the additional need for image registration, which leads to inherent error.

Conclusion

The analysis of ROIs and VOIs using two different DICOM viewers show high levels of intermethod and interobserver agreement for T2W, ADC and early-enhanced DCE images, and are therefore both likely to give valid results. However, the higher levels of intraoberver and interobserver agreement found with Osirix-based single slice analysis means I will use Osirix in preference for the rest of this thesis, and can avoid the need for proprietorial software.

Summary

- Two analytical methods for quantitative mp-prostate MRI were compared, namely single slice ROI analysis using open source Osirix software, and whole tumour VOI analysis using proprietorial MIM software.
- Their intermethod, intraobserver and intraobserver agreement were compared using B-A analysis, intraclass correlation coefficients and Lin's concordance coefficients.
- Whilst both methods demonstrated substantial levels of agreement, higher levels of agreement were observed with single slice Osirix analysis, which is the simpler analytical method.
- Since one of the benefits of MIM software is automatically populating data into spreadsheets for faster analysis, an Osirix plugin was developed for this purpose to further improve image analysis using Osirix.

Section B: Assessing and improving the reproducibility of quantitative mp-prostate MRI metrics

Introduction

I now wish to establish whether other techniques can be used to further improve the multiscanner, multivendor reproducibility of quantitative mp-MRI prostate metrics.

I firstly wish to challenge the received wisdom of normalising T2W SI metrics to the OI muscle, which to the best of my knowledge was first selected as a normalization region in a study by Engelhard et al (246), but the reasons for using this structure were not stated and were probably arbitrary. Although subsequent studies involving quantitative T2nSI, including those from our own group (189,247), have followed the same method, OI normalisation may not represent optimal technique and I therefore wish to discover whether normalising to the bladder (urine) increases the scan-rescan reliability of T2nSI. In addition, I seek to explore whether the reproducibility of ADC values can be improved by normalising to the bladder, to obviate scaling factors as this has been shown to be beneficial in multiscanner studies in other tumour types (248,249) but has uncertain benefit in single scanner prostate studies(250–252).

I then investigate whether statistics derived from imaging histograms (namely SD, entropy, skewness and kurtosis) have higher levels of reproducibility than their mean values for each component of the mp-MRI, as their reproducibility is currently unknown (86,87,253). The benefit of normalising histographic metrics to the mean values of a normalisation region will also be determined.

Materials and methods

Our IRB waived the requirement for patient consent for this retrospective analysis of patient data. 14 men with a median age of 60.7 years (IQR 66.5 – 78.2) were retrospectively identified from the patient database of all mp-MRI examinations performed at UCLH. Inclusion criteria were i) repeat mp-MRI examinations within 3 months or less, ii) examinations performed at 2 different field strengths (1.5 and 3T) and iii) normal (Likert 2) regions within both the TZ and PZ on both scans. Exclusion criteria were i) previous history of treatment for prostate cancer and ii) non-diagnostic image quality. Examinations were performed between October 2009 and May 2015.

Acquisition protocols were performed on the 3T Achieva and one of the 1.5T Avanto scanners (as defined in chapter 1) in no particular order.

Image analysis

Datasets were analysed using Osirix software (v7.0 Bernex, Switzerland) whereby a standard 40mm^2 ROI was placed on the normal (Likert 2) TZ and PZ for scan 1, and then copied ROIs onto the registered slices of scan 2, with subsequent manual refinement if necessary. A 40mm^2 ROI has 205 pixels on a T2W acquisition, 36 pixels on ADC and 57 pixels on DCE images, where slice thickness was 3mm, 5mm and 3mm respectively. ROIs were chosen to be 40mm^2 to reflect a typical small tumour, as the relative measurement error could be expected to be dependent on the size of the ROI, as has previously been confirmed in a liver imaging study(254). In this way, the results presented here should represent 'worst case examples'.

Mean T2W SI metrics were normalized to the largest possible ROI placed on i) the OI ii) the bladder urine signal. ADC values were i) measured directly and ii) normalized to the bladder urine signal (the OI has too low a SNR on ADC maps for use as a normalization reference region). Values for the SD, entropy, skewness and kurtosis of ROI histograms were also extracted using an Osirix plugin written in house, using the following formulae, reproduced from the supplementary materials of (255).

SD:

Equation 15

$$SD = \sqrt{\frac{1}{(XYZ-1)}\sum_{x=1}^{X}\sum_{y=1}^{Y}\sum_{z=1}^{Z}(I(x,y,z)-\mu^2)}$$

Entropy:

Equation 16

$$H = -\sum_{i=1}^{N_g} P(i)log_2\,P(i)$$

Where N_g is the number of discrete grey levels, P is the first order histogram and P(i) is the fraction of pixels with grey level i.

Skewness:

Equation 17

$$\gamma_1 = \frac{1}{XYZ}\sum_{x=1}^{X}\sum_{y=1}^{Y}\sum_{z=1}^{Z}\left[\frac{I(x,y,z)-\mu}{\sigma}\right]$$

Kurtosis:

Equation 18

$$\gamma_2 = \frac{1}{XYZ}\sum_{x=1}^{X}\sum_{y=1}^{Y}\sum_{z=1}^{Z}\left[\frac{I(x,y,z)-\mu}{\sigma}\right]^4 - 3$$

EE DCE metrics were calculated by dividing the value of the EE image (defined as the second image following prostatic contrast enhancement) to the pre-contrast ROI. All normalised metrics are calculated by dividing the value of the prostate metric by the mean SI of the normalisation region.

A typical example of imaging parameter extraction is shown in figure 49.

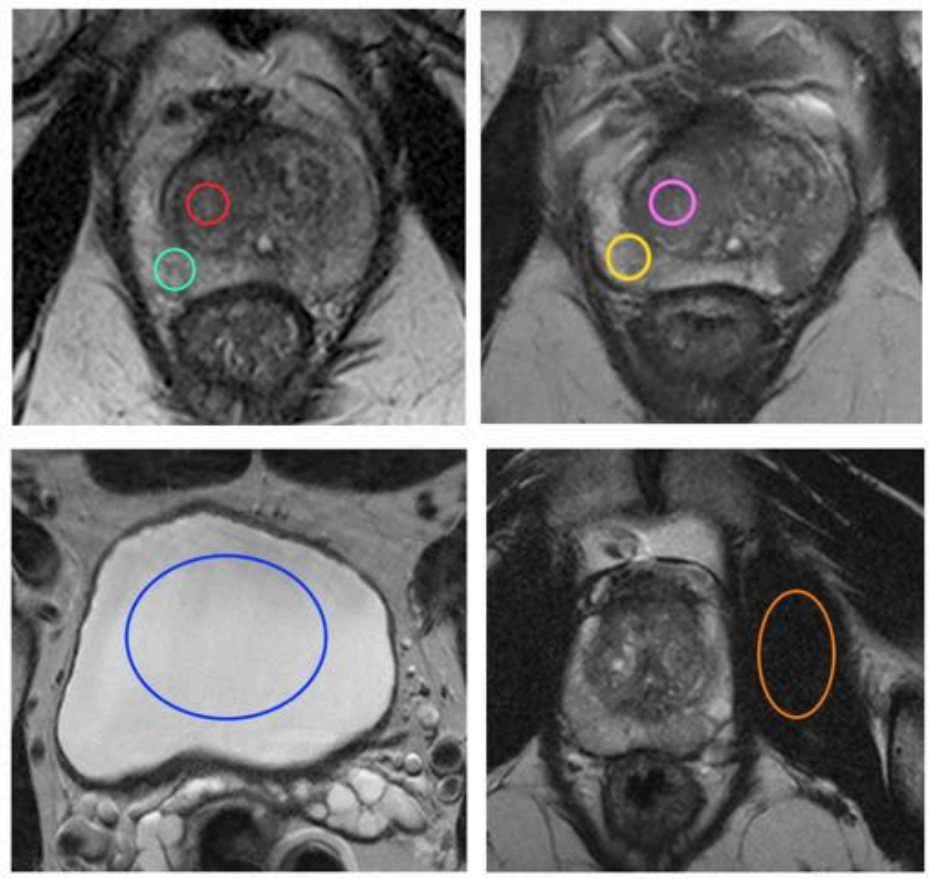

Figure 49: Quantitative imaging parameter extraction

Figure 1: Left: ROIs placed within the transition zone (red circle) and PZ (cyan circle) on scan 1. Middle: ROIs placed upon the transition zone (magenta circle) and PZ (yellow circle) on scan 2. Right: A normalisation ROI placed within the bladder urine signal (blue ellipse) and OI (orange elipse).

Statistical methods

Statistical analysis was performed using GraphPad Prism v6.0 (La Jolla, California, USA) and using SPSS version 22 (IBM, New York, USA).

Lin's concordance correlation coefficients were calculated to assess scan-rescan reproducibility, and are interpreted according to Landis and Koch (243): 0.0–0.20 no to slight agreement, 0.21–0.40 fair agreement, 0.41–0.60 moderate agreement, 0.61–0.80 substantial agreement, and 0.81–1 almost perfect agreement. Scatter plots and B-A plots will be constructed for metrics that achieved 'substantial agreement' or higher.

Results

Lin's concordance correlation coefficients (ρ_c) are provided in table 9 for mean values. Metrics with substantial agreement or higher are starred(*).

Metric	TZ (ρ_c)	PZ (ρ_c)
Non-normalized T2W	0.15 (-0.28 – 0.53)	0.35 (-0.11 – 0.68)
OI normalized T2W	0.13 (-0.18 – 0.42)	0.55 (0.17 – 0.79)
Bladder normalized T2W	0.82 (0.54 – 0.94)*	0.64 (0.22 – 0.86)*
ADC	0.69 (0.33 – 0.88)*	0.68 (0.29 – 0.88)*
Bladder normalized ADC	0.76 (0.46 – 0.90)*	0.54 (0.17 – 0.79)
EE DCE	0.51 (0.18 – 0.73)	0.14 (-0.12 – 0.38)

Table 9: ρ_c for mean MRI derived parameters

Scatterplots are presented in figure 50 for metrics which achieved substantial agreement or higher.

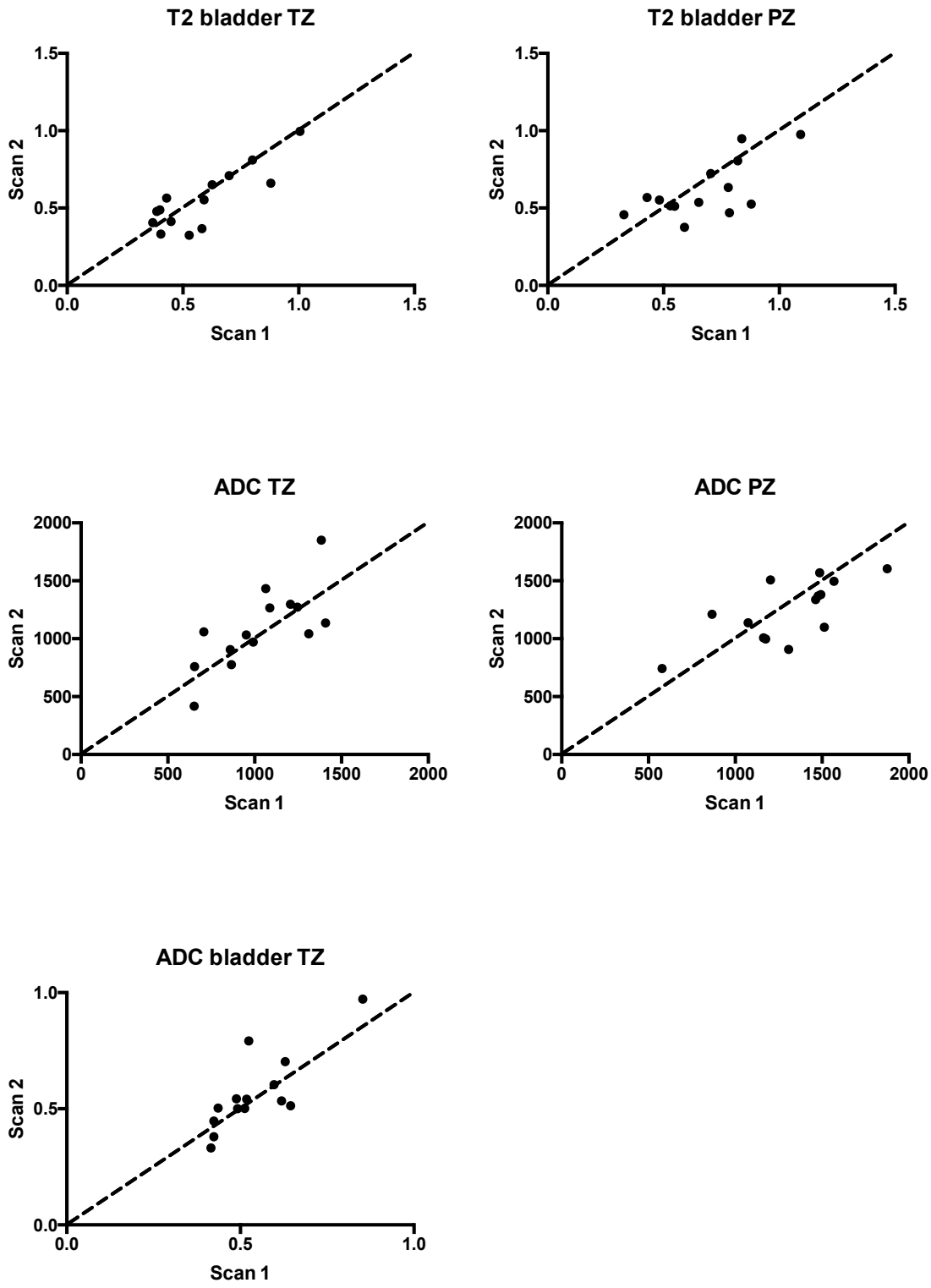

Figure 50: Scatterplots of metrics achieving substantial agreement or higher

BA plots of the same metrics are presented in figure 51.

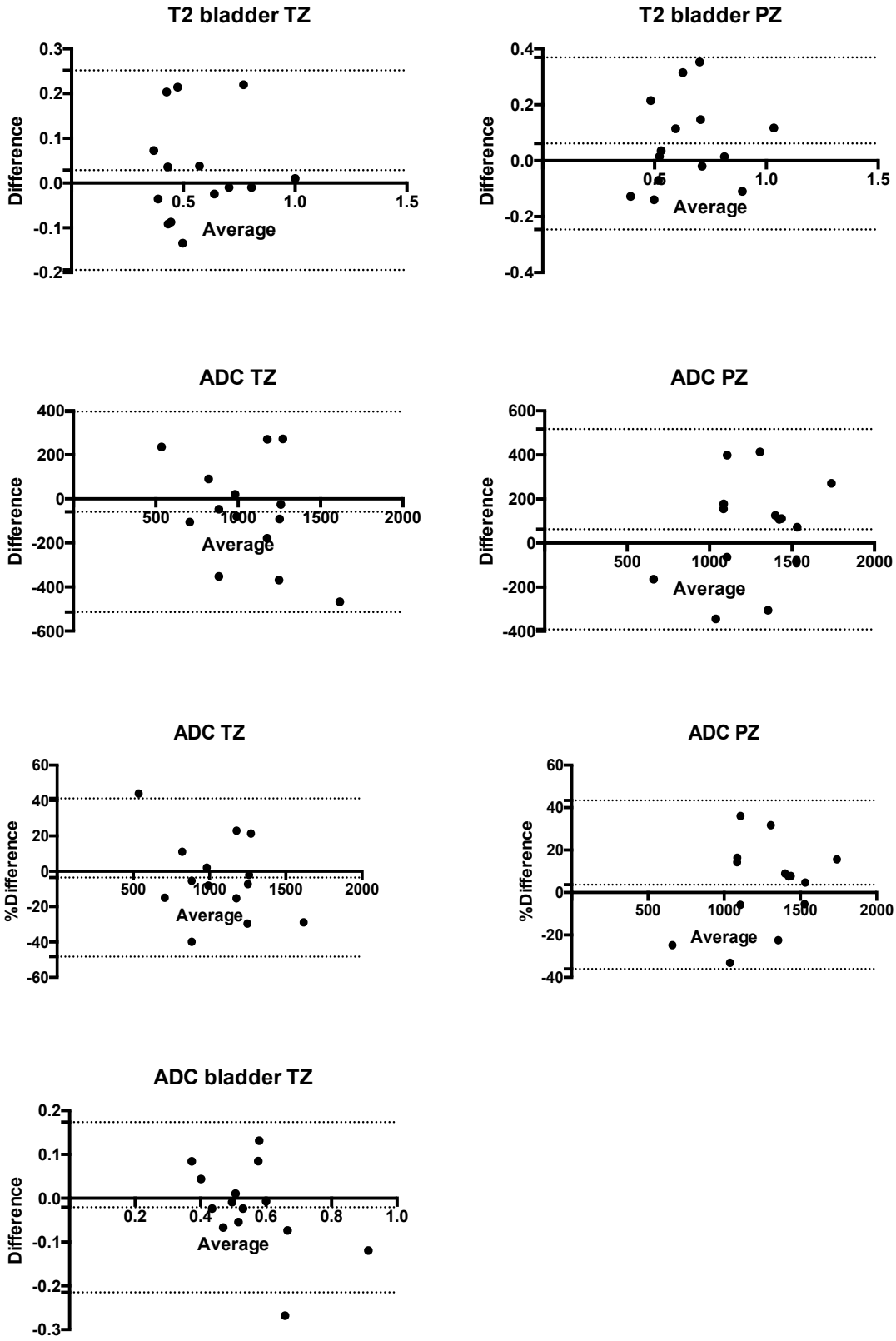

Figure 51: B-A plots of the data presented as scatterplots in figure 46

Results for ADC are also expressed as a percentage of the mean value for comparison with the literature (3rd row).

Lin's concordance correlation coefficients (ρ_c) are provided in table 10 for histographic metrics for T2W, ADC and EE DCE, with and without normalization to the bladder for T2W and ADC metrics, and the precontrast prostate ROI for DCE metrics. No metrics achieved substantial agreement or higher.

	Not normalised (ρ_c)		Normalised (ρ_c)	
Metric	TZ	PZ	TZ	PZ
T2W SD	0.30 (0.84 – 0.44)	0.42 (0.02 – 0.71)	0.54 (0.05 – 0.82)	0.58 (0.19 – 0.84)
T2W entropy	0.28 (-0.19 – 0.64)	0.13 (-0.83 – 0.56)	0.59 (0.16 – 0.83)	0.55 (0.10 – 0.81)
T2W skewness	0.22 (-0.12 – 0.52)	0.05 (-0.39 – 0.46)	0.52 (0.03 – 0.81)	0.18 (-0.24 – 0.55)
T2W kurtosis	-0.08 (-0.22 – 0.06)	0.39 (-0.13 – 0.74)	0.07 (-0.45 – 0.55)	0.54 (0.11 – 0.80)
ADC SD	0.28 (-0.27 – 0.69)	0.09 (-0.36 – 0.57)	0.05 (-0.45 0.53)	0.33 (-0.22, 0.72)
ADC entropy	0.51 (-0.20 – 0.76)	0.47 (0.02 – 0.76)	-0.19 (-0.27, 0.67)	0.32 (-0.20, 0.70)
ADC skewness	0.02 (-0.37 – 0.41)	0.06 (-0.44 – 0.54)	-0.55 (-0.45, 0.35)	0.22 (-0.25, 0.61)
ADC kurtosis	0.19 (-0.30 – 0.60)	-0.13 (-0.60 – 0.41)	0.35, (-0.19, 0.72)	0.00 (-0.51, 0.51)
EE SD	-0.05 (-0.53 – 0.45)	0.09 (-0.34 – 0.50)	0.29 (-0.26, 0.69)	-0.09 (-0.42, 0.26)
EE entropy	-0.05 (-0.45 – 0.36)	0.47 (0.02 – 0.76)	0.14 (-0.33, 0.54)	0.01 (-0.42, 0.44)
EE skewness	0.29 (-0.17 – 0.65)	0.06 (-0.44 – 0.54)	0.36 (-0.53, 0.67)	0.06 (-0.40, 0.49)
EE kurtosis	-0.06 (-0.54 – 0.44)	-0.13 (-0.54 – 0.41)	-0.06 (-0.60, 0.41)	0.11 (-0.32, 0.50)

Table 10: ρ_c for parameters derived from ROI histograms

Discussion

Our results confirm that in order to compare T2W SI between scanners, a normalization region must be selected, and normalising to the bladder urine signal seems vastly preferable than the current convention of using OI. The reason for this is likely explained by the higher SNR of the bladder and the more consistent nature of urine signal. Specifically, the OI muscle can have variable signal intensity due to fatty atrophy (giving rise to high T2W SI amongst low signal muscle) whereas the bladder urine is consistently and uniformly of high SI. In addition, the TZ was shown to be more reproducible than the PZ, which could be partly due to the greater change in SI of the PZ vs. TZ in relation to ejaculation (167). Also, since the TZ has a greater resemblance to tumour than the PZ, the SI of tumour may also be more similar to that of the TZ i.e. more reproducible.

ADC measurements were shown to be slightly less reproducible than bladder urine T2nSI, but still achieved 'substantial' levels of agreement. Whilst normalising ADC values to the bladder urine signal improved the reproducibility of the TZ, the reproducibility of PZ metrics worsened. In this way, the utility of ADC normalisation in multiscanner studies remains uncertain, and requires further investigation with a dedicated and appropriately powered prospective study. However, the effect size is unlikely to be very large.

All histogram metrics were shown to have lower levels of reproducibility than mean values and are therefore unlikely to provide sufficient reproducibility for use in multicentre trials without strict standardisation of imaging protocols. Lower levels of reproducibility could also explain why their predictive performance for Gleason grade were shown to be poor in a multiscanner study (256). However, a number of metrics did improve with normalisation to a reference region, which, to the best of my knowledge has not been performed in studies to date. In this way, normalisation may help to increase the precision of such metrics for use in optimised multicentre trials in the future.

To the best of my knowledge, there are no studies in the literature that consider the effects of different T2 normalisation regions, or report upon the repeatability/reproducibility of such metrics. The reliability of ADC measurements however has been investigated to a much greater extent. Whilst phantom studies with standardised acquisition protocols report multiscanner variability of less than 5% (257–259), *in-vivo* reliability is found to much less consistent (260) with 10% variance quoted in a back-to-back examination with the patient lining supine combined with registration of the scans during analysis (261). However, repeatability coefficients increases further (18%) with ambulation and repositioning (262) and when scans are spaced by a month, single scanner repeatability of up to 35% has been reported (263). Whilst ADC measurements should theoretically be independent of the scanner used (81), multiscanner multivendor studies in human have shown considerably different values, even when acquisition protocols are similar (264). Since the present study was performed on a mix of scanners without protocol optimisation with up to 3 months between both scans, the ADC variability of +/- 40% is unsurprising.

The limitations of the current study include its retrospective nature with inconsistent intervals between both scans and the small number of patients leading to wide confidence intervals in many cases. However, since the effect size of normalising to the bladder urine was so large, the confidence intervals of bladder urine vs. OI

normalisation for the TZ do not overlap meaning there is sufficient evidence to favour normalising to the urine signal. Furthermore, prospective studies regarding repeatability/reproducibility are notoriously difficult to recruit to, which makes the development of such datasets extremely difficult and supports my retrospective study design. For example, a recent prospective repeatability study concerning ADC repeatability approached 189 patients to obtain the largest cohort to date in 15 patients (265).

The imaging biomarker roadmap (79) also recommends single centre repeatability before reproducibility assessments are made, whereby this data is also urgently required. Due to the retrospective nature of the study whereby patients are occasionally recalled for a repeat scan at different field strengths; I could only perform a reproducibility study. However, since multiple imager, multicentre studies provide the most robust level of evidence of clinical efficacy in Radiology research and often the only practical way of achieving statistical power (81), this data is still useful. Finally, I acknowledge that the reproducibility of tumours was not investigated in this study, which was due to an insufficient number of patients with positive Likert scores.

Further work should include dedicated prospective studies with greater numbers of patients, ideally with histologically confirmed tumours. Where possible, studies should be methodically performed according to the imaging biomarker roadmap, with standardised imaging protocols for multiscanner reproducibility studies.

Conclusion

Here I have shown that bladder normalization results in superior reproducibility vs. the current standard practice of using OI, and that histogram metrics are less reproducible than mean values. I will therefore normalize to the bladder, rather than the OI throughout this thesis and will also not use histogram metrics as predictors of Gleason grade as I do not have the resources to optimise them for use as imaging biomarkers.

Summary

- A retrospective single centre, multiscanner scan-rescan reproducibility study was used to investigate whether the precision of quantitative T2W and ADC metrics can be improved by normalizing to different anatomical structures, or by using imaging histogram metrics other than the mean value.
- Statistical analysis was carried out using B-A plots and Lin's concordance

correlation coefficients.

- T2 SI metrics were significantly more reproducible when normalised to the bladder urine signal rather than the OI muscle.
- Normalisation of ADC did not improve reproducibility.
- Mean values are more reproducible than SD, entropy, skewness and kurtosis.
- In this thesis, T2nSI will therefore be calculated by normalising to the bladder rather than OI, ADC will not be normalised to a reference region and only mean values will be used.

5 ZONE-SPECIFIC LOGISTIC REGRESSION MODELS FOR GLEASON PATTERN 4 PREDICTION

Author declaration

All of the work in this chapter was conceived and written by me personally, under the supervision of Dr. Shonit Punwani. Patients were recruited to the PICTURE study (241) by the Academic Urology team at UCLH (Hampstead National research ethics committee REC reference 11/LO/1657). Michela Antonelli from CMIC performed the statistical analysis and I performed quantitative image analysis. Mrishta Brizmohun Appayya, Francesco Giganti and Shonit Punwani were the radiologists who made qualitative assessments of Gleason score.

Introduction

Having established the optimal analytical methods for qualitative imaging metric extraction throughout the thesis, I now wish to combine metrics from the mp-MRI to predict a Gleason pattern 4 component in prostate cancer. As I discussed in chapter 1, prostate cancer is a heterogeneous disease state, with a strong relationship between aggressiveness, as characterised by Gleason grade, and survival (20). Specifically, percentage Gleason 4 has been shown to outperform traditional Gleason grading as a prognostic marker in a multivariate study of 379 prostatectomy specimens (266). A reliable, quantitative and non-invasive test to identify patients at risk of aggressive disease (those with a potential Gleason 4 component) would therefore have significant clinical value but does not currently exist.

Clinical parameters such as tumour volume (TV) (267) and serum PSA level may hold some potential for this purpose as they are known to correlate with Gleason grade (268). However, the predictive value of PSA for aggressive prostate cancer is limited as larger gland volumes (GV) result in elevated PSA levels. Consequently, PSA density (PSAd), which normalises serum PSA level to GV has therefore generated interest as a more specific biomarker for aggressive prostate cancer (269).

Whilst there is some evidence that the subjective opinion of radiologists interpreting mp-MRI can be used to estimate Gleason grade (270), *quantitative* measurements of SI including T2nSI and ADC also moderately correlate with Gleason grade (168,271) and have been shown to differ in PZ vs. TZ tumours (189,247).

The purpose of this study was to develop and test whether separate LR models for TZ and PZ tumours based on clinical and quantitative mp-MRI parameters can classify tumours into those with/without a Gleason 4 component, and compare their performance with the subjective opinion of three radiologists with differing experience levels.

Materials and methods

Our IRB approved the study and waived the requirement for individual consent for retrospective analysis of patient data collected as part of clinical trials/routine care (R&D No: 12/0195, 16 July 2012). The research was conducted according to the principles of the Declaration of Helsinki.

Patient cohorts

In order to build the cohort for deriving the LR model – the model derivation cohort (MDC) – a trial dataset of 330 patients was interrogated. Full details of the trial have been previously reported(242). In brief, inclusion criteria were (i) men who underwent previous TRUS biopsy whereby suspicion remained that cancer was either missed or misclassified and (ii) men suitable for further characterisation using TPM biopsy. Exclusion criteria were (i) previous history of prostate cancer treatment and (ii) men in whom TPM was inadequate for analysis due to lack of complete gland sampling or inadequate sampling density.

A subset of these men was interrogated for this study, whereby selection criteria were: (i) 3T mp-MRI, comprising T2W, diffusion-weighted and DCE imaging; (ii) Likert (42) ≥3/5 index lesion localized on mp-MRI, deemed to be either of TZ or PZ origin. TZ/PZ border lesions, defined as having a component in both the TZ and PZ, were excluded from the analysis. (iii) TPM and targeted index lesion biopsy confirming Gleason score 3+3 tumour or greater, which acted as the reference standard. A flow diagram for patient selection to generate the MDC is shown in Figure 52.

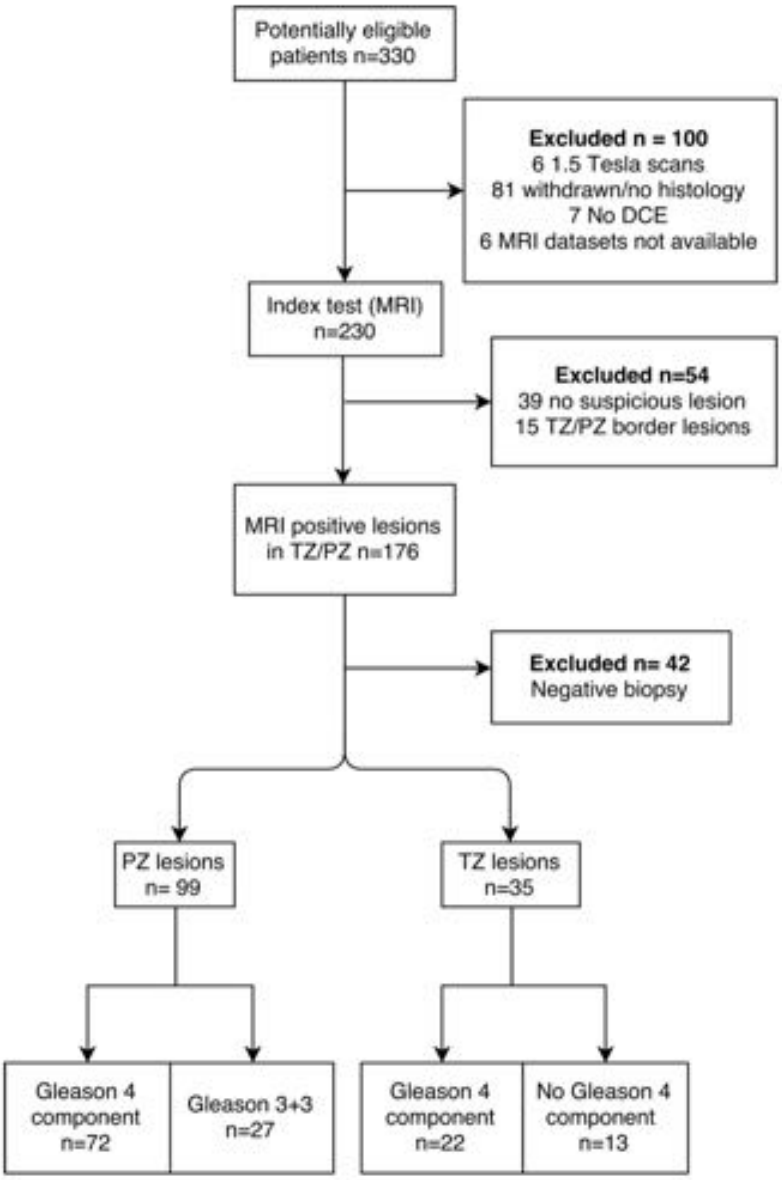

Figure 52: Flow diagram of patient selection for the Model Derivation Cohort (MDC)

For temporal validation we used a temporally separated cohort (TSC) of 30 consecutive men: 20 for the PZ and 10 for the TZ with the same selection criteria and scanning protocol as in the MDC, performed between June 2014 and December 2015. Table 11 shows the minimum, maximum and median values of age, PSA, GV and TV of the two cohorts.

		PZ			TZ		
	Parameter	Min	Max	Median	Min	Max	Median
MDC	Age (yrs)	43	79	63.4	48	83.4	65.5
	PSA (ng/ml)	2.5	19	6.6	2.7	30.3	9.6
	GV (mls)	16	77	35.2	18	65.8	32.1
	TV (mls)	0.02	5.1	0.4	0.03	10	1.2
TSC	Age (yrs)	55.7	80.2	69.8	56.8	70	63.3
	PSA (ng/ml)	2.7	91	8.1	3.4	18	8.6
	GV (mls)	20.8	75.9	43.8	25	100	35
	TV (mls)	0.1	15	0.9	0.05	9.4	0.8

Table 11: clinical patient characteristics

PZ; peripheral zone, TZ; transition zone, PSA; prostate specific Antigen, GV; gland volume TV; tumour volume MDC; model derivation cohort TSC temporally separated cohort

The mp-MRI acquisition was performed on the 3T Achieva using the protocol defined in chapter 1.

Targeted biopsy

For the MDC, a systematic biopsy of the whole gland was performed through a brachytherapy template-grid placed on the perineum at 5-mm sampling frame. Focal index lesions also underwent cognitive MRI-targeted biopsies at the time of TPM whereby two biopsy cores were obtained for the index lesion. A genitourinary pathologist with 12 years of experience analysed all the biopsy cores blinded to the MRI results.

Ultrasound guided TPM ± targeted biopsy acted as the reference standard for the TSC using cognitive MR-guided registration, with a brachytherapy template grid used in 29 patients and freehand targeting for a single case with a 10ml lesion. TPM and targeted biopsies were chosen as the reference standard because they are superior to TRUS biopsy, are the sampling method of choice in the active surveillance population and avoid the spectrum bias associated with a prostatectomy reference standard(272), which favours patients with aggressive disease.

Multiparametric MRI review

Mp-MRI images were qualitatively assessed by three radiologists independently (FG, MB and SP) who had 2, 3 and 10 years of experience respectively using Osirix version 7. The pictorial report of each patients mp-MRI, produced as part of the prospective trial dataset was made available to the Radiologists for localisation of biopsy-targeted

and histologically confirmed Likert ≥3/5 lesions. The three Radiologists were informed of the serum PSA level and made a visual estimate of Gleason grade based on a qualitative image features (lesion size, T2 signal intensity, relative intensity on ADC and b2000 images and intensity of early contrast enhancement), classifying the index lesion into those with an expected histologic Gleason 4 (primary or secondary) and Gleason 3+3 disease pattern, blinded to the biopsy results. The GV and TV were also measured using tri-planar measurements and the prolate ellipsoid formula (273).

Extraction of mp-MRI derived quantitative parameters

MR datasets were analysed with MIM Symphony Version 6.1 (MIM Software Inc., Cleveland, USA). Rigid translational co-registration of volumetric and axial T2W, ADC and DCE images were performed semi-automatically, with subsequent manual refinement.

A VOI was contoured for each index lesion and recorded the mean SI of each VOI on the axial T2W, ADC and DCE images at all time points. A typical contoured lesion is shown in Figure 53. In order to standardize signal intensity between subjects, T2nSI were calculated by dividing the signal intensity of the lesion by that of the bladder urine (274).

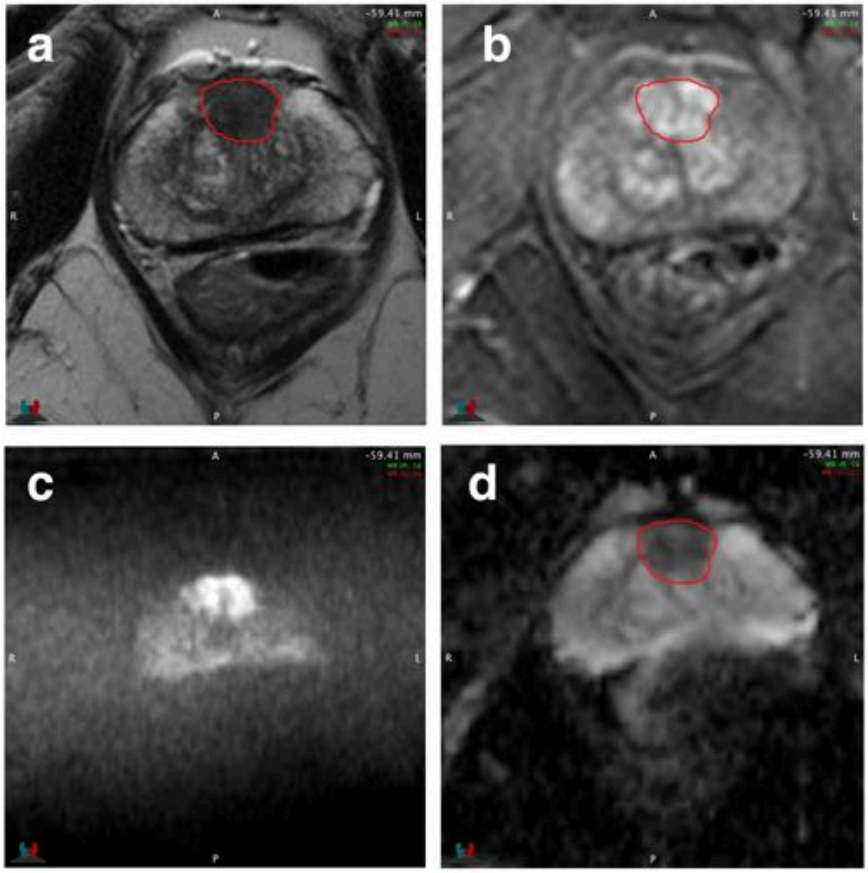

Figure 53: Typical lesion contours using MIM

a. Axial T2W TSE of a 64 year-old male showing the volumetric contour of a TZ prostate tumour for extraction of mp-MRI parameters. b. axial post gadolinium DCE image c; axial b=2000mm/s^2 d. ADC 'map'.

EE and ME metrics were derived from the DCE MRI signal enhancement time curves. EE was defined as the first strongly enhancing postcontrast SI divided by the precontrast SI, and ME as the difference between the peak enhancement SI and the baseline SI normalized to the baseline SI (275). Clinical features of TV, GV and PSAd were also selected as potential features to include in model development.

Model derivation

Data were analysed using MATLAB version 8.2 (MathWorks, MA, USA) and SPSS Statistics 24.0.0 (IBM, NY, USA).

Zone-specific LR models were derived separately for PZ and TZ tumours, to predict the presence of a Gleason 4 or Gleason 3+3 component. First, using the MDC, a forward stepwise feature selection was applied to select the subset of parameters (defined as par_{TZ}, and par_{PZ}, respectively) most likely to contribute significantly to the LR models. Each parameter is included in the model on the basis of the significance of the score statistic (p-value), or excluded using the probability of a likelihood-ratio statistic.

The results of the LR models generated using each single parameter (univariate models) were then compared with the results of the multivariate models. Since the performance of machine learning classifiers decrease when the data used to train the model is imbalanced with a bias towards the majority class (276), which applies to the PZ cohort in our study (72 Gleason 4, vs. 27 Gleason 3+3) due to a higher natural incidence of Gleason 4 containing tumours, a resampling technique called Synthetic Minority Over-sampling TEchnique (SMOTE) (277) was applied to the PZ MDC to generate artificial data to balance the training cohort and reduce this bias. Here, the minority class is over-sampled by using a k nearest neighbour algorithm, which introduces new synthetic examples of data in 'feature space' along the line segments joining any/all of the *k* minority class nearest neighbours of each minority class sample. On the basis of the amount of over-sampling required, a number of neighbours from the *k* nearest neighbours are randomly chosen. After applying SMOTE to the PZ MDC, 45 synthetic samples belonging to the class of 3+3 Gleason cancers were added and this new re-balanced data is used to generate the LR model. SMOTE was not applied to the TZ MDC as this cohort was sufficiently balanced.

Model validation

Two different strategies were used to validate the PZ and TZ models. First, LOO analysis of the MDC was applied to internally validate the models. For LOO, data from one patient was excluded, and a model was generated from the remaining data. This model was tested on the excluded patient to calculate a predictive probability. The process was repeated for all patients to calculate a predictive probability for each patient, from which an ROC curve was constructed. For the PZ cohort, after removing the patient used for testing, SMOTE is applied to the remaining data before using it to generate the model.

Models were then further validated on a temporally separated cohort of patients (TSC) to prove their generalizability. As for the LOO analysis, SMOTE was applied to the MDC before deriving the PZ model. For temporal validation of PZ and TZ models, a ROC curve was constructed using the predictive probability calculated on the MDC, and the threshold T_50 corresponding to a specificity of 50% (allowing for 1 in 2 patients being over called for disease containing a Gleason 4 component) was considered due to its particular clinical relevance.

We then applied the LR models to the TSC and used T_50 to calculate the model sensitivity and specificity on TSC. A flow diagram of the model validation strategies is shown in Figure 54.

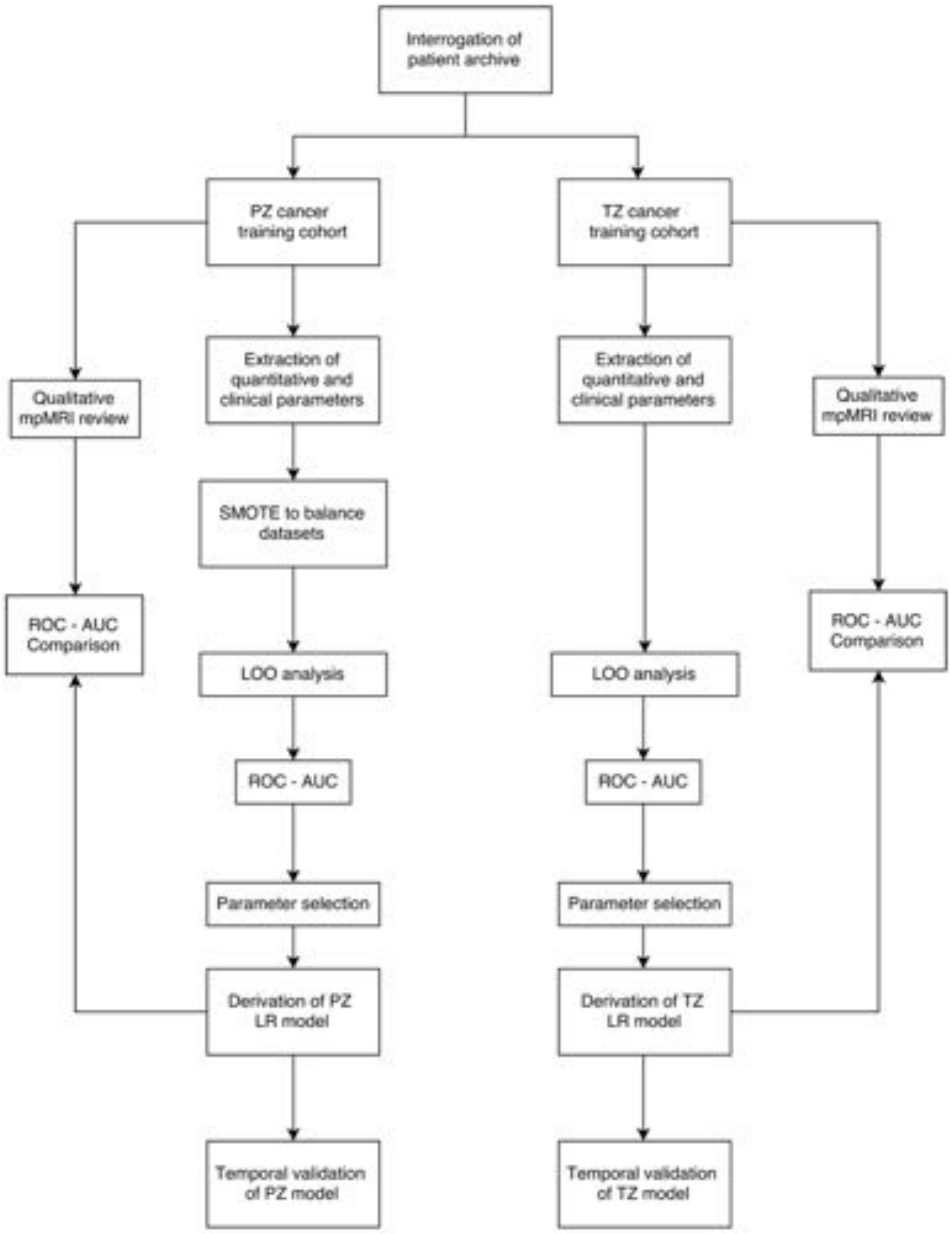

Figure 54: Flow diagram outlining the model validation strategies used in the study

PZ; peripheral zone, TZ; transition zone, LR; logistic regression, SMOTE; Synthetic Minority Over-sampling Technique, ROC-AUC; receiver operating characteristic area-under–the-curve

Results

Model derivation and internal validation

For the TZ model, the forwards stepwise selection procedure stopped after the first step to use only one parameter ($par_{TZ} = \{\text{ME}\}$, p=0.04, ln(odds) 2.53), while for the PZ model the procedure select three parameters ($par_{PZ} = \{ME, ADC, PSAd\}$, p<0.001, ln(odds) 2.71, -2.54 and 5.98 respectively).

To further evaluate par_{TZ} and par_{PZ}, we compared their ROC curves with univariate and multivariate models. Figure 55 shows the ROC curves generated following the univariate and multivariate LOO analysis for TZ and PZ, respectively. Their corresponding AUC values and statistics (Standard Error (SE) and 95% CI) are shown in Table 12.

Model	AUC	SE	95% CI	
			Lower	Upper
Univariate TZ				
ADC	0.54	0.10	0.34	0.74
T2nSI	0.58	0.10	0.38	0.78
PSAd	0.68	0.10	0.49	0.87
ME	0.72	0.09	0.53	0.90
TV	0.43	0.10	0.23	0.62
EE	0.67	0.10	0.48	0.86
Multivariate TZ				
All parameters	0.78	0.09	0.62	0.95
Univariate PZ				
ADC	0.72	0.06	0.60	0.84
T2nSI	0.65	0.06	0.52	0.77
PSAd	0.72	0.06	0.60	0.84
ME	0.78	0.06	0.67	0.89
TV	0.68	0.06	0.55	0.80
EE	0.66	0.06	0.53	0.78
Multivariate PZ				
ADC+PSAd+ME	0.83	0.05	0.73	0.93
All parameters	0.83	0.05	0.73	0.93

Table 12: ROC characteristics following univariate and multivariate LOO analysis

Note: TZ; transition zone; PZ; peripheral zone; ADC; apparent diffusion coefficient, T2nSI; T2 normalized signal intensity; PSAd; prostate specific antigen density; ME; maximum enhancement DCE metric; TV tumour volume; EE; Early enhanced DCE metric.

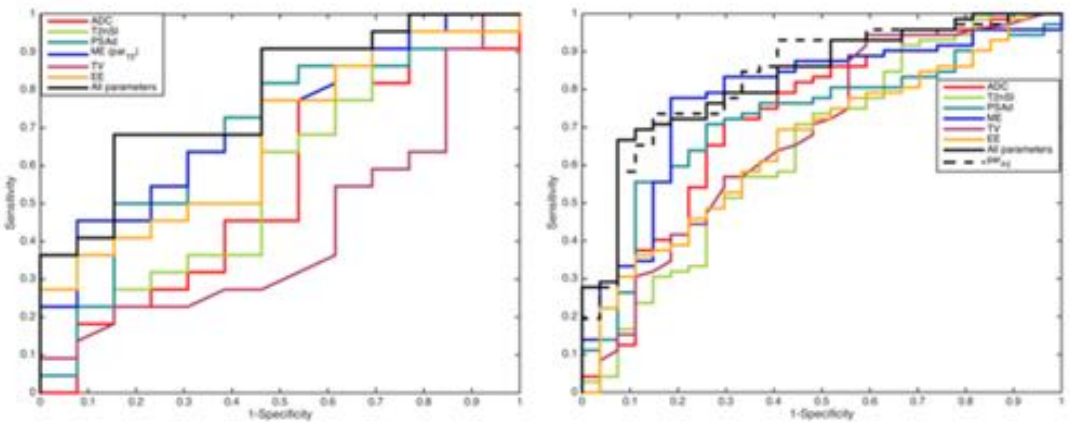

Figure 55: ROC curve generated by applying the univariate and multivariate LOO analysis to both the TZ MDC (left) and PZ MDC (right)

Although the TZ model built using all the parameters obtains a better ROC-AUC than the one built with par_{TZ}, using all the parameters is not justifiable due to the small sample size of 35 patients (278). For the PZ, the LR multivariate model generated with all the parameters and par_{PZ} are characterized by the same ROC-AUC. Since both models outperform all univariate LR models but have the same performance characteristics, we chose the more parsimonious model that uses a lower number of parameters.

Temporal model validation

For the temporal validation, we first derived the LR models using the subset par_{TZ} and par_{PZ} of parameters for, respectively, the TZ MDC and PZ MDC. The two LR models (denoted as LR_{TZ} and LR_{PZ}) are shown in equations 13 and 14 below.

Equation 19

$$LR_{\mathrm{TZ}}\colon \ln(odds)_{TZ} = -0.97 + 2.53 \cdot ME$$

Equation 20

$$LR_{\mathrm{PZ}}\colon \ln(odds)_{PZ} = -1.06 - 2.35 \cdot ADC + 8.27 \cdot PSAd + 2.95 \cdot ME$$

The probability threshold at the cut-off point T_50, was 0.58 for the TZ and 0.22 for the PZ. Table 13 reports for both LR_{TZ} and LR_{PZ} the ROC-AUC and the values of sensitivity

and specificity at the cut-off point achieved on the MD and TSCs with the corresponding number of correctly classified samples.

Model	AUC	SE	95% CI	T_50		
				SN	SP	CCS
MDC						
LR_{TZ}	0.72	0.09	0.53-0.90	0.77	0.46	23/35
LR_{PZ}	0.83	0.05	0.73-0.93	0.93	0.48	80/99
TSC						
LR_{TZ}	0.56	0.19	0.19-0.93	0.60	0.20	4/10
$\mathrm{LR}_{\mathrm{PZ}}$	0.85	0.09	0.67-1.00	0.90	0.50	14/20

Table 13: ROC-AUC, sensitivity and specificity achieved with T_50

Note – SN; sensitivity, SP; specificity; MDC; model derivation cohort; TSC; temporally separated cohort; LRTZ; logistic regression for the transition zone; LRPZ; logistic regression for the peripheral zone; CCS; number of correctly classified samples; T_50

Comparison of the LR models against radiologist performance

To further assess the LR models generated for PZ and TZ, we compared the results obtained by LR_{TZ} and LR_{PZ} on the TZ and PZ MDCs with those achieved by the three radiologists. Figure 56 shows the ROC curves for the TZ and PZ MDCs obtained by the three radiologists, their mean and the ROC curves generated by LR_{TZ} and LR_{PZ}.

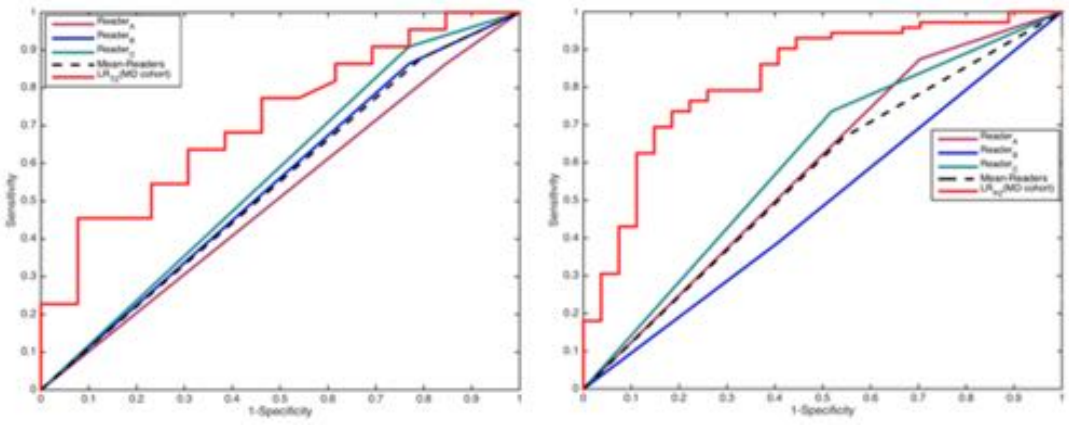

Figure 56: ROC curves obtained by the three radiologists and by the LR models applied to both the TZ MDC (left) and PZ MDC (right).

The LR model ROC-AUC values obtained on TZ and PZ, respectively, are 0.72, and 0.83 vs. mean radiologist ROC-AUC of 0.54 and 0.56.

Discussion

These results show that LR models designed to predict a Gleason 4 component in known prostate cancer have different LR equations and performance characteristics in each zone (TZ/PZ) and thus should be developed in a zone-specific fashion. The PZ model was superior to the subjective opinion of expert radiologists at all probability thresholds and maintained performance at internal and temporal validation.

Whilst the TZ model performance showed promise at internal validation where it outperformed the three radiologists, it showed poor predictive capability at temporal validation, which emphasizes the need for an external patient cohort to test the true generalization capability of predictive models. However, predictive models for PZ tumours present a more important clinical problem as PZ tumours have a higher incidence (80% vs. 20%TZ) and tend to be more aggressive (279).

The findings from this study can immediately inform the reporting of mp-MRI in clinical practice, whereby PSAd, ADC and ME should be considered by radiologists to estimate to the presence of a Gleason 4 component in known tumours. Such models could also be used to target the most suspicious component of tumours, as has been applied in DWI alone (209). With further work, these models could also be applied in active surveillance programs, non-invasively detecting whether tumours have undergone transformation to a higher Gleason grade, thereby provoking biopsy or intervention. This potential application is particularly pertinent in light of the findings from the recently published ProtecT study (280) which showed no significant difference in survival outcomes at 10 year follow up in patients randomized to active surveillance, surgery or radiotherapy; likely to impact the uptake of active surveillance as a management strategy. Indeed, mp-MRI is already advocated by NICE in the UK as part of the active surveillance program (281).

Several studies have previously reported LR and mp-MRI derived parameters for the prediction of Gleason grade in prostate cancer (213,214,282,283). Whilst our study is in agreement that ADC is a useful parameter for this purpose, our study differs from the literature in a number of ways. Firstly, all other studies excluded tumours <0.5ml, meaning such data is not generalizable to smaller index lesions, which can be aggressive (284) and are often followed in active surveillance programs.

Hötker et al (282) studied 195 patients and reported a best performing univariate parameter (ADC) achieved an AUC of 0.69 for distinguishing 3+3 tumours from those

containing a Gleason 4. A possible explanation of their lower reported ROC-AUC could be the multiscanner nature of the study and the combination of PZ and TZ cancers into a single model. Furthermore, the authors showed that K_{trans} failed to add value for discriminating such tumours and the models did not undergo external validation.

Whilst we did not derive Tofts' model parameters due to our institutional preference for higher spatial resolution of DCE MRI over temporal resolution (which is required for a Tofts' fitting), we demonstrated that ME which is a robust, generalizable semiquantitative metric (193) can considerably improve the discriminatory ability for the prediction of Gleason 4 cancer components above ADC alone.

The other studies derive models based on 54 patients (213) or fewer and combine DWI with spectroscopic metrics, which necessitate specialist equipment and knowledge. Indeed, all of our metrics can be extracted from the minimum protocol requirements as recommended by international consensus guidelines (42) and thus are more generalizable to non-specialist centres. However, the failure of our models to characterize tumours in the TZ, where other groups report impressive data suggest TZ tumours may be better classified using metabolic or spectroscopic techniques.

Since our model uses PSAd as a predictor of Gleason 4 tumour, our study affirms that serum and imaging biomarkers can be synergistic (285). Our results are also consistent with another group who found no additive value of TV in Gleason grade prediction (282). In this study we chose to analyse index lesions only, to avoid statistical clustering and because index lesions usually drive management strategy and patient outcome (286).

One possible limitation to our study is the unbalanced nature of the PZ cohort, which is governed by the incidence of tumours in each class. However, we used SMOTE to control for this bias and use all of the available data. The TZ cohort was balanced though smaller than the PZ, due to a lower natural incidence of TZ tumours, which may account for the poorer performance of the TZ model at temporal validation.

We also focused upon the development and initial validation of LR models from a well-characterized cohort of patients scanned in a standardized manner on a single MRI scanner, which provided us with the optimal dataset to develop a maximally performing model. However, whilst we also limited parameters to simple measures that may be reproduced easily, assessment of the generalizability of our developed models by way of large-scale external validation (e.g. at other centres), and consideration of their

impact on patient outcome should be the subject of further work.

Conclusion

LR models combining PSAd and quantitative mp-MRI parameters outperform experienced radiologist opinion for the prediction of Gleason pattern 4 in prostate cancer. Whilst the PZ model maintained its performance on a temporally separated patient cohort, the TZ model failed to do so. LR models could therefore harbour great potential when making management decisions in the prostate cancer pathway, and would be particularly useful to inform decisions regarding patients on active surveillance programs.

Summary

- Quantitative metrics from mp-prostate-MRI were used to predict a Gleason 4 component in known prostate cancer.
- The value of combining multiple parameters into a predictive LR model was also studied for the TZ and PZ separately.
- Whilst the TZ model performed poorly at external validation, the PZ model combining ADC, PSAd and ME outperformed the opinion of experienced radiologists.

6 THE INNOVATE TRIAL

Author declaration

All of the work in this chapter was conceived and written by me personally, under the supervision of Dr. Shonit Punwani.

Introduction

Having established the best performing predictive models to determine the presence of a Gleason pattern 4 component using conventional mp-MRI sequences, I now wish to validate a new quantitative diffusion-weighted MRI biomarker which I hope will provide higher levels of diagnostic accuracy than ADC. At the beginning of my research fellowship, I made an application for ethical approval using the Integrated Research Application System (IRAS), which was granted by the NHS Surrey Borders Research and Ethics committee (reference 15/LO/2099) on 23rd December 2015. The trial in which I wish to achieve this is called INNOVATE; CombIning advaNces in imagiNg with biOmarkers for improVed diagnosis of Aggressive prosTate cancEr. The study was funded by Prostate Cancer UK (PCUK) via the Targeted Call 2014: Translational Research St.2 funding stream and is registered on ClinicalTrials.gov, with reference NCT02689271(287), to improve the reporting of the trial and in accordance with the recommendations of Andre et al. (288). The study protocol has also been published in an open access journal (BMC cancer) (289) to increase its reproducibility, increase transparency and decrease type I errors arising from multiple *post hoc* comparisons(85). The abstract from this paper is provided below and the original paper is provided in appendix E.

Background

Whilst multi-parametric magnetic resonance imaging (mp-MRI) has been a significant advance in the diagnosis of prostate cancer, scanning all patients with elevated prostate specific antigen (PSA) levels is considered too costly for widespread National Health Service (NHS) use, as the predictive value of PSA levels for significant disease is poor. Despite the fact that novel blood and urine tests are available which may predict aggressive disease better than PSA, they are not routinely employed due to a lack of clinical validity studies. Furthermore approximately 40 % of mp-MRI studies are reported as indeterminate, which can lead to repeat examinations or unnecessary biopsy with associated patient anxiety, discomfort, risk and additional costs.

Methods/Design

We aim to clinically validate a panel of minimally invasive promising blood and urine biomarkers, to better select patients that will benefit from a mp-prostate MRI. We will then test whether the performance of the mp-MRI can be improved by the addition of an advanced diffusion-weighted MRI technique, which uses a biophysical model to characterise tissue microstructure called VERDICT (Vascular and Extracellular Restricted Diffusion for Cytometry in Tumours). INNOVATE is a prospective single centre cohort study in 365 patients. Mp-MRI will act as the reference standard for the biomarker panel. A clinical outcome based reference standard based on biopsy, mp-MRI and follow-up will be used for VERDICT MRI.

Discussion

We expect the combined effect of biomarkers and VERDICT MRI will improve care by better detecting aggressive prostate cancer early and make mp-MRI before biopsy economically viable for universal NHS adoption.

7 VERDICT MRI AS A POTENTIAL QUANTIATIVE IMAGING BIOMARKER FOR GLEASON GRADE PREDICTION

Author declaration

All of the work in this chapter was conceived, written and analysed by me personally, under the supervision of Dr. Eleftheria Panagiotaki, Professor Daniel Alexander and Dr. Shonit Punwani. VERDICT maps were produced via an automatic fitting process using a cloud based platform called XNAT (maintained at UCL by Ben Yvernault), which integrates the VERDICT code of Eleftheria Panagiotaki and Elisenda Bonet-Carné. Uran Ferizi carried out the fitting of my ROI data to produce quantitative values of VERDICT estimates for my statistical analysis. Mrishta Brizmohun Appayya and James O' Callaghan scored MRI image quality with myself in consensus. Paul Bassett reviewed the statistical methods, but did not contribute to statistical analysis. Dr Caroline Moore and Professor Hashim Ahmed were the Urologists who performed the targeted biopsies and Drs Alex Freeman, Charles Jameson and Marzena Ratynska were the histopathologists who reported the biopsy specimens.

Introduction

As I discussed in chapter 1, any new biomarker requires rigorous validation to be translated into clinical practice, which was the rationale behind the biomarker roadmap for cancer studies (79). This document recommends that following discovery and demonstration of feasibility, imaging biomarkers undergo technical and biological validation and putative clinical evaluation.

In prostate cancer, biomarkers that can probe tumour aggressiveness non-invasively are highly desirable as they may aid decision to biopsy, guide targeting to the most aggressive tumour components, and could also prove valuable within active surveillance programmes to monitor for changes in cancer grade. Of the currently available imaging biomarkers, ADC is the longest established and best validated, and as discussed in chapter 1, there is a consistent relationship of decreasing ADC as found with increasing Gleason grade (209–219,290). ADC therefore formed part of the best performing PZ model in chapter 5.

However, despite its merits, quantitative ADC measurements are not routinely used in clinical practice due to lack of biological specificity (202). Recently our collaborators

presented the feasibility of a novel Magnetic Resonance Imaging (MRI) technique called VERDICT MRI as a quantitative microstructural imaging tool for prostate cancer (203). VERDICT combines a DWI MRI acquisition with a mathematical model and assigns the diffusion-weighted MR signal to three principal components: i) intracellular water inside cells (f_{IC}) ii) water in the EES (f_{EES}) and iii) water in the microvasculature (f_{vasc}). Since the fraction of each of these compartments differs between each Gleason grade (18), VERDICT derived metrics may provide higher biological specificity than ADC as a marker of Gleason grade.

In the present study, we compare VERDICT MRI metrics and ADC in terms of image quality, repeatability and putative clinical value for Gleason grade differentiation. We are specifically interested in the ability of VERDICT to discriminate between Gleason 3+3 and Gleason 4 containing lesions for reasons considered previously.

Materials and methods

Our IRB approved the study protocol and informed written consent was taken from all study participants. The study is reported using the REMARK (83) guidelines where applicable.

One hundred and nine patients being investigated for prostate cancer were prospectively recruited to the INNOVATE trial for VERDICT MRI between April and November 2016, and following patient exclusion sixty two patients were included in the analysis. Inclusion criteria were i) clinical suspicion of prostate cancer, or ii) undergoing active surveillance for known prostate cancer. Exclusion criteria were i) previous treatment for prostate cancer (prostatectomy, radiotherapy, brachytherapy, ablative therapies) ii) on-going hormonal treatment for prostate cancer and iii) biopsy within 6 months prior to mp-MRI.

Imaging data was used to form two cohorts: cohort 1, the repeatability cohort and cohort 2, the biopsy cohort. A patient recruitment flow diagram is presented in Figure 57.

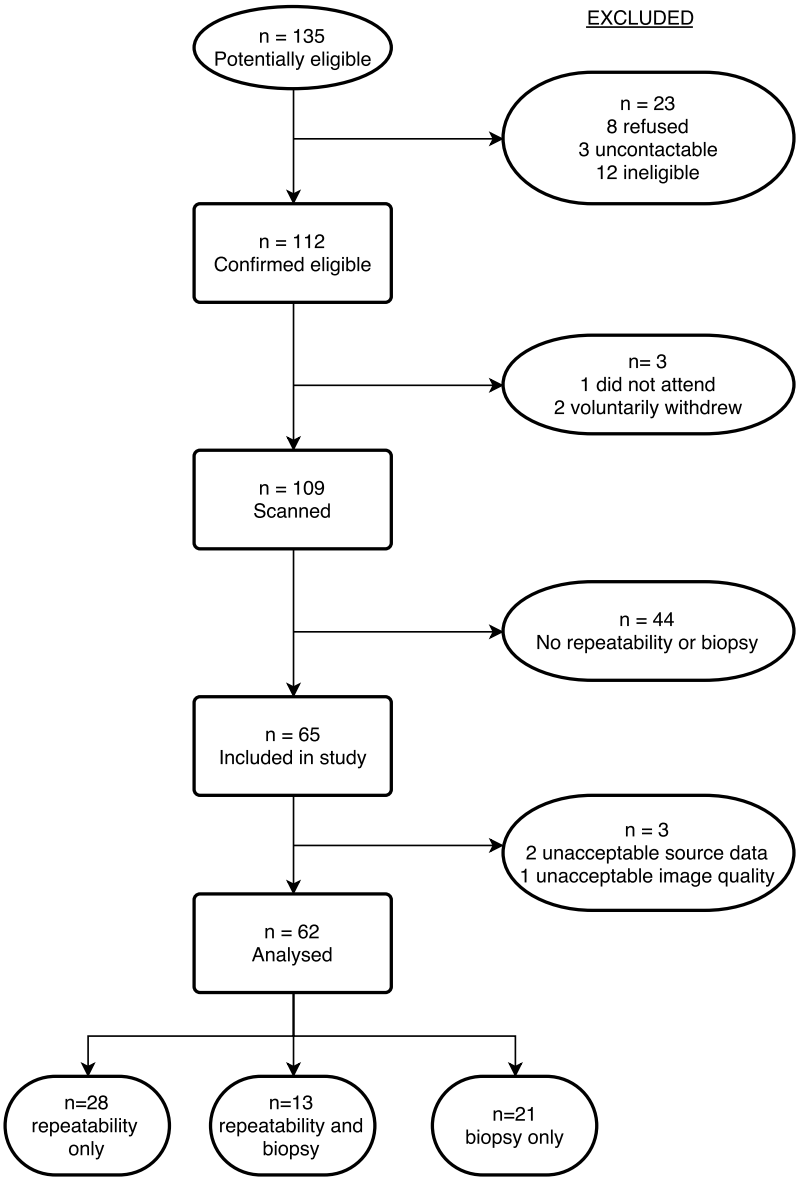

Figure 57: Patient recruitment flow diagram.

Cohort 1: Repeatability cohort

We performed a scan-rescan repeatability study of the VERDICT acquisition protocol in 41 patients. 31 of these patients were scanned without an interval between the two scans (group A) and the remaining 10 patients were scanned with a 5-minute interval between scans, during which time patients walked around the scanner room (group B).

Cohort 2: Biopsy cohort

Following clinical mp-MRI and VERDICT MRI, 34 patients (of whom 13/34 were also in the repeatability cohort) with a focal prostate lesion (defined as PI-RADS 3, 4 or 5 on standard mp-MRI) underwent targeted TPM of the index lesion, using the mp-MRI to

guide cognitive targeted biopsy (performed by Urologists CM and HA, each with 7 years of experience of cognitive targeting biopsy). For an individual patient, 2-6 biopsy cores were taken at the targeted biopsy site. Specialist genitourinary pathologists (AF, CJ and MR with 13, 13 and 10 years of prostate pathology experience respectively) reported the biopsy cores in the standard clinical fashion, to assign each biopsy core with a Gleason score (291). As there is a particular clinical need to distinguish tumours with a Gleason 4 component, we grouped results into three categories, namely benign/Gleason 3+3, Gleason 3+4 and ≥ Gleason 4+3.

Clinical mp-MRI acquisition

All patients underwent conventional mp-MRI, using either the 1.5 or 3 Tesla (T) protocols. ADC maps produced from the clinical acquisition are hereby referred to as $ADC_{CLINICAL}$.

VERDICT MRI acquisition

VERDICT MRI was performed in all patients, either at the same time as, or within 2 weeks of original mp-MRI study. If carried out at the same time as mp-MRI, VERDICT diffusion-weighted MRI sequences were acquired prior to DCE imaging. VERDICT uses an optimized single shot EPI pulse-gradient spin-echo sequence (240) using five b-values of 90-3000s/mm in 3 orthogonal directions with a range of diffusion and echo timings designed to probe tissue microstructure. 14 slices are acquired with a 220 x 220mm field of view and a 176 x 176 reconstruction matrix to give 1.3 x 1.3 x 5mm^3 voxels with the same spatial resolution as the clinical DWI acquisition used in our centre. Acquisition time for VERDICT totals 12min 25s, compared with 8min 27s for the diffusion component of the clinical mp-MRI.

Diffusion gradient parameters for VERDICT MRI are provided in table 14.

b value, s/mm^2	Δ/δ, ms	TE, ms	|G|, T/m	N_{AV}
90	23.8/3.9	50	0.0612	6
500	31.3/11.4	65	0.0443	12
1500	43.8/23.9	90	0.0320	18
2000	34.3/14.4	71	0.0677	18
3000	38.8/18.9	80	0.0600	18

Table 14: Diffusion gradient parameters for VERDICT MRI.

Δ; timing between gradient pulses, δ; gradient pulse duration, |G|; gradient strength, TE; echo time, N_{AV}; number of averages.

Diffusion model

The VERDICT model was fitted to the diffusion MRI data using the AMICO framework (292), which uses linearization and convex optimization for ultrafast fitting. Maps of f_{IC}, f_{EES} and f_{vasc} are produced, along with the objective function map (f_{obj}), which provides a measure of 'goodness-of-fit'. Voxels with an insufficient fit (defined by thresholding the objective function at 2 SD from its expected value given the SNR of the images) were excluded from the quantitative analysis. Since $ADC_{CLINICAL}$ was performed at two different field strengths and could therefore not be used in the quantitative analysis, ADC was also fitted to the VERDICT data for comparison, hereby defined as $ADC_{VERDICT}$. $ADC_{VERDICT}$ was produced using a Levenberg-Marquardt fit and the b= 0, 90, 500 and 1500 images, chosen since they are closest to those used for $ADC_{CLINICAL}$ (b=0, 150, 500 and 1000).

Image analysis

mp-MRI lesion localization

Clinical mp-MRI studies were reported by an experienced Uroradiologist (SP with 10 years of prostate mp-MRI reporting experience), and scored using the PI-RADS™ version 2 scale (61), from which pictorial reports were produced to denote the importance, number and location of focal lesions. The most important lesion was hereby defined as the index lesion.

Comparison of $ADC_{CLINICAL}$ and VERDICT MRI image quality

Two board certified radiologists, fellows in prostate MRI (EJ and MB, both with 3 years of experience in mp-MRI), and a postdoctoral MRI physicist (JOC) assessed the $ADC_{CLINICAL}$ maps and VERDICT maps in consensus, along with their multi-b-value source images for all patients (n=62), using the first acquisition for the repeatability cohort. Overall image quality, in terms of the influence of artefacts, was scored using a subjective 1 – 5 ordinal scale in accordance with (293,294): 1: very poor quality, considered non-diagnostic (artefacts on all slices, scans uninterpretable), 2: poor quality with some impairment of diagnostic quality (substantial artefacts, but still interpretable), 3: satisfactory quality without impairment of diagnostic quality (some artefacts present), 4: good quality (hardly any artefacts), 5: excellent quality (no artefacts present). $ADC_{CLINICAL}$ was used here since image assessment was qualitative. Images with a score of 1 were excluded from quantitative VERDICT metric analysis.

Measurement of quantitative VERDICT and $ADC_{VERDICT}$ metrics

VERDICT MR datasets were analysed using Osirix version 8.0 (Osirix, Bernex, Switzerland). I manually contoured a VOI for each index lesion on the f_{IC} map, using the clinical mp-MRI and the rest of the VERDICT maps for visual guidance. VOIs were kept as large as possible, whilst avoiding inclusion of normal surrounding tissue. Where possible, a standard 40mm^2 ROI was placed on both the normal TZ and PZ, defined as PI-RADS 1 or 2 on clinical mp-MRI.

For the repeatability cohort, VOI/ROIs were copied onto the second acquisition and position manually adjusted to maintain the same anatomical site as for placement on the first acquisition. A typical example of contouring is provided in figure 58. Quantitative mean values of $ADC_{VERDICT}$, f_{IC}, f_{EES} and f_{vasc} were then extracted by fitting the VERDICT model to the data in each voxel within the VOI/ROI.

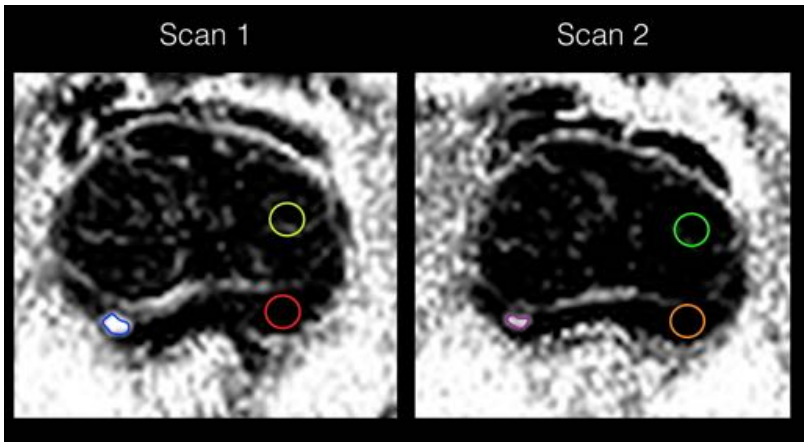

Figure 58: Example of lesion contouring.

For the biopsy cohort, the mean quantitative metrics from VOIs were matched with the Gleason grade of tumour confirmed at targeted biopsy of the lesion. The mean value of the two metrics was used for patients in the repeatability cohort.

Statistical analysis

Data were checked for normality using the Shapiro-Wilk test. Kruskal-Wallis with post hoc testing was performed to determine the differences between the overall image quality of each VERDICT map and ADC.

To assess the repeatability of ADC and VERDICT metrics, in accordance with (73), ICC (3,1) were calculated, and interpreted as: 0.0–0.20 no to slight agreement, 0.21–0.40 fair agreement, 0.41–0.60 moderate agreement, 0.61–0.80 substantial agreement, and 0.81–1 almost perfect agreement (243). B-A plots were also

constructed and mean bias and the 95% limits of agreement determined for each metric.

ANOVA with Bonferroni multiple comparisons correction was performed to determine the differences between the three defined histopathology categories (benign/Gleason 3+3, Gleason 3+4 and ≥ Gleason 4+3) for VERDICT and ADC parameters. ROC-AUC was calculated for the ability of $ADC_{VERDICT}$ and VERDICT maps to discriminate between benign/3+3 and 3+4/≥4+3. Statistical significance was set at $p<0.05$.

Results

Patient demographic data are displayed in table 15. The mean time between VERDICT MRI and biopsy was 82.5 days (interquartile range, IQR 42 – 124 days).

	Whole cohort	Repeatability cohort	Biopsy cohort
Number of patients	62	41	34
Median age, IQR	66.3 (58.5 – 70.0)	67.1 (63.0 – 69.7)	64.8 (58.5 – 70.0)
Maximum PI-RADS score:	11	11	0
2	18	12	9
3	18	11	13
4	15	7	12
5			
Gleason grade:	-	-	12
Benign/3+3	-	-	14
3+4	-	-	8
≥ 4+3			

Table 15: Patient demographic data

Image quality assessment

No significant differences were found in overall image quality between each of the compared maps (adjusted p>0.99 for all comparisons). Results are shown in table 16.

	ADC	f_{IC}	f_{EES}	f_{vasc}	Comment
1: Very poor	1	1	1	1	*Excluded*
2: Poor	10	11	12	12	
3: Fair	28	30	29	30	
4: Good	21	18	18	17	
5: Excellent	3	3	3	3	
Mean	3.23	3.17	3.16	3.14	

Table 16. Results of image quality assessment.

Note: results are number of scans for each VERDICT map scoring each level of image quality.

Metric repeatability

ICCs for $ADC_{VERDICT}$ and VERDICT parameters (measurement 1 vs. measurement 2) are shown in table 17 for the normal TZ and PZ (PI-RADS 1/2), and focal lesions (PI-RADS 3, 4 or 5), for groups A and B. B-A plots are provided in figures 59 – 64.

	ICC					
Parameter	No focal lesion TZ group A *(n=29)*	No focal lesion TZ group B *(n=10)*	No focal lesion PZ group A *(n=30)*	No focal lesion PZ group B *(n=10)*	Focal lesion group A *(n=18)*	Focal lesion group B *(n=7)*
$ADC_{VERDICT}$	0.99 (0.98 – 1.0)	0.83 (0.43 – 0.95)	0.77 (0.57 – 0.89)	0.86 (0.50 – 0.96)	0.89 (0.74 – 0.96)	0.95 (0.76 – 0.99)
f_{IC}	0.89 (0.76 – 0.94)	0.75 (0.27 – 0.93)	0.96 (0.91 – 0.98)	0.94 (0.80 – 0.99)	0.92 (0.77 – 0.97)	0.76 (0.19 – 0.95)
f_{EES}	0.88 (0.76 – 0.94)	0.91 (0.68 – 0.98)	0.88 (0.77 – 0.94)	0.86 (0.53 -0.96)	0.86 (0.67 – 0.95)	0.56 (-0.35 – 0.91)
f_{vasc}	0.81 (0.64 – 0.91)	0.47 (-0.26 – 0.83)	0.87 (0.74 – 0.94)	0.54 (-0.02 – 0.86)	0.83 (0.60 – 0.93)	0.53 (-0.13 – 0.89)

Table 17: ICCs (3,1) of ADC and VERDICT parameters

95% CI are shown in parentheses

B-A plots: Group A

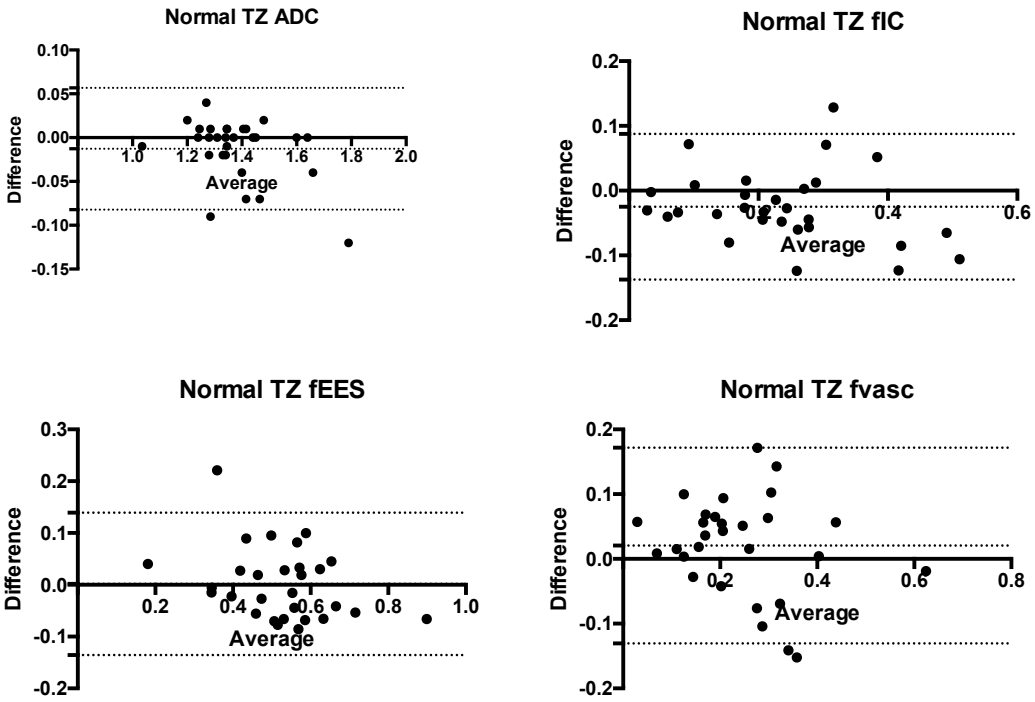

Figure 59. Repeatability of ADC and VERDICT parameters for the normal TZ of group A.

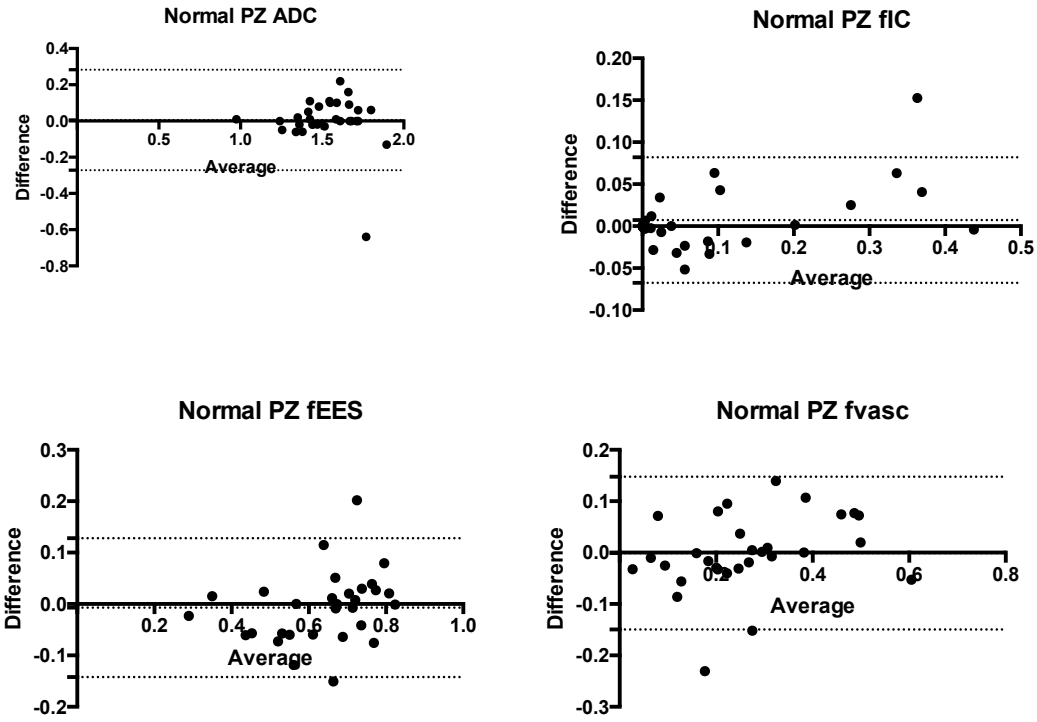

Figure 60. Repeatability of ADC and VERDICT parameters for the normal PZ of group A.

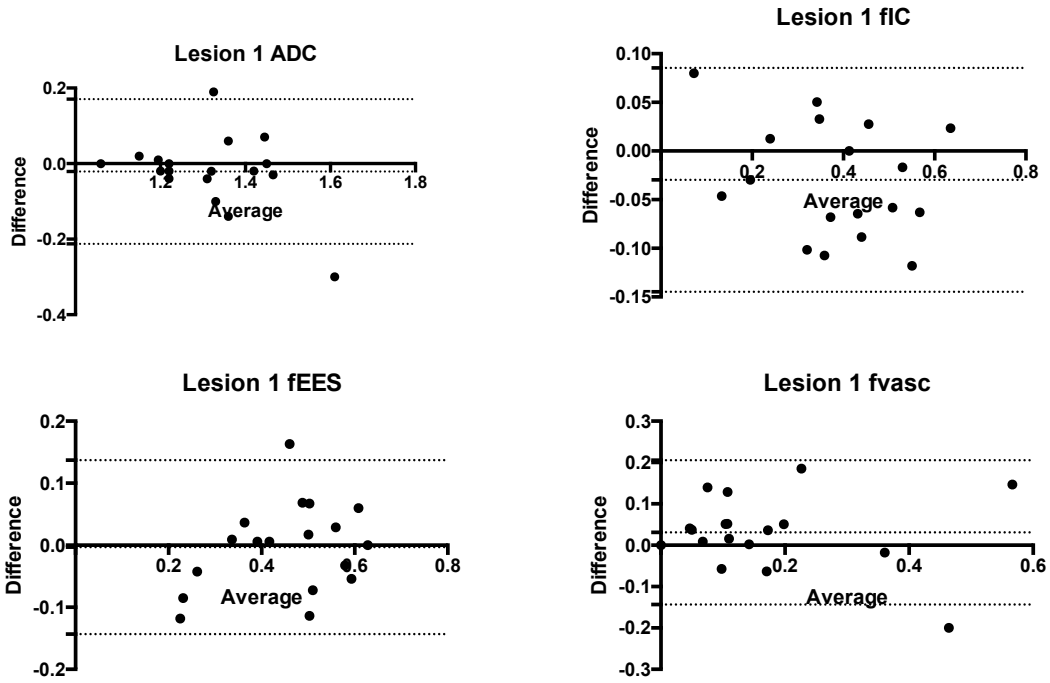

Figure 61. Repeatability of ADC and VERDICT parameters for the index lesion for group A.

B-A plots: Group B

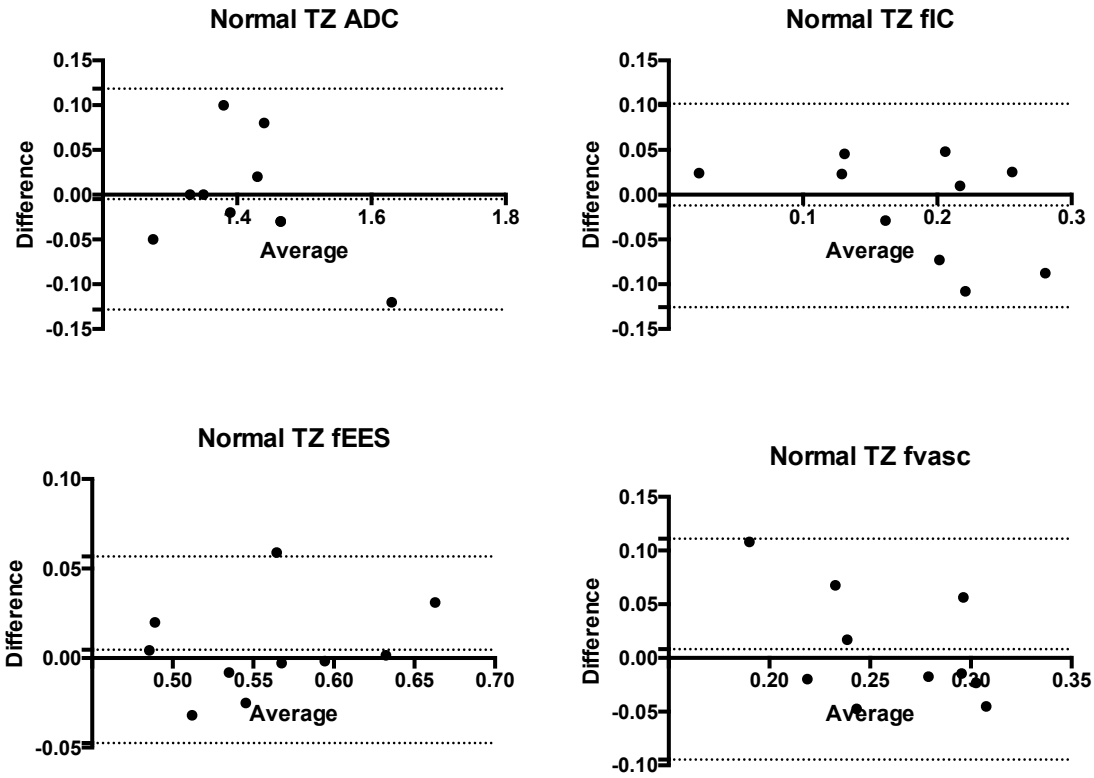

Figure 62:Repeatability of ADC and VERDICT parameters for the normal TZ of group B.

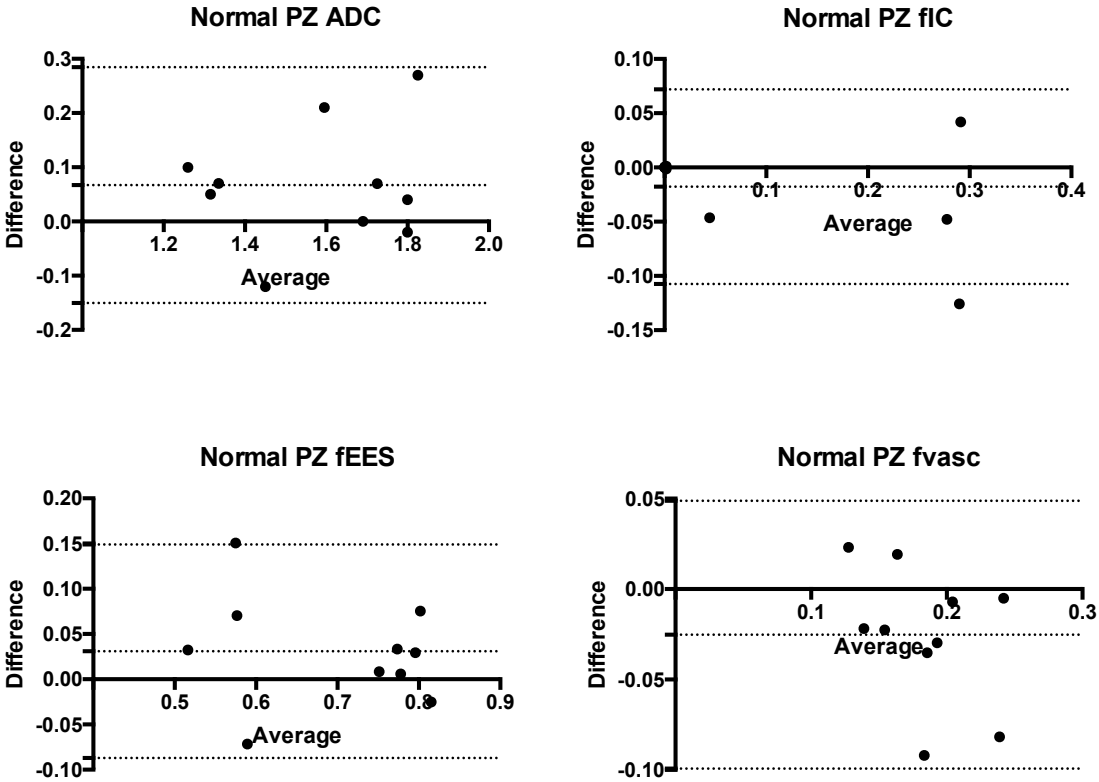

Figure 63:Repeatability of ADC and VERDICT parameters for the normal PZ of group B.

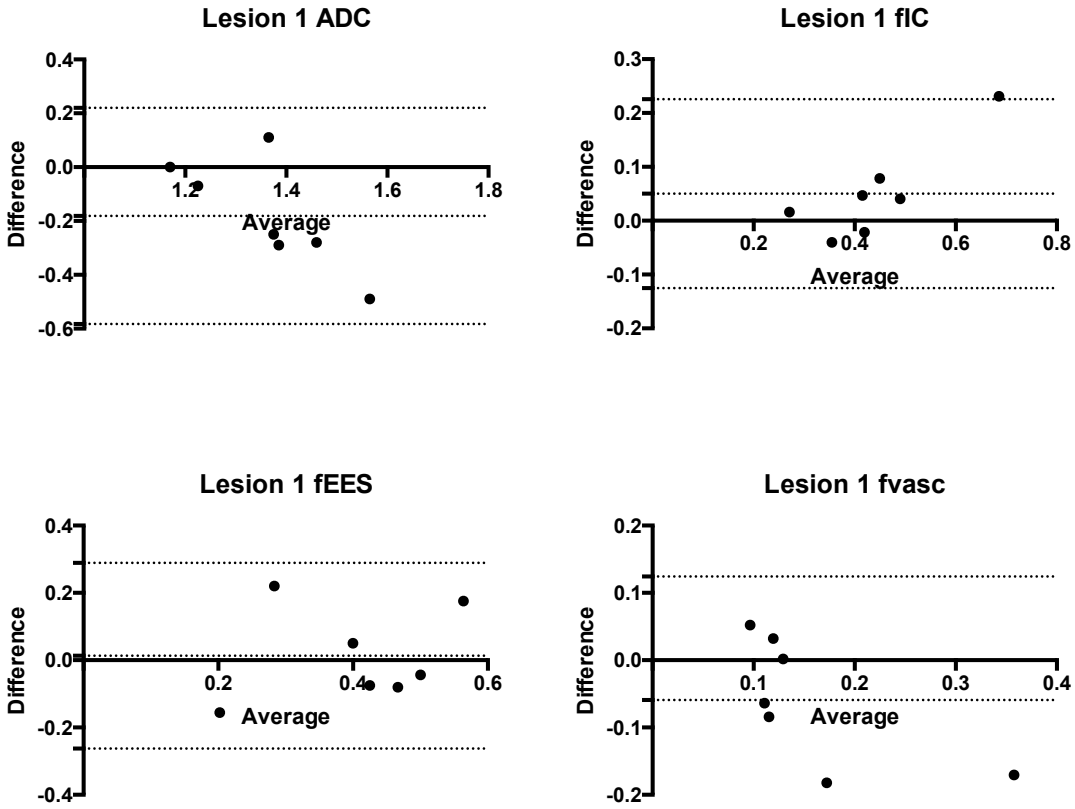

Figure 64:Repeatability of ADC and VERDICT parameters for the index lesion for group B.

Correlation with Gleason grade

The distribution of $ADC_{VERDICT}$ and VERDICT parameters in each Gleason grade group are shown in figure 65, with their values provided in table 18.

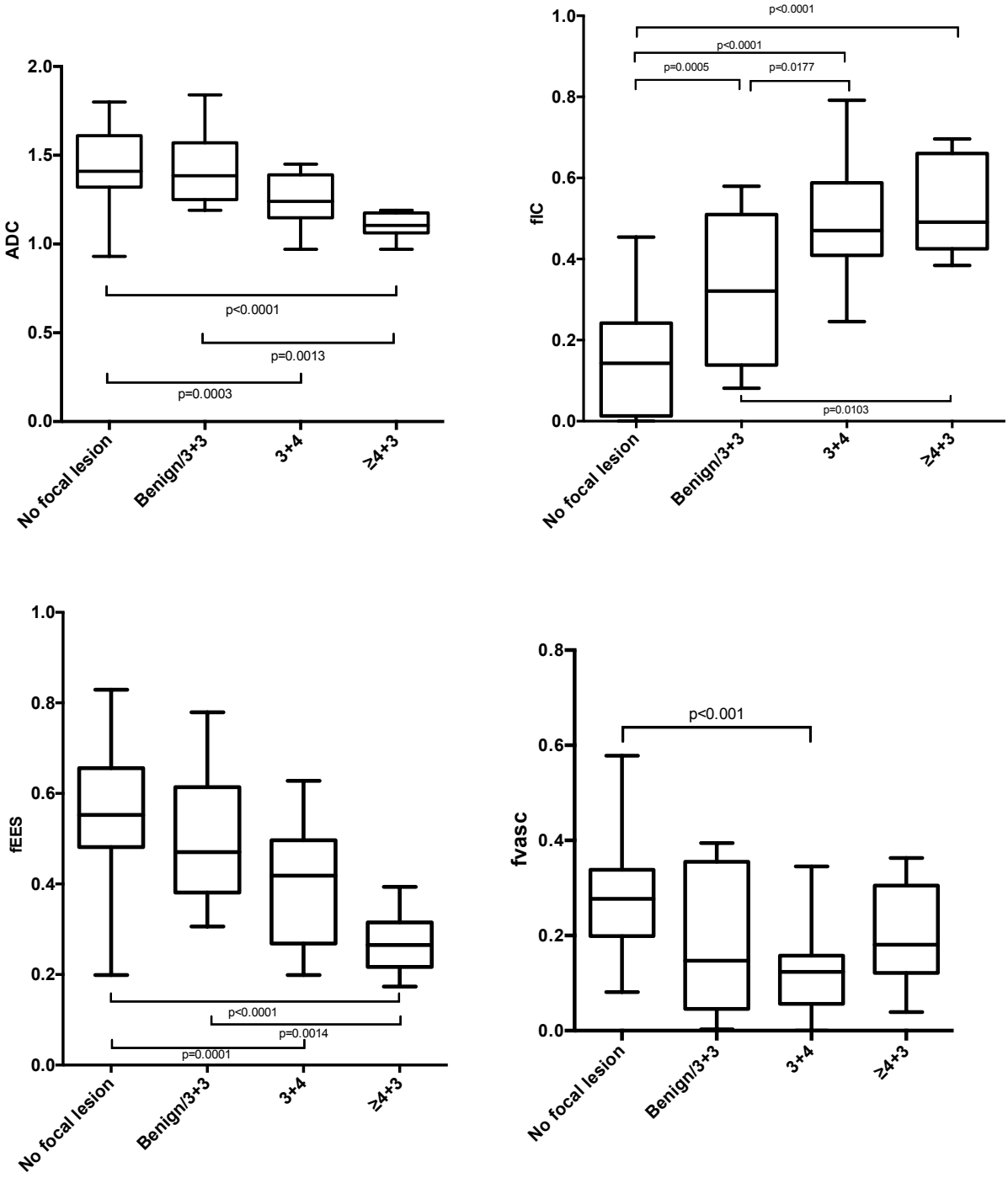

Figure 65:Box and whisker plots showing the distribution of $ADC_{VERDICT}$ and VERDICT parameter values in each Gleason grade group

Corrected p-values following Bonferroni-corrected ANOVA are indicated.

Parameter	No focal lesion	Focal lesion: benign/3+3	Focal lesion: 3+4	Focal lesion: ≥ 4+3
ADC	1.44 ± 0.18	1.42 ± 0.22	1.21 ± 0.16	1.11 ± 0.07
f_{IC}	0.15 ± 0.13	0.33 ± 0.18	0.50 ± 0.14	0.53 ± 0.12
f_{EES}	0.57 ± 0.13	0.49 ± 0.14	0.40 ± 0.13	0.27 ± 0.07
f_{vasc}	0.28 ± 0.10	0.19 ± 0.15	0.12 ± 0.09	0.20 ± 0.11

Table 18: Distribution of ADC and VERDICT parameters in each Gleason grade group.

Parameters are expressed as mean ± SD.

ROC-AUC for the ability of $ADC_{VERDICT}$ and VERDICT parameters to distinguish benign/3+3 vs. 3+4/≥4+3 are shown in figure 66.

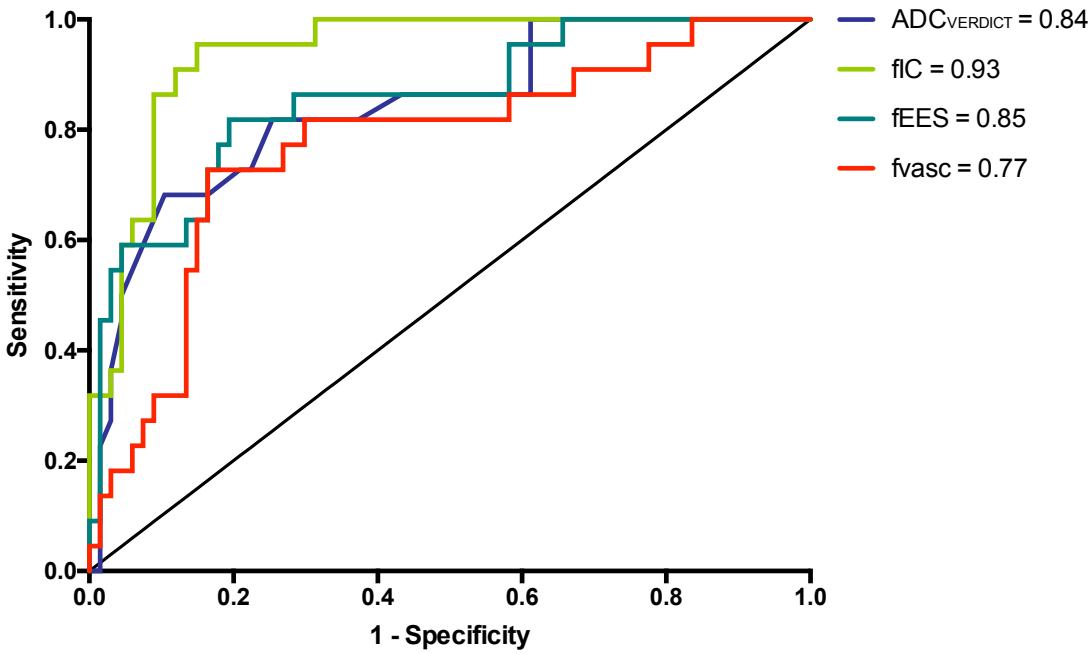

Figure 66.ROC curves and their AUC values for $ADC_{VERDICT}$ and VERDICT maps, to distinguish benign/3+3 vs. 3+4/≥4+3.

Discussion

After its initial conception and subsequent development in a murine model at 9.4 Tesla (T)(205), VERDICT was first tested in human subjects at 3T in an 8 patient pilot study in prostate cancer(203). The aim of the present study was to formally develop its use as a potential biomarker for Gleason grade prediction in prostate cancer in line with the imaging biomarker roadmap(79). As a first step in biomarker validation I evaluated the repeatability of the VERDICT MRI parameter maps and assessed image quality (vs.

$ADC_{CLINICAL}$) in the normal and cancerous prostate.

Since VERDICT images have the same voxel size as $ADC_{CLINICAL}$, the spatial resolution of VERDICT MRI parametric maps and standard ADC maps is equivalent. To our knowledge, there are two studies concerning image quality in mp-prostate MRI which have used a similar 5-point scale to assess the overall image quality of ADC images (293,294). These studies showed a mean image quality of 3.18 and 3.03 out of 5 respectively, meaning our ADC and VERDICT images (3.16 – 3.23) were comparable to those found in the literature. The fact that we found no significant difference in image quality between ADC and VERDICT maps was unsurprising since VERDICT MRI utilises echo-planar-based sequences in the same way as the standard DWI acquisition, and therefore is susceptible to the same causes of image artefact.

In terms of metric repeatability, ADC demonstrated 'almost perfect' repeatability in all but one case (normal PZ) where agreement was 'substantial'. In comparison with the literature, our ADC measurements are slightly more precise compared to those of Gibbs et al. who showed an ADC variation of 13 - 17% in the immediate term and 20 - 25% in scans separated by a month (295), we found around 5-15% variation. We have also shown that f_{IC} and f_{EES} have comparable levels of repeatability vs. ADC, with f_{IC} demonstrating almost perfect repeatability in all but two cases (where agreement was 'substantial') and f_{EES} with 'almost perfect' repeatability in all but one case where agreement was 'moderate'. As could be expected, interval scans demonstrated lower levels of repeatability than immediate scans, which could be due to greater difference in the histological content of each voxel between the two scans and the lower sample size of group B increasing the influence of outliers. Of all VERDICT metric maps, the lowest levels of repeatability were observed in the f_{vasc} map, which is likely to arise from relatively low values of vascular fraction within tissue leading to increased relative noise. Additionally, we found that f_{vasc} was the least useful predictor of Gleason grade, which may arise from its limited repeatability.

The repeatability of all VERDICT parameters compares favourably with other diffusion models in prostate cancer. For example, one group (296) compared the repeatability of ADC with parameter estimates from stretched exponential, DKI and biexponential models in the human prostate with scans separated by a mean interval of 2 days (range 1 – 22), and found that whilst monoexponential fits and DKI achieved ICCs of around 0.75, the repeatability of stretched exponential and biexponential parameters was approximately 0.25. Similarly, another group of investigators showed the ICCs of D* and f from IVIM, and α from stretched exponential to be 0.25, 0.42 and 0.64

respectively, even when calculated from two sets of identical b-values performed in a single acquisition (297).

Our study also demonstrated putative clinical value of VERDICT MRI, showing that f_{IC} was able to better distinguish between Gleason grades vs. $ADC_{VERDICT.}$ In particular f_{IC} could better distinguish a secondary pattern 4 component from benign/3+3 in a focal prostate lesion, and also showed higher ROC-AUC than ADC for benign/3+3 vs. ≥3+4. Given the clinical importance of this distinction, there could be multiple potential clinical applications for VERDICT in prostate cancer management once fully validated as an imaging biomarker. Such applications include the non-invasive monitoring of patients for progression whilst on active surveillance, appropriately avoiding or triggering prostate biopsies and risk-stratifying patients to make treatment decisions.

One of the main limitations of this study is the relatively low number of interval repeatability scans, at 10 patients. However, other similar studies have had 8 or fewer subjects (295), which emphasizes that interval repeatability examinations are difficult to perform given the time limitations of clinical workflows. Secondly, since clinical mp-MRI was often performed on a different scanner to the VERDICT acquisition, $ADC_{CLNICAL}$ could not be used in quantitative analysis, meaning $ADC_{VERDICT}$ was used instead. However, $ADC_{VERDICT}$ was selected to have similar b-values and also has comparable acquisition parameters to the $ADC_{CLINICAL}$. Additionally, as a single scanner study, the next step in validation should be to test reproducibility across multiple scanners and institutions (79).

Whilst we have used targeted biopsy to avoid potential sampling errors inherent with TRUS biopsy (69); the biological interpretation of VERIDCT parameters estimates remains unconfirmed due to the simplicity of the mathematical tissue model, whereby direct comparisons with histology are required to establish the extent to which they reflect their target quantities. For example, f_{vasc} may not provide a reliable estimate of vascular volume fraction, because of model assumptions e.g. fixed intrinsic diffusivity. As a subject of further work, our group therefore wishes to use apparatus which accurately register MRI to histological slices (280 - appendix E) to biologically validate VERDICT maps.

Conclusion

VERDICT MRI derived metrics are similar to ADC in image quality and repeatability, but we showed early indications of improved estimation of prostate cancer Gleason grade. With further work, VERDICT metrics could be combined in predictive models such as that provided in chapter 5 to better predict Gleason grade in prostate cancer non-invasively.

Summary

- VERDICT MRI has shown significant promise for estimating tissue microstructure in the preclinical setting and in a prostate cancer pilot study.
- Prior to translation into clinical practice, VERDICT requires further validation according to the imaging biomarker roadmap for cancer studies, which was the focus of this chapter.
- VERDICT maps were shown to have similar image quality and repeatability vs. ADC, but showed early indications of improved ability to estimate Gleason grade, and in particular a Gleason 4 component.
- With further validation, VERDICT MRI could prove to be a useful clinical tool for non-invasive Gleason grade estimation.

8 WHOLE-BODY MRI AS A STAGING MODALITY IN PRIMARY PROSTATE CANCER

Author declaration

All of the work in this chapter was conceived, written and analysed by me personally, under the supervision of Dr. Shonit Punwani. Ethical approval and the first half of patient recruitment were carried out by Dr Arash Latifoltojar (Bromley National Research Ethics Committee reference 12/LO/0428), whilst I carried out the second half of patient recruitment. Drs. Arash Latifoltojar and Alan Bainbridge developed the scanning protocol. Drs Harbir Sidhu and Navin Ramachandran reported the clinical scans during reporting sessions during which time Case Report Forms (CRFs) were filled in by myself.

Introduction

Having developed biomarkers that can better discriminate aggressive tumours within the prostate itself, I now wish to consider whether mp-WB-MRI can be used to accurately detect and stage *extraprostatic* disease, for purposes of further prognostication.

As I discussed in chapter 1, patient survival in intermediate and high-risk prostate cancer depends heavily on 'TNM' stage (100) and therefore accurate cancer staging underpins all prognostication and management decisions. Despite the emergence of a number of imaging platforms for this purpose, the mainstay of imaging-based staging decisions are still dependent upon BS +/- pelvic CT, as supported by at least eight international guidelines (111). Whilst such modalities are simple to implement, their performance characteristics are limited (112,113), and have not been fully addressed by the inception of choline PET/CT.

Whole body (WB)-MRI is a promising alternative, whereby reported performance is comparable to choline PET/CT in a number of early studies (131,145,299–301) yet has higher spatial and contrast resolution than PET, does not use ionising radiation and can be performed as a 'one stop' examination in combination with mp-MRI. However, its interobserver agreement has only been reported in a single study, further assessment of diagnostic accuracy would be welcome (especially using a robust reference standard) and the optimal balance of pulse sequences which can achieve

acceptable levels of diagnostic accuracy within a clinically acceptable time frame has not been established.

The purpose of the present study is to determine the interobserver concordance of mp-WB-MRI and compare lesion distribution and intermodality concordance with BS and PET/CT for the primary staging of intermediate and high-risk prostate cancer. The diagnostic accuracy of each modality will also be assessed using a one-year follow-up mp-WB-MRI based reference standard and a locked sequential read (LSR) paradigm to determine the additive value of each MRI sequence.

Materials and Methods

Our IRB approved this prospective single centre study. Informed written consent was obtained from each participant, whereby 56 consecutive men (mean age 67.9 years, range 51.9 – 84.4) were identified at Multidisciplinary Team (MDT) meetings between July 2012 and November 2015. Inclusion criteria were i) men aged 18 or over ii) new diagnosis of intermediate or high-risk prostate cancer, as defined by the D'Amico criteria (302). Exclusion criteria were i) contraindications to MRI e.g. severe claustrophobia or MR unsafe device ii) prior therapy for prostate cancer iii) men unable to provide informed consent. A recruitment flow diagram is shown in Figure 67.

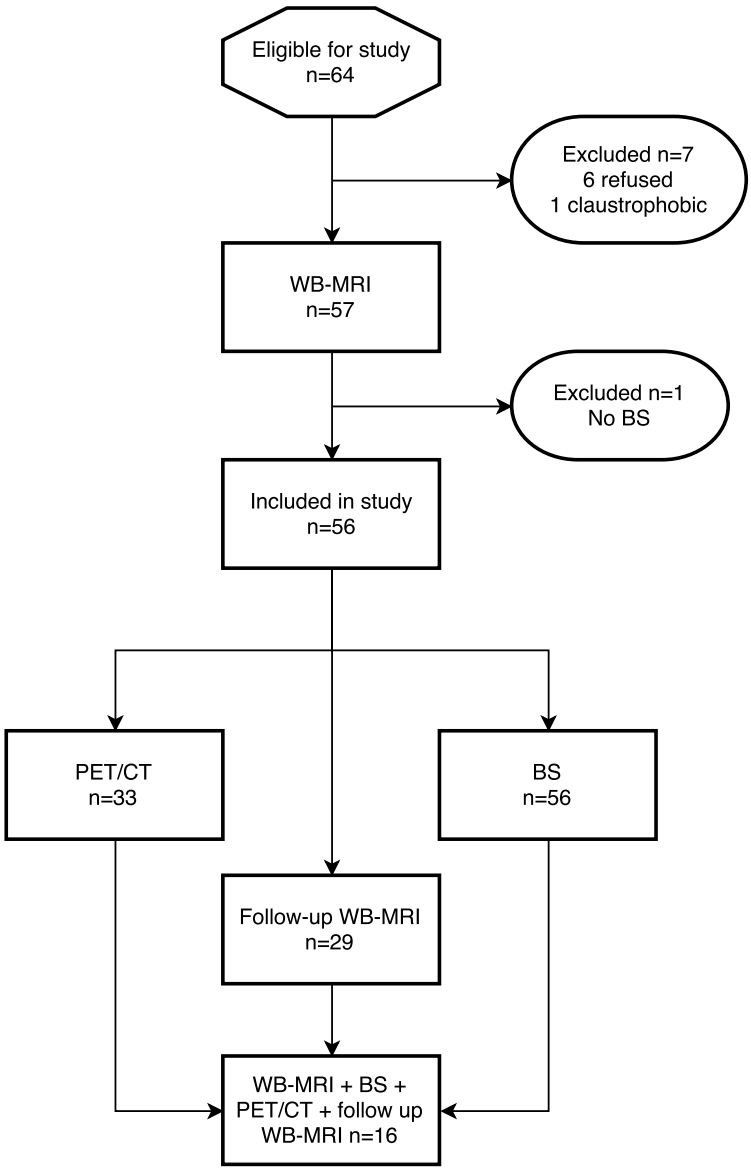

Figure 67. Patient recruitment flow diagram.

BS = Bone scan

Standard imaging comprised BS in all patients +/- ^{18}F-choline-PET/CT in 33 patients. The decision to perform a ^{18}F-choline-PET/CT was made on a case-by-case basis whereby the risk of extraprostatic disease was considered to be high at multidisciplinary team (MDT) discussion. WB-MRI was performed within a mean of 15.9 days (range 0 – 49) of BS.

Multi-parametric WB-MRI Protocol

All patients were imaged on a 3.0 Tesla wide bore system (Ingenia, Philips, Best, NL), with WB coverage from vertex to feet using a 6 station acquisition, a head coil, two anterior surface coils and table-embedded posterior coils. A coronal pre-contrast mDixon, axial T2W TSE and axial DWI with body signal suppression at 4 b-values (b0,

b100, 300 and 1000) were performed, from which an ADC map was constructed. Post-contrast mDixon imaging was then carried out following a 20ml injection of intravenous gadoterate meglumine (Dotarem®, Guebert, France) (Figure 68). Full acquisition parameters are provided in table 19. Images were prepared for review by combining multiple stacks into single datasets using the scanner workstation for mDixon images (figure 65) and Osirix version 7.0 (Bernex, Switzerland) for axial images.

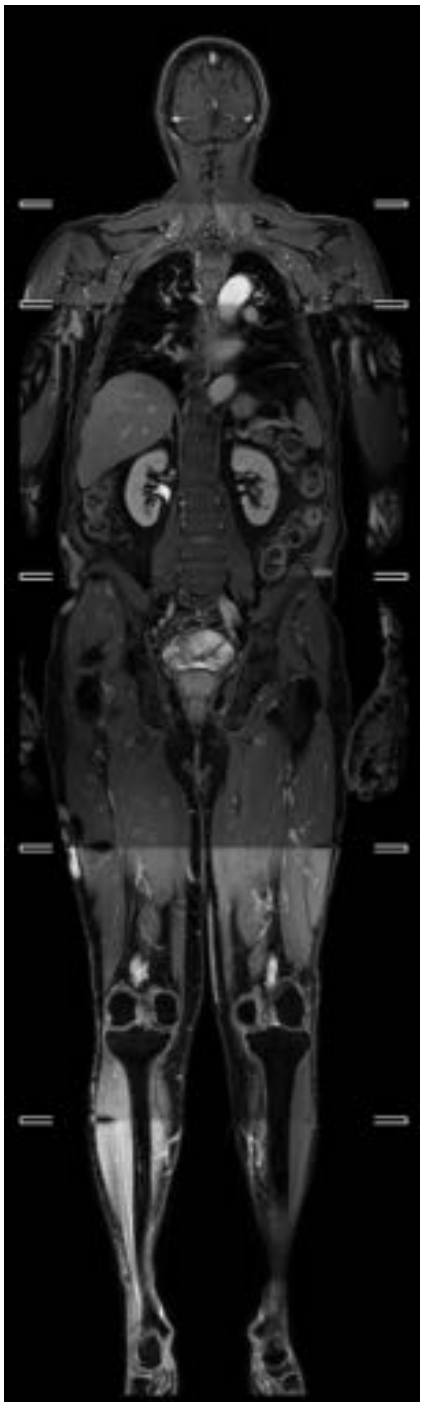

Figure 68. Stitched WB post-contrast WB-mDixon

	T2W-TSE	mDixon (pre- and post-contrast)	DWI (b=0, 100, 300, 1000s/mm^2)
Imaging plane	Transverse	Coronal	Transverse
TE (ms)	80	1·02/1·8	71
TR (ms)	1228	3·0	6371
FOV (mm*mm)	500*300	502*300	500*306
Voxel size (mm*mm)	1*1	2·1*2·1	4*4·2
Number of slices	40	120	40
Slice thickness (mm)	5	5	5
Acquisition matrix	500*286	144*238	124*72
ETL	91	2	39
Acceleration factor	2	2	2·5
Pixel bandwidth (Hz)	537	1992	3369
Scan time (min)	15.2	5.5 x 2	47

Table 19. WB-MRI acquisition parameters

^{99m}Tc scintigraphy protocol

WB imaging was performed in all patients, using anterior and posterior views, 256 x 1024 matrix and energy window(s) of 140 KeV, 2 – 4 hours after a single injection of Tc^{99}m-methylene diphosphonate (MDP).

Choline PET/CT protocol

33 patients underwent ^{18}F-choline-PET/CT on an integrated 64-slice scanner (Discovery VCT; GE Healthcare) from vertex to mid thigh, 60min after an intravenous injection of ^{18}F-fluoro-ethyl-choline tracer (198–410 MBq; average activity, 327.4 MBq). A low-dose, unenhanced CT scan was initially performed for attenuation correction and image fusion at 120 keV and 10mA (couch movement 0.8 s and 30 mm per rotation). WB-PET emission images were then acquired and reconstructed using the Hounsfield units from the CT to a resolution of 128 x 128 with 5mm slice thickness.

Follow-up WB-MRI

Patients were invited to attend a follow-up WB-MRI 1 year after their initial scan – using the same acquisition protocol – to inform the reference standard. 29 patients attended in total. Of the 27 who did not attend, two patients died, 9 were lost to follow-up and 16 declined a second attendance. WB-MRI was chosen as the follow up test due to the limited performance characteristics of BS and CT and ionizing radiation associated with choline PET/CT.

BS and PET/CT image review

Nuclear medicine physicians reviewed the BS and ^{18}F-choline-PET/CT staging studies as part of their standard clinical care using GE Advantage workstations. Disease positivity was defined as accumulation of radiotracer, greater than the surrounding background and incompatible with normal physiological activity.

WB-MRI review

Two board certified radiologists (NR with 12 years experience, HS with 9 years experience) independently reviewed anonymised MR datasets using an Osirix workstation (v. 7.0 Pixmeo, Bernex, Switzerland), aware of the presenting PSA level only and blinded to all other clinical and imaging results.

The body was divided into 9 nodal regions (external iliac, internal iliac, common iliac, paraaortic, presacral, other abdominal, inguinal, thoracic and neck) using standard anatomic definitions. 10 skeletal sites were assessed for the presence of disease (skull, cervical spine, thoracic spine, lumbar spine, pelvis, sternum, clavicle/scapula, ribs, upper limb and lower limb), as were 8 soft tissue sites (brain, lung, pleura, liver, adrenal, mesenteric, soft tissue and other). Scans were reviewed using a locked sequential read (LSR) paradigm, whereby each radiologist initially reviewed the mDixon and DWI and scored the suspicion of disease at each site using a 1 – 6 ordinal scale (1; definitely not present, 2; probably not present, 3; possibly not present, 4; possibly present, 5; probably present, 6; definitely present) for each disease site, according to the 'TNM' 7th edition staging system (N0/N1, M1a/M1b/M1c). T2W images were then revealed and sites re-scored. Lastly, post-contrast mDixon was revealed and a final mp-MRI score assigned. The time to report WB-MRI studies was recorded for both readers. Where discordancy arose between the two radiologists, a third board certified radiologist with 12 years experience (SP) adjudicated and rescored discordant sites using all available MR images, also aware of the PSA level only.

Derivation of reference standard

The third board certified radiologist then independently reviewed follow-up WB-MRIs in combination with clinical information at the time of the scan to assign patients into the following categories using the definitions below:

True positive (TP) sites: i) Lesion on WB-MRI (defined as suspicion level 4/5/6) which is BS and ^{18}F-choline-PET/CT positive (if performed). Follow up WB-MRI (if performed) also demonstrates lesion progression without systemic therapy, decrease with systemic therapy, or new lesions. ii) Lesion on WB-MRI which is BS or PET/CT negative (if performed) but progresses on WB MRI follow up without systemic therapy, decreases with systemic therapy, or new lesions identified.

True negative (TN) sites: No lesion on WB MRI (defined as suspicion level 1/2/3) or BS or PET/CT, unchanged at follow up and without evidence of biochemical failure, as per the Phoenix definition (303).

False positive (FP) sites: Lesion on WB-MRI that was BS or PET/CT negative and unchanged at follow-up up. No evidence of biochemical failure.

False negative (FN) sites: No lesion on WB MRI but positive BS or PET/CT, which increased without, or decreased in size with systemic therapy at follow-up.

Statistical analysis

Data were analysed using SPSS Statistics version 23 (2015, IBM, NY, USA). The following statistics were calculated:

1. The distribution of positive lesions for each staging modality (BS, PET/CT and WB-MRI) for local nodal and metastatic disease using the 'TNM' classification. Percentages were recorded i) for all patients (n=56), ii) for patients undergoing PET/CT (n=33).

2. The interreader agreement of WB-MRI (n=56) and agreement between WB-MRI and BS (n=56) and PET/CT (n=33) were assessed using κ statistics, interpreted according to Landis and Koch (243), whereby < 0 indicates no agreement, 0–0.20; slight, 0.21–0.40; fair, 0.41–0.60; moderate, 0.61–0.80; substantial and 0.81–1 as almost perfect agreement.

3. ROC-AUC was calculated for both WB-MRI readers following each component of the LSR, applying thresholds for each level of suspicion (1 – 6) vs. the reference standard. Differences in ROC-AUC values were assessed according to (304), using a significance level of $p < 0.05$. 29

patients underwent follow-up MRI. Four patients with suspected bone metastases on WB-MRI without follow-up had a concordant BS, to give n=33 patients. Two patients and one patient with suspected N1 and M1a disease on WB-MRI respectively had a concordant PET/CT, to give n=31 and 30. Youden's index (305) was used to determine the optimal cut-off of the ROC curve, and thus provide the highest combination of sensitivity and specificity.

4. The sensitivity, specificity positive (PPV) and negative (NPV) predictive values were then determined at each 'TNM' stage for the BS, PET/CT and WB-MRI against the reference standard. The simplest combination of LSR that gives no statistically significant difference in ROC-AUC will be used for further analysis. Here, a comparison was made between patients with the reference standard, who also underwent initial staging PET/CT. Group sizes were n=18, 17 and 18 for N0/N1, M0/M1a and M0/M1b respectively.

Results

56 patients had a median PSA of 20.05 (IQR 10.07 – 61.20). 50 patients were 'high-risk' and 6 patients 'intermediate-risk'. Maximum Gleason score was 3+3 for two patients, 3+4 for nineteen patients, 4+3 for fourteen patients, 4+4 for five patients, 4+5 for thirteen patients and 5+5 for one patient. The mean time of radiologists to report each component of the LSR was 15 min for mDixon + DWI, 6.5 min for T2W and 4 min for post-contrast scans.

The distribution of disease for each staging modality (BS, ^{18}F-choline-PET/CT and WB-MRI) is presented in table 20. No suspicious lesions (3/4/5) were identified below the mid thigh level on any staging modality. Two cases had suspicious lesions in the neck and thoracic spine; otherwise no disease was identified above the diaphragm.

	BS	PET/CT	WB-MRI
N0	-	23/33 (69.7%)	26/33 (78.8%)
	-	-	44/56 (78.6%)
N1	-	10/33 (30.3%)	7/33 (21.2%)
	-	-	13/56 (23.2%)
M0	30/33 (90.9%)	22/33 (66.7%)	24/33 (72.7%)
	43/56 (76.8%)	-	38/56 (67.9%)
M1a	-	7/33 (21.2%)	3/33 (9.1%)
	-	-	6/56 (10.7%)
M1b	3/33 (9.1%)	6/33 (18.2%)	8/33 (24.2%)
	13/56 (23.2%)	-	16/56 (28.6%)
M1c	-	0/33 (0%)	0/33 (0%)
	-	-	0/56 (0%)

Table 20. Distribution of lesions on each staging modality.

No lesions were detected on BS or WB-MRI outside of the PET field of view. Example image comparisons between WB-MRI, PET/CT and BS are shown in figures 69 and 70.

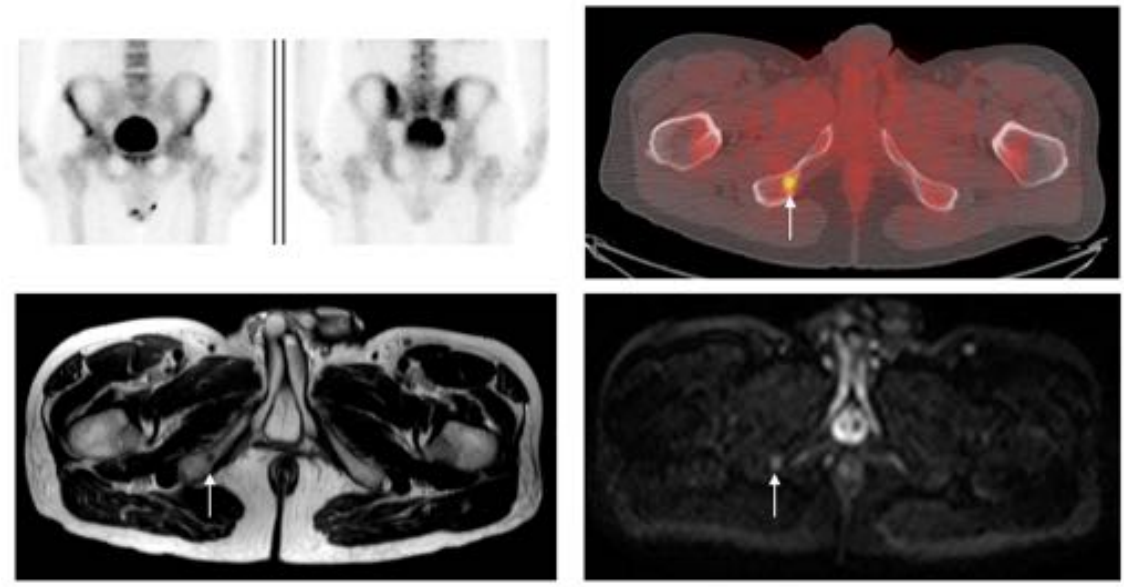

Figure 69. True positive WB-MRI, false negative PET/CT and BS.

Top left: Negative bone scan, Top right: positive ^{18}F-choline PET/CT showing a metastasis at the right inferior pubic ramus (white arrow), Bottom left: visible metastasis on T2W T2 TSE, Bottom right: visible metastasis on b=1000s/mm^2

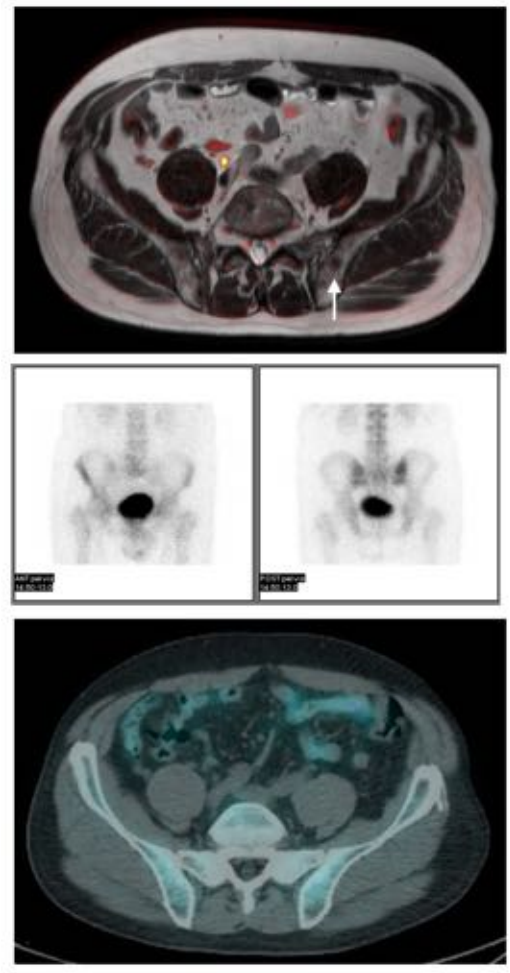

Figure 70. True positive WB-MRI and PET/CT, false negative BS.

Top: Axial T2W TSE with fused b=1000s/mm^2 showing a metastasis at the left iliac bone (white arrow), middle: negative bone scan, bottom: negative ^{18}F-choline PET/CT.

Concordance statistics (κ) between WB-MRI readers; between WB-MRI consensus vs. bone scan; and WB-MRI consensus vs. ^{18}F-choline-PET/CT are presented in table 21.

	Local nodes (N1)	Metastatic nodes (M1a)	Metastatic bones (M1b)
Interobserver concordance for WB-MRI (n=56)	0.79	0.68	0.58
Concordance of WB-MRI vs. BS (n=56)	-	-	0.68
Concordance of WB-MRI vs. PET/CT (n=33)	0.77	0.37	0.64

Table 21. Interobserver and intermodality concordance.

ROC-AUC statistics for 'TNM'-based nodal and metastatic status following each part of the LSR are presented in table 22 against the follow-up based reference standard.

	N0/N1 (n=31)	M1a (n=30)	M1b (n=33)	Mean
Reader 1				
mDixon + DWI	0.97 (0.91 – 1.00)	0.99 (0.96 – 1.00)	0.86 (0.72 – 1.00)	0.94
+ T2W	0.98 (0.94 – 1.00)	0.99 (0.95 – 1.00)	0.93 (0.84 – 1.00)	0.96
+ contrast	0.98 (0.94 – 1.00)	0.97 (0.91 – 1.00)	0.90 (0.76 – 1.00)	0.95
Reader 2				
mDixon + DWI	0.94 (0.81 – 1.00)	0.87 (0.60 – 1.00)	0.86 (0.73 – 1.00)	0.89
+ T2W	0.94 (0.82 – 1.00)	0.87 (0.60 – 1.00)	0.94 (0.83 – 1.00)	0.91
+ contrast	0.94 (0.82 – 1.00)	0.87 (0.60 – 1.00)	0.93 (0.82 – 1.00)	0.91

Table 22. ROC-AUC for each component of the LSR

No significant differences were detected between the mean ROC-AUC for each component of the LSR ($p<0.05$), so the simplest WB-MRI combination was chosen for further analysis (DWI + mDixon). Youden's index confirmed the optimal cutoff of the ROC-AUC was ≥4 in all cases. The sensitivity and specificity for BS, ^{18}F-choline-choline PET CT and WB-MRI were therefore calculated using a threshold of ≥4 as positive against the follow-up reference standard. Results are displayed in table 23, along with their numerators and denominators.

	N1 (n=18)	M1a (n=17)	M1b (n=18)
BS			
Sensitivity	-	-	0.60 (3/5)
Specificity			1.00 (13/13)
PPV			1.00 (3/3)
NPV			0.87 (13/15)
PET/CT			
Sensitivity	1.00 (7/7)	0.75 (3/4)	0.80 (4/5)
Specificity	0.82 (9/11)	0.92 (12/13)	0.92 (12/13)
PPV	0.77 (7/9)	0.75 (3/4)	0.80 (4/5)
NPV	1.00 (9/9)	0.92 (12/13)	0.92 (12/13)
WB-MRI: Reader 1			
Sensitivity	1.00 (7/7)	1.00 (4/4)	0.80 (4/5)
Specificity	0.91 (10/11)	0.85 (11/13)	1.00 (13/13)
PPV	0.88 (7/8)	0.67 (4/6)	1.00 (4/4)
NPV	1.00 (10/10)	1.00 (11/11)	0.93 (13/14)
WB-MRI: Reader 2			
Sensitivity	1.00 (7/7)	0.50 (2/4)	1.00 (5/5)
Specificity	1.00 (11/11)	1.00 (13/13)	0.76 (10/13)
PPV	1.00 (7/7)	1.00 (2/2)	0.62 (5/8)
NPV	1.00 (11/11)	0.86 (13/2)	1.00 (10/10)
WB-MRI: Mean			
Sensitivity	1.00	0.75	0.90
Specificity	0.96	0.93	0.88
PPV	0.94	0.83	0.81
NPV	1.00	0.93	0.97

Table 23. Performance characteristics of BS, PET/CT and WB-MRI.

Discussion

The results from this study show that both WB-MRI and ^{18}F-choline-PET/CT detected more positive bony metastatic (M1b) lesions than BS with 8, 6 and 3 positive lesions respectively. Indeed, for M1b disease, WB-MRI was shown to have the highest sensitivity of all modalities: 0.90 vs. 0.80 for ^{18}F-choline-PET/CT and 0.60 for BS with specificities of 0.88, 0.92 and 1.00 respectively. A meta-analysis which compared the diagnostic accuracy of BS, ^{18}F-choline-PET/CT and WB-MRI for the detection of bone metastases confirmed superior sensitivity of cross sectional imaging over BS with respective pooled sensitivities and specificities of 0.97/0.95, 0.91/0.99, and 0.79/0.82 for WB-MRI, ^{18}F-choline-PET/CT and BS (112). This high sensitivity is likely explained by the sensitivity of DWI sequences to small changes in tissue microstructure, which

can be detected in the early cellular phase of a metastasis, before a sclerotic reaction has been effected (306).

Our results also show high and very similar sensitivities/specificities of WB-MRI and PET/CT for detection of nodal disease, with values of 1.00/0.96 and 1.00/0.82 for N1 disease and 0.75/0.93 and 0.75/0.92 for M1a disease respectively. In this way, both modalities appear more accurate than conventional CT, with meta-analysis (113) reporting pooled sensitivities and specificities of 0.42/0.82, in comparison with 0.49/0.95 for choline PET/CT (115). WB-MRI studies which incorporate diffusion into scanning protocols report a variable sensitivity ranging from 0.17(136) to 0.73(137). Whilst both of these studies used extended ePLND as the reference standard, the study with the lower sensitivity selected b-values of 0 and 100s/mm^2, which emphasizes the need for optimised scanning technique. In concordance with the findings of our study, the specificity of WB-MRI for nodal detection is thought to be high, with a limited number of studies quoting values ranging from 86%(137) to 98%(139).

The LSR paradigm allowed the incremental value of additional sequences to be assessed, whereby adding T2W and post-contrast mDixon sequences did not improve ROC-AUC significantly. These results can be used to improve the efficiency of WB-MRI in research and clinical practice. For example, performing mDixon + DWI would save 10min of reporting time; 20min scan time and avoid the need for cannulation and Gadolinium administration. Furthermore, as suggested by MET-RADS-P (307), use of 2 b-values rather than 4 could be sufficient - especially for primary staging purposes, which would reduce scan time by a further 25 min. In these consensus guidelines based on expert opinion, WB-Dixon and DWI combined with whole spine T1 and STIR were recommended, meaning our findings support a similar scanning protocol.

Complete coverage of the body has been both suggested (144,307) and deemed unnecessary (145), perhaps exacerbated by uncertainty regarding disease distribution in the PSA screening era. Since no lesions were detected below the knee or extravertebral lesions above the diaphragm, including the below the knee may be unnecessary and a spinal MRI above the diaphragm may be satisfactory, which is in keeping with the findings of another study (145). Here, in all 60 patients with high-risk prostate cancer, it was shown that peripheral metastases always occurred in combination vertebral metastases, and that no metastases were seen below the knee. With further confirmatory work, scanning the abdomen, pelvis and femora using mDixon and DWI at 2 b-values paired with a whole spine MRI as a routine staging

examination would have approximately 700 images, vs. 12 000 images per patient in the present study. Reducing number of images is also likely to improve interobserver concordance, which was 'substantial' for N1 and M1a disease (κ=0.79 and 0.68 respectively), but 'moderate' for M1b (0.58).

The limitations of this study include patient number, its single centre nature and a low number of positive cases. Whilst incorporation bias likely gave rise to the high values of sensitivity and specificity (vs. PLND as a nodal reference standard), it would not have been practical or ethically acceptable to perform nodal dissection for the purposes of the study, and selecting patients who are undergoing PLND would incur spectrum bias.

We chose to use a reference standard that was based around follow-up MRI, rather than best value comparator (BVC) alternatives that rely upon other imaging tests with limited performance characteristics. Whilst TP were assigned without follow-up imaging when BS and MRI were concordant due to the high specificity of BS in the context of prostate cancer, we did not assign TN without MRI follow-up, since genuine lack of sensitivity i.e. FN results on both modalities is also possible. Another potential strength of the scanning protocol was its vertex-to-feet nature enabling direct comparison with BS, and assessment for possible lesions outside of the field-of-view for PET/CT. Whole-body cross-sectional studies regarding disease distribution in the PSA screening era are also welcome since the disease distribution in prostate cancer was best characterised by an autopsy study prior to PSA screening, which did not routinely examine the peripheral skeleton (97).

Further work should be carried out in multicentre trials where economic and clinical utility could also be considered. Since prostate-specific membrane antigen (PSMA) PET-CT is gaining popularity as a staging tool (308–310), a similar study comparing the diagnostic accuracy of modalities would also be of significant interest, but could not be performed for the present study since PSMA was not available in the UK until 2016. Indeed the findings of this study are not limited to WB-MRI, and could be used to inform rational PET-MRI protocols, or design dedicated similar studies for this purpose.

Conclusion

WB-MRI provides high levels of interobserver concordance, intermodality concordance and diagnostic accuracy for both nodal and metastatic bone disease, with higher levels of sensitivity than BS for metastatic disease, and similar performance to PET/CT overall. T2W and post contrast mDixon also have no significant additive value above

mDixon and DWI alone.

Summary

- The primary staging of extraprostatic disease is an important clinical problem but currently hinges upon the inaccurate techniques of CT and BS.
- In this chapter, the interobserver concordance and diagnostic accuracy of WB-MRI was assessed for comparison with BS and choline PET/CT.
- The interobserver concordance of WB-MRI was shown to be high.
- Diagnostic accuracy (sensitivity, specificity, PPV and NPV) levels of WB-MRI were very similar to PET/CT, and could be achieved using a protocol comprised of T1W Dixon and DWI sequences alone.

9 WHOLE BODY MRI AS A STAGING MODALITY IN BIOCHEMICAL FAILURE FOLLOWING RADICAL PROSTATECTOMY

Author declaration

PROPS is a multicentre, multinational study based at 10 sites over 3 continents. UK ethical permission was carried out by Dr Sue Chua at the Royal Marsden Hospital (REC London – Chelsea, reference 14/LO/1587). Patients were recruited locally at each site. Scanning protocols at all sites were optimised Dr Alan Bainbridge and myself. All of the work in this chapter was conceived, written and statistically analysed by me peronally, under the supervision of Dr. Shonit Punwani. Drs. Shonit Punwani, Harbir Sidhu and Nina Tunariu acted as the MRI readers and completed the MRI CRFs. Prof. Rod Hicks, from Peter McCallum Cancer Centre completed the central PET reads.

Introduction

Having established that WB-MRI achieved high levels of diagnostic accuracy achievable using T1W and DWI in the context of primary prostate cancer, I wish to apply a similar scanning protocol to stage suspected recurrence following radical prostatectomy (RP), as this remains essentially undefined.

Staging in this context represents an unmet clinical need because whilst biochemical failure is defined by the American Urological Association as a PSA≥0.2 with a subsequent confirmatory PSA of ≥0.2ng/ml (311), BS and CT are unlikely to be positive until PSA levels exceed 10ng/ml (312,313) and choline PET/CT is only sensitive when PSA levels exceed 1.0 - 5ng/ml(314,315). More sensitive imaging techniques that can detect the site of recurrence would we welcome and could rationalise clinical management in the 20 – 40 % of patients that develop suspected recurrence in this context (316). For example, salvage radiotherapy (RT) may be targeted to the site of local or nodal recurrence, or avoided in the case of extrapelvic metastatic disease. Specifically, higher sensitivity may be achieved by whole-body DWI which commonly has an in plane spatial resolution of 1- 2mm vs. PET which is limited to 5mm isotropically (121).

Whilst multicentre trials provide a higher level of evidence than single centre studies (81),considerations regarding image quality in WB-MRI have not yet been reported, and its interobserver agreement in suspected recurrence remains uncertain (317).

The aim of the present study is to evaluate the image quality, interobserver agreement and diagnostic accuracy of WB-MRI in the context of biochemical failure following radical prostatectomy in a multicentre, multinational study carried out over 3 continents (Australia, USA and Europe).

Materials and methods

This prospective multicentre, multinational cohort study was carried out at seven sites between September 2014 and February 2017. IRBs based in each country (Australia, Canada, United Kingdom) granted ethical approval of the study protocol. Patients were identified in range of settings including MDT meetings, outpatient clinics and through patient referrals for imaging studies. Written informed consent was obtained for each participant. 86 men with a median age of 65.2 (IQR 56.6 – 71.1) were consecutively selected.

Inclusion criteria were: i) men with suspected recurrent prostate cancer following previous radical prostatectomy ii) being considered for salvage radiotherapy iii) ^{99m}Tc bone scan and abdominopelvic CT within 12 weeks of enrolment negative or equivocal for metastatic disease in bone, viscera or lymph nodes iv) N0 or NX on basis of original prostatectomy v) PSA ≥ 0.2ng/mL vi) Documented PSA rise measured on 3 occasions vii) at least one adverse feature of: current PSA $\geq$ 1.0, initial Gleason Grade $\geq$ 8, positive surgical margin, pT3b, PSA doubling time (PSAdt) $\leq$ 10 months. Exclusion criteria were: i) significant sarcomatoid or spindle cell or neuroendocrine small cell components ii) proven metastatic disease iii) evidence of unequivocal disease outside the prostate bed on conventional imaging iv) refusing salvage prostate bed radiotherapy v) ADT within 6 months prior to enrolment.

A paired study design was implemented, whereby patients underwent both ^{18}F-FCH PET/CT and WB-MRI examinations. The diagnostic accuracy of choline PET/CT was the primary outcome measure and will be reported separately.

WB-MRI protocol

All patients underwent mDixon or T1W and axial DWI at 1.5 or 3 Tesla (T) using gradients of b=50 and 1000 s/mm^2. Coverage was from skull base to mid thighs for both sequences. For T1WI, precontrast fat saturated volume interpolated GE imaging (3D) was performed and a Dixon based technique was preferred. Imaging was performed either in the coronal plane using an isotropic image resolution of 2 or 3 mm adjusted to allow a maximum breath-hold time for acquisition time of 20s per station, or in the axial plane with a 5mm slice thickness. For DWI, any fat saturation technique could be used with a slice thickness of 5 to 7mm. Full details of MR scanners and acquisition protocols are provided in tables 24 to 26.

Site	Field strength (T)	Manufacturer	Model	Number of scans
1	1.5	Siemens	Aera	20
2	3	Siemens	Skyra	16
3	3	Siemens	Biograph	13
6	1.5	Philips	Ingenia	9
7	3	Siemens	Trio tim	8
9	1.5	Siemens	Aera	1
10	3	Siemens	Skyra	19

Table 24. Details of machines and scans performed at each site.

Site	Plane	Sequence	S	Slice mm	SS mm	TR (ms)	TE (ms)	FA	BW (Hz/p)	AM	RM	Pixel spacing	FoV (cm)	PE	Time (min)
1	Coronal	Dixon	3	2	2.2	6.23	2.39/4.77	10	605	192 x 134	175 x 497	2.19 x 2.19	42 x 105	Row	6
2	Axial	Dixon	3	5	5	3.86	1.23/2.46	9	1085	256 x 230	258 x 735	1.56 x 1.56	40 x 115	Row	6
3	Coronal	Dixon	3	3	3.1	3.6	1.23/2.46	10	965	192 x 192	192 x 430	1.98 x 1.98	50 x 112	Row	9
6	Coronal	Dixon	3	3	1.5	6.23	2.39/4.77	15	618	280 x 277	560 x 560	0.99 x 0.99	55 x 100	Row	7
7	Coronal	T1	2	3	3	4.28	2.45	11	651	256 x 243	256 x 483	1.95 x 1.95	50 x 94	Row	5
9	Coronal	Dixon	2	2.8	2.8	7.63	2.39/4.77	14	400	160 x 120	160 x 375	2.81 x 2.81	45 x 105	Row	7
10	Coronal	Dixon	3	2	2	4.02	2.46/1.23	9	750	256 x 256	258 x 610	1.88 x 1.88	50 x 110	Row	8

Table 25. MR acquisition protocols performed for T1WI.

S =number of stations, SS = slice spacing, AM = acquisition matrix, RM = reconstruction matrix, PE = phase encode direction.

Site	Stations	Slice mm	SS	TI	TR	TE	FA	ETL	BW (Hz/p)	AM	RM	Pixel spacing	FoV (cm)	NEX	PE	FS	Time (min)
1	4	5	5	180	13400	69	90	55	2300	128 x 128	384 x 384	1.68 x 1.68	43 x 43	2	Col	STIR	20
2	3	5	5	230	18900	60	90	48	2055	128 x 128	192 x 192	2.03 x 2.03	40 x 40	2	Col	STIR	18
3	4	6	6.6	220	13500	78	90	1	2131	138 x 136	276 x 272	1.38 x 1.38	38 x 38	4	Col	STIR	44
6	4	6	6	180	7754	92	90	77	2079	169 x 164	336 x 336	1.48 x 1.48	50 x 50	1	Col	STIR	22
7	6	7	9.1	248	6300	77	90	1	2003	192 x 192	228 x 228	1.74 x 1.74	50 x 50	4	Col	STIR	17
9	5	5	5	180	10600	66	90	51	1955	128 x 104	256 x 208	1.12 x 1.12	30 x 40	6	Col	STIR	20
10	5	6	6	-	7200	77	90	71	1530	192 x 192	192 x 193	2.50 x 2.50	45 x 45	4	Col	CHESS	19

Table 26. MR acquisition protocols performed for DWI.

Note. FS = fat saturation

Datasets were uploaded onto an online repository and downloaded by a designated central MRI site for preparation into single image stacks prior to review.

^{18}F-choline-PET/CT protocol

Patients underwent dynamic pelvic and WB-^{18}F-choline-PET/CT imaging 60 minutes after intravenous administration of [^{18}F]-fluoromethyl-choline (3.6 MBq/kg to a maximum of 400MBq at time of injection). A low-dose unenhanced WB-CT scan was initially performed for attenuation correction and image fusion with coverage from skull base to proximal thighs in the supine position. Dynamic scans frames were acquired at 4 x 30s, 4 x 1min and 2 x 2min, after which time the whole-body PET acquisition was acquired towards the head. Full acquisition parameters for each site are provided in table 27.

Site	Vendor	Model	DR	kVp	mA	RT (s)	Matrix	Slice mm	ToF
1	Philips	Ingenuity TF	128	120	83	0.5	512 x 512	4	Yes
2	Siemens	Biograph 6	6	110	90	0.8	512 x 512	4	No
3	GE	Discovery STE	16	140	31	0.5	512 x 512	3.75	No
6	Philips	Ingenuity TF	128	120	83	0.5	512 x 512	5	Yes
7	GE	Discovery STE	16	140	132	0.5	512 x 512	3.75	No
9	Philips	Gemini TF	64	120	46	0.5	512 x 512	5	Yes
10	Siemens	Biograph 40	40	120	92	0.5	512 x 512	3	No

Table 27. ^{18}F-choline-PET/CT acquisition protocols

DR = number of detector rows, kVp = peak kilovoltage, RT = rotation time, ToF = time of flight

Treatment protocols

Patients either underwent i) no treatment, ii) conformal or intensity modulated (IM) RT to the prostate bed +/- pelvic lymph nodes, commenced within 6 weeks of enrolment, iii) ADT iv) combination therapy of RT and ADT, according to institutional guidelines/physician discretion and with awareness of the PET/CT findings.

WB-MRI review

A board certified radiologist (SP with 12 years experience) reviewed anonymised MR datasets using Osirix workstations (Pixmeo, Bernex, Switzerland), blinded to all clinical and imaging results. A CRF was completed which included assessment of image quality and suspicion of nodal and metastatic disease. Overall image quality was scored for each imaged region (head, neck, thorax, abdomen, pelvis, thigh) using a 1 – 5 ordinal scale modified from (293,294,318) (1= uninterpretable, non-diagnostic 2 = poor, non-diagnostic, 3= acceptable for diagnosis, 4 = good, 5 = excellent) for both T1WI and DWI sequences.

To record the suspicion of nodal and metastatic disease, the body was divided into 9 nodal regions (external iliac, internal iliac, common iliac, paraaortic, presacral, other abdominal, inguinal, thoracic and neck) using standard anatomic definitions. 10 skeletal sites were assessed (skull, cervical spine, thoracic spine, lumbar spine, pelvis, sternum, clavicle/scapula, ribs, upper limb and lower limb), as were 8 soft tissue sites (brain, lung, pleura, liver, adrenal, mesenteric, soft tissue and other). A 1 – 4 ordinal scale (1 - likely / definitely benign, 2 - probably benign, 3-probably malignant, 4- likely/ definitely malignant) was used to score the suspicion of disease at each site (56). The most likely nodal and metastatic cancer stage was then assigned according to the AJCC 'TNM' 7th edition staging system, namely N0/N1, M1a/M1b/M1c (101). A second board certified radiologist (NT, with 9 years experience) independently reviewed 40 datasets, and completed the same CRF for the assessment of interobserver agreement.

^{18}F-choline-PET/CT review

The suspicion of nodal and metastatic disease was recorded using a binary scale (positive/negative) for the same sites as the WB-MRI, using the 'TNM' 7 staging system by a central reader with 16 years of experience of PET/CT (RH).

Statistical methods

Data were analysed using SPSS Statistics version 23 (2015, IBM, NY, USA) and GraphPad Prism version 6 (2014, San Jolla, CA, USA). Statistical significance was set at $p<0.05$ and data were checked for normality using the Shapiro-Wilk test.

A flow diagram of the statistical methods is shown in figure 71.

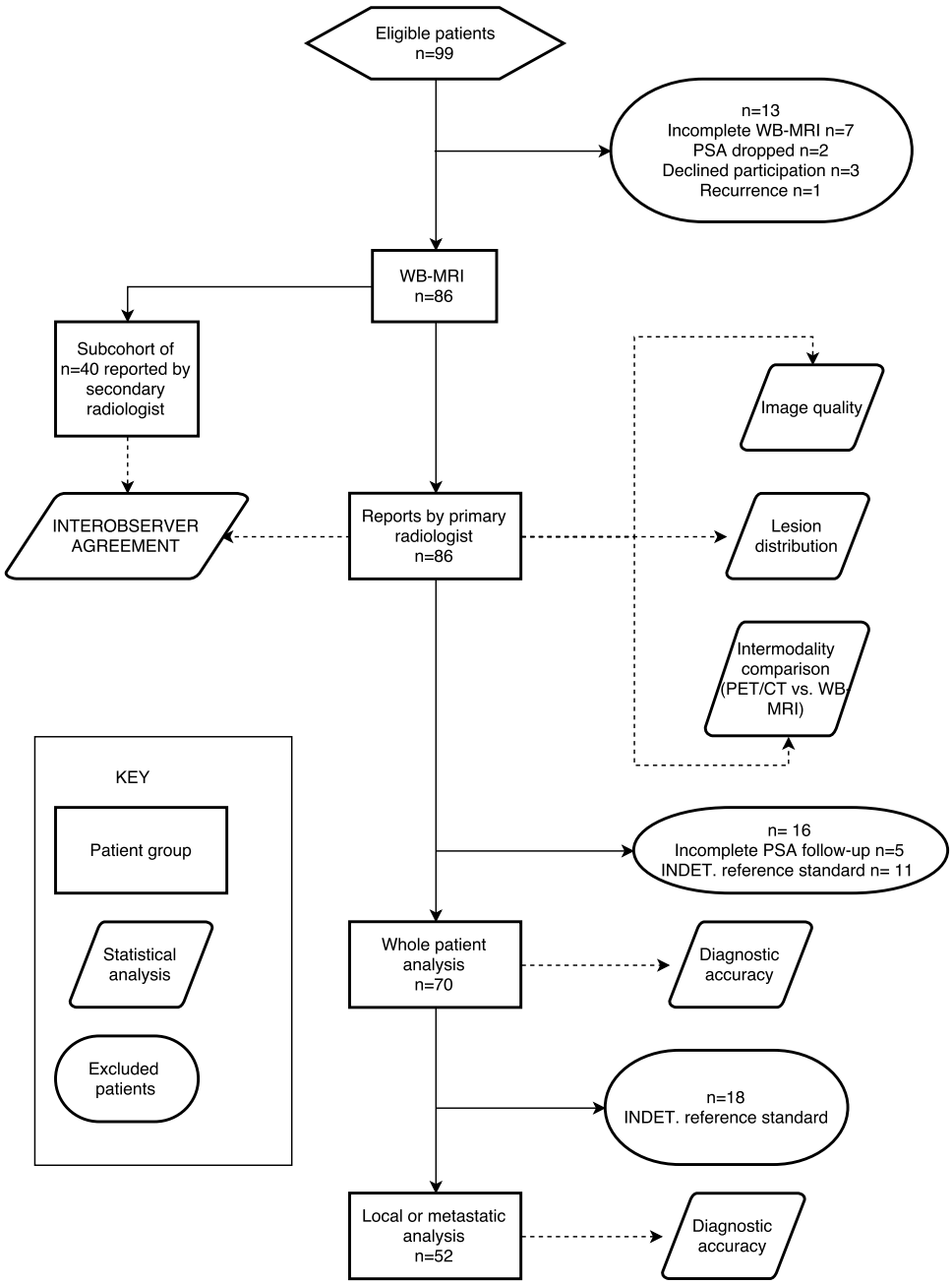

Figure 71. Patient recruitment flow diagram and the formation of 3 separate cohorts for statistical analysis.

INDET = indeterminate

The following statistics were used to assess image quality in all patients (n=86):

- Comparison of the mean overall image quality of all anatomical regions for T1WI vs. DWI using Wilcoxon matched pairs testing.

- Comparison of overall image quality of each anatomical region for T1WI and DWI using Friedman's test with Dunn's multiple comparison correction.

- Comparison of T1WI and DWI sequences across different sites using Kruskal-Wallis testing and Dunn's multiple comparisons correction.

For the suspicion of disease, the following analyses were carried out:

- The distribution of positive lesions (3/4) on both WB-MRI and ^{18}F-choline-PET/CT according to 'TNM' stage (n=86).

- Interobserver agreement of WB-MRI using percentage agreement for each 'TNM' stage (n=40).

- Intermodality percentage agreement of WB-MRI and ^{18}F-choline-PET/CT for each 'TNM' stage (n=86). Cohen's κ was not used due to the low numbers of positive sites, giving rise to a prevalence effect (319) which causes κ to fall considerably.

Measures of diagnostic accuracy for WB-MRI and ^{18}F-choline-PET/CT were calculated using two different methods. The first analysis (in 70 patients) considered the 'whole patient' accuracy of each test (positive/negative for the presence of any disease) and the second analysis (in 52 patients) considered the presence of local (prostate bed) or metastatic (N1/M1a/M1b/M1c) disease.

Whilst reference standards were slightly different for each analysis, both reference standards were based on a combination of tissue biopsy (if performed) and PSA follow-up at three, six, nine and twelve months. Flow diagrams of the reference standards for whole patient analysis and local/metastatic analysis are given in figure 72 and 73 respectively. Decisions regarding lesion biopsy were based on local protocols the results of the PET/CT (as clinicians were kept blind to WB-MRI results). PSA treatment failure was defined as a PSA level of ≥0.2ng/ml above the nadir, followed by a higher value or a single value ≥0.5ng/ml (320).

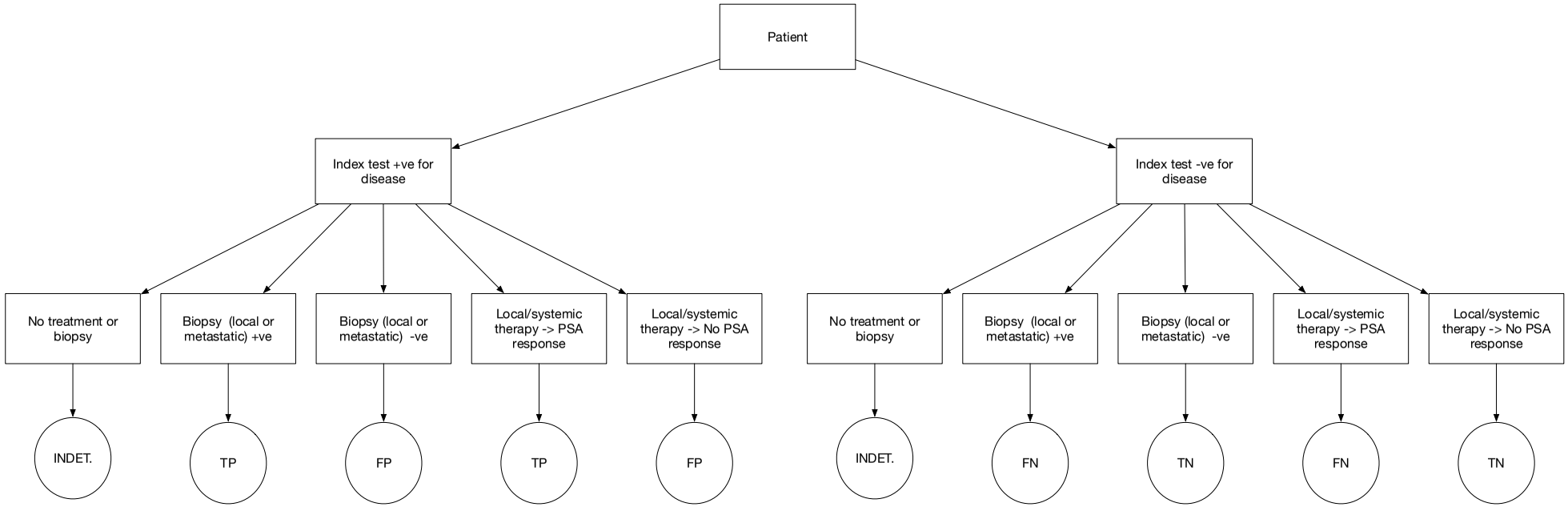

Figure 72. Flow diagram of the reference standard used for whole patient analysis

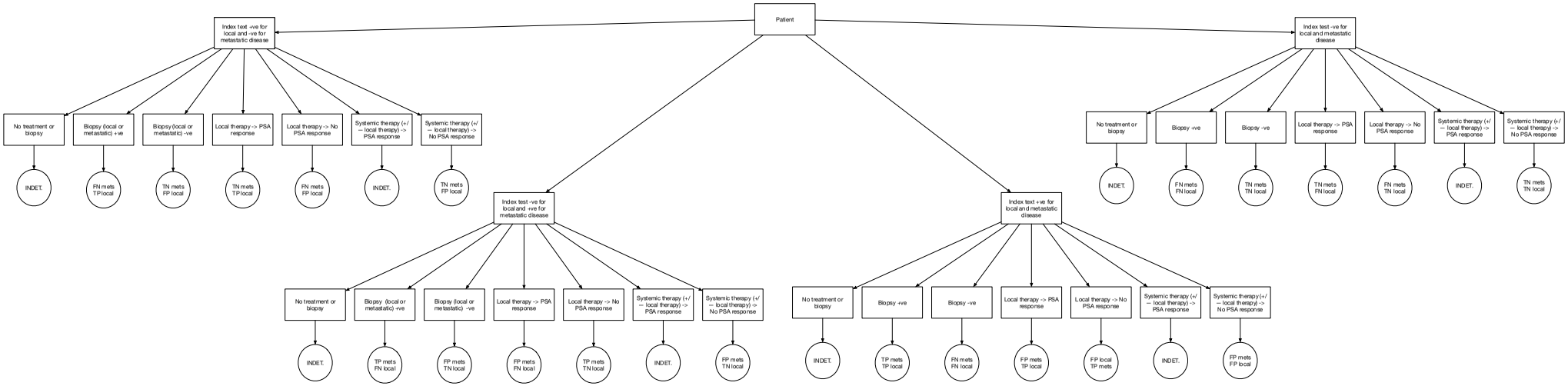

Figure 73. Flow diagram of the reference standard used for local/metastatic disease analysis

The following statistics of diagnostic accuracy were then calculated:

- The diagnostic accuracy of WB-MRI and ^{18}F-choline-PET/CT vs. each reference standard (sensitivity, specificity, positive predictive value (PPV), negative predictive value (NPV)) using a threshold of ≥3 as positive for the WB-MRI.
- ROC-AUC for extrapelvic disease as shown on WB-MRI by applying thresholds for each level of suspicion (1 – 4) of disease presence. Youden's index (305) was used to calculate the optimal cut-off of highest diagnostic accuracy.

Results

Descriptive data for patient baseline characteristics are shown in table 28.

Attribute (n=86)	
Age (yrs): median, IQR	65.2 (56.6 – 71.1)
Baseline PSA (ng/ml): median, IQR	0.44 (0.29 – 1.09)
PSAdt (months): median, IQR	3.99 (3.00 – 6.98)
Gleason score	
N/A	48
6	0
7	13 (34.2%)
8	12 (31.6%)
9	13 (34.2%)
10	0
pT2a	3 (3.5%)
pT2b	5 (5.8%)
pT2c	24 (27.9%)
pT3a	32 (37.2%)
pT3b	22 (25.5%)
pT4	0
Surgical margin positive	26
Negative	60
Seminal vesicles positive	22
Negative	64
Treatment strategy	
None	15
ADT only	5
Pelvic RT only	39
Pelvic and nodal RT only	2
ADT + RT	25

Table 28. Baseline patient characteristics.

The mean time interval between ^{18}F-choline-PET/CT and WB-MRI was 2.4 months (SD: 13.52). The mean time interval between prostatectomy and WB-MRI was 2.87 years (SD: 2.79).

Image quality

A comparison of T1 and DWI image quality for the mean of all anatomical regions is shown in figure 74, with the results of the Wilcoxon matched pairs test also indicated. The mean score of T1W sequences was 4.28 (SD: 0.50) vs. 3.58 (SD: 0.37) for DWI.

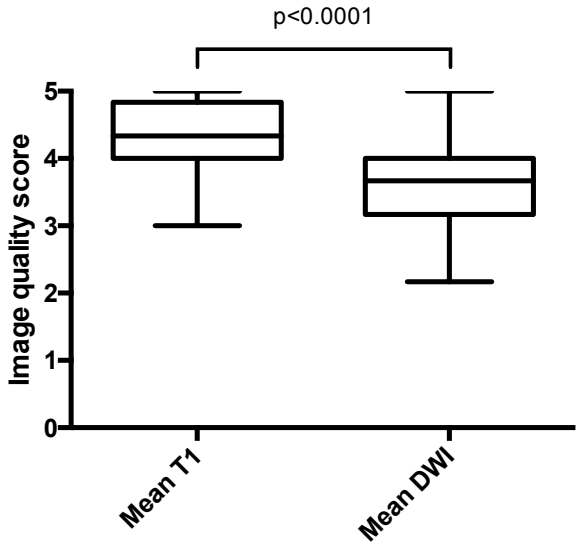

Figure 74.Comparison of overall image quality for T1WI vs. DWI.

The mean image quality of each anatomical region for both T1 and DWI is shown in table 29.

	T1WI	DWI
Head	4.54	3.92
Neck	4.44	3.44
Thorax	3.79	3.40
Abdomen	4.13	3.55
Pelvis	4.27	3.56
Thigh	4.48	3.72

Table 29. Mean image quality of each anatomical region.

Friedman's testing showed the thorax had significantly lower image quality than the head ($p<0.0001$), neck ($p<0.0001$), abdomen ($p=0.009$), pelvis ($p=0.0001$) and thigh ($p<0.0001$), with the abdomen vs. thigh also achieving statistical significance ($p=0.02$).

For DWI, the head had statistically higher values than the neck (p=0.005), thorax (p<0.0001), abdomen (p=0.01) and pelvis (p=0.03). The thorax and thigh also reached statistical significance than the thigh (p=0.01).

The mean image quality of T1WI and DWI sequences across centres are shown in figure 75, with significant differences following Kruskal-Wallis testing with Dunn's multiple comparison correction indicated.

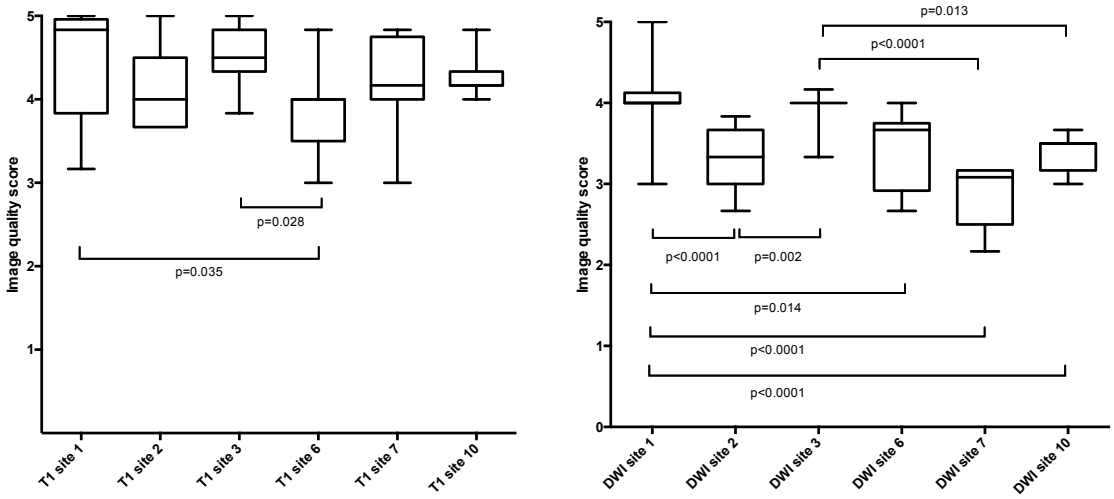

Figure 75. Image quality of T1WI and DWI scans performed at each site.

Distribution and agreement of suspected disease

The distribution of probable disease (defined as a suspicion ≥3 for WB-MRI) is shown in table 30 for both WB-MRI and ^{18}F-choline-PET/CT.

	PET/CT (n=86)	WB-MRI (n=86)
Local	9/86 (10.5%)	8/86 (9.3%)
N0	65/86 (75.6%)	78/86 (90.7%)
N1	16/86 (18.6%)	8/86 (9.3%)
M0	78/86 (90.7%)	78/86 (90.1%)
M1a	6/86 (7.0%)	3/86 (3.5%)
M1b	2/86 (2.3%)	5/86 (5.8%)
M1c	1/86 (1.2%)	0/86 (0.0%)

Table 30. Distribution of lesions on each staging modality

The results of interobserver and intermodality agreement are presented in table 31.

	Local nodes (N1)	Metastatic nodes (M1a)	Metastatic bones (M1b)	Metastatic soft tissue (M1c)
Interobserver percentage agreement	87.5% (35/40)	97.5% (39/40)	97.5% (39/40)	100% (40/40)
Intermodality percentage agreement	82.6% (71/86)	93.0% (80/86)	94.2% (81/86)	98.8% (85/86)

Table 31. Interobserver and intermodality agreement

Diagnostic accuracy of WB-MRI and PET/CT

The performance characteristics of WB-MRI and ^{18}F-choline-PET/CT vs. the reference standards are shown in table 32 for whole patient and local/metastatic analyses.

	Whole patient (n=70)	Local disease (n=52)	Metastatic disease (n=52)
PET/CT			
Sensitivity	0.37 (22/60)	0.06 (2/30)	0.55 (10/18)
Specificity	0.80 (8/10)	1.00 (15/15)	0.85 (28/33)
PPV	0.91(22/24)	1.00 (2/2)	0.66 (10/15)
NPV	0.17 (8/46)	0.35 (15/43)	0.78 (28/36)
WB-MRI			
Sensitivity	0.27 (5/18)	0.13 (4/30)	0.28 (5/18)
Specificity	0.90 (9/10)	0.94 (15/16)	0.94 (32/34)
PPV	0.94 (16/17)	0.80 (4/5)	0.71 (5/7)
NPV	0.17 (9/53)	0.37 (15/41)	0.71 (32/45)

Table 32. Performance characteristics of each staging modality for whole patient and local/metastatic analyses

For extrapelvic disease, the ROC-AUC was 0.65 (95%CI 0.48 – 0.80) for WB-MRI, whereby the optimal suspicion threshold according to Youden's index was 2/4, with values of 0.56 and 0.73 for sensitivity and specificity respectively. In comparison, ^{18}F-choline-PET/CT had a sensitivity and specificity of 0.50 and 0.79 respectively.

Discussion

Whilst PET/CT has been recommended for use as a staging modality in cases of biochemical recurrence with a PSA >1ng/ml(107), its use is limited by availability, cost and ionizing radiation exposure and has low sensitivity at lower PSA levels. Whilst WB-MRI offers a potential solution to such problems, issues surrounding image quality, interobserver agreement and diagnostic accuracy need to be elucidated.

Image quality in multicentre studies is important since suboptimal scanning protocols may compromise diagnostic performance. The observation that the overall image quality of T1WI sequences was significantly higher than DWI is perhaps unsurprising since the latter are acquired using EPI acquisitions, which are more prone to artefacts such as distortion and ghosting. We also found that image quality can differ significantly between centres for both sequences, and were again more pronounced for diffusion sequences. This emphasizes the importance of effective protocol optimisation in WB-MRI practice whereby the number technical false errors due to suboptimal image quality can be reduced. The finding that image quality varies between stations, and is specifically lower in the thorax vs. the head, which is likely to be due to lower SNR and movement artefact associated with cardiac motion, chest wall and diaphragmatic excursion. Poorer image quality in the neck and shoulder stations is consistently found with diffusion-weighted sequences (321,322). Such findings are important targets for sequence development and should also be considered when constructing reports, as images are commonly compromised in these regions.

Whilst all disease detected on ^{18}F-choline-PET/CT and WB-MRI in the present study was occult on BS and abdominopelvic CT, the majority of patients still had negative examinations. This low incidence of possible nodal and osseous metastases (9 and 6% respectively) is comparable to the findings of Robertson et al., who in the only paper to date concerning the diagnostic accuracy of WB-MRI in biochemical failure following prostatectomy quoted figures of 8 and 9% (323).

Interobserver agreement was high for both local nodal and M1a disease (≥85%) for all sites according to the 'TNM' staging system. Even higher levels have been reported in the context of primary staging (94%) (299), which could be due to greater levels of experience with the technique in this setting.

Since this was a multicentre study, the findings are highly generalizable and its paired design whereby patients underwent both WB-MRI and ^{18}F-choline-PET/CT means the

power is higher than for independent sampling(324). On the whole patient level, both PET/CT and WB-MRI had a similar low sensitivity but high specificity for disease presence. Whilst the whole patient sensitivity of ^{18}F-choline-PET/CT (37%) was lower in this study than that quoted in a recent meta-analysis in biochemical failure of 75.4% (95%CI: 66.9% - 82.6%), the median PSA level in the present study was lower than most studies (325–329), whereby PSA level has been shown to strongly increase diagnostic yield (117,330). The similar performance of WB-MRI suggests the technique is also influenced by PSA level and has not yet closed the gap between the definitions used for biochemical failure and the pinpointing of the source of PSA rise. Whilst groups have advocated rationalising scans to patients with PSA >1ng/ml, the present study confirms that nodal and osseous metastases do still occur in patients with low PSA levels, and imaging could potentially change management in these patients, which should act as a stimulus for further research into developing more sensitive techniques.

The lower sensitivity of WB-MRI vs. ^{18}F-choline-PET/CT for extrapelvic disease (0.28 vs. 0.55) may be a genuine finding, or could also be explained by the perceptual error of a single observer, which is supported fact that optimal performance was obtained when a threshold of ≥2/4 as positive was used. The training effect of observers reporting WB-MRI in this context will be the subject of further work.

The present study builds upon the work of Robertson and colleagues (317) by increasing the number of cases in a prospective study with multiple scanners, field strengths and paired examinations with choline PET/CT (rather than FDG). We also chose to use a biopsy and PSA-based reference standard to calculate sensitivity and specificity, as opposed to follow-up imaging as such reference standards would be subject to incorporation bias.

We acknowledge a number of limitations in the present study. Firstly, since the primary outcome measure was choline PET/CT, recruitment for adequate WB-MRI examinations fell slightly short of the 90 cases that were required to achieve a type I error rate of 5% and a type II error rate of 20%. Secondly, secondary lymphadenectomy + bone biopsy would have been preferable to the reference standard used. However, this does not represent standard practice in any of our institutions, and would have made ethical approval difficult. Where biopsy was not performed, reliance upon PSA kinetics suffers from a lack of agreed consensus to define treatment response and could impact upon the apparent diagnostic test performance.

The impact of individual pulse sequences on diagnostic performance, confirmation of the impact of baseline PSA level on diagnostic yield and clinical utility studies regarding the impact on patient management should all be the subject of further work, as should the utility of mp-prostate MRI to stage local disease in combination with emerging techniques such as PSMA PET (CT/MRI) for metastases.

Conclusion

The image quality of WB-MRI varies substantially between centres, particularly for diffusion-weighted sequences, which emphasizes the need to optimise sequences carefully prior to establishing a WB-MRI practice. Whilst both ^{18}F-choline-PET/CT and WB-MRI demonstrate superior performance over BS and conventional abdominopelvic CT, with WB-MRI showing 'substantial' interobserver agreement, their sensitivity is still limited at PSA levels below 1ng/ml which may be addressed with further developments such as PSMA PET/MRI.

Summary

- Staging distant disease in the context of biochemical relapse is an important but unsolved clinical problem.
- Whilst this would be best answered by a multinational study, image quality is an issue in such trials.
- In this chapter I studied the image quality and interobserver agreement of WB-MRI, and compared its diagnostic accuracy with choline PET/CT.
- I showed that image quality is variable between centres, scanners and regions of the body with particular heterogeneity for DWI sequences, emphasizing the requirement for careful protocol optimisation for research and clinical studies alike.
- Whilst interobserver agreement for WB-MRI was high, and the diagnostic accuracy was comparable with choline PET/CT, neither modality is sufficient for accurate staging in the context of biochemical relapse at present.

10 THESIS SUMMARY, DISCUSSION AND CONCLUSIONS

In this thesis, I aimed to develop multiple quantitative and semiquantitative magnetic resonance imaging biomarkers, as driven by clinical need, according to the biomarker development roadmap for cancer studies. I have focused upon a number of potential biomarkers ranging from those with a large evidence base (e.g. 'TNM' stage), through conventional mp-MRI to translational techniques such as VERDICT. A broad range of study designs have been intentionally chosen and range from retrospective studies with small patient numbers to prospective single and multicentre studies requiring ethics applications. Following review of the relevant literature and MRI physics to unravel the deficiencies in the current application of MRI to prostate cancer, the aims of my thesis were stated as follows:

1. *'To improve the quality of analytical methods used for quantitative mp-MRI throughout this thesis'.*

This was achieved in chapter 4, where I showed that single slice analysis using Osirix produces slightly more reliable results than volumetric analysis using proprietorial software. I then showed that normalisation to the bladder is preferable to the current convention of using OI, and that histographic metrics are less reproducible than mean values.

Further work could include performing similar studies prospectively using appropriately powered sample size whereby both repeatability and reproducibility should be assessed in a systematic fashion with standardised imaging protocols as should be performed for dedicated quantitative imaging trials.

2. '*To combine components of mp-MRI with clinical parameters in zone-specific predictive models that best predict a Gleason 4 component in known prostate cancers'.*

I achieved this aim in chapter 5, whereby the best preforming LR model in the PZ demonstrated a superior diagnostic accuracy vs. the opinion of experienced radiologists at all diagnostic thresholds at both internal LOO validation and using an external cohort of patients.

Further work could include broader external validation, firstly by using a larger number of patients with the same scanning protocol, then applying the model to other scanners and centres. A clinical validation study would also be of particular interest to see whether such models could be used to improve diagnosis, as the clinical benefit of such models remains undetermined.

3. *'To develop maps from VERDICT prostate MRI as quantitative imaging biomarkers, according to the imaging biomarker roadmap'.*

This aim was addressed in chapters 6 and 7, whereby I used the INNOVATE ethics to study the image quality, metric repeatability and the ability of VERDICT MRI maps to discriminate between different Gleason grades. Here, I showed that whilst VERDICT maps are similar to ADC in terms of image quality and repeatability, early indications show improved estimation of a Gleason 4 component.

Further work is currently underway and considers rigorous biological validation of VERDICT MRI vs. segmented histological correlates and consideration of metric reproducibility across multiple centres.

4. *'To develop WB-MRI using semiquantitative scoring systems for the primary 'TNM' staging of aggressive prostate cancer'.*

I achieved this in chapter 8, where I assess disease status in WB-MRI using a semiquantiative scoring system. I discovered that high levels of diagnostic accuracy could be achieved using a limited protocol of T1 and DWI, which achieved a higher sensitivity than BS and ^{18}F-choline-PET/CT for the detection of bone metastases. The interobserver agreement of WB-MRI was also found to be 'moderate' to 'substantial'.

Opportunities for further work include increasing patient number, selecting cases that are known to have positive nodal or bony disease, carrying out a multicentre study, and using a PLND based reference standard. Scanning protocols could also be refined as a result of this work and performance characteristics compared with new emerging techniques such as PSMA PET and superparamagnetic iron oxide.

5. *'To assess the value of WB-MRI vs. ^{18}F-choline PET/CT in combination with a semiquantitative scoring system for staging patients with biochemical failure following radical prostatectomy in a multicentre, multivendor, multinational study'*

This was achieved in chapter 9, where I discovered that the image quality in WB-MRI is variable between sequences, anatomical regions and centres, suggesting rigorous protocol optimisation is an important aspect of practice in WB-MRI. Whilst the interobserver agreement was 'substantial', the sensitivity of WB-MRI was found to be similarly low as for ^{18}F-choline-PET/CT, and is likely to depend on the PSA level of the patient in a similar fashion as it does for PET/CT.

Further work could include the assessment whether perceptual FN may be reduced by radiologist training, the assessment of the impact of combining mp-prostate MRI and emerging techniques such as PSMA PET/CT on diagnostic accuracy. The effect of PSA level on scanning yield should also be clarified in this context, as it has been for PET/CT, as should consideration into the clinical utility of the technique, by way of changing patient management. Finally, semiquantitative scoring systems in WB-MRI should be validated prospectively, potentially identifying specific diagnostic features that should suggest a particular score, as has been carried out with BI-RADS.

References

1. Mcneal JE. The Zonal Anatomy of the. Prostate. 1981;2:35–49.
2. Hricak H, Dooms GC, McNeal JE, et al. MR imaging of the prostate gland: normal anatomy. AJR Am J Roentgenol. 1987;148:51–58.
3. Ayala AG, Ro JY, Babaian R, Troncoso P, Grignon DJ. The prostatic capsule: does it exist? Its importance in the staging and treatment of prostatic carcinoma. Am J Surg Pathol. 1989;13:21–27http://www.ncbi.nlm.nih.gov/pubmed/2909195. Accessed May 22, 2016.
4. Bilhim T, Tinto HR, Fernandes L, Martins Pisco J. Radiological Anatomy of Prostatic Arteries. Tech Vasc Interv Radiol. 2012;15:276–285.
5. Helpap GAB. The Prostate. Georg Thieme Verlag. 1998. p. 82 (vii, 82 pages)http://www.isbnplus.com/313104781X. Accessed May 23, 2016.
6. Hayward SW, Cunha GR. The prostate: development and physiology. Radiol Clin North Am. 2000;38:1–14.
7. McNeal JE. Normal histology of the prostate. Am J Surg Pathol. 1988;12:619–633http://www.ncbi.nlm.nih.gov/pubmed/2456702. Accessed January 9, 2016.
8. Cheng GTML. Atlas of Genitourinary Pathology. Springer-Verlag London. 2011. p. XXVIII, 404http://www.springer.com/la/book/9781848823945. Accessed May 23, 2016.
9. Shapiro E, Becich MJ, Hartanto V, Lepor H. The relative proportion of stromal and epithelial hyperplasia is related to the development of symptomatic benign prostate hyperplasia. J Urol. 1992;147:1293–1297http://www.ncbi.nlm.nih.gov/pubmed/1373778. Accessed May 23, 2016.
10. Cancer Research UK. Prostate cancer statistics. http://www.cancerresearchuk.org/health-professional/cancer-statistics/statistics-by-cancer-type/prostate-cancer. Accessed May 23, 2016.
11. Grönberg H. Prostate cancer epidemiology. Lancet (London, England). 2003;361:859–864.
12. Sakr WA, Haas GP, Cassin BF, Pontes JE, Crissman JD. The frequency of carcinoma and intraepithelial neoplasia of the prostate in young male patients. J Urol. 1993;150:379–385http://www.ncbi.nlm.nih.gov/pubmed/8326560. Accessed May 23, 2016.
13. Abate-Shen C, Shen MM. Mouse models of prostate carcinogenesis. Trends Genet. Humana Press; 2002;18:S1-5http://www.ncbi.nlm.nih.gov/pubmed/12047956. Accessed May 6, 2017.
14. McNeal JE, Redwine EA, Freiha FS, Stamey TA. Zonal distribution of prostatic adenocarcinoma. Correlation with histologic pattern and direction of spread. Am J Surg Pathol. 1988;12:897–906http://www.ncbi.nlm.nih.gov/pubmed/3202246. Accessed January 24, 2016.
15. Gleason DF. Classification of prostatic carcinomas. Cancer Chemother Rep. 1966;50:125–128http://www.ncbi.nlm.nih.gov/pubmed/5948714. Accessed January 21, 2015.
16. Humphrey P a. Gleason grading and prognostic factors in carcinoma of the prostate. Mod Pathol. 2004;17:292–306.
17. Epstein JI. Gleason score 2-4 adenocarcinoma of the prostate on needle biopsy: a diagnosis that should not be made. Am J Surg Pathol. 2000;24:477–478http://www.ncbi.nlm.nih.gov/pubmed/10757394. Accessed May 6, 2017.
18. Chatterjee A, Watson G, Myint E, Sved P, McEntee M, Bourne R. Changes in Epithelium, Stroma, and Lumen Space Correlate More Strongly with Gleason Pattern and Are Stronger Predictors of Prostate ADC Changes than Cellularity Metrics. Radiology. 2015;277:751–762http://pubs.rsna.org/doi/10.1148/radiol.2015142414. Accessed November 15, 2016.
19. Langer DL, van der Kwast TH, Evans AJ, et al. Prostate tissue composition and MR measurements: investigating the relationships between ADC, T2, K(trans),

v(e), and corresponding histologic features. Radiology. 2010. p. 485–494.
20. Albertsen PC, Hanley JA, Fine J. 20-year outcomes following conservative management of clinically localized prostate cancer. JAMA. American Medical Association; 2005;293:2095–2101http://jama.jamanetwork.com/article.aspx?articleid=200821. Accessed December 18, 2015.
21. Sauter G, Steurer S, Clauditz TS, et al. Clinical Utility of Quantitative Gleason Grading in Prostate Biopsies and Prostatectomy Specimens. Eur Urol. 2015;1–7http://www.sciencedirect.com/science/article/pii/S030228381501012X.
22. Tomlins SA, Mehra R, Rhodes DR, et al. Integrative molecular concept modeling of prostate cancer progression. Nat Genet. 2007;39:41–51http://www.nature.com/doifinder/10.1038/ng1935.
23. True L, Coleman I, Hawley S, et al. A molecular correlate to the Gleason grading system for prostate adenocarcinoma. Proc Natl Acad Sci U S A. 2006;103:10991–10996http://www.pubmedcentral.nih.gov/articlerender.fcgi?artid=1544162&tool=pmcentrez&rendertype=abstract. Accessed December 18, 2015.
24. Eggener SE, Scardino PT, Walsh PC, et al. Predicting 15-year prostate cancer specific mortality after radical prostatectomy. J Urol. 2011;185:869–875http://www.pubmedcentral.nih.gov/articlerender.fcgi?artid=4058776&tool=pmcentrez&rendertype=abstract. Accessed December 18, 2015.
25. Tefilli M V, Gheiler EL, Tiguert R, et al. Should Gleason score 7 prostate cancer be considered a unique grade category? Urology. 1999;53:372–377http://www.ncbi.nlm.nih.gov/pubmed/9933057.
26. Ahmed HU, Arya M, Freeman A, Emberton M. Do low-grade and low-volume prostate cancers bear the hallmarks of malignancy? Lancet Oncol. Elsevier Ltd; 2012;13:e509-17http://www.ncbi.nlm.nih.gov/pubmed/23117005. Accessed December 10, 2014.
27. Lavery HJ, Droller MJ. Do gleason patterns 3 and 4 prostate cancer represent separate disease states? J Urol. Elsevier Inc.; 2012;188:1667–1675http://dx.doi.org/10.1016/j.juro.2012.07.055.
28. Carter HB, Partin AW, Walsh PC, et al. Gleason score 6 aadenocarcinoma: Should it be labeled as cancer? J Clin Oncol. 2012;30:4294–4296http://www.ncbi.nlm.nih.gov/pubmed/23032616.
29. Ross HM, Kryvenko ON, Cowan JE, Simko JP, Wheeler TM, Epstein JI. Do adenocarcinomas of the prostate with Gleason score (GS) ≤6 have the potential to metastasize to lymph nodes? Am J Surg Pathol. 2012;36:1346–1352http://www.pubmedcentral.nih.gov/articlerender.fcgi?artid=3421030&tool=pmcentrez&rendertype=abstract. Accessed April 5, 2016.
30. Catalona WJ, Smith DS, Ratliff TL, et al. Measurement of prostate-specific antigen in serum as a screening test for prostate cancer. N Engl J Med. Massachusetts Medical Society; 1991;324:1156–1161http://www.nejm.org/doi/full/10.1056/NEJM199104253241702. Accessed March 31, 2016.
31. Smith DS, Catalona WJ. Interexaminer variability of digital rectal examination in detecting prostate cancer. Urology. 1995;45:70–74.
32. Candas B, Cusan L, Gomez JL, et al. Evaluation of prostatic specific antigen and digital rectal examination as screening tests for prostate cancer. Prostate. 2000;45:19–35http://www.ncbi.nlm.nih.gov/pubmed/10960839. Accessed May 23, 2016.
33. Balk SP. Biology of Prostate-Specific Antigen. J Clin Oncol. 2003;21:383–391http://www.jco.org/cgi/doi/10.1200/JCO.2003.02.083. Accessed December 29, 2014.
34. Parimi V, Goyal R, Poropatich K, Yang XJ. Neuroendocrine differentiation of prostate cancer: a review. Am J Clin Exp Urol. 2014;2:273–285http://www.pubmedcentral.nih.gov/articlerender.fcgi?artid=4297323&tool=pmcentrez&rendertype=abstract. Accessed April 13, 2016.

35. Thompson IM, Ankerst DP, Chi C, et al. Operating Characteristics of Prostate-Specific Antigen in Men With an Initial PSA Level of 3 . 0 ng / mL or Lower. 2014;78229.
36. Roobol MJ. Re: PSA Density Improves Prediction of Prostate Cancer. Eur Urol. European Association of Urology; 2014;66:964–965http://linkinghub.elsevier.com/retrieve/pii/S0302283814007805.
37. Sfoungaristos S, Perimenis P. PSA density is superior than PSA and Gleason score for adverse pathologic features prediction in patients with clinically localized prostate cancer. Can Urol Assoc J. 2012;6:46–50http://www.pubmedcentral.nih.gov/articlerender.fcgi?artid=3289697&tool=pmcentrez&rendertype=abstract. Accessed May 23, 2016.
38. Krughoff K, Eid K, Phillips J, et al. The accuracy of prostate cancer localization diagnosed on transrectal ultrasound-guided biopsy compared to 3-dimensional transperineal approach. Adv Urol. 2013;2013:249080http://www.pubmedcentral.nih.gov/articlerender.fcgi?artid=3891607&tool=pmcentrez&rendertype=abstract. Accessed May 23, 2016.
39. Hu Y, Ahmed HU, Carter T, et al. A biopsy simulation study to assess the accuracy of several transrectal ultrasonography (TRUS)-biopsy strategies compared with template prostate mapping biopsies in patients who have undergone radical prostatectomy. BJU Int. 2012;110:812–820http://www.ncbi.nlm.nih.gov/pubmed/22394583. Accessed December 29, 2014.
40. Scattoni V, Zlotta A, Montironi R, Schulman C, Rigatti P, Montorsi F. Extended and saturation prostatic biopsy in the diagnosis and characterisation of prostate cancer: a critical analysis of the literature. Eur Urol. 2007;52:1309–1322.
41. Kirkham APS, Emberton M, Allen C. How good is MRI at detecting and characterising cancer within the prostate? Eur Urol. 2006;50:1163–74; discussion 1175http://www.ncbi.nlm.nih.gov/pubmed/16842903. Accessed December 17, 2014.
42. Barentsz JO, Richenberg J, Clements R, et al. ESUR prostate MR guidelines 2012. Eur Radiol. 2012;22:746–757http://www.pubmedcentral.nih.gov/articlerender.fcgi?artid=3297750&tool=pmcentrez&rendertype=abstract. Accessed July 9, 2014.
43. Rosenkrantz AB, Kim S, Campbell N, Gaing B, Deng F-M, Taneja SS. Transition Zone Prostate Cancer: Revisiting the Role of Multiparametric MRI at 3 T. Am J Roentgenol. 2015;204:W266–W272http://www.ajronline.org/doi/10.2214/AJR.14.12955.
44. Hoeks CCM a, Barentsz JJO, Hambrock T, et al. Prostate cancer: multiparametric MR imaging for detection, localization, and staging. Radiology. 2011;261:46–66http://radiology.cornfeld.org/MRI/articles/Prostate Cancer Multiparametric MR Imaging for Detection Localization and Staging.pdf%5Cnhttp://www.ncbi.nlm.nih.gov/pubmed/21931141.
45. Bonekamp D, Bonekamp S, Mullins JK, Epstein JI, Carter HB, Macura KJ. Multiparametric magnetic resonance imaging characterization of prostate lesions in the active surveillance population: Incremental value of magnetic resonance imaging for prediction of disease reclassification. J Comput Assist Tomogr. 2013;37:948–956http://www.scopus.com/inward/record.url?eid=2-s2.0-84889027505&partnerID=40&md5=9469ea6b4f8c787780c9483f00815ec1.
46. Cornud F, Delongchamps NB, Mozer P, et al. Value of multiparametric MRI in the work-up of prostate cancer. Curr Urol Rep. 2012;13:82–92.
47. Sciarra A, Barentsz J, Bjartell A, et al. Advances in magnetic resonance imaging: How they are changing the management of prostate cancer. Eur Urol. European Association of Urology; 2011;59:962–977http://dx.doi.org/10.1016/j.eururo.2011.02.034.
48. Ahmed HU, El-Shater Bosaily A, Brown LC, et al. Diagnostic accuracy of multi-parametric MRI and TRUS biopsy in prostate cancer (PROMIS): a paired validating confirmatory study. Lancet. The Author(s). Published by Elsevier Ltd.

This is an Open Access article under the CC BY license; 2017;6736:1–8http://linkinghub.elsevier.com/retrieve/pii/S0140673616324011.
49. Appayya MB, Johnston EW, Punwani S. The role of multi-parametric MRI in loco-regional staging of men diagnosed with early prostate cancer. 2506;25:510–517.
50. Ahmed HU. Introduction--Targeting the lesion, not the organ. Urol Oncol. 2014;32:901–902http://www.ncbi.nlm.nih.gov/pubmed/25037484. Accessed May 16, 2016.
51. Siddiqui MM, Rais-Bahrami S, Turkbey B, et al. Comparison of MR/Ultrasound Fusion–Guided Biopsy With Ultrasound-Guided Biopsy for the Diagnosis of Prostate Cancer. 2016;1210:390–397.
52. de la Rosette J, Ahmed H, Barentsz J, et al. Focal Therapy in Prostate Cancer—Report from a Consensus Panel. J Endourol. 2010;24:775–780.
53. Moore CM, Ridout A, Emberton M. The role of MRI in active surveillance of prostate cancer. Curr Opin Urol. Hindawi Publishing Corporation; 2013;23:261–267http://www.ncbi.nlm.nih.gov/pubmed/23478498.
54. Notley M, Yu J, Fulcher AS, Turner MA, Cockrell CH, Nguyen D. Pictorial review. Diagnosis of recurrent prostate cancer and its mimics at multiparametric prostate MRI. Br J Radiol. 2015;88:20150362http://www.ncbi.nlm.nih.gov/pubmed/26268143. Accessed May 23, 2016.
55. Sullivan DC. Imaging as a quantitative science. Radiology. 2008;248:328–332http://eutils.ncbi.nlm.nih.gov/entrez/eutils/elink.fcgi?dbfrom=pubmed&id=18641239&retmode=ref&cmd=prlinks%5Cnfile:///Users/ket/Documents/Library.papers3/Articles/2008/Sullivan/Radiology_2008_Sullivan.pdf%5Cnpapers3://publication/doi/10.1148/radiol.2482080242.
56. Dickinson L, Ahmed HU, Allen C, et al. Scoring systems used for the interpretation and reporting of multiparametric MRI for prostate cancer detection, localization, and characterization: could standardization lead to improved utilization of imaging within the diagnostic pathway? J Magn Reson Imaging. 2013;37:48–58http://www.ncbi.nlm.nih.gov/pubmed/22566285. Accessed October 30, 2014.
57. Baker JA, Kornguth PJ, Floyd CE. Breast imaging reporting and data system standardized mammography lexicon: observer variability in lesion description. AJR Am J Roentgenol. American Public Health Association; 1996;166:773–778http://www.ncbi.nlm.nih.gov/pubmed/8610547. Accessed May 6, 2017.
58. Orel SG, Kay N, Reynolds C, Sullivan DC. BI-RADS Categorization As a Predictor of Malignancy. Radiology. 1999;211:845–850http://pubs.rsna.org/doi/10.1148/radiology.211.3.r99jn31845. Accessed November 15, 2016.
59. Dickinson L, Ahmed HU, Allen C, et al. Magnetic resonance imaging for the detection, localisation, and characterisation of prostate cancer: recommendations from a European consensus meeting. Eur Urol. European Association of Urology; 2011;59:477–494http://www.ncbi.nlm.nih.gov/pubmed/21195536. Accessed September 13, 2014.
60. PIRADS V2.pdf. .
61. ACR American College of Radiology. PI-RADS v2 Prostate Imaging and Reporting and Data System: Version 2. 2015;http://www.acr.org/Quality-Safety/Resources/PIRADS.
62. Barrett T, Turkbey B, Choyke PL. PI-RADS version 2: What you need to know. Clin Radiol. The Royal College of Radiologists; 2015;70:1165–1176http://dx.doi.org/10.1016/j.crad.2015.06.093.
63. Vaché T, Bratan F, Mège-Lechevallier F, Roche S, Rabilloud M, Rouvière O. Characterization of Prostate Lesions as Benign or Malignant at Multiparametric MR Imaging: Comparison of Three Scoring Systems in Patients Treated with Radical Prostatectomy. Radiology. 2014;272:446–

455http://www.ncbi.nlm.nih.gov/pubmed/24937690.
64. Rosenkrantz AB, Ginocchio LA, Cornfeld D, et al. Interobserver Reproducibility of the PI-RADS Version 2 Lexicon: A Multicenter Study of Six Experienced Prostate Radiologists. Radiology. 2016;0:152542http://pubs.rsna.org/doi/abs/10.1148/radiol.2016152542?af=R.
65. Muller BG, Shih JH, Sankineni S, et al. Prostate Cancer: Interobserver Agreement and Accuracy with the Revised Prostate Imaging Reporting and Data System at Multiparametric MR Imaging. Radiology. 2015;277:142818http://www.ncbi.nlm.nih.gov/pubmed/26098458.
66. Rosenkrantz AB, Babb JS, Taneja SS, Ream JM. Proposed Adjustments to PI-RADS Version 2 Decision Rules: Impact on Prostate Cancer Detection. Radiology. Radiological Society of North America; 2017;283:119–129http://pubs.rsna.org/doi/10.1148/radiol.2016161124. Accessed May 6, 2017.
67. Crawford ED, Wilson SS, Torkko KC, et al. Clinical staging of prostate cancer: a computer-simulated study of transperineal prostate biopsy. BJU Int. 2005;96:999–1004http://www.ncbi.nlm.nih.gov/pubmed/16225516. Accessed May 23, 2016.
68. Crawford ED, Rove KO, Barqawi AB, et al. Clinical-pathologic correlation between transperineal mapping biopsies of the prostate and three-dimensional reconstruction of prostatectomy specimens. Prostate. 2013;73:778–787http://www.pubmedcentral.nih.gov/articlerender.fcgi?artid=4625901&tool=pmcentrez&rendertype=abstract. Accessed May 23, 2016.
69. Ahmed HU, Hu Y, Carter T, et al. Characterizing clinically significant prostate cancer using template prostate mapping biopsy. J Urol. American Urological Association Education and Research, Inc.; 2011;186:458–464http://dx.doi.org/10.1016/j.juro.2011.03.147.
70. Transperineal template biopsy and mapping of the prostate | 2-The-procedure | Guidance and guidelines | NICE. NICE; https://www.nice.org.uk/guidance/ipg364/chapter/2-the-procedure. Accessed May 23, 2016.
71. Melia J, Moseley R, Ball RY, et al. A UK-based investigation of inter- and intra-observer reproducibility of Gleason grading of prostatic biopsies. Histopathology. 2006;48:644–654.
72. Kessler LG, Barnhart HX, Buckler AJ, et al. The emerging science of quantitative imaging biomarkers terminology and definitions for scientific studies and regulatory submissions. Stat Methods Med Res. 2014;24:9–26http://www.ncbi.nlm.nih.gov/pubmed/24919826.
73. Sullivan DC, Obuchowski NA, Kessler LG, et al. Metrology Standards for Quantitative Imaging. 2015;277:813–825.
74. Obuchowski N a, Reeves AP, Huang EP, et al. Quantitative imaging biomarkers: A review of statistical methods for computer algorithm comparisons. Stat Methods Med Res. 2014;http://www.ncbi.nlm.nih.gov/pubmed/24919829.
75. Society E. White paper on imaging biomarkers. Insights Imaging. 2010;1:42–45.
76. Society E. ESR statement on the stepwise development of imaging biomarkers. Insights Imaging. 2013;4:147–152.
77. Hayes DF. Biomarker validation and testing. Mol Oncol. Elsevier B.V; 2015;9:960–966http://dx.doi.org/10.1016/j.molonc.2014.10.004.
78. Group F-NBW. BEST (Biomarkers, EndpointS, and other Tools) Resource. BEST (Biomarkers, EndpointS, other Tools) Resour. Food and Drug Administration (US); 2016.http://www.ncbi.nlm.nih.gov/pubmed/27010052. Accessed May 6, 2017.
79. O'Connor J, Aboagye E, Adams J, Aerts H, Barrington S, Beer A. Imaging biomarker roadmap for cancer studies. Nat Rev Clin Oncol. 2017;14:169–186.
80. Baker M. 1,500 scientists lift the lid on reproducibility. Nature. 2016;533:452–454http://www.nature.com/doifinder/10.1038/533452a. Accessed May 6, 2017.
81. Tofts PS, Collins DJ. Multicentre imaging measurements for oncology and in the brain. Br J Radiol. 2011;84.

82. Tofts P. QA: quality assurance, accuracy, precision and phantoms. 2003;http://discovery.ucl.ac.uk/188427/.
83. McShane LM, Altman DG, Sauerbrei W, et al. REporting recommendations for tumour MARKer prognostic studies (REMARK). Br J Cancer. Nature Publishing Group; 2005;93:387–391http://www.ncbi.nlm.nih.gov/pubmed/16106245. Accessed May 6, 2017.
84. Hayes DF, Allen J, Compton C, et al. Breaking a Vicious Cycle. 2013;5:1–8.
85. Laine C, Goodman SN, Griswold ME, Sox HC. Reproducible research: moving toward research the public can really trust. Ann Intern Med. 2007;146:450–453http://www.ncbi.nlm.nih.gov/pubmed/17339612. Accessed May 6, 2017.
86. O'Connor JPB. Cancer heterogeneity and imaging. Semin Cell Dev Biol. Elsevier Ltd; 2016;1–10http://dx.doi.org/10.1016/j.semcdb.2016.10.001.
87. O'Connor JPB, Rose CJ, Waterton JC, Carano RAD, Parker GJM, Jackson A. Imaging intratumor heterogeneity: Role in therapy response, resistance, and clinical outcome. Clin Cancer Res. 2015;21:249–257.
88. McMahon CJ, Rofsky NM, Pedrosa I. Lymphatic metastases from pelvic tumors: anatomic classification, characterization, and staging. Radiology. 2010;254:31–46.
89. Briganti A, Blute ML, Eastham JH, et al. Pelvic Lymph Node Dissection in Prostate Cancer. Eur Urol. 2009;55:1251–1265.
90. Briganti A, Suardi N, Gallina A, Abdollah F, Montorsi F. Pelvic lymph node dissection in prostate cancer: The mystery is taking shape. Eur Urol. 2013;63:459–461.
91. Briganti A, Suardi N, Capogrosso P, et al. Lymphatic spread of nodal metastases in high-risk prostate cancer: The ascending pathway from the pelvis to the retroperitoneum. Prostate. 2012;72:186–192.
92. Paget S. THE DISTRIBUTION OF SECONDARY GROWTHS IN CANCER OF THE BREAST. Lancet. 1889;133:571–573http://linkinghub.elsevier.com/retrieve/pii/S0140673600499150. Accessed May 8, 2017.
93. Neoplastic Diseases: A Treatise on Tumours. By James Ewing, A.M., M.D., Sc.D., Professor of Pathology at Cornell University Medical College, N.Y.; Pathologist to the Memorial Hospital. Third edition. Royal 8vo. Pp. 1127, with 546 illustrations. 1928. Philadelphia and London: W. B. Saunders Co. Ltd. 63s. net. Br J Surg. John Wiley & Sons, Ltd.; 1928;16:174–175http://doi.wiley.com/10.1002/bjs.1800166126. Accessed May 9, 2017.
94. Fidler IJ. The pathogenesis of cancer metastasis: the "seed and soil" hypothesis revisited. Nat Rev Cancer. 2003;3:453–458http://www.nature.com/doifinder/10.1038/nrc1098.
95. Arya M, Bott SR, Shergill IS, Ahmed HU, Williamson M, Patel HR. The metastatic cascade in prostate cancer. Surg Oncol. 2006;15:117–128.
96. Batson O V. the Function of the Vertebral Veins and Their Rôle in the Spread of Metastases*. Ann Surg. 1940;112:138–149.
97. Bubendorf L, Schöpfer A, Wagner U, et al. Metastatic patterns of prostate cancer: an autopsy study of 1,589 patients. Hum Pathol. 2000;31:578–583http://www.ncbi.nlm.nih.gov/pubmed/10836297. Accessed July 7, 2015.
98. Vinjamoori a. H, Jagannathan JP, Shinagare a. B, et al. Atypical Metastases From Prostate Cancer: 10-Year Experience at a Single Institution. Am J Roentgenol. 2012;199:367–372.
99. Gandaglia G, Abdollah F, Schiffmann J, et al. Distribution of metastatic sites in patients with prostate cancer: A population-based analysis. Prostate. 2014;74:210–216.
100. Buyyounouski MK, Choyke PL, McKenney JK, et al. Prostate cancer - major changes in the American Joint Committee on Cancer eighth edition cancer staging manual. CA Cancer J Clin. 2017;67:245–253http://www.ncbi.nlm.nih.gov/pubmed/28222223. Accessed May 9, 2017.
101. AJCC - AJCC 7th Ed Cancer Staging Manual.

https://cancerstaging.org/references-tools/deskreferences/Pages/AJCC-7th-Ed-Cancer-Staging-Manual.aspx. Accessed May 8, 2017.
102. Johansson J-E. Natural History of Early, Localized Prostate Cancer. JAMA. 2004;291:2713http://jama.jamanetwork.com/article.aspx?doi=10.1001/jama.291.22.2713. Accessed November 16, 2016.
103. Bill-Axelson A, Holmberg L, Fil??n F, et al. Radical prostatectomy versus watchful waiting in localized prostate cancer: The Scandinavian prostate cancer group-4 randomized trial. J Natl Cancer Inst. 2008;100:1144–1154.
104. Davidson PJT, Hop W, Kurth KH, Fossa SD, Waehre H, Schroder FH. Progression in Untreated Carcinoma of the Prostate Metastatic to Regional Lymph Nodes (Stage T0 to 4,N1 to 3,M0,D1). J Urol. 1995;154:2118–2122.
105. James ND, Spears MR, Clarke NW, et al. Survival with Newly Diagnosed Metastatic Prostate Cancer in the "Docetaxel Era": Data from 917 Patients in the Control Arm of the STAMPEDE Trial (MRC PR08, CRUK/06/019). Eur Urol. 2015;67:1028–1038http://linkinghub.elsevier.com/retrieve/pii/S0302283814009695. Accessed November 16, 2016.
106. Briganti A, Passoni N, Ferrari M, et al. When to Perform Bone Scan in Patients with Newly Diagnosed Prostate Cancer: External Validation of the Currently Available Guidelines and Proposal of a Novel Risk Stratification Tool. Eur Urol. 2010;57:551–558.
107. Heidenreich a, Bolla M, Joniau S, et al. Guidelines on Prostate Cancer. Update. 2011;53:31–45http://www.uroweb.org/fileadmin/tx_eauguidelines/2005/Pocket/Prostate_Cancer.pdf.
108. Henry J, Nicholas N. Dead in the water--are we killing the hospital autopsy with poor consent practices? J R Soc Med. 2012;105:288–295http://jrs.sagepub.com/content/105/7/288.full.
109. Eka I, Rowan C, Osborn M, I. E, C. R. Mind the gap: are NHS trusts falling short of recommended standards for consent to autopsy?. J Clin Pathol. 2014;67:10–13http://jcp.bmj.com/content/67/1/10.full.pdf+html%5Cnhttp://ovidsp.ovid.com/ovidweb.cgi?T=JS&PAGE=reference&D=emed12&NEWS=N&AN=2014079957%5Cnhttp://ovidsp.ovid.com/ovidweb.cgi?T=JS&PAGE=reference&D=medl&NEWS=N&AN=24062359.
110. Jacobs SC. Spread of prostatic cancer to bone. Urology. 1983;21:337–344http://www.ncbi.nlm.nih.gov/pubmed/6340324.
111. Bjurlin MA, Rosenkrantz AB, Beltran LS, Raad RA, Taneja SS. Imaging and evaluation of patients with high-risk prostate cancer. Nat Rev Urol. Nature Publishing Group; 2015;12:617–628http://www.nature.com/doifinder/10.1038/nrurol.2015.242%5Cnhttp://www.ncbi.nlm.nih.gov/pubmed/26481576.
112. Shen G, Deng H, Hu S, Jia Z. Comparison of choline-PET/CT, MRI, SPECT, and bone scintigraphy in the diagnosis of bone metastases in patients with prostate cancer: a meta-analysis. Skeletal Radiol. 2014;1503–1513.
113. Hövels a. M, Heesakkers R a M, Adang EM, et al. The diagnostic accuracy of CT and MRI in the staging of pelvic lymph nodes in patients with prostate cancer: a meta-analysis. Clin Radiol. 2008;63:387–395.
114. DeGrado TR, Baldwin SW, Wang S, et al. Synthesis and evaluation of (18)F-labeled choline analogs as oncologic PET tracers. J Nucl Med. 2001;42:1805–1814.
115. Evangelista L, Guttilla A, Zattoni F, Muzzio PC, Zattoni F. Utility of choline positron emission tomography/computed tomography for lymph node involvement identification in intermediate- to high-risk prostate cancer: A systematic literature review and meta-analysis. Eur Urol. 2013;63:1040–1048.
116. Beheshti M, Imamovic L, Broinger G, et al. ^{18} F Choline PET/CT in the Preoperative Staging of Prostate Cancer in Patients with Intermediate or High Risk of Extracapsular Disease: A Prospective Study of 130 Patients. Radiology.

Radiological Society of North America, Inc.; 2010;254:925–933http://pubs.rsna.org/doi/10.1148/radiol.09090413. Accessed November 16, 2016.
117. Treglia G, Ceriani L, Sadeghi R, Giovacchini G, Giovanella L. Relationship between prostate-specific antigen kinetics and detection rate of radiolabelled choline PET/CT in restaging prostate cancer patients: A meta-analysis. Clin Chem Lab Med. 2014;52:725–733.
118. Picchio M, Spinapolice EG, Fallanca F, et al. [11C]Choline PET/CT detection of bone metastases in patients with PSA progression after primary treatment for prostate cancer: Comparison with bone scintigraphy. Eur J Nucl Med Mol Imaging. 2012;39:13–26.
119. Smith-Bindman R. Is Computed Tomography Safe? N Engl J Med. Massachusetts Medical Society ; 2010;363:1–4http://www.nejm.org/doi/abs/10.1056/NEJMp1002530. Accessed November 16, 2016.
120. Huang B, Law MW-M, Khong P-L. Whole-Body PET/CT Scanning: Estimation of Radiation Dose and Cancer Risk. Radiology. Radiological Society of North America; 2009;251:166–174http://pubs.rsna.org/doi/10.1148/radiol.2511081300. Accessed November 16, 2016.
121. Kapoor V, McCook BM, Torok FS. An Introduction to PET-CT Imaging. RadioGraphics. Radiological Society of North America ; 2004;24:523–543http://pubs.rsna.org/doi/10.1148/rg.242025724. Accessed November 16, 2016.
122. Davis GL. Sensitivity of frozen section examination of pelvic lymph nodes for metastatic prostate carcinoma. Cancer. Wiley Subscription Services, Inc., A Wiley Company; 1995;76:661–668http://doi.wiley.com/10.1002/1097-0142%2819950815%2976%3A4%3C661%3A%3AAID-CNCR2820760419%3E3.0.CO%3B2-S. Accessed November 16, 2016.
123. Damadian R. Letter. 1969.
124. Engelhard K, Hollenbach HP, Wohlfart K, Imhoff E Von, Fellner FA. Comparison of whole-body MRI with automatic moving table technique and bone scintigraphy for screening for bone metastases in patients with breast cancer. 2004;99–105.
125. Lambregts DMJ, Maas M, Cappendijk VC, et al. Whole-body diffusion-weighted magnetic resonance imaging: Current evidence in oncology and potential role in colorectal cancer staging. Eur J Cancer. Elsevier Ltd; 2011;47:2107–2116http://dx.doi.org/10.1016/j.ejca.2011.05.013.
126. Messiou C, Kaiser M. Whole body diffusion weighted MRI – a new view of myeloma. 2015;29–37.
127. Brennan DD, Gleeson T, Coate LE, Cronin C, Carney D, Eustace SJ. A comparison of whole-body MRI and CT for the staging of lymphoma. Am J Roentgenol. 2005;185:711–716.
128. Atkin KL, Ditchfield MR. The Role of Whole-Body MRI in Pediatric Oncology. J Pediatr Hematol Oncol. 2013;0:1–11http://www.ncbi.nlm.nih.gov/pubmed/24072253.
129. Messiou C, Kaiser M. Whole body diffusion weighted MRI--a new view of myeloma. Br J Haematol. Wiley-Blackwell; 2015;171:29–37http://www.ncbi.nlm.nih.gov/pubmed/26013304. Accessed November 16, 2016.
130. Ballon D, Watts R, Dyke JP, et al. Imaging therapeutic response in human bone marrow using rapid whole-body MRI. Magn Reson Med. 2004;52:1234–1238http://www.ncbi.nlm.nih.gov/pubmed/15562475. Accessed November 16, 2016.
131. Pasoglou V, Larbi A, Collette L, et al. One-step TNM staging of high-risk prostate cancer using magnetic resonance imaging (MRI): toward an upfront simplified “all-in-one” imaging approach? Prostate. 2014;74:469–477http://www.ncbi.nlm.nih.gov/pubmed/24375774. Accessed December 29, 2014.

132. Linton KD, Catto JWF. Whole-body magnetic resonance imaging and prostate cancer metastases: A new gold standard of detection, but does it help us and at what cost? Eur Urol. 2012;62:76–77.
133. Venkitaraman R, Cook GJR, Dearnaley DP, et al. Does Magnetic Resonance Imaging of the Spine Have a Role in??the Staging of Prostate Cancer? Clin Oncol. The Royal College of Radiologists; 2009;21:39–42http://dx.doi.org/10.1016/j.clon.2008.09.006.
134. Taoka T, Mayr NA, Lee HJ, et al. Factors influencing visualization of vertebral metastases on MR imaging versus bone scintigraphy. Am J Roentgenol. 2001;176:1525–1530.
135. Ghanem N, Altehoefer C, Hogerle S, et al. Comparative diagnostic value and therapeutic relevance of magnetic resonance imaging and bone marrow scintigraphy in patients with metastatic solid tumors of the axial skeleton. Eur J Radiol. 2002;43:256–261http://www.ncbi.nlm.nih.gov/entrez/query.fcgi?cmd=Retrieve&db=PubMed&dopt=Citation&list_uids=12204408.
136. Pinaquy J-B, De Clermont-Galleran H, Pasticier G, et al. Comparative effectiveness of [18 F]-fluorocholine PET-CT and pelvic MRI with diffusion-weighted imaging for staging in patients with high-risk prostate cancer. Prostate. 2015;75:323–331http://doi.wiley.com/10.1002/pros.22921.
137. Thoeny HC, Froehlich JM, Triantafyllou M, et al. Metastases in Normal-sized Pelvic Lymph Nodes: Detection with Diffusion-weighted MR Imaging. Radiology. 2014;273:125–135http://www.ncbi.nlm.nih.gov/pubmed/24893049%5Cnhttp://www.ncbi.nlm.nih.gov/pubmed/24893049%5Cnhttp://pubs.rsna.org.ludwig.lub.lu.se/doi/full/10.1148/radiol.14132921.
138. Padhani AR, Liu G, Koh DM, et al. Diffusion-weighted magnetic resonance imaging as a cancer biomarker: consensus and recommendations. Neoplasia. 2009;11:102–125.
139. Van Den Bergh L, Lerut E, Haustermans K, et al. Final analysis of a prospective trial on functional imaging for nodal staging in patients with prostate cancer at high risk for lymph node involvement. Urol Oncol Semin Orig Investig. 2015;33:109.e23-109.e31.
140. Traill ZC, Talbot D, Golding S, Gleeson F V. Magnetic resonance imaging versus radionuclide scintigraphy in screening for bone metastases. Clin Radiol. 1999;54:448–451.
141. Gutzeit A, Doert A, Froehlich JM, et al. Comparison of diffusion-weighted whole body MRI and skeletal scintigraphy for the detection of bone metastases in patients with prostate or breast carcinoma. Skeletal Radiol. 2010;39:333–343http://www.ncbi.nlm.nih.gov/pubmed/20205350. Accessed October 8, 2014.
142. Jambor I, Kuisma A, Ramadan S, et al. Prospective evaluation of planar bone scintigraphy, SPECT, SPECT/CT, 18 F-NaF PET/CT and whole body 1.5T MRI, including DWI, for the detection of bone metastases in high risk breast and prostate cancer patients: SKELETA clinica. Acta Oncol (Madr). 2015;1–9http://informahealthcare.com/doi/abs/10.3109/0284186X.2015.1027411.
143. Minamimoto R, Loening A, Jamali M, et al. MRI in Patients with Breast and Prostate Cancer. 2015;56:1862–1869.
144. Zurich U. Nuclear Medicine Original article The value of bone scintigraphy , bone marrow scintigraphy. 1993;20.
145. Lecouvet FE, Simon M, Tombal B, Jamart J, Vande Berg BC, Simoni P. Whole-body MRI (WB-MRI) versus axial skeleton MRI (AS-MRI) to detect and measure bone metastases in prostate cancer (PCa). Eur Radiol. 2010;20:2973–2982.
146. Lauffer RB. Paramagnetic Metal Complexes as Water Proton Relaxation Agents for NMR Imaging: Theory and Design. Chem Rev. 1987;87:901–927.
147. Rogosnitzky M, Branch S. Gadolinium-based contrast agent toxicity: a review of known and proposed mechanisms. BioMetals. Springer Netherlands;

2016;29:365–376.
148. Kanal E. Gadolinium based contrast agents (GBCA): Safety overview after 3 decades of clinical experience. Magn Reson Imaging. Elsevier Inc.; 2016;34:1341–1345http://dx.doi.org/10.1016/j.mri.2016.08.017.
149. Brady Quist, Brian A. Hargreaves1, Bruce L. Daniel MS. Balanced SSFP Dixon Imaging with Banding-Artifact Reduction at 3T. Magn Reson Med. 2015;74:1–23.
150. Dixon WT. Simple Proton Spectroscopic Imaging. Radiology. 1984;153:189–194.
151. Einstein a. On the movement of small particles suspended in a stationary liquid demanded by the molecular-kinetic theory of heat. Ann Phys. 1905;17:549–560http://doi.wiley.com/10.1002/andp.19053220806.
152. Galletti G. Circulating tumor cells in prostate cancer diagnosis and monitoring : an appraisal of clinical potential. 2015;18:389–402.
153. Bloch F. Nuclear Induction. Phys Rev. American Physical Society; 1946;70:460–474http://link.aps.org/doi/10.1103/PhysRev.70.460. Accessed November 15, 2016.
154. Kiricuta IC, Simplăceanu V. Tissue water content and nuclear magnetic resonance in normal and tumor tissues. Cancer Res. 1975;35:1164–1167.
155. Bloembergen N, Purcell EM, Pound R V. Relaxation Effects in Nuclear Magnetic Resonance Absorption. Phys Rev. American Physical Society; 1948;73:679–712http://link.aps.org/doi/10.1103/PhysRev.73.679. Accessed November 15, 2016.
156. Fullerton GD. Physiologic basis of magnetic relaxation. In: D.D. Stark, W.G. Bradley. C.V. Mosby; 1988.
157. Staudinger H, Fritschi J. Über Isopren und Kautschuk. 5. Mitteilung. Über die Hydrierung des Kautschuks und über seine Konstitution. Helv Chim Acta. WILEY-VCH Verlag GmbH; 1922;5:785–806.
158. Bottomley PA, Foster TH, Argersinger RE, Pfeifer LM. A review of normal tissue hydrogen NMR re1. Bottomley PA, Foster TH, Argersinger RE, Pfeifer LM (1984) A review of normal tissue hydrogen NMR relaxation times and relaxation mechanisms from 1–100 MHz: Dependence on tissue type, NMR frequency, temperature,. Med Phys. 1984;11:425http://scitation.aip.org/content/aapm/journal/medphys/11/4/10.1118/1.595535.
159. Mauss Y, Grucker D, Fornasiero D, Chambron J. NMR compartmentalization of free water in the perfused rat heart. Magn Reson Med. 1985;2:187–194http://onlinelibrary.wiley.com/doi/10.1002/mrm.1910020302/abstract%5Cnhttp://www.ncbi.nlm.nih.gov/pubmed/3831688.
160. Sabouri S, Chang SD, Savdie R, et al. Luminal Water Imaging: A New MR Imaging T2 Mapping Technique for Prostate Cancer Diagnosis. Radiology. 2017;161687http://www.ncbi.nlm.nih.gov/pubmed/28394754. Accessed May 11, 2017.
161. Sabouri S, Fazli L, Chang SD, et al. MR measurement of luminal water in prostate gland: Quantitative correlation between MRI and histology. J Magn Reson Imaging. 2017;http://www.ncbi.nlm.nih.gov/pubmed/28130866. Accessed May 11, 2017.
162. Braunschweiger PG, Schiffer LM, Furmanski P. 1H-NMR relaxation times and water compartmentalization in experimental tumor models. Magn Reson Imaging. 1986;4:335–342.
163. Fullerton GD, Cameron IL, Ord A, Ph D. in Biological of Magnetic. :135–138.
164. Mitchell D, Burk D, Vinitski S, Rifkin M. The biophysical basis of tissue contrast in extracranial MR imaging. Am J Roentgenol. 1987;149:831–837http://www.ajronline.org/doi/10.2214/ajr.149.4.831. Accessed November 15, 2016.
165. Tannock I, Rotin D. Acid pH in tumors and its potential for therapeutic exploitation. Cancer Res. 1989;49:4373–4384.

166. Jakobsen I, Lyng H, Kaalhus O, Rofstad EK. MRI of human tumor xenografts in vivo: proton relaxation times and extracellular tumor volume. Magn Reson Imaging. 1995;13:693–700http://www.ncbi.nlm.nih.gov/pubmed/8569443. Accessed November 15, 2016.
167. Medved M, Sammet S, Yousuf A, Oto A. MR Imaging of the Prostate and Adjacent Anatomic Structures before, during, and after Ejaculation: Qualitative and Quantitative Evaluation. Radiology. 2014;271:452–460http://www.ncbi.nlm.nih.gov/pubmed/24495265.
168. Wang L, Mazaheri Y, Zhang J, Ishill NM, Kuroiwa K, Hricak H. Assessment of biologic aggressiveness of prostate cancer: correlation of MR signal intensity with Gleason grade after radical prostatectomy. Radiology. 2008;246:168–176.
169. Hanahan D, Weinberg R a. The hallmarks of cancer. Cell. 2000;100:57–70.
170. Hanahan D, Folkman J. Patterns and emerging mechanisms of the angiogenic switch during tumorigenesis. Cell. 1996;86:353–364.
171. Russo G, Mischi M, Scheepens W, De La Rosette JJ, Wijkstra H. Angiogenesis in prostate cancer: Onset, progression and imaging. BJU Int. 2012;110:794–808.
172. Battegay EJ, Rupp J, Iruela-Arispe L, Sage EH, Pech M. PDGF-BB modulates endothelial proliferation and angiogenesis in vitro via PDGF ??-receptors. J Cell Biol. 1994;125:917–928.
173. Egeblad M, Werb Z. New functions for the matrix metalloproteinases in cancer progression. Nat Rev Cancer. 2002;2:161–174http://www.nature.com/doifinder/10.1038/nrc745.
174. Fukumura D, Duda DG, Munn LL, Jain RK. Tumor microvasculature and microenvironment: novel insights through intravital imaging in pre-clinical models. Microcirculation. 2010;17:206–225http://www.ncbi.nlm.nih.gov/pubmed/20374484. Accessed November 15, 2016.
175. Sherwood LM, Parris EE, Folkman J. Tumor Angiogenesis: Therapeutic Implications. N Engl J Med. 1971;285:1182–1186http://www.nejm.org/doi/abs/10.1056/NEJM197111182852108. Accessed November 15, 2016.
176. Ogawa Y, Chung YS, Nakata B, et al. Microvessel quantitation in invasive breast cancer by staining for factor VIII-related antigen. Br J Cancer. Nature Publishing Group; 1995;71:1297–1301http://www.ncbi.nlm.nih.gov/pubmed/7779727. Accessed November 15, 2016.
177. Engel CJ, Bennett ST, Chambers AF, Doig GS, Kerkvliet N, O'Malley FP. Tumor angiogenesis predicts recurrence in invasive colorectal cancer when controlled for Dukes staging. Am J Surg Pathol. 1996;20:1260–1265http://www.ncbi.nlm.nih.gov/pubmed/8827033. Accessed November 15, 2016.
178. Bono A, Celato N, Cova V, Salvadore M, Chinetti S, Novario R. Microvessel density in prostate carcinoma. Prostate Cancer Prostatic Dis. 2002;5:123–127.
179. Tretiakova M, Antic T, Binder D, et al. Microvessel density is not increased in prostate cancer: Digital imaging of routine sections and tissue microarrays. Hum Pathol. Elsevier Inc.; 2013;44:495–502http://dx.doi.org/10.1016/j.humpath.2012.06.009.
180. van Niekerk CG, van der Laak J a WM, Hambrock T, et al. Correlation between dynamic contrast-enhanced MRI and quantitative histopathologic microvascular parameters in organ-confined prostate cancer. Eur Radiol. 2014;2597–2605.
181. Lissbrant IF, Stattin P, Damber JE, Bergh A. Vascular density is a predictor of cancer-specific survival in prostatic carcinoma. Prostate. 1997;33:38–45http://www.ncbi.nlm.nih.gov/pubmed/9294625. Accessed November 15, 2016.
182. Rubin MA, Buyyounouski M, Bagiella E, et al. Microvessel density in prostate cancer: lack of correlation with tumor grade, pathologic stage, and clinical outcome. Urology. 1999;53:542–547.
183. Miyata Y, Sakai H. Reconsideration of the clinical and histopathological significance of angiogenesis in prostate cancer: Usefulness and limitations of

microvessel density measurement. Int J Urol. 2015;22:806–815.
184. Weidner N, Carroll PR, Flax J, Blumenfeld W, Folkman J. Tumor angiogenesis correlates with metastasis in invasive prostate carcinoma. Am J Pathol. 1993;143:401–409.
185. Iyama Y, Nakaura T, Kidoh M, et al. Fat Suppressed Contrast-Enhanced T1-Weighted Dynamic Magnetic Resonance Imaging at 3T. J Comput Assist Tomogr. 2017;41:382–387http://insights.ovid.com/crossref?an=00004728-201705000-00008.
186. Tannús A, Garwood M. Adiabatic pulses. NMR Biomed. 1997;10:423–434.
187. Del Grande F, Santini F, Herzka DA, et al. Fat-suppression techniques for 3-T MR imaging of the musculoskeletal system. Radiographics. 2014;34:217–233http://www.ncbi.nlm.nih.gov/pubmed/24428292.
188. Kirkham a PS, Haslam P, Keanie JY, et al. Prostate MRI: who, when, and how? Report from a UK consensus meeting. Clin Radiol. The Royal College of Radiologists; 2013;68:1016–1023http://www.ncbi.nlm.nih.gov/pubmed/23827086. Accessed November 4, 2014.
189. Dikaios N, Alkalbani J, Sidhu HS, et al. Logistic regression model for diagnosis of transition zone prostate cancer on multi-parametric MRI. Eur Radiol. 2014;http://www.ncbi.nlm.nih.gov/pubmed/25226842. Accessed October 23, 2014.
190. Hansford BG, Thomas S, Mccann S. Dynamic Contrast-enhanced MR Imaging Curve-type Analysis : Is It Helpful in the Differentiation of Prostate Cancer from Healthy Peripheral Zone ? 1. 2015;0:1–10.
191. García-Figueiras R, Padhani AR, Beer AJ, et al. Imaging of Tumor Angiogenesis for Radiologists-Part 1: Biological and Technical Basis. Curr Probl Diagn Radiol. Elsevier; 2015;44:407–424http://dx.doi.org/10.1067/j.cpradiol.2015.02.010.
192. Galbraith SM, Lodge M a., Taylor NJ, et al. Reproducibility of dynamic contrast-enhanced MRI in human muscle and tumours: Comparison of quantitative and semi-quantitative analysis. NMR Biomed. 2002;15:132–142.
193. Buckley DL. Uncertainty in the analysis of tracer kinetics using dynamic contrast-enhanced T1-weighted MRI. Magn Reson Med. 2002;47:601–606http://www.ncbi.nlm.nih.gov/pubmed/11870848. Accessed May 23, 2016.
194. Leach MO, Brindle KM, Evelhoch JL, et al. The assessment of antiangiogenic and antivascular therapies in early-stage clinical trials using magnetic resonance imaging: issues and recommendations. Br J Cancer. 2005;92:1599–1610.
195. Beuzit L, Eliat P-A, Brun V, et al. Dynamic contrast-enhanced MRI: Study of inter-software accuracy and reproducibility using simulated and clinical data. J Magn Reson Imaging. 2015;n/a-n/ahttp://doi.wiley.com/10.1002/jmri.25101.
196. Vos EK, Litjens GJS, Kobus T, et al. Assessment of prostate cancer aggressiveness using dynamic contrast-enhanced magnetic resonance imaging at 3 T. Eur Urol. European Association of Urology; 2013;64:448–455http://dx.doi.org/10.1016/j.eururo.2013.05.045.
197. Engelbrecht MR, Huisman HJ, Laheij RJF, et al. Discrimination of prostate cancer from normal peripheral zone and central gland tissue by using dynamic contrast-enhanced MR imaging. Radiology. 2003;229:248–254.
198. Chen YJ, Chu WC, Pu YS, Chueh SC, Shun CT, Tseng WYI. Washout gradient in dynamic contrast-enhanced MRI is associated with tumor aggressiveness of prostate cancer. J Magn Reson Imaging. 2012;36:912–919.
199. Padhani AR, Gapinski CJ, Macvicar D a., et al. Dynamic contrast enhanced MRI of prostate cancer: Correlation with morphology and tumour stage, histological grade and PSA. Clin Radiol. 2000;55:99–109.
200. Oto A, Yang C, Kayhan A, et al. Diffusion-weighted and dynamic contrast-enhanced MRI of prostate cancer: correlation of quantitative MR parameters with Gleason score and tumor angiogenesis. AJR Am J Roentgenol. 2011;197:1382–1390http://www.ncbi.nlm.nih.gov/pubmed/22109293. Accessed October 30, 2014.

201. Le Bihan D. Diffusion and IVIM. Radiology. 1988;566–567.
202. Bourne R, Panagiotaki E. Limitations and Prospects for Diffusion-Weighted MRI of the Prostate. Diagnostics. 2016;6:21http://www.mdpi.com/2075-4418/6/2/21.
203. Panagiotaki E, Chan RW, Dikaios N, et al. Microstructural Characterization of Normal and Malignant Human Prostate Tissue With Vascular , Extracellular , and Restricted Diffusion for Cytometry in Tumours Magnetic Resonance Imaging. Invest Radiol. 2015;50:218–227.
204. Pang Y, Turkbey B, Bernardo M, et al. Intravoxel incoherent motion MR imaging for prostate cancer: An evaluation of perfusion fraction and diffusion coefficient derived from different b-value combinations. Magn Reson Med. 2013;69:553–562.
205. Panagiotaki E, Walker-Samuel S, Siow B, et al. Noninvasive quantification of solid tumor microstructure using VERDICT MRI. Cancer Res. 2014;74:1902–1912http://www.ncbi.nlm.nih.gov/pubmed/24491802. Accessed October 15, 2014.
206. Bihan D Le. and Beyond : What Diffusion MR Imaging Can Tell Us about Tissue. 2013;268.
207. Rosenkrantz AB, Prabhu V, Sigmund EE, Babb JS, Deng FM, Taneja SS. Utility of diffusional kurtosis imaging as a marker of adverse pathologic outcomes among prostate cancer active surveillance candidates undergoing radical prostatectomy. Am J Roentgenol. 2013;201:840–846.
208. Basser PJ, Pierpaoli C. A Simplified Method to Measure the Diffusion Tensor from Seven MR Images. Magn Reson Med. 1998;64:928–934.
209. Hambrock T, Hoeks C, Hulsbergen-Van De Kaa C, et al. Prospective assessment of prostate cancer aggressiveness using 3-T diffusion-weighted magnetic resonance imaging-guided biopsies versus a systematic 10-core transrectal ultrasound prostate biopsy cohort. Eur Urol. 2012;61:177–184.
210. Vargas HA, Akin O, Franiel T, et al. Diffusion-weighted endorectal MR imaging at 3 T for prostate cancer: tumor detection and assessment of aggressiveness. Radiology. 2011;259:775–784.
211. Donati OF, Mazaheri Y, Afaq a, et al. Prostate cancer aggressiveness: assessment with whole-lesion histogram analysis of the apparent diffusion coefficient. Radiology. 2014;271:143–152http://www.ncbi.nlm.nih.gov/pubmed/24475824.
212. Rosenkrantz a. B, Sigmund EE, Johnson G, et al. Prostate Cancer: Feasibility and Preliminary Experience of a Diffusional Kurtosis Model for Detection and Assessment of Aggressiveness of Peripheral Zone Cancer. Radiology. 2012;264:126–135.
213. Kobus T, Vos PC, Hambrock T, et al. Prostate Cancer Aggressiveness: In Vivo Assessment of MR Spectroscopy and Diffusion-weighted Imaging at 3 T. Radiology. 2012;265:457–467.
214. Nagarajan R, Margolis D, Raman S, et al. MR spectroscopic imaging and diffusion-weighted imaging of prostate cancer with Gleason scores. J Magn Reson Imaging. 2012;36:697–703.
215. Hoeks CM, Vos EK, Bomers JG, Barentsz JO, Hulsbergen-van de Kaa C a, Scheenen TW. Diffusion-weighted magnetic resonance imaging in the prostate transition zone: histopathological validation using magnetic resonance-guided biopsy specimens. Invest Radiol. 2013;48:693–701.
216. Verma S, Rajesh A, Morales H, et al. Assessment of aggressiveness of prostate cancer: Correlation of apparent diffusion coefficient with histologic grade after radical prostatectomy. Am J Roentgenol. 2011;196:374–381.
217. Bittencourt LK, Barentsz JO, De Miranda LCD, Gasparetto EL. Prostate MRI: Diffusion-weighted imaging at 1.5T correlates better with prostatectomy Gleason grades than TRUS-guided biopsies in peripheral zone tumours. Eur Radiol. 2012;22:468–475.
218. Itou Y, Nakanishi K, Narumi Y, Nishizawa Y, Tsukuma H. Clinical utility of apparent diffusion coefficient (ADC) values in patients with prostate cancer: Can

ADC values contribute to assess the aggressiveness of prostate cancer? J Magn Reson Imaging. 2011;33:167–172.
219. Donati OF, Afaq A, Vargas HA, et al. Prostate MRI: Evaluating tumor volume and apparent diffusion coefficient as surrogate biomarkers for predicting tumor Gleason score. Clin Cancer Res. 2014;20:3705–3711.
220. De Cobelli F, Ravelli S, Esposito A, et al. Apparent Diffusion Coefficient Value and Ratio as Noninvasive Potential Biomarkers to Predict Prostate Cancer Grading: Comparison With Prostate Biopsy and Radical Prostatectomy Specimen. Am J Roentgenol. 2015;204:550–557http://www.ajronline.org/doi/10.2214/AJR.14.13146.
221. Zelhof B, Pickles M, Liney G, et al. Correlation of diffusion-weighted magnetic resonance data with cellularity in prostate cancer. BJU Int. 2009;103:883–888.
222. Gibbs P, Liney GP, Pickles MD, Zelhof B, Rodrigues G, Turnbull LW. Correlation of ADC and T2 measurements with cell density in prostate cancer at 3.0 Tesla. Invest Radiol. 2009;44:572–576http://www.ncbi.nlm.nih.gov/pubmed/19692841.
223. Kuru TH, Roethke MC, Stieltjes B, et al. Intravoxel Incoherent Motion (IVIM) Diffusion Imaging in Prostate Cancer - What Does It Add? J Comput Assist Tomogr. 2014;38:558–564http://content.wkhealth.com/linkback/openurl?sid=WKPTLP:landingpage&an=00004728-201407000-00012. Accessed November 15, 2016.
224. Shinmoto H, Oshio K, Tanimoto A, et al. Biexponential apparent diffusion coefficients in prostate cancer. Magn Reson Imaging. 2009;27:355–359http://linkinghub.elsevier.com/retrieve/pii/S0730725X08002191. Accessed November 15, 2016.
225. Döpfert J, Lemke A, Weidner A, Schad LR. Investigation of prostate cancer using diffusion-weighted intravoxel incoherent motion imaging. Magn Reson Imaging. 2011;29:1053–1058http://linkinghub.elsevier.com/retrieve/pii/S0730725X11002293. Accessed November 15, 2016.
226. Sinha S, Sinha U. In Vivo Diffusion Tensor Imaging of the Human Prostate. 2004;537:530–537.
227. Manenti G, Carlani M, Mancino S, et al. Diffusion tensor magnetic resonance imaging of prostate cancer. Invest Radiol. 2007;42:412–419http://www.ncbi.nlm.nih.gov/pubmed/17507813.
228. Gibbs P, Pickles MD, Hons BHS, Turnbull LW. Diffusion Imaging of the Prostate at 3 . 0 Tesla. 2006;41:185–188.
229. Gürses B, Kiliçkesmez Ö, Taşdelen N, Firat Z, Gürmen N. Diffusion tensor imaging of the kidney at 3 Tesla MRI: Normative values and repeatability of measurements in healthy volunteers. Diagnostic Interv Radiol. 2011;17:317–322.
230. Quentin M, Blondin D, Klasen J, et al. Comparison of different mathematical models of diffusion-weighted prostate MR imaging. Magn Reson Imaging. Elsevier Inc.; 2012;30:1468–1474http://dx.doi.org/10.1016/j.mri.2012.04.025.
231. Uribe CF, Jones EC, Chang SD, Goldenberg SL, Reinsberg SA, Kozlowski P. In vivo 3T and ex vivo 7T diffusion tensor imaging of prostate cancer: Correlation with histology. Magn Reson Imaging. Elsevier Inc.; 2015;33:577–583http://dx.doi.org/10.1016/j.mri.2015.02.022.
232. Bourne R. Magnetic resonance microscopy of prostate tissue: How basic science can inform clinical imaging development. J Med Radiat Sci. 2013;60:5–10.
233. Assaf Y, Alexander DC, Jones DK, et al. The CONNECT project: Combining macro- and micro-structure. Neuroimage. Elsevier Inc.; 2013;80:273–282http://dx.doi.org/10.1016/j.neuroimage.2013.05.055.
234. White NS, McDonald CR, Farid N, et al. Diffusion-weighted imaging in cancer: physical foundations and applications of restriction spectrum imaging. Cancer Res. 2014;74:4638–4652http://www.ncbi.nlm.nih.gov/pubmed/25183788. Accessed December 1, 2014.

235. Bourne R, Kurniawan N, Cowin G, Sved P, Watson G. 16 T Diffusion microimaging of fixed prostate tissue: Preliminary findings. Magn Reson Med. 2011;66:244–247.
236. Le Bihan D. The “wet mind”: water and functional neuroimaging. Phys Med Biol. 2007;52:R57-90http://www.ncbi.nlm.nih.gov/pubmed/17374909. Accessed November 22, 2014.
237. White NS, Dale AM. Distinct effects of nuclear volume fraction and cell diameter on high b-value diffusion MRI contrast in tumors. Magn Reson Med. 2014;72:1435–1443.
238. Chen KC, Nicholson C, Tsien RW. Changes in brain cell shape create residual extracellular space volume and explain tortuosity behavior during osmotic challenge. .
239. Panagiotaki E, Schneider T, Siow B, Hall MG, Lythgoe MF, Alexander DC. Compartment models of the diffusion MR signal in brain white matter: a taxonomy and comparison. Neuroimage. Elsevier Inc.; 2012;59:2241–2254http://dx.doi.org/10.1016/j.neuroimage.2011.09.081. Accessed August 11, 2014.
240. Eleftheria Panagiotaki, Andrada Ianus, Edward Johnston, Rachel W Chan, David Atkinson, Shonit Punwani, David J Hawkes DCA. Optimised VERDICT MRI protocol for prostate cancer characterisation. Proc 23rd Meet Int Soc Magn Reson Med 2015. 2015;
241. Simmons LAM, Kanthabalan A, Arya M, et al. The PICTURE study : diagnostic accuracy of multiparametric MRI in men requiring a repeat prostate biopsy. Nat Publ Gr. Nature Publishing Group; 2017;1–7http://dx.doi.org/10.1038/bjc.2017.57.
242. Simmons L a M, Ahmed HU, Moore CM, et al. The PICTURE study -- prostate imaging (multi-parametric MRI and Prostate HistoScanning^{TM}) compared to transperineal ultrasound guided biopsy for significant prostate cancer risk evaluation. Contemp Clin Trials. Elsevier Inc.; 2014;37:69–83http://www.ncbi.nlm.nih.gov/pubmed/24291455. Accessed October 30, 2014.
243. Landis JR, Koch GG. The measurement of observer agreement for categorical data. Biometrics. 1977;33:159–174http://www.ncbi.nlm.nih.gov/pubmed/843571. Accessed July 20, 2014.
244. http://www.osirix-viewer.com. .
245. Chalian H, Tochetto SM, Tore HG, Rezai P, Yaghmai V. Hepatic Tumors: Region-of-Interest versus Volumetric Analysis for Quantification of Attenuation at CT. Radiology. 2012;262:853–861.
246. Engelhard K, Hollenbach HP, Deimling M, Kreckel M, Riedl C. Combination of signal intensity measurements of lesions in the peripheral zone of prostate with MRI and serum PSA level for differentiating benign disease from prostate cancer. Eur Radiol. 2000;10:1947–1953.
247. Dikaios N, Alkalbani J, Abd-Alazeez M, et al. Zone-specific logistic regression models improve classification of prostate cancer on multi-parametric MRI. Eur Radiol. 2015;2727–2737http://link.springer.com/10.1007/s00330-015-3636-0.
248. Do RKG, Chandanara H, Felker E, et al. Diagnosis of liver fibrosis and cirrhosis with diffusion-weighted imaging: Value of normalized apparent diffusion coefficient using the spleen as reference organ. Am J Roentgenol. 2010;195:671–676.
249. Barral M, Sebbag-Sfez D, Hoeffel C, et al. Characterization of focal pancreatic lesions using normalized apparent diffusion coefficient at 1.5-Tesla: Preliminary experience. Diagn Interv Imaging. Elsevier Masson SAS; 2013;94:619–627http://dx.doi.org/10.1016/j.diii.2013.02.011.
250. Itatani R, Namimoto T, Yoshimura A, et al. Clinical utility of the normalized apparent diffusion coefficient for preoperative evaluation of the aggressiveness of prostate cancer. Jpn J Radiol. 2014;32:685–691.
251. Rosenkrantz AB, Khalef V, Xu W, Babb JS, Taneja SS, Doshi AM. Does normalisation improve the diagnostic performance of apparent diffusion

coefficient values for prostate cancer assessment? A blinded independent-observer evaluation. Clin Radiol. 2015;70:1032–1037.
252. Litjens GJS, Hambrock T, Hulsbergen-van de Kaa C, Barentsz JO, Huisman HJ. Interpatient Variation in Normal Peripheral Zone Apparent Diffusion Coefficient: Effect on the Prediction of Prostate Cancer Aggressiveness. Radiology. 2012;265:260–266.
253. Jackson A, Connor JPBO, Parker GM, Jayson GC. ImagingT umor Vascular Heterogeneity and Angiogenesis using Dynamic Contrast-Enhanced Magnetic Resonance Imaging. 2007;13:3449–3460.
254. Colagrande S, Pasquinelli F, Mazzoni LN, Belli G, Virgili G. MR-diffusion weighted imaging of healthy liver parenchyma: Repeatability and reproducibility of apparent diffusion coefficient measurement. J Magn Reson Imaging. 2010;31:912–920.
255. Aerts HJWL, Velazquez ER, Leijenaar RTH, et al. Decoding tumour phenotype by noninvasive imaging using a quantitative radiomics approach. Nat Commun. 2014;5:4006http://www.pubmedcentral.nih.gov/articlerender.fcgi?artid=4059926&tool=pmcentrez&rendertype=abstract.
256. Hoang Dinh A, Melodelima C, Souchon R, et al. Quantitative Analysis of Prostate Multiparametric MR Images for Detection of Aggressive Prostate Cancer in the Peripheral Zone: A Multiple Imager Study. Radiology. 2016;280:117–127http://pubs.rsna.org/doi/10.1148/radiol.2016151406. Accessed May 27, 2017.
257. Doblas S, Almeida GS, Blé F-X, et al. Apparent diffusion coefficient is highly reproducible on preclinical imaging systems: Evidence from a seven-center multivendor study. J Magn Reson Imaging. 2015;n/a-n/ahttp://doi.wiley.com/10.1002/jmri.24955.
258. Chenevert TL, Ph D, Galbán CJ, et al. Diffusion coefficient measurement using a temperature controlled fluid for quality control in multi-center studies Thomas. 2012;34:983–987.
259. Malyarenko D, Galbán CJ, Londy FJ, et al. Multi-system repeatability and reproducibility of apparent diffusion coefficient measurement using an ice-water phantom. J Magn Reson Imaging. 2013;37:1238–1246.
260. Jafar MM. Diffusion-weighted magnetic resonance imaging in cancer: Reported apparent diffusion coefficients, *in-vitro* and *in-vivo* reproducibility. World J Radiol. 2016;8:21http://www.wjgnet.com/1949-8470/full/v8/i1/21.htm.
261. Sadinski M, Medved M, Karademir I, et al. Short-term reproducibility of apparent diffusion coefficient estimated from diffusion-weighted MRI of the prostate. Abdom Imaging. 2015;http://link.springer.com/10.1007/s00261-015-0396-x.
262. Babourina-Brooks B, Cowin GJ, Wang D. Diffusion-weighted imaging in the prostate: An apparent diffusion coefficient comparison of half-Fourier acquisition single-shot turbo spin-echo and echo planar imaging. Magn Reson Imaging. Elsevier Inc.; 2012;30:189–194http://dx.doi.org/10.1016/j.mri.2011.09.024.
263. Gibbs P, Pickles MD, Sreenivas M, Knowles a, Turnbull LW. Repeatability of Diffusion Imaging of the Prostate at 3T. 2005;13:2005.
264. Sasaki M, Yamada K, Watanabe Y, et al. Variability in absolute apparent diffusion coefficient values across different platforms may be substantial: a multivendor, multi-institutional comparison study. Radiology. 2008;249:624–630.
265. Fedorov A, Vangel MG, Tempany CM, Fennessy FM. Multiparametric Magnetic Resonance Imaging of the Prostate. Invest Radiol. 2017;1http://insights.ovid.com/crossref?an=00004424-900000000-99098. Accessed May 27, 2017.
266. Stamey T a, McNeal JE, Yemoto CM, Sigal BM, Johnstone IM. Biological determinants of cancer progression in men with prostate cancer. JAMA. 1999;281:1395–1400http://www.ncbi.nlm.nih.gov/pubmed/10217055.
267. Song SY, Kim SR, Ahn G, Choi HY. Pathologic characteristics of prostatic adenocarcinomas: a mapping analysis of Korean patients. Prostate Cancer Prostatic Dis. 2003;6:143–147http://dx.doi.org/10.1038/sj.pcan.4500636.

Accessed April 9, 2016.
268. Shih WJ, Gross K, Mitchell B, et al. Prostate adenocarcinoma using Gleason scores correlates with prostate-specific antigen and prostate acid phosphatase measurements. J Natl Med Assoc. 1992;84:1049–1050.
269. Verma A, St Onge J, Dhillon K, Chorneyko A. PSA density improves prediction of prostate cancer. Can J Urol. 2014;21:7312–7321http://www.ncbi.nlm.nih.gov/pubmed/24978363. Accessed February 28, 2016.
270. Borofsky MS, Rosenkrantz AB, Abraham N, Jain R, Taneja SS. Does suspicion of prostate cancer on integrated T2 and diffusion-weighted MRI predict more adverse pathology on radical prostatectomy? Urology. Elsevier Inc.; 2013;81:1279–1283http://dx.doi.org/10.1016/j.urology.2012.12.026.
271. Vargas MI, Becker M, Garibotto V, et al. Approaches for the optimization of MR protocols in clinical hybrid PET/MRI studies. Magn Reson Mater Physics, Biol Med. 2013;26:57–69.
272. Robertson NL, Emberton M, Moore CM. MRI-targeted prostate biopsy: a review of technique and results. Nat Rev Urol. Nature Publishing Group; 2013;10:589–597http://www.ncbi.nlm.nih.gov/pubmed/24061532. Accessed October 20, 2014.
273. Mazaheri Y, Goldman D a., Di Paolo PL, Akin O, Hricak H. Comparison of Prostate Volume Measured by Endorectal Coil MRI to Prostate Specimen Volume and Mass After Radical Prostatectomy. Acad Radiol. Elsevier Ltd; 2015;22:556–562http://www.sciencedirect.com/science/article/pii/S107663321500015X. Accessed February 13, 2016.
274. Johnston E, Punwani S. Can We Improve the Reproducibility of Quantitative Multiparametric Prostate MR Imaging Metrics? Radiology. 2016;281:652–653http://pubs.rsna.org/doi/10.1148/radiol.2016161197. Accessed March 1, 2017.
275. Zelhof B, Lowry M, Rodrigues G, Kraus S, Turnbull L. Description of magnetic resonance imaging-derived enhancement variables in pathologically confirmed prostate cancer and normal peripheral zone regions. BJU Int. 2009;104:621–627http://www.ncbi.nlm.nih.gov/pubmed/19281464. Accessed January 13, 2015.
276. López V, Fernández A, García S, Palade V, Herrera F. An insight into classification with imbalanced data: Empirical results and current trends on using data intrinsic characteristics. Inf Sci (Ny). 2013;250:113–141http://linkinghub.elsevier.com/retrieve/pii/S0020025513005124. Accessed December 29, 2016.
277. Chawla N V, Bowyer KW, Hall LO, Kegelmeyer WP. SMOTE: Synthetic Minority Over-sampling Technique. J Artif Intell Res. 2002;16:321–357.
278. Peduzzi P, Concato J, Kemper E, Holford TR, Feinstem AR. A simulation study of the number of events per variable in logistic regression analysis. J Clin Epidemiol. 1996;49:1373–1379.
279. Lee JJ, Thomas I-C, Nolley R, Ferrari M, Brooks JD, Leppert JT. Biologic differences between peripheral and transition zone prostate cancer. Prostate. 2015;75:183–190http://www.ncbi.nlm.nih.gov/pubmed/25327466. Accessed January 5, 2017.
280. Hamdy FC, Donovan JL, Lane JA, et al. 10-Year Outcomes after Monitoring, Surgery, or Radiotherapy for Localized Prostate Cancer. N Engl J Med. 2016;NEJMoa1606220http://www.nejm.org/doi/10.1056/NEJMoa1606220.
281. Prostate cancer: diagnosis and management | Guidance and guidelines | NICE. NICE; https://www.nice.org.uk/guidance/cg175. Accessed February 22, 2016.
282. Hötker AM, Mazaheri Y, Aras Ö, et al. Assessment of Prostate Cancer Aggressiveness by Use of the Combination of Quantitative DWI and Dynamic Contrast-Enhanced MRI. AJR Am J Roentgenol. 2016;1–8http://www.ncbi.nlm.nih.gov/pubmed/26900904.
283. Vos EK, Kobus T, Litjens GJSS, et al. Multiparametric Magnetic Resonance Imaging for Discriminating Low-Grade From High-Grade Prostate Cancer. Invest

Radiol. 2015;50:490–497http://content.wkhealth.com/linkback/openurl?sid=WKPTLP:landingpage&an=00004424-201508000-00004.
284. Horninger W, Berger AP, Rogatsch H, et al. Characteristics of prostate cancers detected at low PSA levels. Prostate. 2004;58:232–237http://www.ncbi.nlm.nih.gov/pubmed/14743461. Accessed January 4, 2017.
285. Sciarra A, Panebianco V, Cattarino S, et al. Multiparametric magnetic resonance imaging of the prostate can improve the predictive value of the urinary prostate cancer antigen 3 test in patients with elevated prostate-specific antigen levels and a previous negative biopsy. BJU Int. 2012;110:1661–1665http://doi.wiley.com/10.1111/j.1464-410X.2012.11146.x. Accessed January 4, 2017.
286. Stamey TA, McNeal JM, Wise AM, Clayton JL. Secondary cancers in the prostate do not determine PSA biochemical failure in untreated men undergoing radical retropubic prostatectomy. Eur Urol. 2001;39 Suppl 4:22–23http://www.ncbi.nlm.nih.gov/pubmed/11340281. Accessed January 4, 2017.
287. CombIning advaNces in imagiNg With biOmarkers for improVed Diagnosis of Aggressive prosTate cancEr - Full Text View - ClinicalTrials.gov. https://clinicaltrials.gov/ct2/show/NCT02689271?term=INNOVATE&rank=3. Accessed February 28, 2016.
288. Andre F, McShane LM, Michiels S, et al. Biomarker studies: a call for a comprehensive biomarker study registry. Nat Rev Clin Oncol. Nature Publishing Group; 2011;8:171–176http://www.nature.com/doifinder/10.1038/nrclinonc.2011.4.
289. Johnston E, Pye H, Bonet-Carne E, et al. INNOVATE: A prospective cohort study combining serum and urinary biomarkers with novel diffusion-weighted magnetic resonance imaging for the prediction and characterization of prostate cancer. BMC Cancer. BMC Cancer; 2016;16:816http://bmccancer.biomedcentral.com/articles/10.1186/s12885-016-2856-2.
290. Nagarajan R, Margolis D, Raman S, et al. Correlation of gleason scores with diffusion-weighted imaging findings of prostate cancer. Adv Urol. 2012;2012.
291. Epstein, Jonathan I. MD; Egevad, Lars MD, PhD; Amin, Mahul B. MD; Delahunt, Brett MD; Srigley, John R. MD; Humphrey, Peter A. MD P and the GC. The 2014 International Society of Urological Pathology (ISUP) Consensus Conference on Gleason Grading of Prostatic Carcinoma: Definition of Grading Patterns and Proposal for a New Grading System. Am J Surg Pathol. 2016;40:244–252http://www.ncbi.nlm.nih.gov/pubmed/26492179.
292. Daducci A, Canales-Rodríguez EJ, Zhang H, Dyrby TB, Alexander DC, Thiran J-P. Accelerated Microstructure Imaging via Convex Optimization (AMICO) from diffusion MRI data. Neuroimage. 2015;105:32–44http://linkinghub.elsevier.com/retrieve/pii/S1053811914008519. Accessed November 8, 2016.
293. Heijmink SWTPJ, Fütterer JJ, Hambrock T, et al. Prostate cancer: body-array versus endorectal coil MR imaging at 3 T--comparison of image quality, localization, and staging performance. Radiology. 2007;244:184–195.
294. Barth BK, Cornelius A, Nanz D, Eberli D, Donati OF. Comparison of image quality and patient discomfort in prostate MRI: pelvic phased array coil vs. endorectal coil. Abdom Radiol. Springer US; 2016;41:1–9.
295. Gibbs P, Pickles MD, Turnbull LW. Repeatability of echo-planar-based diffusion measurements of the human prostate at 3 T. Magn Reson Imaging. 2007;25:1423–1429.
296. Jambor I, Merisaari H, Taimen P, et al. Evaluation of different mathematical models for diffusion-weighted imaging of normal prostate and prostate cancer using high b-values: A repeatability study. Magn Reson Med. 2015;73:1988–1998.
297. Mazaheri Y, Afaq A, Rowe DB, Lu Y, Shukla-Dave A, Grover J. Diffusion-

weighted magnetic resonance imaging of the prostate: improved robustness with stretched exponential modeling. J Comput Assist Tomogr. 2012;36:695–703http://www.ncbi.nlm.nih.gov/pubmed/23192207.
298. Bourne RM, Bailey C, Johnston EW, et al. Apparatus for Histological Validation of In Vivo and Ex Vivo Magnetic Resonance Imaging of the Human Prostate. Front Oncol. 2017;7:1–8http://journal.frontiersin.org/article/10.3389/fonc.2017.00047/full.
299. Lecouvet FE, El Mouedden J, Collette L, et al. Can whole-body magnetic resonance imaging with diffusion-weighted imaging replace tc 99m bone scanning and computed tomography for single-step detection of metastases in patients with high-risk prostate cancer? Eur Urol. 2012;62:68–75.
300. Mosavi F, Johansson S, Sandberg DT, et al. Whole-Body Diffusion-Weighted MRI Compared With 18F-NaF PET/CT for Detection of Bone Metastases in Patients With High-Risk Prostate Carcinoma. Am J Roentgenol. 2012;199:1114–1120http://www.ajronline.org/doi/abs/10.2214/AJR.11.8351.
301. Venkitaraman R, Venkitaraman R, Cook G, et al. Whole-body magnetic resonance imaging in the detection of skeletal metastases in patients with prostate cancer. J Med Imaging Radiat Oncol. 2009;53:241–247.
302. Boorjian SA, Karnes RJ, Rangel LJ, Bergstralh EJ, Blute ML. Mayo Clinic Validation of the D'Amico Risk Group Classification for Predicting Survival Following Radical Prostatectomy. J Urol. 2008;179:1354–1361http://www.ncbi.nlm.nih.gov/pubmed/18289596. Accessed June 7, 2017.
303. Roach M, Hanks G, Thames H, et al. Defining biochemical failure following radiotherapy with or without hormonal therapy in men with clinically localized prostate cancer: Recommendations of the RTOG-ASTRO Phoenix Consensus Conference. Int J Radiat Oncol. 2006;65:965–974http://www.ncbi.nlm.nih.gov/pubmed/16798415. Accessed June 7, 2017.
304. Hanley JA, McNeil BJ. The meaning and use of the area under a receiver operating characteristic (ROC) curve. Radiology. 1982;143:29–36http://www.ncbi.nlm.nih.gov/pubmed/7063747. Accessed June 8, 2017.
305. Youden WJ. Index for rating diagnostic tests. Cancer. 1950;3:32–35http://onlinelibrary.wiley.com/store/10.1002/1097-0142(1950)3:1%3C32::AID-CNCR2820030106%3E3.0.CO;2-3/asset/2820030106_ftp.pdf?v=1&t=j3n2clhh&s=3d55a20e25161e48f9ee1bb50e2c0346fb61a628. Accessed June 7, 2017.
306. Padhani AR, Gogbashian A. Bony metastases: assessing response to therapy with whole-body diffusion MRI. Cancer Imaging. BioMed Central; 2011;11 Spec No A:S129-45http://www.ncbi.nlm.nih.gov/pubmed/22185786. Accessed June 15, 2017.
307. Padhani AR, Lecouvet FE, Tunariu N, et al. Practical guidelines for acquisition, reading and reporting of WB-MRI based evaluations of multiorgan involvement in advanced prostate cancer: METastasis Response Assessment Diagnostic System for Prostate cancer (MET-RADS-P). Eur Urol. European Association of Urology; 2016;1–12http://dx.doi.org/10.1016/j.eururo.2016.05.033.
308. Afshar-Oromieh A, Zechmann CM, Malcher A, et al. Comparison of PET imaging with a 68Ga-labelled PSMA ligand and 18F-choline-based PET/CT for the diagnosis of recurrent prostate cancer. Eur J Nucl Med Mol Imaging. 2014;41:11–20.
309. Afshar-Oromieh a., Malcher a., Eder M, et al. PET imaging with a [68Ga]gallium-labelled PSMA ligand for the diagnosis of prostate cancer: biodistribution in humans and first evaluation of tumour lesions. Eur J Nucl Med Mol Imaging. 2013;40:486–495.
310. Afshar-Oromieh A, Haberkorn U, Schlemmer HP, et al. Comparison of PET/CT and PET/MRI hybrid systems using a 68Ga-labelled PSMA ligand for the diagnosis of recurrent prostate cancer: Initial experience. Eur J Nucl Med Mol Imaging. 2014;41:887–897.
311. Cookson MS, Aus G, Burnett AL, et al. Variation in the Definition of Biochemical

Recurrence in Patients Treated for Localized Prostate Cancer: The American Urological Association Prostate Guidelines for Localized Prostate Cancer Update Panel Report and Recommendations for a Standard in the Reporting of Surgical Outcomes. J Urol. 2007;177:540–545http://www.ncbi.nlm.nih.gov/pubmed/17222629. Accessed June 30, 2017.
312. Cher ML, Bianco FJ, Lam JS, et al. Limited role of radionuclide bone scintigraphy in patients with prostate specific antigen elevations after radical prostatectomy. J Urol. 1998;160:1387–1391http://www.ncbi.nlm.nih.gov/pubmed/9751361.
313. Beresford MJ, Gillatt D, Benson RJ, Ajithkumar T. A Systematic Review of the Role of Imaging before Salvage Radiotherapy for Post-prostatectomy Biochemical Recurrence. Clin Oncol. Elsevier Ltd; 2010;22:46–55http://dx.doi.org/10.1016/j.clon.2009.10.015.
314. Evangelista L, Zattoni F, Guttilla A, et al. Choline PET or PET/CT and biochemical relapse of prostate cancer: a systematic review and meta-analysis. ClinNuclMed. 2013;38:305–314.
315. Heinisch M, Dirisamer A, Loidl W, et al. Positron Emission Tomography/Computed Tomography with F-18-fluorocholine for Restaging of Prostate Cancer Patients: Meaningful at PSA < 5?ng/ml? Mol Imaging Biol. Springer-Verlag; 2006;8:43–48http://link.springer.com/10.1007/s11307-005-0023-2. Accessed June 30, 2017.
316. Ward JF, Moul JW. Rising prostate-specific antigen after primary prostate cancer therapy. Nat Clin Pract Urol. 2005;2:174–182http://www.ncbi.nlm.nih.gov/pubmed/16474760. Accessed June 30, 2017.
317. Robertson NL, Sala E, Benz M, et al. Combined whole-body and multi-parametric prostate MRI as a single-step approach for the simultaneous assessment of local recurrence and metastatic disease after radical prostatectomy. J Urol. Elsevier Ltd; 2017;198:65–70http://linkinghub.elsevier.com/retrieve/pii/S0022534717302926.
318. Hausmann D, Bittencourt LK, Attenberger UI, et al. Diagnostic accuracy of 18F choline PET/CT using time-of-flight reconstruction algorithm in prostate cancer patients with biochemical recurrence. Clin Nucl Med. 2014;39:e197–e201http://www.embase.com/search/results?subaction=viewrecord&from=export&id=L52799474%5Cnhttp://dx.doi.org/10.1097/RLU.0b013e3182a23d37%5Cnhttp://sfx.library.uu.nl/utrecht?sid=EMBASE&issn=03639762&id=doi:10.1097/RLU.0b013e3182a23d37&atitle=Diagnostic+accurac.
319. Hoehler FK. Bias and prevalence effects on kappa viewed in terms of sensitivity and specificity. J Clin Epidemiol. 2000;53:499–503http://linkinghub.elsevier.com/retrieve/pii/S0895435699001742. Accessed July 26, 2017.
320. Stephenson AJ, Scardino PT, Kattan MW, et al. Predicting the outcome of salvage radiation therapy for recurrent prostate cancer after radical prostatectomy. J Clin Oncol. 2007;25:2035–2041.
321. Attariwala R, Picker W. Whole body MRI: Improved lesion detection and characterization with diffusion weighted techniques. J Magn Reson Imaging. 2013;38:253–268.
322. Eiber M, Holzapfel K, Ganter C, et al. Whole-body MRI including diffusion-weighted imaging (DWI) for patients with recurring prostate cancer: Technical feasibility and assessment of lesion conspicuity in DWI. J Magn Reson Imaging. 2011;33:1160–1170.
323. Robertson NL, Sala E, Benz M, et al. Combined whole-body and multi-parametric prostate MRI as a single-step approach for the simultaneous assessment of local recurrence and metastatic disease after radical prostatectomy. J Urol. Elsevier Inc.; 2017;http://linkinghub.elsevier.com/retrieve/pii/S0022534717302926.
324. Shiraishi J, Pesce LL, Metz CE, Doi K. Experimental Design and Data Analysis in Receiver Operating Characteristic Studies: Lessons Learned from Reports in

Radiology. 1997;http://pubs.rsna.org/doi/pdf/10.1148/radiol.2533081632. Accessed July 24, 2017.
325. Scattoni V, Picchio M, Suardi N, et al. Detection of Lymph-Node Metastases with Integrated [11C]Choline PET/CT in Patients with PSA Failure after Radical Retropubic Prostatectomy: Results Confirmed by Open Pelvic-Retroperitoneal Lymphadenectomy. Eur Urol. 2007;52:423–429.
326. Rinnab L, Mottaghy FM, Blumstein NM, et al. Evaluation of [11C]-choline positron-emission/computed tomography in patients with increasing prostate-specific antigen levels after primary treatment for prostate cancer. BJU Int. 2007;100:786–793.
327. Picchio M, Messa C, Landoni C, Gianolli L, Sironi S, Brioschi M, Matarrese M, Matei DV, De Cobelli F, Del Maschio A, Rocco F, Rigatti P FF. Value of [11C]choline-Positron Emission Tomography for Re-Staging Prostate Cancer: A Comparison With [18F]fluorodeoxyglucose-Positron Emission Tomography. J Urol. 2003;169:1337–1340http://linkinghub.elsevier.com/retrieve/pii/S0022534705637536.
328. Husarik DB, Miralbell R, Dubs M, et al. Evaluation of [(18)F]-choline PET/CT for staging and restaging of prostate cancer. Eur J Nucl Med Mol Imaging. 2008;35:253–263http://www.ncbi.nlm.nih.gov/pubmed/17926036. Accessed December 29, 2014.
329. Giovacchini G, Picchio M, Coradeschi E, et al. Predictive factors of [11C]choline PET/CT in patients with biochemical failure after radical prostatectomy. Eur J Nucl Med Mol Imaging. 2010;37:301–309.
330. Krause BJ, Souvatzoglou M, Tuncel M, et al. The detection rate of [11C]Choline-PET/CT depends on the serum PSA-value in patients with biochemical recurrence of prostate cancer. Eur J Nucl Med Mol Imaging. 2008;35:18–23.

APPENDICES

Appendix A

Clinical achievements

FRCR exam

Clinical skills developed during PhD

1. Whole body MRI reporting
    - 20 STREAMLINE C reports (primary staging of colorectal cancer)
    - 19 STREAMLINE L reports (primary staging of lung cancer)
    - 37 MASTER reports
    - Total = 76

2. I attended focal prostate MDTs and mp-MRI reporting sessions

3. I gained experience with radiotherapy planning software as part of a multidisciplinary collaboration with the UCLH Clinical Oncology team during the PROPS study

Appendix B

Courses attended during PhD

April	2017	The International Society for Magnetic Resonance in Medicine, Honolulu, Hawai'i
February	2017	Introduction to Regression Analysis, ICH Centre for Advanced Statistics. London
September	2016	Sample size and power calculations, ICH Centre for Advanced Statistics
May	2016	The 24th Annual meeting of the International Society for Magnetic Resonance in Medicine, Singapore
April	2016	Comprehensive Imaging Cancer Centre Conference, London
May	2015	British Uro-oncology Group, London
March	2015	Introduction to SPSS, University College London
January	2015	MRI Physics Course, University College London
November	2014	MATLAB computer programming course, UCL Centre for Medical Imaging

Appendix C

Funding obtained for PhD-related activities

2017	UCL School of Life and Medical Sciences stipend to attend the 25th Annual Meeting of the International Society for Magnetic Resonance in Medicine	£590
2017	UCL Centre for Medical Imaging stipend to attend the 25th Annual Meeting of the International Society for Magnetic Resonance in Medicine	£800
2017	Clinical Stipend to attend the 25th Annual Meeting of the International Society for Magnetic Resonance in Medicine	$1225
2016	Radiology Research Trust Travel Grant to attend the International Society for Magnetic Resonance in Medicine	£1000
2016	Educational stipend to attend the 24th Annual Meeting of the International Society for Magnetic Resonance in Medicine	$1090

Appendix D

Trial information

INNOVATE trial

Patient information sheet

University College London Hospitals NHS
NHS Foundation Trust

Imaging Department
UCL Hospitals
University College Hospital
235 Euston Road
London
NW1 2BU

Telephone: 020 3456 7890 ext 79324
Website: www.uclh.org

PATIENT INFORMATION SHEET

Study title: Combining advaNces in imagiNg with biOmarkers for improVed diagnosis of Aggressive prosTate cancEr

Short title: INNOVATE

PART 1

We would like to invite you to take part in a research study. Before you decide you need to understand why the research is being done and what it would involve for you. Please take time to read the following information carefully.

Part 1 tells you the purpose of this study and what will happen to you if you take part.

Part 2 gives you more detailed information about the conduct of the study. Please ask us if there is anything that is not clear or if you would like more information and take time to decide whether or not you wish to take part. You can also talk to your family, friends or your GP about the study if you wish.

What is the purpose of the study?

Your doctor is already trying to detect prostate cancer by performing a Prostate Specific Antigen (PSA) blood test and a prostate MRI.

We plan on using an additional advanced MRI technique, paired with new blood and urine tests to improve the diagnosis of aggressive prostate cancer. We will address two interlinked problems.

1) We are currently unsure which patients will benefit most from having an MRI and current methods of patient selection including a raised PSA level are

imperfect. Despite the fact that new blood and urine tests are available which may provide a better performance than PSA, they are not routinely used as they have not been fully tested in large research studies.

2) University College London (UCL) has led the way in the accurate diagnosis of prostate cancer, using MRI before biopsy to determine the location of tumours and guide accurate tissue sampling with biopsy. Although this represents a huge leap forward, around 40% MRIs are indeterminate, which means we are unsure whether aggressive cancer is present or not. This can lead to repeat MRIs and biopsies, which are associated with additional risks, discomfort and more hospital visits. We therefore propose to improve the diagnostic accuracy of prostate MRI by adding a new MRI technique called 'VERDICT' to the scan protocol. Based on our previous work, we expect that this will allow us to image the prostate in much greater detail and reduce the number of uncertain imaging results.

We hope to recruit around 365 participants into the INNOVATE study.

Why have I been invited?

You have been chosen because of the suspicion that you could have prostate cancer and;

i) Haven't had a prostate biopsy within the last 6 months
ii) Haven't had previous treatment(s) for prostate cancer

Do I have to take part?

No. It is up to you to decide. We will describe the research study in this information sheet and you may ask questions at any stage. Useful contacts are provided at the end of the information sheet. If you agree to participate, you will be asked to sign a participant consent form on the day of the scan, together with the study investigator or a coinvestigator.

You are free to withdraw at any time, without giving a reason. This would not affect the standard of care you receive.

What will happen if I agree to take part?

One of the members of the study team will ask some questions to confirm you are eligible to enrol in the study, collect your signed consent form and answer any questions you may have.

Because of the high magnetic field, all patients need to undergo a thorough safety questionnaire and assessment to ensure that any metallic implants or

devices (such as pacemakers, stents, joint replacements or even shrapnel) are compatible and safe within the scanner. In occasional circumstances, this may result in the examination being rebooked while we get further information about the metallic objects.

Once this is done, you will be asked to provide a urine and blood sample and undergo the MRI scan. There is no further special preparation for the study but you will need to lie still for the duration of the scan.

We would also inform your GP of your participation in this trial, if you decide to participate.

Blood and urine samples

A small plastic tube (cannula) will be inserted into an arm or hand vein prior to the scan. This allows MRI contrast to be given for the scan, but will also allow us to collect some blood samples at the same time for research purposes where possible. 32ml blood (less than 2 tablespoons) will be collected.

A 40ml urine sample pot will be provided, and may be filled before or after the scan.

MRI

There are two parts of the MRI scan – the clinical scan you would normally have and the additional VERDICT research scan. They are done at the same time, so you do not have to come back for another scan. Contrast agent is routinely used for the clinical part of the scan but is not required for the VERDICT scan.

The normal scan takes 40 minutes, and will proceed as normal. This scan will inform your doctor in making treatment decisions with you if prostate cancer is confirmed.

The VERDICT research scan requires 20 minutes of extra scanning time, meaning all images will be acquired within a one hour combined slot. Since the value of VERDICT MRI in assessing prostate cancer is not well known, this information will NOT be made available to your doctor, or influence your treatment. Instead, the scans will be interpreted separately, and their results are stored and assessed at a later date.

By taking part in the INNOVATE study you will have the same routine imaging investigations that you would if you didn't take part. Your participation in the research study would not affect your routine clinical care in any way, which would continue as per National Institute of Clinical Excellence (NICE) and UCLH trust guidelines.

What is the drug, device or procedure that is being tested?

The urine and blood will be analysed for levels of compounds, called 'biomarkers' which are similar to PSA. We are planning on testing a panel of 8 of these biomarkers, which we have identified as having significant promise for future clinical use.

We would also use the blood to analyse "Exosomes". Exosomes are like the body's own fleet of incredibly small vans, transporting materials between cells. Exosomes released by cancer have recently emerged as a novel therapeutic target in cancer care, as they have been implicated in cancer survival, growth, and spread.

We will compare the blood and urine test results with tissue biopsy specimens and MRI images to see if these new tests can help identify more aggressive forms of prostate cancer.

The VERDICT (**V**ascular and **E**xtracellular **R**estricted **D**iffusion for **C**ytometry **I**n **T**umours) MRI is an advanced scan, which is used to gain information about the makeup of prostate cancer. Our research so far has shown significant promise in the characterisation of prostate cancer but still needs to be validated in a clinical trial. By comparing the results of the scan to subsequent tissue biopsy specimens, we hope to improve the diagnostic performance of prostate MRI, in order to reduce needless biopsies.

What are the alternatives to participation?

Participation in this study is not your only option. You may choose to undergo only the routine investigations that would usually be undertaken in your situation. You can discuss these options with the study doctor before deciding whether or not to take part in this study project.

What are the possible benefits of taking part?

We cannot guarantee or promise that you will receive any benefits from this research. However, the information we get from this study will help improve the treatment of people with prostate cancer. If successful, the techniques we are investigating could be used routinely in all hospitals.

What are the possible disadvantages and risks of taking part?

There are few disadvantages of taking part in the study. You will have to spend 20 minutes extra time on the scanner at the same time as your routine prostate MRI. You will also have to provide a blood and urine sample, which would take a few additional minutes. The main risks of blood tests are discomfort and bruising at the site where the needle goes in. These complication are usually minor and go away shortly after the tests are done.

What are the side effects of any treatment received when taking part?

MRI is a safe technique that has no harmful side effects with the magnets used in routine clinical practice. There are certain precautions that we undertake to ensure that the individuals having the MRI scan can do so safely for example making sure that you do not have any metal in the body. We will ask you a set of routine questions before you are allowed to enter the MRI scanner room. If you participate in the study the additional time spent in the MRI scanner has no harmful side effects.

As parts of the scan could be noisy, we will provide you with earplugs and headphones through which we can play music during the scan.

Some people may experience symptoms of claustrophobia from lying in a confined space. If you do experience discomfort at any time during the scan, you will be able to alert staff by pressing on a buzzer and can communicate with them through the headphones provided. The exam will be stopped immediately on your request.

What happens when the research study stops?

After your participation in the INNOVATE study is complete, the routine standard of care will continue as normal. After the study itself is complete, we aim to analyse the results, write them up in medical journals and hopefully change the way we assess Prostate cancer.

What if there is a problem?

Any complaint about the way you have been dealt with during the clinical trial or any possible harm you might suffer will be addressed. Detailed information concerning this is given in Part 2 of this information sheet.

Will my participation in the study be kept confidential?

All information collected about you during the course of the research will be kept strictly confidential. All data is stored in accordance with the principal of the Data Protection Act 1998.

This completes part 1.

If the information in Part 1 has interested you and you are considering participation, please read the additional information in Part 2 before making a decision.

PART 2

What if relevant new information becomes available?

Sometimes during the course of a study, new information becomes available about the treatment or procedure that is being studied. If this happens, your doctor will tell you about it and discuss with you whether you want to continue in the study. If you decide to withdraw your study doctor will make arrangements for your regular health care to continue. If you decide to continue in the study you will be asked to sign an updated consent form.

Occasionally, on receiving new information your study doctor might consider it to be in your best interests to withdraw you from the study. He/ she will explain the reasons and arrange for your regular health care to continue.

What will happen if I don't want to carry on with the study?

You can withdraw from the study at any time.

What if there is a problem or what happens if something goes wrong?

If you wish to complain about your treatment by members of staff due to your participation in the research, National Health Service or UCL complaints mechanisms are available to you. Please ask your research doctor if you would like more information on this.

In the unlikely event that you are harmed by taking part in this study, or if you have concern about any about any aspect of this study, you should ask to speak to a member of the study team who will do their best to answer your questions. If you remain unhappy or wish to complain formally, you can do this through the NHS Complaints Procedure. Details can be obtained from the hospital Patient Advice and Liaison Service on 020 3456 7898 ext 73018.

If you suspect that the harm is the result of the Sponsor's (University College London Hospitals) or the hospital's negligence then you may be able to claim compensation. After discussing with your research doctor, please make the claim in writing to the Dr Shonit Punwani, who is the Chief Investigator for the research and is based at Wolfson House, University College London. The Chief Investigator will then pass the claim to the Sponsor's Insurers, via the Sponsor's office. You may have to bear the costs of the legal action initially, and you should consult a lawyer about this.

What will happen to my data?

We will create a database for the trial, which will hold your initials, date of birth and a unique trial identification number. No identifiable information (name, address and medical record number) will be recorded. The list of identification numbers and database will be held on a password protected secure NHS computer and trial images are identifiable only via the unique trial identification number. We will also securely store record the results of previous imaging/blood tests and the results of your MRI scan. All information will be held by UCLH who will collect, store, handle and process the data. Only the trial personnel will have access to the data and will be responsible for the safely and security of the data. With your permission we may use your data for future studies, although again it will be anonymised as above. For this reason we expect to keep the data for 15 years.

What will happen to my blood and urine samples?

We would like to retain your samples for future ethically approved research for 15 years. They will be stored in lab 2.4, Cruciform building, Gower Street, London, WC1E6BT. At the end of the 15-year retention period, all samples will be destroyed in accordance with the Human Tissue Authority's code of practice.

Will any genetic tests be done?

DNA tests will be performed, but will only focus on genes related to prostate cancer. We will not be able to tell your risk of other diseases. You may opt out of these tests if you wish.

Who is organising and funding the research?

This study is being conducted by Dr Shonit Punwani, Reader in Magnetic Resonance and Cancer Imaging, University College London and Honorary Consultant Radiologist, University College London Hospitals.

The study is funded by Prostate Cancer UK (PCUK).

No local or international pharmaceutical company is involved with this study. None of the researchers associated with this study are direct financial beneficiaries and do not indirectly benefit financially from your contribution or from knowledge gained through analysis of your results. You will not benefit financially from your involvement in this study. No investigator or member of research staff will receive personal financial benefit from your involvement in this study.

Who has reviewed the study?

This study has been reviewed and received favourable opinion by NHS NRES Committee London - Surrey Borders Ethics Committee and University College London Hospitals (UCLH) sponsor this project locally.

Thank you

Thank you for considering taking part and taking the time to read this sheet.

Further information and who to contact:

Principal Investigator: Dr Shonit Puwani, Reader and Honorary Consultant Radiologist in Cancer Imaging

Research Fellow: Dr Edward Johnston, Clinical Research Fellow (UCL) and Honorary Radiology Registrar (UCLH). Tel: 07944 212332

E: Edward.Johnston@uclh.nhs.uk

Consent form

University College London Hospitals NHS
NHS Foundation Trust

Site Name: University College Hospital
Patient ID:

CONSENT FORM

INNOVATE: CombIning advaNces in imagiNg with biOmarkers for impreoVed diagnosis of Aggressive prosTate canceEr

Name of Principal Investigator: Dr Shonit Punwani

		Please initial box
1.	I confirm that I have read and understand the information sheet dated ..... (version .....) for the above trial. I have had the opportunity to consider the information, ask questions and have had these answered satisfactorily.	☐
2.	I understand that my participation is voluntary and that I am free to withdraw at any time, without giving any reason, without my medical care or legal rights being affected.	☐
3.	I understand that relevant sections of any of my medical notes and data collected during the trial, may be looked at by appropriate individuals from the University College Hospital, the sponsor (and representatives of the sponsor) and relevant regulatory bodies, or from the institution where it is relevant to my taking part in this research. I give permission for these individuals to have access to my records.	☐
4.	I agree to my GP being informed of my participation in this trial.	☐
5.	I give permission for my anonymised data and a copy of this consent form to be retained in University College Hospital.	☐
6.	I agree to my anonymised data being used in future ethically approved research (data will be destroyed after 15 years).	☐
7.	I agree for my samples to be stored and used in future ethically approved research. Samples will be stored for 15 years, and then disposed of.	☐

8.	I agree to give a urine sample and 24 - 40 ml of blood	☐
9.	I agree to future biopsy/prostatectomy specimens being analysed for research purposes	☐
10.	I DO/DO NOT (please delete) consent to DNA testing	☐
11.	I agree to take part in the above trial	☐

Name of Patient	Date	Signature
_____	_____	_____
Name of person taking consent (Designated responsible person)	Date	Signature
_____	_____	_____

When completed: Take 3 copies. Original and 1 copy to be kept in medical notes and investigator site file and a copy to be given to the patient.
Data Protection Act 1998: This research project is registered for data protection and the requirements of the Act apply in full. The information held will be used for medical research purposes only and will be stored and disposed of in a secure manner.

Clinicaltrials.gov entry

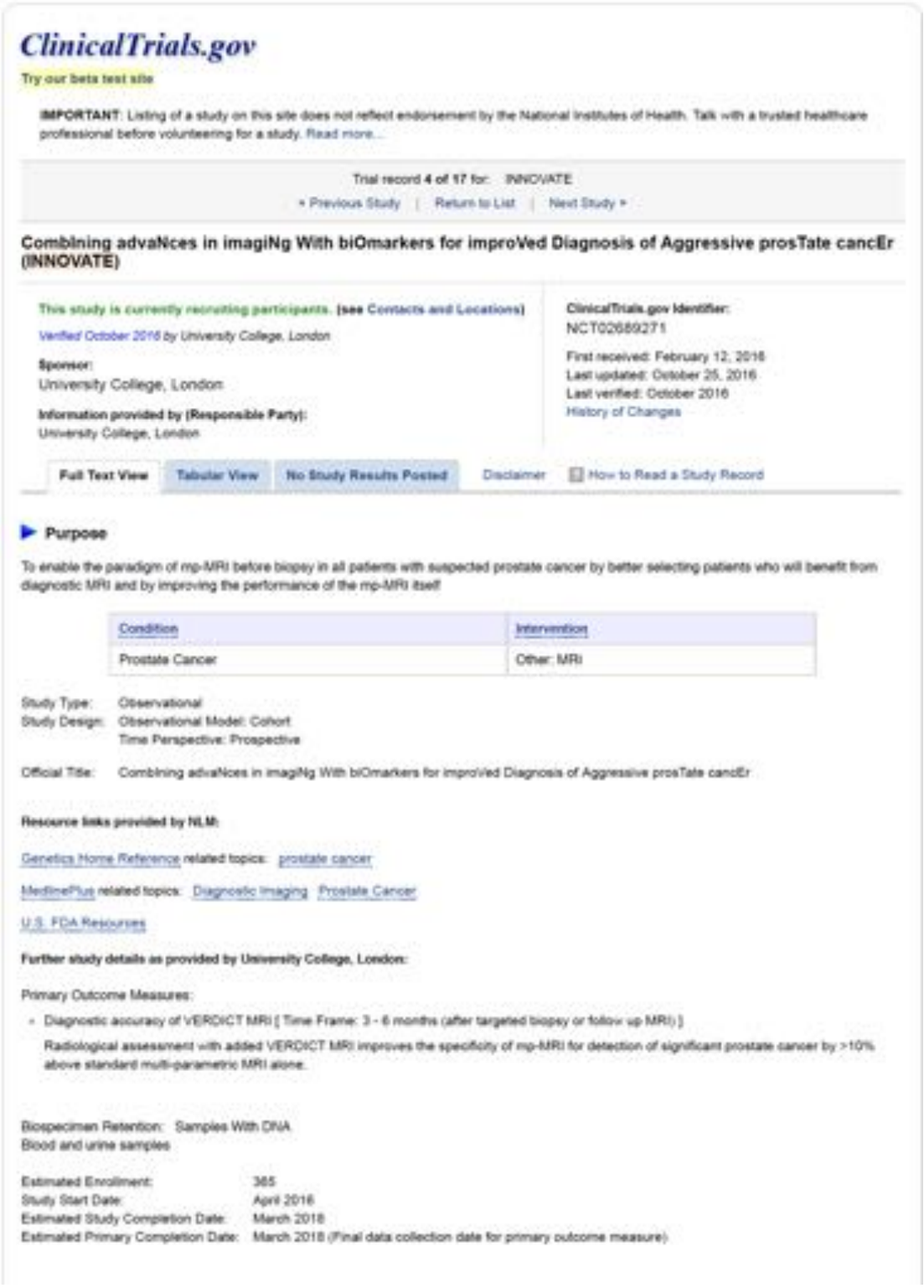

ClinicalTrials.gov

Try our beta test site

IMPORTANT: Listing of a study on this site does not reflect endorsement by the National Institutes of Health. Talk with a trusted healthcare professional before volunteering for a study. Read more...

Trial record **4 of 17** for: INNOVATE

« Previous Study | Return to List | Next Study »

Combining advaNces in imagiNg With biOmarkers for improVed Diagnosis of Aggressive prosTate cancEr (INNOVATE)

This study is currently recruiting participants. (see Contacts and Locations)

Verified October 2016 by University College, London

Sponsor:
University College, London

Information provided by (Responsible Party):
University College, London

ClinicalTrials.gov Identifier:
NCT02689271

First received: February 12, 2016
Last updated: October 25, 2016
Last verified: October 2016
History of Changes

Full Text View | Tabular View | No Study Results Posted | Disclaimer | How to Read a Study Record

Purpose

To enable the paradigm of mp-MRI before biopsy in all patients with suspected prostate cancer by better selecting patients who will benefit from diagnostic MRI and by improving the performance of the mp-MRI itself

Condition	Intervention
Prostate Cancer	Other: MRI

Study Type: Observational
Study Design: Observational Model: Cohort
Time Perspective: Prospective

Official Title: Combining advaNces in imagiNg With biOmarkers for improVed Diagnosis of Aggressive prosTate cancEr

Resource links provided by NLM:

Genetics Home Reference related topics: prostate cancer

MedlinePlus related topics: Diagnostic Imaging Prostate Cancer

U.S. FDA Resources

Further study details as provided by University College, London:

Primary Outcome Measures:

- Diagnostic accuracy of VERDICT MRI [Time Frame: 3 - 6 months (after targeted biopsy or follow up MRI)]

  Radiological assessment with added VERDICT MRI improves the specificity of mp-MRI for detection of significant prostate cancer by >10% above standard multi-parametric MRI alone.

Biospecimen Retention: Samples With DNA
Blood and urine samples

Estimated Enrollment: 385
Study Start Date: April 2016
Estimated Study Completion Date: March 2018
Estimated Primary Completion Date: March 2018 (Final data collection date for primary outcome measure)

Intervention Details:

Other: MRI

VERDICT diffusion-weighted microstructure imaging sequence

Detailed Description:

Patients will undergo an advanced diffusion-weighted MRI sequence called VERDICT with the intention of better characterising prostate cancer. A panel of serum and urine biomarkers will also be analysed, which we hope will predict those patients who go on have a positive MRI.

OBJECTIVES:

- To establish a fluidic marker - prostate MRI paradigm which: (i) utilises fluidic markers to rationalise selection of patients with significant prostate cancer; and (ii) improves the diagnostic accuracy of imaging over and above standard multiparametric (mp) MRI
- Enable a pathway for rapid clinical evaluation of emerging fluidic markers and exosomes
- Assess the repeatability of VERDICT MRI
- Ascertain whether VERDICT derived quantitative parameters correlate with quantitative histological parameters
- Develop a database of fluidic marker and VERDICT characterised, mp-MRI, histologically validated patients for subsequent exploratory and longitudinal outcome analysis

Eligibility

Ages Eligible for Study:	18 Years and older (Adult, Senior)
Sexes Eligible for Study:	Male
Accepts Healthy Volunteers:	No
Sampling Method:	Non-Probability Sample

Study Population

Men with suspected prostate cancer

Criteria

Inclusion Criteria:

- Men referred to UCLH for prostate mp-MRI following biopsy elsewhere and biopsy naive men presenting to UCLH with a clinical suspicion of prostate cancer.

Exclusion Criteria:

- Men unable to have a MRI scan, or in whom artefact would reduce quality of MRI
- Men unable to given informed consent
- Previous treatment (prostatectomy, radiotherapy, brachytherapy) of prostate cancer
- On-going hormonal treatment for prostate cancer
- Previous biopsy within 6 months of scheduled mp-MRI

Contacts and Locations

Choosing to participate in a study is an important personal decision. Talk with your doctor and family members or friends about deciding to join a study. To learn more about this study, you or your doctor may contact the study research staff using the Contacts provided below. For general information, see Learn About Clinical Studies.

Please refer to this study by its ClinicalTrials.gov identifier: NCT02689271

Locations

United Kingdom

University College London Hospital **Recruiting**
London Borough of Camden, United Kingdom, NW12BU
Contact: Edward Johnston edward.johnston@nhs.net

Sponsors and Collaborators

University College, London

More Information

Publications automatically indexed to this study by ClinicalTrials.gov Identifier (NCT Number):

Johnston E, Pye H, Bonet-Carne E, Panagiotaki E, Patel D, Galazi M, Heavey S, Carmona L, Freeman A, Trevisan G, Allen C, Kirkham A, Burling K, Stevens N, Hawkes D, Emberton M, Moore C, Ahmed HU, Atkinson D, Rodriguez-Justo M, Ng T, Alexander D, Whitaker H, Punwani S. INNOVATE: A prospective cohort study combining serum and urinary biomarkers with novel diffusion-weighted magnetic resonance imaging for the prediction and characterization of prostate cancer. BMC Cancer. 2016 Oct 21;16(1):816.

Responsible Party:	University College, London
ClinicalTrials.gov Identifier:	NCT02689271 History of Changes
Other Study ID Numbers:	15/0692
Study First Received:	February 12, 2016
Last Updated:	October 25, 2016
Individual Participant Data Plan to Share IPD:	No

Keywords provided by University College, London:
MRI
Magnetic resonance imaging
Biomarkers
Fluidics
Diffusion MRI

Additional relevant MeSH terms:

Prostatic Neoplasms	Neoplasms
Genital Neoplasms, Male	Genital Diseases, Male
Urogenital Neoplasms	Prostatic Diseases
Neoplasms by Site	

ClinicalTrials.gov processed this record on May 30, 2017

PROPS trial

Case Report Form

UCL

University College London Hospitals NHS

PROPS CRF: WB-MRI (QA) 1/6

Version 2.0, October 2016 Trial number _____

a. Image availability and coverage

Map	Yes	No	Comment
Whole body T1 (skull base to mid thigh, full AP coverage)			
Whole body diffusion (skull base to mid thigh, full AP coverage)			

b. Overall image quality (score 1 - 5):

1. Uninterpretable 2. Poor (non-diagnostic) 3. Acceptable 4. Good 5. Excellent

Map	Head	Neck	Thorax	Abdomen	Pelvis	Thigh
Whole body T1						
Whole body diffusion						

Comment _____

c. Quality of diffusion fat saturation (score 1 - 5):

1. None, 2. Poor, 3. Fair, 4. Good, 5. Excellent

Head	Neck	Thorax	Abdomen	Pelvis	Thigh

Comment _____

d. Tick artefacts:

	Ghosting	Distorsion	Susceptibility	Motion inc. pulsation	Other (state)
Whole body T1					
Whole body diffusion					

Comment _____

PROPS CRF: WB-MRI 2/6
Version 2.0, October 2016 Trial number _____

REFERENCE

American Joint Committee on Cancer

Prostate Cancer Staging

7th EDITION

Figure 1. T4 tumor invading adjacent structures other than seminal vesicles, such as bladder, rectum, levator muscles, and/or pelvic wall.

ANATOMIC STAGE/PROGNOSTIC GROUPS*

Group	T	N	M	PSA	Gleason
I	T1a–c	N0	M0	PSA <10	Gleason ≤6
	T2a	N0	M0	PSA <10	Gleason ≤6
	T1–2a	N0	M0	PSA ≥	Gleason ≥
IIA	T1a–c	N0	M0	PSA <20	Gleason 7
	T1a–c	N0	M0	PSA ≥10 <20	Gleason ≤6
	T2b	N0	M0	PSA <20	Gleason 7
	T2b	N0	M0	PSA <20	Gleason ≥7
	T2c	N0	M0	PSA ≥	Gleason ≥
IIB	T2c	N0	M0	Any PSA	Any Gleason
	T1–2	N0	M0	PSA ≥20	Any Gleason
	T1–2	N0	M0	Any PSA	Gleason ≥8
III	T3a–b	N0	M0	Any PSA	Any Gleason
IV	T4	N0	M0	Any PSA	Any Gleason
	Any T	N1	M0	Any PSA	Any Gleason
	Any T	Any N	M1	Any PSA	Any Gleason

American Cancer Society

ajcc

Financial support for AJCC 7th Edition Staging Posters provided by the American Cancer Society

Definitions

Primary Tumor (T)

CLINICAL

- TX Primary tumor cannot be assessed
- T0 No evidence of primary tumor
- T1 Clinically inapparent tumor neither palpable nor visible by imaging
- T1a Tumor incidental histologic finding in 5% or less of tissue resected
- T1b Tumor incidental histologic finding in more than 5% of tissue resected
- T1c Tumor identified by needle biopsy (for example, because of elevated PSA)
- T2 Tumor confined within prostate[1]
- T2a Tumor involves one-half of one lobe or less
- T2b Tumor involves more than one-half of one lobe but not both lobes
- T2c Tumor involves both lobes
- T3 Tumor extends through the prostate capsule[2]
- T3a Extracapsular extension (unilateral or bilateral)
- T3b Tumor invades seminal vesicle(s)
- T4 Tumor is fixed or invades adjacent structures other than seminal vesicles, such as external sphincter, rectum, bladder, levator muscles, and/or pelvic wall (Figure 4)

Pathologic (pT)[3]

- pT2 Organ-confined
- pT2a Unilateral, one-half of one side or less
- pT2b Unilateral, involving more than one-half of side but not both sides
- pT2c Bilateral disease
- pT3 Extraprostatic extension
- pT3a Extraprostatic extension or microscopic invasion of bladder neck[4]
- pT3b Seminal vesicle invasion
- pT4 Invasion of rectum, levator muscles, and/or pelvic wall

Regional Lymph Nodes (N)

CLINICAL

- NX Regional lymph nodes were not assessed
- N0 No regional lymph node metastasis
- N1 Metastasis in regional lymph node(s)

PATHOLOGIC

- pNX Regional nodes not sampled
- pN0 No positive regional nodes
- pN1 Metastasis in regional node(s)

Distant Metastasis (M)[5]

- M0 No distant metastasis
- M1 Distant metastasis
- M1a Nonregional lymph node(s)
- M1b Bone(s)
- M1c Other site(s) with or without bone disease

Notes

[1] Tumor found in one or both lobes by needle biopsy, but not palpable or reliably visible by imaging, is classified as T1c.

[2] Invasion into the prostatic apex or into (but not beyond) the prostatic capsule is classified not as T3 but as T2.

[3] There is no pathologic T1 classification.

[4] Positive surgical margin should be indicated by an R1 descriptor (residual microscopic disease).

[5] When more than one site of metastasis is present, the most advanced category is used. pM1c is most advanced.

[6] When either PSA or Gleason is not available, grouping should be determined by T stage and/or either PSA or Gleason as available.

University College London Hospitals NHS

PROPS CRF: WB-MRI 3/6
Version 2.0, October 2016 Trial number _____

WB-MRI T1 and DWI: T and N staging

1. Possible disease in prostatectomy bed?

YES ☐ NO ☐ → Q 2

	1 - Possibly	2 - Probably	3 - Very probably	4 - Almost certainly

	Clockface*	Size (mm)	Score (1-4)	Comment
Largest lesion				
Second largest lesion				

Number of additional lesions

For illustrative purposes if required

2. **Nodal sites:**

Score ≥ 2 ☐ All '1' ☐ → Go to next page

(Score all)

	Negative 1 - Highly likely not present	Equivocal 2 - Unlikely present 3 - Likely present	Positive 4 - Highly likely present

	Score (1 - 4)	Short axis diameters R nodes	Short axis diameters L nodes
Regional: Presacral			
Regional: External iliac			
Regional: Internal iliac			
Regional: Obturator			
Metastatic: Inguinal			
Metastatic: Common iliac			
Metastatic: Para-aortic			
Metastatic: Other abdominal			
Metastatic: Thoracic nodes			
Metastatic: Neck nodes			
Other _____			

N stage (circle)	NX	N0	N1	N2		Confidence (circle) 1 - low 2 - equivocal 3 - adequate 4 - good

PROPS CRF: WB-MRI 4/6
Version 2.0, October 2016 **Trial number** _____

3. WB-MRI T1 and DWI: Skeletal M staging

Metastatic bone sites:

Score ≥ 2 ☐ All '1' ☐ → Go to next page

(Score all) ↓

Negative	Equivocal	Positive
1- highly likely not present	2- unlikely present 3- likely present	4- Highly likely present

	Score (1 – 4)	Size of largest deposit	Size of second largest deposit	Number of additional deposits
Skull				
Cervical spine				
Thoracic spine				
Lumbar spine				
Pelvis				
Sternum				
R Clavicle/scapula				
L Clavicle/scapula				
R Ribs				
L Ribs				
R upper limb				
L upper limb				
R lower limb				
L lower limb				

4. WB-MRI T1 and DWI: Non-skeletal M staging

Metastatic soft tissue sites:

Score ≥ 2 ☐ All '1' ☐ → Go to next page

(Score all) ↓

Negative	Equivocal	Positive
1- highly likely not present	2- unlikely present 3- likely present	4- Highly likely present

	Score (1 - 4)	Size of largest deposit	Size of second largest deposit	Number of additional deposits
R lung				
L lung				
Liver				
Spleen				
R adrenal				
L adrenal				
R kidney				
L kidney				
Pancreas				
Mesentery/peritoneum				
Bowel				
Muscle/soft tissues State_____				
Other				

INCIDENTAL FINDINGS _____

PROPS CRF: WB-MRI 6/6
Version 2.0, October 2016 **Trial number** _____

5. FINAL MULTI-PARAMETRIC PELVIC MRI AND WHOLE-BODY MRI DISEASE STAGING:

LOCAL TUMOUR					
LOCATION (circle)	R	L	BOTH SIDES		Confidence (circle) 1- low 2 - equivocal 3 - adequate 4 - good 5 - excellent
MAX DIMENSION OF LOCAL DISEASE (CM)					
N-STAGE (CIRCLE)	NX	N0	N1		Confidence (circle) 1- low 2 - equivocal 3 - adequate 4 - good 5 - excellent
M-STAGE (CIRCLE)	M0	M1a	M1b	M1c	Confidence (circle) 1- low 2 - equivocal 3 - adequate 4 - good 5 - excellent

Signature:	Author Name:	Report Date: d d m m y y y y

Appendix E

Relevant published peer-reviewed articles

INNOVATE: A prospective cohort study combining serum and urinary biomarkers with novel diffusion-weighted magnetic resonance imaging for the prediction and characterization of prostate cancer. **Johnston E,** Pye H, Bonet-Carne E, Panagiotaki E, Patel D, Galazi M, Heavey S, Carmona L, Freeman A, Trevisan G, Allen C, Kirkham A, Burling K, Stevens N, Hawkes D, Emberton M, Moore C, Ahmed HU, Atkinson D, Rodriguez-Justo M, Ng T, Alexander D, Whitaker H, Punwani S. BMC Cancer. 2016 Oct 21;16(1):816. DOI: 10.1186/s12885-016-2856-2

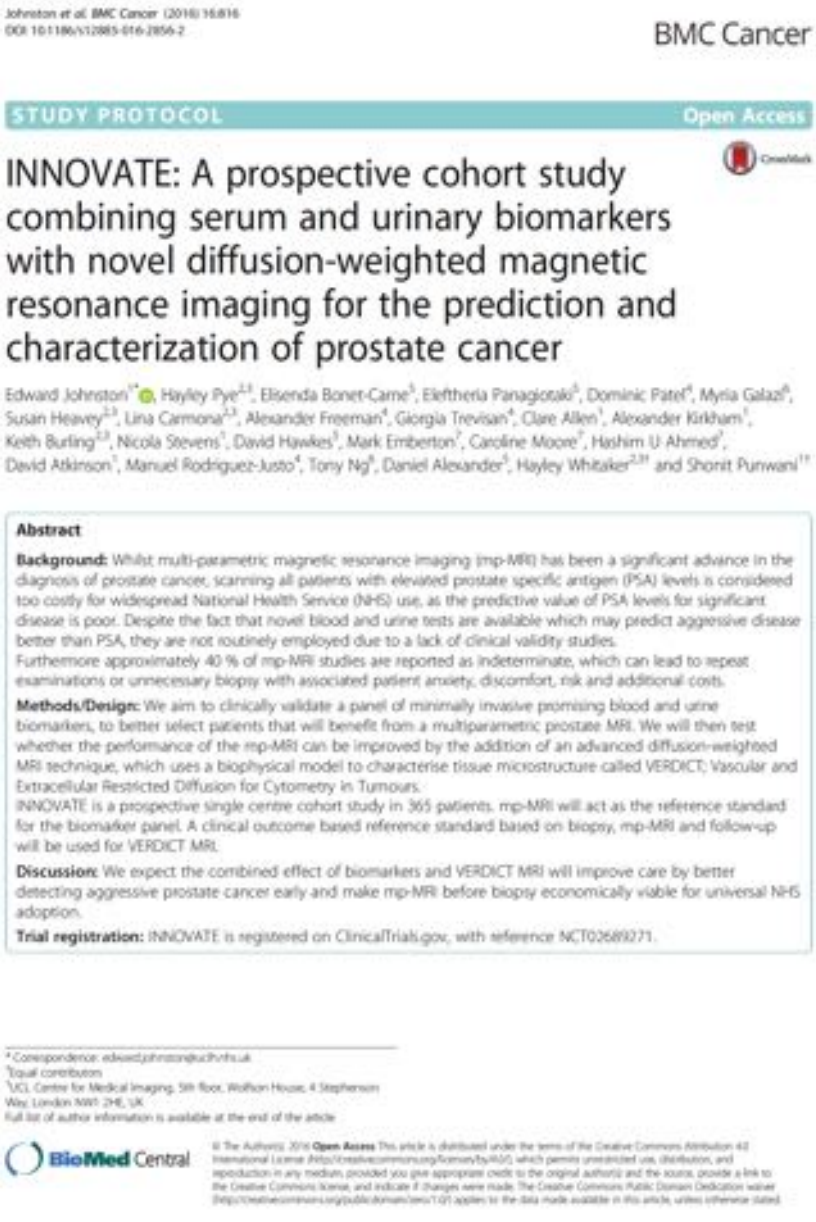

Johnston et al. BMC Cancer (2016) 16:816
DOI 10.1186/s12885-016-2856-2

BMC Cancer

STUDY PROTOCOL Open Access

INNOVATE: A prospective cohort study combining serum and urinary biomarkers with novel diffusion-weighted magnetic resonance imaging for the prediction and characterization of prostate cancer

Edward Johnston[1*], Hayley Pye[2,3], Elisenda Bonet-Carne[3], Eleftheria Panagiotaki[3], Dominic Patel[4], Myria Galazi[5], Susan Heavey[2,3], Lina Carmona[2,3], Alexander Freeman[4], Giorgia Trevisan[4], Clare Allen[1], Alexander Kirkham[1], Keith Burling[2,3], Nicola Stevens[1], David Hawkes[3], Mark Emberton[2], Caroline Moore[2], Hashim U Ahmed[2], David Atkinson[1], Manuel Rodriguez-Justo[4], Tony Ng[5], Daniel Alexander[3], Hayley Whitaker[2,3†] and Shonit Punwani[1†]

Abstract

Background: Whilst multi-parametric magnetic resonance imaging (mp-MRI) has been a significant advance in the diagnosis of prostate cancer, scanning all patients with elevated prostate specific antigen (PSA) levels is considered too costly for widespread National Health Service (NHS) use, as the predictive value of PSA levels for significant disease is poor. Despite the fact that novel blood and urine tests are available which may predict aggressive disease better than PSA, they are not routinely employed due to a lack of clinical validity studies.
Furthermore approximately 40 % of mp-MRI studies are reported as indeterminate, which can lead to repeat examinations or unnecessary biopsy with associated patient anxiety, discomfort, risk and additional costs.

Methods/Design: We aim to clinically validate a panel of minimally invasive promising blood and urine biomarkers, to better select patients that will benefit from a multiparametric prostate MRI. We will then test whether the performance of the mp-MRI can be improved by the addition of an advanced diffusion-weighted MRI technique, which uses a biophysical model to characterise tissue microstructure called VERDICT; Vascular and Extracellular Restricted Diffusion for Cytometry in Tumours.
INNOVATE is a prospective single centre cohort study in 365 patients. mp-MRI will act as the reference standard for the biomarker panel. A clinical outcome based reference standard based on biopsy, mp-MRI and follow-up will be used for VERDICT MRI.

Discussion: We expect the combined effect of biomarkers and VERDICT MRI will improve care by better detecting aggressive prostate cancer early and make mp-MRI before biopsy economically viable for universal NHS adoption.

Trial registration: INNOVATE is registered on ClinicalTrials.gov, with reference NCT02689271.

* Correspondence: edward.johnston@uclh.nhs.uk
†Equal contributors
[1]UCL Centre for Medical Imaging, 5th floor, Wolfson House, 4 Stephenson Way, London NW1 2HE, UK
Full list of author information is available at the end of the article

Background

The management of prostate cancer poses difficult challenges, which is largely because we lack the necessary tools to predict its presence, and discern between indolent disease with a small chance of clinical manifestation and aggressive tumours that are more likely to be lethal. Since prostate cancer is a complex disease, it is unlikely to be fully characterised with a single fluidic or diagnostic imaging marker.

The standard and our institutional diagnostic pathways

After presenting with symptoms, or requesting screening for prostate cancer, patients typically undergo a digital rectal exam (DRE), combined with a prostate-specific antigen (PSA) blood test.

PSA

PSA is a glycoprotein enzyme produced by normal prostate epithelium and is routinely used as a serum biomarker for prostate cancer, with raised levels typically provoking trans rectal ultrasound (TRUS) biopsy. However, in addition to prostate cancer, raised PSA levels are encountered in benign prostatic hyperplasia (BPH), prostatitis and normal prostate tissue, the PSA test has a fairly flat receiver operator characteristic curve, resulting in false positive and negative results meaning it is relatively poor at predicting or excluding significant prostate cancer [1, 2], which drives the need for more specific circulating biomarkers in its diagnosis. Circulating biomarkers in serum, plasma, urine, and prostatic fluid have all been explored, but thus far remain invalidated to a defined standard in a cohort collected under standardised conditions.

PCA3

PCA3 (prostate cancer antigen 3) is the only other routinely available biomarker, it is currently only available in a private healthcare setting. The PCA3 test is carried on urine out after DRE and detects a prostate specific non-coding ribonucleic acid (RNA). The test has shown clinical utility in diagnosing prostate cancer and can discriminate tumour cells from benign [3–5]. When used alongside magnetic resonance imaging (MRI) it shows a correlation with tumour volume but PCA3 does not appear to correlate with other clinical parameters such as stage and grade [6]. When used alongside MRI the accuracy of the PCA3 test can be improved, PCA3 score has also been shown to correlate with suspicious MRI findings and therefore could be used to select patients that require an MRI, or because MRI outperforms the PCA3 it may have greater utility in stratifying patients for active surveillance or further biopsy [7–9].

MRI

In the last 5 years, the prostate cancer community has undergone a pivotal change away from random transrectal ultrasound (TRUS) sampling of the prostate and towards image guided biopsy requiring multiparametric (mp)-MRI, including T2 weighted (T2W), diffusion weighted (DWI) and often dynamic contrast enhanced (DCE) imaging.

In January 2014 the National Institute of Clinical Excellence (NICE) issued revised guidelines on the management of prostate cancer, which included the use of mp-MRI in prostate cancer diagnostics [10]. In this document, MRI was only recommended in those with a negative TRUS and for staging where a change in tumour (T) or nodal (N) staging would alter management. The reason for this is likely to be due to the fact that mp-MRI remains a less than perfect test. For example, mp-MRI is relatively expensive, approximately 40 % of patients have equivocal findings and performance is modest for detection of small volume (<0.5 cc) tumour, lower grade aggressive disease (secondary Gleason pattern 4) and for lesions within the transition zone. In addition, the correlation of mp-MRI derived quantitative metrics with Gleason grade is only moderate; meaning it lacks biological specificity. This means further repeat multiparametric MRI studies or unnecessary biopsies are often necessitated, with associated patient discomfort, additional risks and costs.

Our proposed new pathway

To address these limitations, we propose an approach integrating promising fluidic markers together with advanced diffusion weighted MRI (VERDICT: Vascular, Extracellular and Restricted Diffusion for Cytometry in Tumours) within the diagnostic paradigm (Fig. 1).

Novel serum and urine biomarkers

The fluidic biomarkers we propose to investigate in our study have been selected based on the number of studies, patient reports and the ability of a marker to discriminate tumour from benign or predict poor outcome (Additional file 1). All markers can be tested in minimally invasive samples e.g. whole blood, serum, plasma or urine. We envision that these markers would help select patients most likely to benefit from subsequent mp-MRI, thereby rationalising valuable NHS resources. Horizon scanning will continue throughout the study to include any new and promising markers.

VERDICT MRI

Most diffusion-weighted MRI studies have used the technique in its simplest form by calculating the apparent diffusion coefficient (ADC) to identify clinically significant tumor foci more clearly [11, 12]. In general, ADC values

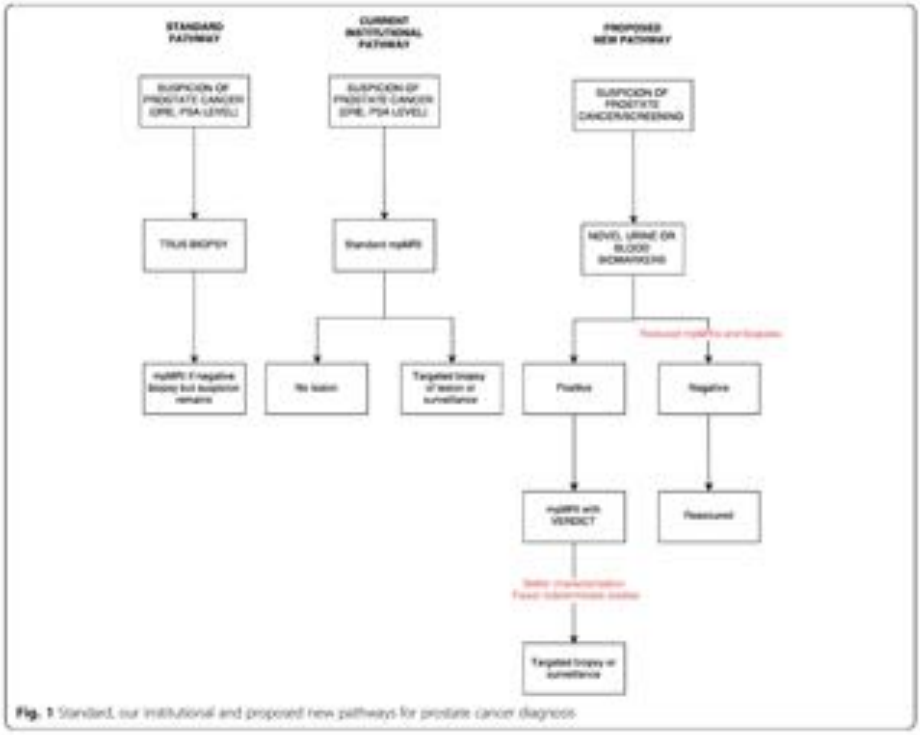

Fig. 1 Standard, our institutional and proposed new pathways for prostate cancer diagnosis

are lower in prostate carcinoma compared with healthy tissue but ADC values in both tissue types vary widely and overlap substantially [12–14].

The recent VERDICT MRI technique [15] offers the potential for explicit characterisation of tissue histology non-invasively. A proof-of-concept study for assessment of human prostate cancer [16] provided the basis for a first-in-man study of clinical validity. In this study, we imaged 8 patients with histologically confirmed peripheral zone cancer and demonstrated significant elevation in tumour fractional intracellular and fractional vascular volume, and a reduction in fractional extracellular extravascular volume, in keeping with disease histology.

Since this work, the MRI protocol has been optimised, using a computational optimisation framework [17] to reduce the VERDICT scan time from 40 min to a more clinically acceptable time of 15 min.

This is the world's first clinical trial to investigate the use of VERDICT MRI. We envision that application of VERDICT MRI will improve the specificity of mp-MRI, reduce the number of indeterminate examination results and provide evaluation of the specific histological feature changes associated with cancer.

Methods and analysis

Design

INNOVATE is a prospective cohort study with single centre recruitment. The primary objective is to assess whether supplementary VERDICT MRI improves the diagnostic accuracy of mp-MRI for detection of significant prostate cancer by a minimum of 10 %. The definitions of significant cancer have been provided previously [18].

Participants undergo standard mp-MRI [19] ± biopsy, together with studied index tests (fluidic markers and VERDICT MRI). A 50 patient pilot phase held over 1 year will provide histologically validated VERDICT MRI studies in order to familiarise radiologists and ascend the learning curve necessary for clinically interpreting VERDICT images. Initial evaluation of fluidic biomarker performance for prediction of a negative mp-MRI result will be conducted at the end of year 1 to derive thresholds for prospective application. An evaluation phase held over

2 years will prospectively test the added diagnostic accuracy of VERDICT to standard mp-MRI. During the evaluation phase, selected fluidic biomarker thresholds will be applied to collected samples to prospectively categorise patients into those expected to achieve negative and positive (with a lesion) mp-MRI scores.

Patient population

Inclusion, exclusion and withdrawal criteria are provided in Table 1 below.

Informed consent

Informed consent is a prerequisite and will be carried out on the day of the trial interventions, following a minimum 24-h period of consideration to participate in the study.

Trial Interventions

The index test – VERDICT MRI

All studies will be performed on a 3 T MRI scanner (Achieva, Philips, Amsterdam, NL). The total MRI protocol including routine mp-MRI will be limited to a maximum of 1-h scan time inclusive of 15 additional minutes allowed for VERDICT MRI. The mp-MRI protocol will be standardized, as recommended as per the UK consensus guidelines on prostate MRI [19], Table 2 below. 20 patients with tumours will undergo repeat studies, with one group having immediate repeatability (back to back scans) and another undergoing repeat studies within a week to gauge the short term repeatability of the parametric maps generated by VERDICT.

This is supplemented by an optimised VERDICT MRI technique based on previously reported work [15], which uses a Pulse-gradient spin-echo sequence and a 32 channel cardiac coil with b values of 90-3000 s/mm^2 in 3 orthogonal directions. For $b < 500$ the number of averages (NAV) = 6, for $500 < b < 1000$ NAV = 12 and for $b > 1000$ NAV = 18 with voxel size = 1.3 × 1.3 × 5 mm, matrix size = 176 × 176. The data is normalized with a $b = 0$ image for every echo time (TE) to avoid T2 dependence. Scanning parameters for VERDICT MRI are provided in Table 3.

Table 1 Inclusion, exclusion and withdrawal criteria

Patient Inclusion Criteria
1. Men referred to our center for prostate mp-MRI following biopsy elsewhere
2. Biopsy naive men presenting to our institution with a clinical suspicion of prostate cancer
Patient Exclusion Criteria
1. Men unable to have a MRI scan, or in whom artifact would reduce quality of MRI
2. Men unable to given informed consent
3. Previous treatment (prostatectomy, radiotherapy, brachytherapy) of prostate cancer
4. On-going hormonal treatment for prostate cancer
5. Previous biopsy within 6 months of scheduled mp-MRI
Withdrawal criteria
1. Images inadequate for analysis due to artifact or image acquisition problems even after a repeat scan

The parametric maps generated from the VERDICT scans produce measurements of the intracellular volume fraction (fIC), cell radius (R), cellularity, extravascular extracellular volume fraction (fEES) and vascular volume fraction (fVasc). We also retain the fitting chi-squared objective function (fobj), which is a sum of square differences adjusted to account for offset Rician noise bias, as in [15, 16], to confirm successful fitting of the biophysical VERDICT model has been or highlight regions where the model is not appropriate. A typical example of such parameter maps is provided in Fig. 2.

Reporting of mp-MRI and VERDICT MRI

MRI examination reports should record the suspicion of cancer using an ordinal Likert scale (1 to 5): 1- tumour highly unlikely, 2- tumour unlikely, 3- equivocal, 4- tumour likely and 5- tumour highly likely. Strong evidence from multiple institutions confirms mp-MRI is able to accurately detect and localise ≥0.5 cc prostate cancer ≥ Gleason 4 [19–21].

The first 50 patients VERDICT MRI studies will be used to familiarise radiologists with VERDICT MRI derived parameter maps, as they ascend the learning curve. Radiologists will be allowed to *review* the VERDICT MRI with access to biopsy results for correlation once available. Potential conclusions drawn from VERDICT datasets will not be included in clinical MRI reports as at this stage we will not know the sensitivity or specificity of VERDICT. These patients will not form part of the main trial cohort.

A locked sequential read report for mp-MRI prior to and following evaluation of VERDICT MRI will be performed for the main trial cohort. mp-MRI results will be made available to the clinical team as per standard practice. VERDICT MRI results will be collected using a case report form but will not be revealed to the clinical care team so as not to negatively influence patient care. A radiologist will compare in *vivo* MR images and note areas of abnormality as defined by the conventional mp-MRI, and corresponding regions of interest (ROIs) on the parametric VERDICT maps. In the case of prostatectomy specimens, MR slices will be visually registered to the pathological specimen. For biopsies targeted using MRI, the lesion location can be ascertained from the operation note/pathology report and in the case of positive cores, specimens can be considered to be a successful target.

Table 2 MRI phasing details for standard multiparametric prostate MRI

Sequence	Coil	TR	TE	FA degrees	WFS(pix)	BW Hz/Px	Fov mm	Slice thickness mm	Gap	TSE factor	Phasing direction	FS	ACQ matrix	TFE shots	TFE shot interval (ms)	Total scan duration
T2 TSE coronal	Dual	6128	100	90	2.704	160.7	180	3	3	16	R>L	No	300 x 290			05:55.4
T2 TSE axial	Dual	5407	100	90	2.704	160.7	180	3	0	16	R>L	No	300 x 290			05:13.6
T2 sag REF	Dual	1579	100	90	1.999	217.3	240	5	5	20	A>P	No	120 x 89			00:18.9
T1W TSE	Dual	487	8	90	1.997	217.6	240	3	3	4	R>L	No	184 x 184			03:06.8
DWI 0 150 500 1000	Dual	2753	80	90	40.353	10.8	220	5	0		A>P	SPAIR	168 x 169			05:16.5
DWI b.2000	Dual	2000	78	90	44.106	9.9	220	5	0		A>P	SPIR	168 x 169			03:40.0
DCE 2 dyn mod SENSE	Dual	5.8	2.8	90	1.766	246.1	180	3	0	88 (TFE)	R>L	SPAIR	140 x 177	49	280	00:28.9
DCE 20 dyn mod SENSE	Dual	5.8	2.8	90	1.766	246.1	180	3	0		R>L	SPAIR	140 x 162	45	280	04:14.1

Table 3 VERDICT MRI diffusion gradient parameters

b value s/mm^2	Δ/δ ms	TE ms	|G| T/m
3000	19.7/38.8	80	0.0579
2000	15.2/32.3	67	0.0758
1500	24.7/43.8	90	0.0311
500	12.2/31.3	65	0.0415
90	4.7/23.8	50	0.0506

Quantitative measurements of vascular volume fraction, extracellular extravascular volume fraction, intracellular volume fraction, cell radius and cell density will be derived from VERDICT for correlation against histological measures (see section 3.4.3).

Fluidic markers from blood and urine

Whole blood, serum, plasma and urine will be collected from all patients in the study using existing standard operating procedures (SOPs) and assayed for diagnostic markers (PCA3, AGR2 (Anterior gradient protein 2 homolog), SPON2 (spondin 2), TMPRSS2 (Transmembrane protease serine 2), EN2(Homeobox protein engrailed-2), MSMB(Beta-microseminoprotein), GDF15(Growth differentiation factor 15), SIK2 (Serine/threonine-protein kinase) and CD10(cluster of differentiation 10)). Protein markers in all matrices will be assayed on a MesoScale discovery (MSD) platform and deoxyribonucleic acid (DNA) will be extracted from whole blood to investigate 22 prognostic single nucleotide polymorphisms (SNPs) associated with aggressive disease. RNA for the PCA3 and TMPRSS2 quantification from urine will be extracted according to an SOP already developed in our laboratory. qPCR for PCA3, TMPRSS2, 3 control genes (TBP (TATA binding protein), SDH (succinate dehydrogenase), RPLP2 (60S acidic ribosomal protein P)) and PSA will be used in triplicate to quantify gene expression. During the pilot phase we will continue to horizon scan for new markers and have included scope to add 2 further markers as evidence comes to light and assays are developed e.g. GOLM1 (golgi membrane protein 1), NAALADL2 (N-Acetylated Alpha-Linked Acidic Dipeptidase-Like 2).

We will also extract exosomes from the serum and plasma (when possible) of patients to derive molecular tumour characteristics using fluorescence-lifetime imaging microscopy (FLIM) based measurements as well as analysis of exosomal micro RNA (miRNA) that are known to be associated with cell-to-cell communication

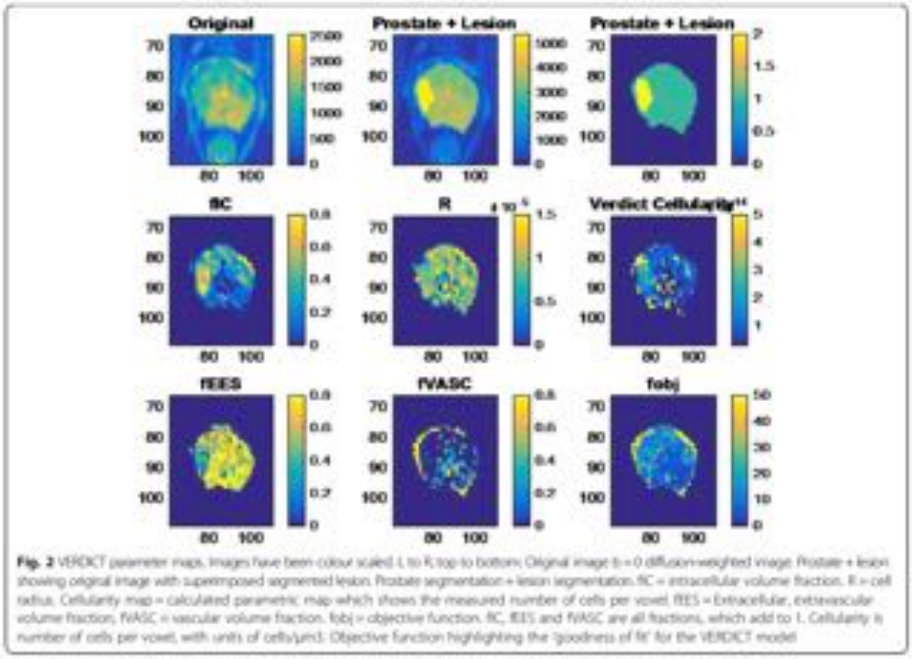

Fig. 2 VERDICT parameter maps. Images have been colour scaled. L to R, top to bottom: Original image b = 0 diffusion-weighted image. Prostate + lesion showing original image with superimposed segmented lesion. Prostate segmentation + lesion segmentation. fIC = intracellular volume fraction. R = cell radius. Cellularity map = calculated parametric map which shows the measured number of cells per voxel. fEES = Extracellular, extravascular volume fraction, fVASC = vascular volume fraction. fobj = objective function. fIC, fEES and fVASC are all fractions, which add to 1. Cellularity is number of cells per voxel, with units of cells/μm3. Objective function highlighting the 'goodness of fit' for the VERDICT model

and the development of cancer as well as immunosuppression leading to the development of further pre-metastatic niche. Functional blood-derived miRNAs have been recognised as potential robust biomarkers in the detection of various types of cancer. The ability to screen for these miRNAs and to perform FLIM of the epidermal growth factor receptor (ErbB) family members will add important prognostic and predictive information for diagnosis and stratification of patients to treatment. Finally, we will separate peripheral blood mononuclear cells (PBMCs) from whole blood of newly diagnosed prostate cancer patients to perform immunophenotyping of immune cell populations with an ultimate goal to provide multi-modality patient stratification.

Defining reference standards

Biomarker panel: mp-MRI result

Since it is envisaged that diagnostic biomarker thresholds in the blood or urine will be able to predict a negative mp-MRI result, and act as a gatekeeper to effectively rationalise its use, conventional mp-MRI result will form the reference standard. Any lesion (Likert score 3 and above) will be considered to be a positive result. VERDICT MRI will not be considered as part of the reference standard for fluidic markers as the utility of VERDICT MRI remains unknown.

VERDICT MRI: histology/mpMRI based reference standard

A lesion based reference standard will be derived (Fig. 3). mp-MRI has a 90-95 % negative predictive value for exclusion of aggressive disease [22] and will therefore form the reference for the index tests when mp-MRI is negative (Likert score 1-2/5). The positive predictive value of mp-MRI is limited and reported between 60-70 %. Therefore, where mp-MRI is positive (Likert score 3-5/5) a prostatectomy or biopsy will be performed if clinically appropriate. The prostatectomy or biopsy will then supersede the mp-MRI as the reference standard. Where a biopsy or prostatectomy is not performed, patients will be followed up with interval (6 months-1 year) mp-MRI as part of standard clinical care. A progressive Likert score (3/5 - > 4/5 or 5/5) or a progressive lesion (previously scored 4-5) on repeat mp-MRI will be considered as positive for the reference standard. A negative Likert score (1-2/5) on the repeat mp-MRI will be considered as negative for the reference standard. Lesions that remain stable with Likert score 3/5 will be deemed indeterminate and excluded from analysis unless biopsied. Based on previous internal audit, the total number of excluded patients is predicted to be approximately 10 %.

Histopathological data processing and collection

The clinically most appropriate biopsy route for each patient will be used to obtain tissue, as informed by the mp-MRI and discussed and documented at the prostate Multi-disciplinary Team (MDT). Decision to biopsy or perform prostatectomy will be based on mp-MRI (not VERDICT MRI).

Tissue samples will be collected, fixed in formalin and embedded in paraffin. Sections will be and stained with hematoxylin and eosin (H&E) as per standard national health service (NHS) protocols. Immunohistochemical staining will also be performed for blood vessels and capillaries as per standard methods.

Histopathological assessment will be performed by two blinded histopathologists independently and then in consensus. Biopsy and whole block sections taken will be analysed after conventional H&E staining to assess tumor morphology including Gleason score, tumor volume/cancer core length, cell density, cell size distribution and percentage of epithelium/stroma. In addition immunohistochemistry for vascular markers will be performed for assessment of microvessel density.

To quantify the prostatic tissue components, automated segmentation of the core biopsies shall be performed, mapping blood vessels, lumen, epithelial cells and stroma using software developed in house.

In addition, detailed histological correlation will be sought for each of the specific imaging findings. A database table will be constructed listing the imaging observations and the histological findings listed in Table 4, with histological scores provided for each main observation.

Statistical considerations

Sample size calculation

A sample size of 280 subjects achieves 80 % power to detect a difference of 0.1 between two diagnostic tests whose specificities are 0.7 and 0.6. This calculation uses a two-sided McNemar test with a significance level of 0.05. The prevalence of patients with no cancer or insignificant cancer (≤Gleason 3 + 3) is estimated at 0.6. The proportion of discordant pairs is estimated at 0.2. Allowing for 10 % of patients being excluded from the reference standard, a total of 365 patients (50 to allow radiologist training, followed by 315 patients for the main study) will be recruited. Based on current practice at our institution, approximately 10 mp-MRI studies are performed per week in men that meet the eligibility criteria. With a 50 % recruitment rate (note our audit data from previous similar studies supports a recruitment rate of 90 %), complete recruitment is expected to take 73 weeks.

Outcome measures

All primary and secondary outcomes are presented in Table 5 below.

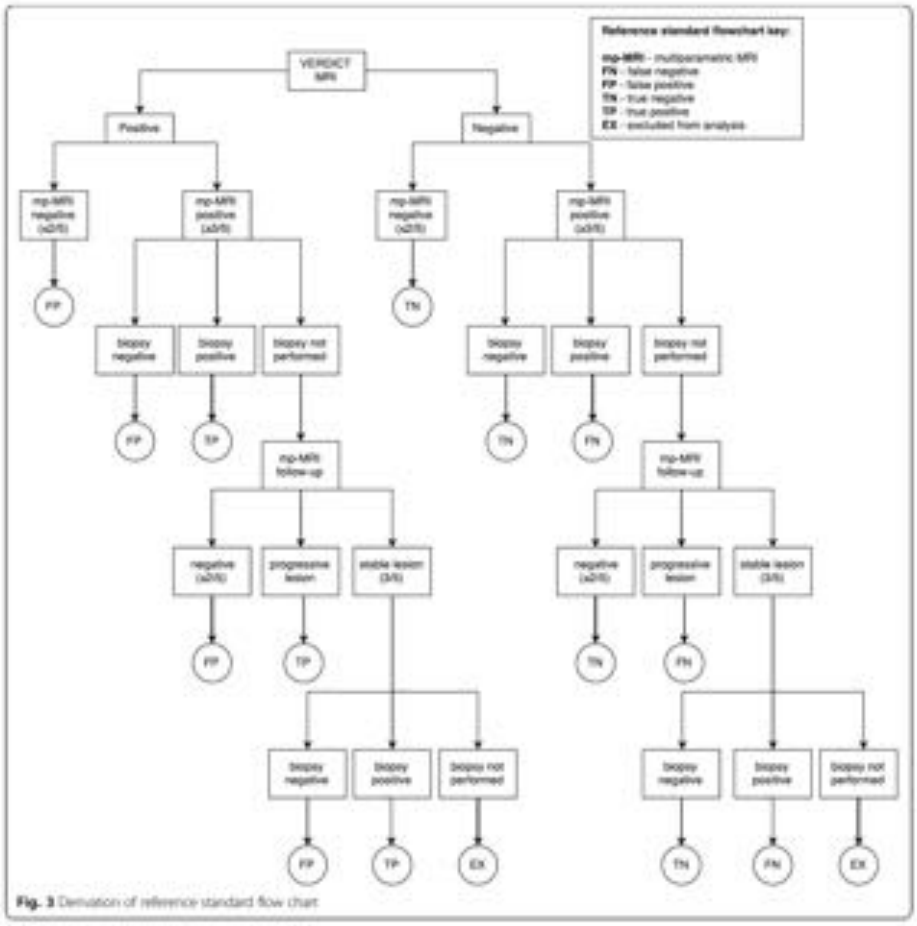

Fig. 3 Derivation of reference standard flow chart

Table 4 Imaging parameters vs. histological correlates

VERDICT parameter	Histological parameter
Intracellular volume fraction	Cell coverage fraction per high power field
Vascular volume fraction	Vascular coverage fraction per high power field
Extravascular extracellular volume fraction	Glandular + stromal coverage fraction per high power field
Cell radius	Average cell radius in a high power field
Cellularity	Cell count per high power field

Table 5 Primary and secondary outcome measures

Primary outcome

- Radiological assessment with added VERDICT MRI improves the diagnostic accuracy of mp-MRI for detection of significant prostate cancer by a minimum of 10 %

Secondary outcomes

- A group of diagnostic fluidic markers measured on the MesoScale discovery (MSD) platform and/or in DNA and RNA, can predict patients with a negative mp-MRI result (i.e. 1-2/5 Likert score).
- The use of patient serum-derived exosomes as 'liquid biopsies' for the identification of genomic and molecular aberrations that can be used to better predict patients with aggressive or high volume prostate cancer
- Technical validation of VERDICT:
  - VERDICT MRI is qualitatively and quantitatively repeatable
- Biological validation of VERDICT:
  - VERDICT cellularity measure correlates with histological cell density
  - VERDICT intracellular volume fraction correlates with segmented fractional histological intracellular component
  - VERDICT vascular volume fraction correlates with segmented fractional histological vascular component
  - VERDICT extracellular extravascular volume fraction correlates with fractional segmented histological glandular component + stromal component
- Set-up of imaging/fluidic marker outcome linked database

Data analysis and outcome assessment

Fluidic markers

The diagnostic accuracy of fluidic markers will also be evaluated against the Likert score from the mpMRI, to gauge whether they may be used as a sensitive gatekeeper to reliably exclude patients in whom the mpMRI result is likely to be negative (Likert 1/2). To do this, results of each fluidic marker will be compared against the Likert score and a sensitivity and specificity will be acquired allowing for Receiver operating curve (ROC) and area under curve (AUC) analysis to subsequently be performed. Cancer volume and Gleason grade will be correlated with exosome levels, to judge whether they may have any useful clinical application as biomarkers in the future.

VERDICT MRI

Lesion based analysis will be performed to compare specificity of mp-MRI with and without VERDICT MRI (at a Likert threshold of 3/5 as positive) against the reference standard, to ascertain whether VERDICT has any added diagnostic value. Correlation of VERDICT derived maps and quantitative histological parameters will also be assessed using correlation coefficients, and Bland-Altman plots.

Finally, a full clinical demographic, fluidic marker, qualitative and quantitative mp-MRI, and quantitative VERDICT parameter database will be established for future exploratory assessment and prediction of longer-term patient outcome.

We believe the INNOVATE study will be important, because it is one of the first clinical trials to bring together two important communities involved in prostate cancer research in a single project, namely imaging and fluidic biomarkers, who have traditionally worked in parallel. The findings of this study will also be particularly interesting, as the results from clinical trials of potential biomarkers are urgently needed and it also represents the world's first clinical trial involving VERDICT MRI.

Discussion

The INNOVATE study has some potential limitations. Firstly, as an observational trial, we are unable to take additional biopsies based on the VERDICT MRI result. This is because it would be unethical to perform additional biopsies at this stage of biomarker development, as it would lead to unnecessary increased risk.

However, if VERDICT MRI is shown to be successful in characterizing lesions within the prostate, additional biopsies would be particularly desirable where lesions are VERDICT positive but negative on conventional mpMRI, to determine whether such discrepancies are due to tumour.

Similarly, is also uncertain how many mp-MRIs will have lesions that are subsequently biopsied, as diagnostic and treatment decisions are made according to the standard clinical pathway. In addition, since PSA is a poor gatekeeper for MRI positive lesions, there will be a considerable number of scans which are mp-MRI negative, which could be said to increase the cost and reduce the efficiency of this trial, but will also allow us to better understand the appearances of normal VERDICT signal.

As with any quantitative imaging study testing a new sequence, the generalizability of data will be limited in the first instance, and will only apply to our scanner. However, if VERDICT is confirmed to be a repeatable and clinically useful test for the diagnosis and characterization of prostate cancer, our next step would be to conduct a reproducibility study, using the VERDICT scan protocol established on a different scanner. If the VERDICT sequence is confirmed to be acceptably reproducible, it would need to be programmed and made available on other scanners to confirm its usefulness as part of a multicenter trial. In this way, the development of the VERDICT sequence as a useful imaging biomarker should follow a logical stepwise progression, according to biomarker roadmaps, such as those outlined in the consensus document for use of diffusion-weighted MRI as a cancer biomarker [23], or by Cancer Research UK [24].

This study is also limited to using a combined histological/imaging/follow-up reference standard. Such

standards are commonly employed in radiological studies when developing new techniques. Whilst tissue is usually preferable, it would be unethical to sample patients with no evident tumour at this stage of VERDICT development. Where tissue is obtained, there is some debate as to what forms the ideal histological reference standard. Whilst whole mount prostatectomy provides the most complete information with excellent spatial localization of tumors, which can later be registered to MRI datasets, prostatectomy cannot be used in all patients and therefore suffers from spectrum bias, whereby more aggressive tumors are selected [22]. Whilst template biopsy does not experience this problem, registration of the biopsy coordinates with the MRI is limited, and as a sampling technique is subject to sampling error [25], and may miss smaller tumors <0.2 cc [26]. Despite these controversies, both prostatectomy and template biopsy remain preferable to TRUS biopsy, which remains the standard of care in most centers but systematically misses 20 – 30 % of clinically significant cancers [27], particularly in the anterior gland [28].

Conclusion

INNOVATE is a 365 patient cohort study being carried out over 3 years, whereby we wish to validate a biomarker panel to act as an effective gatekeeper to rationalize mp-MRI for widespread NHS adoption. We aim to confirm for the first time that VERDICT MRI is a repeatable technique and consider whether it can provide additional sensitivity and specificity for the detection of prostate cancer. If the parametric maps generated from VERDICT are shown to correlate with Gleason grade better than current quantitative multiparametric MRI measurands, VERDICT MRI could prove useful in a range of circumstances including the prevention or triggering prostate biopsy in biopsy naive patients, patients being monitored under active surveillance and when assessing for disease recurrence following surgical, focal or radiotherapy.

Trial status

Investigators from UCLH designed the trial and UCLH acts as the study sponsor. The UCLH Joint Research Office maintains responsibility for monitoring of Good Clinical Practice within the trial. A trial management group for the study comprises specialists from the disciplines of Radiology, Radiography and Biomarker science. Currently INNOVATE is open for recruitment in 1 Centre in the United Kingdom. Recruitment commenced in April 2016 and is expected to finish in March 2019. INNOVATE received UK Research Ethics Committee approval on 23rd December 2015 by the NRES Committee London—Surrey Borders with REC reference 15/LO/0692. INNOVATE is published on clinicaltrials.gov [29].

Additional file

Additional file 1: A referenced list of the fluidic biomarkers to be tested in the cohort. (DOCX 163 kb)

Abbreviations

ADC: Apparent diffusion coefficient; AGR 2: Anterior gradient protein 2 homolog; AUC: Area under curve; BPH: Benign prostatic hyperplasia; CD10: Cluster of differentiation 10; DCE: Dynamic contrast enhanced imaging; DNA: Deoxyribonucleic acid; DRE: Digital rectal examination; DWI: Diffusion-weighted imaging; EN2: Homeobox protein engrailed-2; ErbB: Epidermal growth factor receptor; IEE3: Extravascular extracellular volume fraction; IC: Intracellular volume fraction; FLIM: Fluorescence-lifetime imaging microscopy; fobj: Objective function; fVasc: Vascular volume fraction; GDF15: Growth differentiation factor 15; GOLM 1: Golgi membrane protein 1; H&E: Hematoxylin and eosin; MDT: Multi-disciplinary team; miRNA: micro RNA; mp-MRI: Multi-parametric magnetic resonance imaging; MRD: MessScale discovery; MR: Magnetic resonance imaging; MSMB: Beta-microseminoprotein; NAALADL2: N-acetylated alpha-linked acidic dipeptidase-like 2; NAV: Number of averages; NHS: National Health Service; NICE: National Institute of Clinical Excellence; PBMC: Peripheral blood mononuclear cell; PCA3: Prostate cancer antigen 3; PSA: Prostate specific antigen; R: Cell radius; RNA: Ribonucleic acid; ROC: Receiver operating curve; ROI: Region of interest; RPLP2: 60S acidic ribosomal protein P; SDH: Succinate dehydrogenase; SKO: Serine/threonine-protein kinase; SNP: Single nucleotide polymorphism; SOP: Standard operating procedure; SPON2: Spondin 2; T2W: T2-weighted imaging; TBP: TATA binding protein; TE: Echo time; TMPRSS2: Transmembrane protease serine 2; TRUS: Transrectal ultrasound; VERDICT: Vascular and extracellular restricted diffusion for cytometry in tumours

Acknowledgements

The work of Edward Johnston, Shonit Punwani, Manuel Rodriguez-Justo and Dominic Patel is supported by the UCL/UCLH Biomedical Research Centre. EPSRC grants G007748 and H046410 support Daniel Alexander's, Eleanda Bonet-Carne, and Eleftheria Panagiotaki work on this topic. The work of Tony Ng and Myria Galazi are in part supported by Cancer Research UK (grants C1519/A16906 and C5255/A15935) the King's College London-UCL Comprehensive Cancer Imaging Centre (CR-UK & EPSRC) and in association with the MRC and DoH (grants C1519/ A16463 and C1519/A10331); and a Clinical Fellowship from the UCL Cancer Research UK Cancer Centre. CMM is funded by the NIHR Cambridge Biomedical Research Centre.

Funding

This work is supported by Prostate Cancer UK Targeted Call 2014: Translational Research St.2; project reference PG14-016-TR2. Department of Health Disclaimer: The views and opinions expressed therein are those of the authors and do not necessarily reflect those of Prostate Cancer UK, the NHS or the Department of Health.

Availability of data and materials

Not applicable.

Authors' contributions

Study concept and initial design: SP, HW, DA, DH. Study design and statistical analysis: SP, HW, EJ, HP, E B-C, EP. Acquisition of data and Data analysis and interpretation: EJ, HP, E B-C, EP, DP, MG, SH, LC, AF, GT, CA, AK, KB, NS, DH, ME, CM, HA, DA, MI R-J, TN, DA, HW, SP. All authors read and approved the final manuscript.

Competing interests

Dr. Hashim Ahmed receives funding from the Medical Research Council (UK), Sonacare Medical, Sophiris and Trod Medical for other trials. Travel allowance was previously provided from Sonacare Inc. David Hawkes is a founder Shareholder of IXICO plc. Adviser and shareholder VisionRT.

Consent for publication

Not applicable.

Ethics approval and consent to participate
The study abides by the principles of the Declaration of Helsinki and the UK Research Governance Framework version 2. INNOVATE received UK Research Ethics Committee approval on 23rd December 2015 by the NRES Committee London—Surrey Borders with REC reference 15/LO/0602. Findings from this research will be disseminated at conferences and submitted for peer-reviewed publications.

Author details
[1]UCL Centre for Medical Imaging, 5th floor, Wolfson House, 4 Stephenson Way, London NW1 2HE, UK. [2]Research Department for Tissue & Energy, Division of Surgery & Interventional Science, Wing 2.4 Cruciform Building, Gower Street, London WC1E 6BT, UK. [3]Addenbrookes Hospital, Level 4, Pathology Block, Hills Road, Cambridge CB20QQ, UK. [4]Department of Research Pathology, UCL Cancer Institute, Rockefeller Building, 21 University Street, London WC1E 6JJ, UK. [5]Department of Computer Science, UCL, Gower Street, London WC1E 6BT, UK. [6]Molecular Oncology group, UCL Cancer Institute, Paul O'Gorman Building, 72 Huntley Street, London WC1E 6DD, UK. [7]Division of Surgery, 4th floor, 21 University Street, London WC1E, UK.

Received: 20 April 2016 Accepted: 12 October 2016
Published online: 21 October 2016

References

1. Roobol MW, Duffy MJ, Hamdy FC, et al. Use of prostate-specific antigen (PSA) isoforms for the detection of prostate cancer in men with a PSA level of 2-10 ng/ml: systematic review and meta-analysis. Eur Urol. 2005;48:386–99. doi:10.1016/j.eururo.2005.04.015. discussion 398–9.
2. Catalona WJ, Hudson MA, Scardino PT, et al. Selection of optimal prostate specific antigen cutoffs for early detection of prostate cancer: receiver operating characteristic curves. J Urol. 1994;152:2037–42.
3. de Kok JB, Verhaegh GW, Roelofs RW, et al. DD3(PCA3), a very sensitive and specific marker to detect prostate tumors. Cancer Res. 2002;62:2695–8.
4. van Gils MPMQ, Hessels D, van Hooij O, et al. The time-resolved fluorescence-based PCA3 test on urinary sediments after digital rectal examination; a Dutch multicenter validation of the diagnostic performance. Clin Cancer Res. 2007;13:939–43. doi:10.1158/1078-0432.CCR-06-2679.
5. Hessels D, Schalken JA. The use of PCA3 in the diagnosis of prostate cancer. Nat Rev Urol. 2009;6:255–61. doi:10.1038/nrurol.2009.40.
6. Ploussard G, Durand X, Xylinas E, et al. Prostate cancer antigen 3 score accurately predicts tumour volume and might help in selecting prostate cancer patients for active surveillance. Eur Urol. 2011;59:422–9. doi:10.1016/j.eururo.2010.11.044.
7. Sciarra A, Panebianco V, Cattarino S, et al. Multiparametric magnetic resonance imaging of the prostate can improve the predictive value of the urinary prostate cancer antigen 3 test in patients with elevated prostate-specific antigen levels and a previous negative biopsy. BJU Int. 2012;110:1661–5. doi:10.1111/j.1464-410X.2012.11146.x.
8. Leyten GHJM, Wieringa EA, Sedelaar JPM, et al. Value of PCA3 to predict biopsy outcome and its potential role in selecting patients for multiparametric MRI. Int J Mol Sci. 2013;14:11947–55. doi:10.3390/ijms140611947.
9. Panebianco V, Sciarra A, Del Berardinis E, et al. PCA3 urinary test versus 1H-MRSI and DCEMRI in the detection of prostate cancer foci in patients with biochemical alterations. Anticancer Res. 2011;31:1399–405.
10. Prostate cancer: diagnosis and management. NICE, January 2014. Available via http://www.nice.org.uk/guidance/CG175. Accessed 16 Oct 2016.
11. Sato C, Naganawa S, Nakamura T, et al. Differentiation of noncancerous tissue and cancer lesions by apparent diffusion coefficient values in transition and peripheral zones of the prostate. J Magn Reson Imaging. 2005;21:258–62. doi:10.1002/jmri.20251.
12. Lim HK, Kim JK, Kim KA, Cho K. Prostate cancer: apparent diffusion coefficient map with T2-weighted images for detection — a multireader purpose : methods : results : conclusion. Radiology. 2009;250:145–51.
13. Gibbs P, Liney GP, Pickles MD, et al. Correlation of ADC and T2 measurements with cell density in prostate cancer at 3.0 Tesla. Invest Radiol. 2009;44:572–6. doi:10.1097/RLI.0b013e3181b4c10e.
14. Riches SF, Hawtin K, Charles-Edwards EM, de Souza NM. Diffusion-weighted imaging of the prostate and rectal wall: comparison of biexponential and monoexponential modelled diffusion and associated perfusion coefficients. NMR Biomed. 2009;22:318–25. doi:10.1002/nbm.1328.
15. Panagiotaki E, Walter-Sonnen S, Siow B, et al. Noninvasive quantification of solid tumor microstructure using VERDICT MRI. Cancer Res. 2014;74:1902–12. doi:10.1158/0008-5472.CAN-13-2511.
16. Panagiotaki E, Chan RW, Dikaios N, et al. Microstructural characterization of normal and malignant human prostate tissue with vascular, extracellular, and restricted diffusion for cytometry in tumours magnetic resonance imaging. Invest Radiol. 2015;001:1–10.
17. Alexander DC. A general framework for experiment design in diffusion MRI and its application in measuring direct tissue-microstructure features. Magn Reson Med. 2008;60:439–48. doi:10.1002/mrm.21646.
18. Ahmed HU, Hu Y, Carter T, et al. Characterizing clinically significant prostate cancer using template prostate mapping biopsy. J Urol. 2011;186:458–64. doi:10.1016/j.juro.2011.03.147.
19. Kirkham a PS, Haslam P, Keanie JY, et al. Prostate MRI: who, when, and how? Report from a UK consensus meeting. Clin Radiol. 2013;68:1016–23. doi:10.1016/j.crad.2013.03.030.
20. Barentsz JO, Richenberg J, Clements R, et al. ESUR prostate MR guidelines 2012. Eur Radiol. 2012;22:746–57. doi:10.1007/s00330-011-2377-y.
21. Dickinson L, Ahmed HU, Allen C, et al. Magnetic resonance imaging for the detection, localisation, and characterisation of prostate cancer: recommendations from a European consensus meeting. Eur Urol. 2011;59:477–94. doi:10.1016/j.eururo.2010.12.009.
22. Arumainayagam N, Ahmed HU, Moore CM, et al. Multiparametric MR imaging for detection of clinically significant prostate cancer: a validation cohort study with transperineal template prostate mapping as the reference standard. Radiology. 2013;268:761–9. doi:10.1148/radiol.13120640.
23. Padhani AR, Liu G, Koh DM, et al. Diffusion-weighted magnetic resonance imaging as a cancer biomarker: consensus and recommendations. Neoplasia. 2009;11:102–25. doi:10.1593/neo.81328.
24. Lourie M, Newell D, CR-UK biomarker roadmaps. Clin Cancer Res. 2010;16:693. doi:10.1158/1078-0432.CCR-09-2670.
25. Ukimura O, Coleman JA, De La Taille A, et al. Contemporary role of systematic prostate biopsies: indications, techniques, and implications for patient care. Eur Urol. 2013;63:214–30. doi:10.1016/j.eururo.2012.06.033.
26. Lecornet E, Ahmed HU, Hu Y, et al. The accuracy of different biopsy strategies for the detection of clinically important prostate cancer: a computer simulation. J Urol. 2012;188:974–80. doi:10.1016/j.juro.2012.04.104.
27. Djavan B, Ravery V, Zlotta A, et al. Prospective evaluation of prostate cancer detected on biopsies 1, 2, 3 and 4: when should we stop? J Urol. 2001;166:79–83.
28. McNeal JE, Redwine EA, Freiha FS, Stamey TA. Zonal distribution of prostatic adenocarcinoma. Correlation with histologic pattern and direction of spread. Am J Surg Pathol. 1988;12:897–906.
29. Combining advances in imaging With biOmarkers for improVed Diagnosis of Aggressive proSTate cancEr. ClinicalTrials.gov. https://clinicaltrials.gov/ct2/show/NCT02668071?term=prostate+INNOVATE&rank=1.

R. Bourne, C. Bailey, **E. Johnston**, H. Pye, S. Heavey, H. Whitaker, B. Siow, A. Freeman, G. Shaw, A. Sridhar, T. Mertzanidou, D. Hawkes, D. Alexander, S. Punwani, E. Panagiotaki. "Apparatus for histological validation of in vivo and ex vivo magnetic resonance imaging of the human prostate". Frontiers in Oncology. 47: 7, 2017.

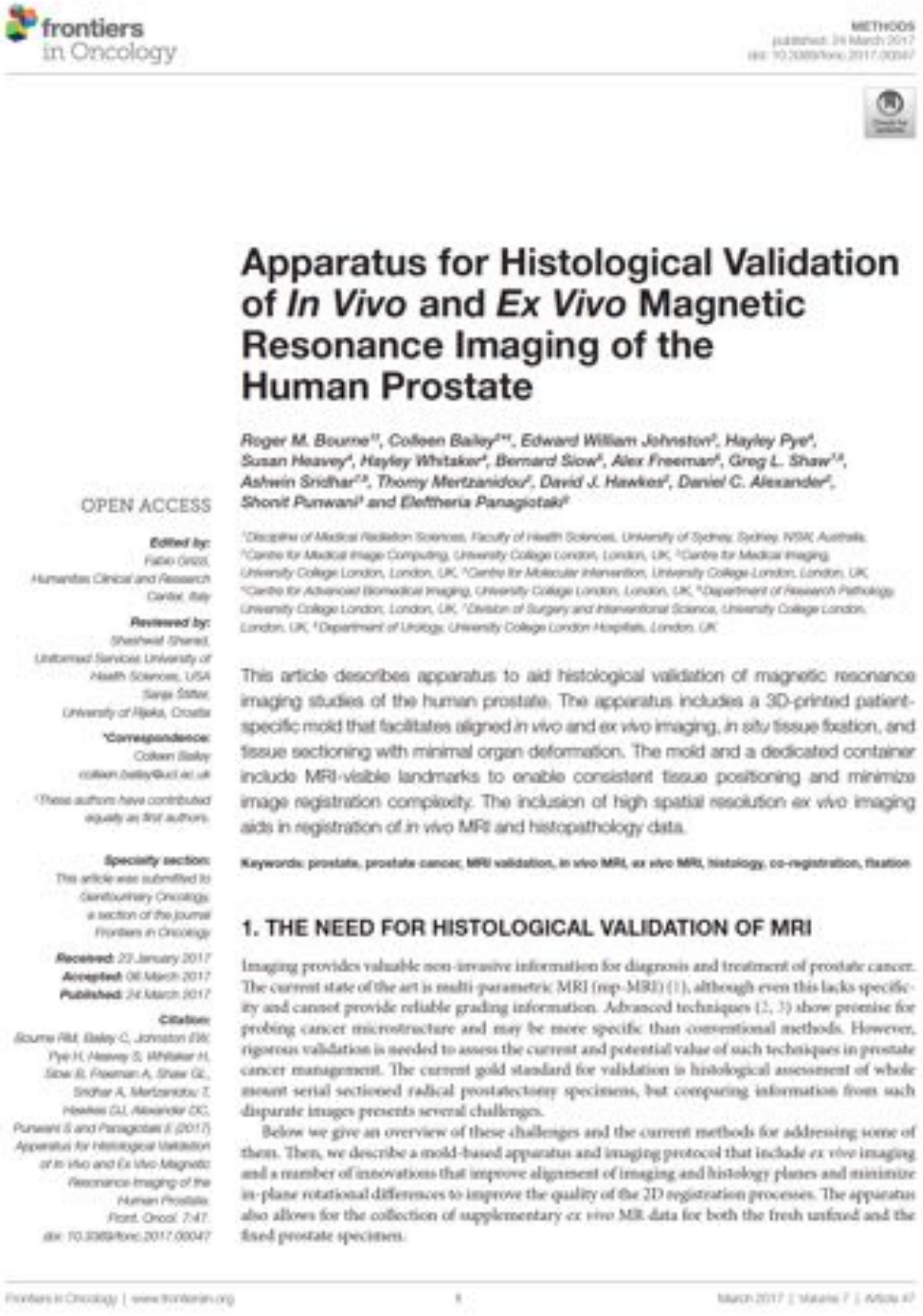

frontiers in Oncology

METHODS

Apparatus for Histological Validation of *In Vivo* and *Ex Vivo* Magnetic Resonance Imaging of the Human Prostate

Roger M. Bourne[1†], Colleen Bailey[2†], Edward William Johnston[2], Hayley Pye[3], Susan Heavey[4], Hayley Whitaker[4], Bernard Siow[5], Alex Freeman[6], Greg L. Shaw[1,8], Ashwin Sridhar[7,8], Thomy Mertzanidou[7], David J. Hawkes[7], Daniel C. Alexander[2], Shonit Punwani[3] and Eleftheria Panagiotaki[2]*

[1]Discipline of Medical Radiation Sciences, Faculty of Health Sciences, University of Sydney, Sydney, NSW, Australia, [2]Centre for Medical Image Computing, University College London, London, UK, [3]Centre for Medical Imaging, University College London, London, UK, [4]Centre for Molecular Intervention, University College London, London, UK, [5]Centre for Advanced Biomedical Imaging, University College London, London, UK, [6]Department of Research Pathology, University College London, London, UK, [7]Division of Surgery and Interventional Science, University College London, London, UK, [8]Department of Urology, University College London Hospitals, London, UK

This article describes apparatus to aid histological validation of magnetic resonance imaging studies of the human prostate. The apparatus includes a 3D-printed patient-specific mold that facilitates aligned *in vivo* and *ex vivo* imaging, *in situ* tissue fixation, and tissue sectioning with minimal organ deformation. The mold and a dedicated container include MRI-visible landmarks to enable consistent tissue positioning and minimize image registration complexity. The inclusion of high spatial resolution *ex vivo* imaging aids in registration of *in vivo* MRI and histopathology data.

Keywords: prostate, prostate cancer, MRI validation, in vivo MRI, ex vivo MRI, histology, co-registration, fixation

OPEN ACCESS

Edited by:
Fabio Grizzi,
Humanitas Clinical and Research Center, Italy

Reviewed by:
Shashwat Sharad,
Uniformed Services University of Health Sciences, USA
Sanja Sattar,
University of Rijeka, Croatia

***Correspondence:**
Colleen Bailey
colleen.bailey@ucl.ac.uk

†These authors have contributed equally as first authors.

Specialty section:
This article was submitted to Genitourinary Oncology, a section of the journal Frontiers in Oncology

Received: 22 January 2017
Accepted: 06 March 2017
Published: 24 March 2017

Citation:
Bourne RM, Bailey C, Johnston EW, Pye H, Heavey S, Whitaker H, Siow B, Freeman A, Shaw GL, Sridhar A, Mertzanidou T, Hawkes DJ, Alexander DC, Punwani S and Panagiotaki E (2017) Apparatus for Histological Validation of In Vivo and Ex Vivo Magnetic Resonance Imaging of the Human Prostate. Front. Oncol. 7:47. doi: 10.3389/fonc.2017.00047

1. THE NEED FOR HISTOLOGICAL VALIDATION OF MRI

Imaging provides valuable non-invasive information for diagnosis and treatment of prostate cancer. The current state of the art is multi-parametric MRI (mp-MRI) (1), although even this lacks specificity and cannot provide reliable grading information. Advanced techniques (2, 3) show promise for probing cancer microstructure and may be more specific than conventional methods. However, rigorous validation is needed to assess the current and potential value of such techniques in prostate cancer management. The current gold standard for validation is histological assessment of whole mount serial sectioned radical prostatectomy specimens, but comparing information from such disparate images presents several challenges.

Below we give an overview of these challenges and the current methods for addressing some of them. Then, we describe a mold-based apparatus and imaging protocol that include *ex vivo* imaging and a number of innovations that improve alignment of imaging and histology planes and minimize in-plane rotational differences to improve the quality of the 2D registration processes. The apparatus also allows for the collection of supplementary *ex vivo* MR data for both the fresh unfixed and the fixed prostate specimen.

2. PROBLEMS IN HISTOLOGICAL VALIDATION OF MRI METHODS

There are a number of major technical problems complicating any attempt to directly match and correlate MRI and histology data (4). These difficulties include

- **Unmatched tissue planes**. In practice there is usually no direct coordination of presurgical imaging methods and surgical specimen processing. This results in MRI slice planes usually having different plane orientation and plane spacing from the histology images with no clear correspondence between the two so that, at best, only a qualitative correlation of MRI and pathology data is feasible.
- **Unmatched spatial resolution**. A volume element ("voxel") in prostate MRI (the source of each semi-discrete item of measurement data) has a typical size that may vary from 0.2 mm × 0.2 mm in-plane by 1 mm slice thickness to 2 mm × 2 mm in-plane by 5 mm slice thickness. By contrast, a typical histological image used for pathology assessment is based on a 3–5 μm thick tissue section and has an in-plane resolution <1 μm. Even under highly idealized conditions, where the histology and MRI slices are "co-planar," the MRI signal originates from a much larger tissue volume than is represented in the histology slice. Thus, there may be tissue structure heterogeneity within the MRI slice that is not reflected in the histological data.
- **Tissue deformations**. The prostate is deformed *in vivo* by voluntary and involuntary body movements, bowel contents, and by the imaging system itself if an endorectal coil is employed for signal detection. Upon resection, the prostate is detached from its supporting tissues and associated vasculature, resulting in shape changes due to removal of mechanical tension and compression and hemodynamic pressure (5). Dehydration and embedding of the tissue during processing for histology results in tissue shrinkage and thin sectioning may cause further deformations.
- **Unmatched image features**. MRI and histological staining produce image contrast according to very different tissue properties. The features present in MR images may not be easily identified in histology images and *vice versa*, leading to a difficulty in assessing the accuracy of any co-registration process.

3. SURVEY OF METHODS

The validation problems mentioned earlier have been addressed with varying degrees of completeness by various methods, some of which have been reviewed in Ref. (4, 6). Here, we provide a brief overview of the approaches and problems addressed by the method we describe.

A partial 3D histology "map" can be reconstructed from a stack of histology slices and registered with MR images by a 3D process (7, 8); however, the accuracy of this approach is severely limited by the low out of plane resolution of the MRI data. The problem of missing inter-plane histology data can be addressed by manual (9, 10) or automatic (11) selection of the most closely aligned histology and image planes. Ideally, this reduces the problematic 3D registration to a more tractable 2D process. As the accuracy of this approach is highly dependent on co-alignment of imaging planes with histology sections, a number of methods have been described based on production of a patient-specific 3D-printed mold, the shape of which is defined by the *in vivo* imaging data. The aim of the mold is to hold the prostate in the same conformation in which it was imaged while guides in the mold align the tissue cutting planes with the image slice positions (12–15). The precision of these mold-based methods is dependent on the degree to which the mold matches the shape of the excised prostate specimen and the amount of any mispositioning or rotation of the prostate in the mold. Rotation errors are more likely around the axes in which the specimen has greatest rotational symmetry. Inclusion of a urethral catheter in the specimen and mold design can decrease rotation errors about the left–right axes of the prostate (6).

High spatial resolution *ex vivo* imaging of the prostate specimen has been used as an intermediate "stepping-stone" to improve the accuracy of co-registration of *in vivo* MRI and histology data, both with (6) and without (16) a patient-specific mold. However, the mold design can be improved to better facilitate comparison between MR and histological images.

4. OUTLINE OF IMAGING AND SPECIMEN HANDLING

The following points outline the method of imaging and construction of a patient-specific 3D-printed mold to optimize physical location of the prostate in *in vivo* MR images, *ex vivo* MR images, and histology images. The aim is to reduce the inherent 3-dimensional co-registration problem to a more tractable and precise 2-dimensional process.

4.1. *In Vivo* Imaging

This study was carried out in accordance with the recommendations of the UK Research Governance Framework version 2, UK Research Ethics Committee with written informed consent from all subjects and approved by the NRES Committee London-Surrey Borders (REC 15/LO/0692). All subjects gave written informed consent in accordance with the Declaration of Helsinki.

The geometry for the *in vivo* imaging needs to be compatible with the local clinical histopathology processing and reporting protocol. In our case, the pathology department uses 5 mm thick sections cut approximately transaxial to the prostatic urethra and perpendicular to the posterior face of the prostate. We perform T2-weighted imaging with 2.5 mm slice thickness (with no gap or 2.5 mm gap) in the "true axial" scanner XY plane. The central slice is centered approximately mid-organ and is defined as the reference for all subsequent imaging and processing and is defined by MR visible landmarks in the patient-specific mold.

For the data illustrating the methods in this paper mp-MRI was performed on a 3-T scanner (Achieva, Philips, Best, the Netherlands), using pelvic phased array coils. The 0.2 mg/kg (up to 20 mg) of a spasmolytic agent (Buscopan; Boehringer

Ingelheim, Germany) was administered intravenously prior to imaging to reduce bowel peristalsis. mp-MRI comprises axial and coronal T2 turbo spin echo (TSE) imaging, supplemented with diffusion-weighted imaging at b-values 0, 150, 500, and 1,000 s/mm^2. A dynamic contrast enhanced (DCE) acquisition was subsequently performed using spoiled gradient echo with fat saturation and a 12-s time resolution. Intravenous contrast agent (0.2 mL/kg; Prohance, Bracco, Milan, Italy) was injected at the beginning of the 6th acquisition at 3 mL/s followed by 20 mL of saline.

4.2. Contouring of *In Vivo* Images for Patient-Specific Mold Specification

MR datasets were analyzed using Osirix Version 7.0 (Bernex, Switzerland). A board certified Radiologist (Edward William Johnston) manually contoured the entire prostate (from base to apex) using the closed polygon tool on high-resolution axial T2-weighted images. Contoured landmarks comprise the hypointense prostate capsule and the anterior fibromuscular stroma where the capsule is absent anteriorly. The periprostatic fat, neurovascular bundles, seminal vesicles, distal urethral sphincter, and bladder were not included inside the contoured volume but provided useful information as to the extent of the prostate. The positions of contours were checked in all planes and adjusted accordingly until their appearance was satisfactory. Where available, at least 3 slices of coronal and/or sagittal images were contoured at the center of the gland to corroborate axial contours, but the edge of the prostate was not contoured as it is poorly delineated in these planes. To estimate urethral catheter position, the urethra was demarcated where visible using axial T2-weighted images and interpolating based on normal anatomy and adjacent slice position where invisible.

4.3. Prostatectomy and Specimen Preparation

The radical prostatectomy specimen was collected immediately upon resection to minimize ischemia time and taken to the pathology department without formalin fixation. The fresh specimen was inked and dried, and the seminal vesicles and any metal clips that would cause magnetic susceptibility artifacts were removed. A 4.2-mm diameter silicon rubber catheter was inserted through the urethra, the prostate placed into the mold, and the mold halves fastened with four plastic cable ties. The specimen inside the closed mold was then inserted into the canister, which had been pre-filled with saline. Gentle agitation was used to eliminate air bubbles, and then the sealing piston was inserted fully to ensure alignment of the mold reference plane with the external reference landmarks. Excess fluid was ejected through the vent, which was then capped.

4.4. *Ex Vivo* Prostate Imaging

Fresh *ex vivo* scanning was performed on both a 3-T clinical MRI scanner (Philips Achieva, Best, the Netherlands) and a 9.4-T 20-cm horizontal bore MRI (Varian Inc., Palo Alto, CA, USA). Fixed imaging was conducted only at 9.4 T. The reference plane landmarks on the exterior of the mold canister (see section 6 below) were used to position the reference slice of the sample near the isocenter of the magnet.

For 3-T MRI, the sample was positioned at the center of an 8-channel knee coil (Philips, Best). T2-weighted TSE images (TE = 100 ms, echo train length = 16, TR = 5.2 s, field of view 18 cm × 18 cm) were acquired with 0.4 mm × 0.4 mm resolution in-plane, 2 mm slice thickness, and 0.5 mm slice gap.

Imaging at 9.4 T was performed using 400 mT/m gradients and a 72 mm internal diameter quadrature coil (RAPID Biomedical, Rimpar, Germany). A multi-slice gradient echo sequence (TE = 5 ms, TR = 75 ms, field of view 8 cm × 8 cm) was acquired giving 0.625 mm × 0.625 mm in-plane resolution, 1 mm slice thickness, and no slice gap. These images were used to locate the reference slice using the reference plane landmarks (see section 5.1 below), as shown in **Figure 1**. The same procedure for reference slice location was repeated following specimen fixation.

5. MOLD DESIGN AND 3D PRINTING

5.1. Mold Template

The mold template is 62 mm diameter, designed to fit inside a 63.5 mm internal diameter canister that contains the prostate immersed in saline during *ex vivo* imaging. The mold design is based on the abilities and constraints of nylon powder printing (selective laser sintering using EOSINT P100 with PA2200 powder; 40–50 μm grain size). Note that the mold design described here could not be produced on a typical low-cost plastic filament printer due to the lower dimensional precision and the need for these devices to print support material that would be extremely difficult to remove from the design we describe. A more basic mold design suitable for a filament printer is described in Ref. (6). The mold features are illustrated in **Figure 2** and include

- A chamfer at one end of the mold indicates the apex end of the prostate, so that orientation of the prostate during *ex vivo* imaging is as for *in vivo* imaging with the patient lying in feet-first supine position.
- **LP.** Two 4-mm diameter locator pins ensure alignment of the mold halves.
- **CP.** Two 0.4-mm wide slots, spaced 5.0 mm apart, define the cutting planes for organ sectioning.
- **B.** 0.5-mm diameter braces stabilize the mold shape during *ex vivo* imaging. These are removed immediately prior to organ sectioning.
- **RPLM.** Reference plane land marks (1.5-mm diameter axial channels) are filled with liquid when the prostate and mold are inserted in the imaging canister and provide MR visible landmarks that enable precise matching of *in vivo* and *ex vivo* imaging planes. Relative to the cutting planes the landmarks are offset toward the apex of the prostate to bring the center of the MRI planes into closer alignment with the histology sections that are routinely cut from the apex face of the tissue blocks.
- **U.** A 4.2-mm diameter saline-filled silicon rubber urethral catheter is inserted in the prostate with curvature and

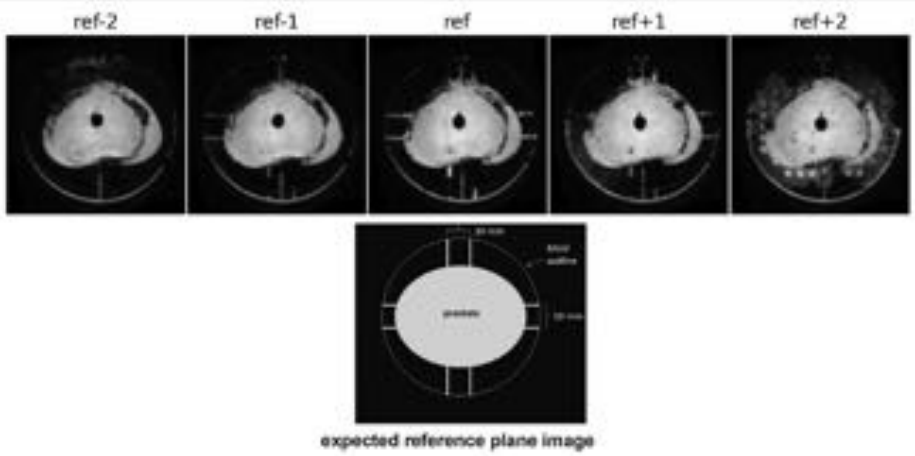

FIGURE 1 | Images acquired at 1 mm spacing demonstrate the use of the reference plane landmark channels (some of which are obscured by air bubbles here) to locate the reference slice. When correctly positioned and aligned the reference image will show the water filled channels on the A/P and L/R sides of the prostate.

orientation defined during contouring of the *in vivo* images. The catheter assists in constraining any rotations of the prostate in the sagittal plane.

- **S.** Flexible springs printed into the mold press against the wall of the canister and minimize any movement or vibration of the mold in the canister during imaging.
- **G.** A groove in the top of the mold matches the internal rib in the canister (**Figure 3**) and precludes any rotation of the mold in the axial plane.
- **CT.** The corners of the mold halves are fastened with four plastic cable ties.

6. MOLD CONTAINER FOR *EX VIVO* IMAGING

For *ex vivo* imaging (both before and after formalin fixation), the specimen in the mold is constrained inside a plastic canister. A liquid-tight seal is made with a piston that also serves as the mounting base for attachment of the sample to the scanner's small animal bed. Details are described in **Figure 3** and below:

- **Canister**. The canister is 68 mm outside diameter, 63.5 mm internal, to fit with 2 mm clearance inside the 72 mm internal diameter RF coil used for 9.4-T *ex vivo* imaging. The canister is printed in rigid photopolymer (Objet, Stratasys), which is non-porous. Landmarks on the external surface of the canister define the position of the reference slice and top midline of the mold. An internal rib fits the groove in the top of the mold and prevents any rotation of the mold inside the canister, thus ensuring minimal axial plane rotational differences between *in vivo* and *ex vivo* images (see **Figure 2**).
- **Piston.** The canister is sealed liquid tight with a piston (also printed in rigid photopolymer) fitted with three O-rings lubricated with light grease. To immerse the prostate in liquid and minimize inclusion of air bubbles the canister is placed vertically and filled with 200 mL of saline. The prostate in the mold is inserted, pushed to the bottom of the canister, and agitated to expel air bubbles. The piston is then inserted and excess liquid is expelled into the central well via the vent which is then sealed with a plastic pin. The center line landmark (CL) on the piston is aligned with the center line mark on the canister. The fully inserted piston fixes the mold at the base of the canister, so that the mold reference plane is aligned with the external landmarks. The mold and prostate are thus fixed in a defined position relative to the external landmarks on the canister and piston.
- **Mounting bracket**. The base of the piston is attached to a mounting bracket that is designed specifically for the small animal bed of the MRI scanner. The bracket is printed on the SLS printer that provides a rigid product (slightly porous so unsuitable for canister and piston).

7. FORMALIN FIXATION OF PROSTATE IN MOLD

The porous mold design enables fixation of the prostate *in situ*. The mold/prostate is removed from the canister and immersed in 1-L fixative solution in a narrow vessel placed on a magnetic stirrer overnight. The low density of the nylon mold provides

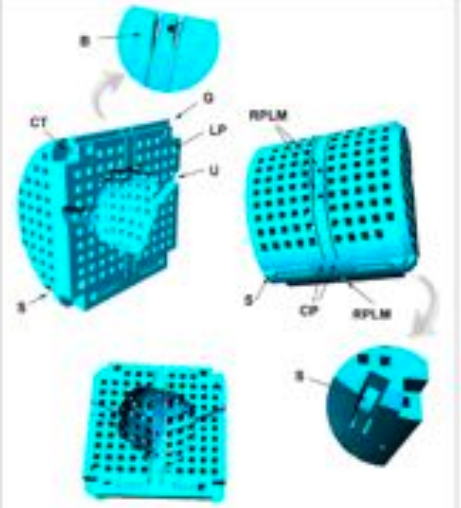

FIGURE 2 | Mold design features. See text for label descriptions.

sufficient buoyancy for the prostate to float just below the liquid surface. Use of the stirrer enhances penetration of the fixative through the mold structure and into the prostate. Post fixation, the immersion solution is replaced with 1-L saline for 8 h to dilute the formalin which, at full strength, severely reduces the sample T2 leading to poor signal quality.

Formalin fixation leads to tissue shrinkage (17) and shape changes (18). Fixation of the prostate in the mold constrains any shape changes.

8. APPARATUS FOR SECTIONING PROSTATE IN MOLD

Upon completion of fixation and *ex vivo* imaging, the prostate is sectioned for histological processing (**Figure 4**). The mold defines two cutting planes spaced 5 mm apart on either side of the imaging reference plane. Prior to cutting, the mold stabilizer braces (**Figure 2**) are removed with a scalpel blade, and the mold placed in a dedicated cradle (C). The two cuts on either side of the reference slice are made simultaneously using a pair of skin graft blades (R55170, Rocket Medical, Washington, UK) mounted in an SLS-printed handle (H). The handle and a detachable spacer (S) maintain the blades at 5-mm spacing that aids insertion of the blades into the slots in the top of the mold.

After cutting of the reference plane section, the mold is opened and the prostate removed. The base and apex volumes are then progressively sectioned at 5-mm thickness using a flat plate with 5-mm high rails to guide the blade.

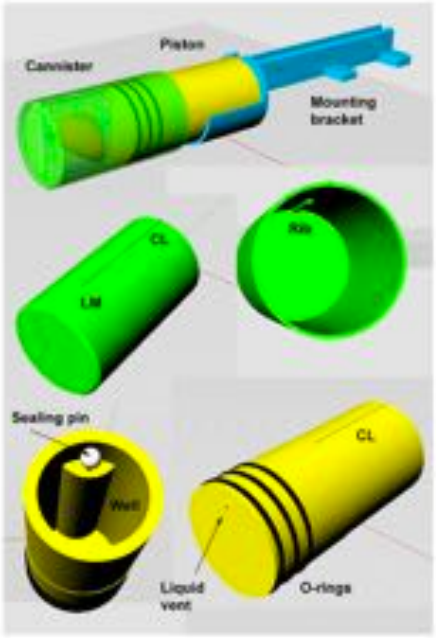

FIGURE 3 | Apparatus for ex vivo imaging of the prostate immersed in saline. See text for design features description.

FIGURE 4 | Prostate slicing in mold. The mold is stabilized in a cradle (C). The handle (H) and separate spacer (S) maintain two skin graft blades (B) at the same 5 mm spacing as the mold cutting planes.

Whole mount tissue sections are processed according to standard laboratory protocol. These sections are cut from the prostate apex face of each block. Note that the reference plane landmarks in the mold are offset toward the apex to account for the histology slice position typically being closer to the apex side of each tissue section than to the base side.

9. IMAGE REGISTRATION

There is a very wide range of 2D image registration methods that could be applied for alignment of the MRI and histology images. As the focus of this paper is on the apparatus used for prostate imaging and sectioning, we present here only an outline of the methods used to produce the example data presented in the figures.

Hematoxylin and eosin stained whole mount sections were digitally scanned with a 20x objective (Hamamatsu NanoZoomer). Histological images were downsampled to 0.25x and converted to grayscale for registration. The high-resolution *ex vivo* T2 MRI slice for registration was selected based on the mold landmarks. Registration to the corresponding histological slice used an intensity-based 2D rigid registration based on a block-matching strategy (19, 20) with the correlation coefficient as similarity measure. The *ex vivo* MRI was registered to the *in vivo* MRI using 2D affine registration, restricting the block matching in the *in vivo* image to the prostate region using the contour from section 4.2.

10. SAMPLE RESULTS

An example case is shown in **Figure 5**.

Registered MRI and histology slices are shown in **Figure 6**. Slicing artifacts, particularly near the urethra, are visible and may be corrected by additional non-rigid registration techniques. Nevertheless, the spatial correspondence between the *ex vivo* and histology images can be seen, including in the peripheral zone shape and in the outline of glandular regions within the transition zone. The peripheral zone partially collapses between *in vivo* and *ex vivo* imaging, but internal structures within the transition zone show correspondence.

11. LIMITATIONS AND FUTURE DIRECTIONS

The apparatus detailed here addresses many of the issues described in section 2 and extends previous methods by improving the alignment of *in vivo* and *ex vivo* imaging planes with each other and with histopathology sections. Nevertheless, a number of problems remain

- **Prostate contouring from *in vivo* images**. Contour delineation on the *in vivo* images aims to trace the expected surgical margins. These are normally close to the prostatic capsule but may vary case by case and the capsule is absent around the prostatic apex. Depending on the T2 image quality and characteristics of the individual prostate, it is sometimes difficult to discriminate the capsule from adjacent intra and extra-prostatic structures. One strategy to accommodate these uncertainties is to print multiple versions of the mold

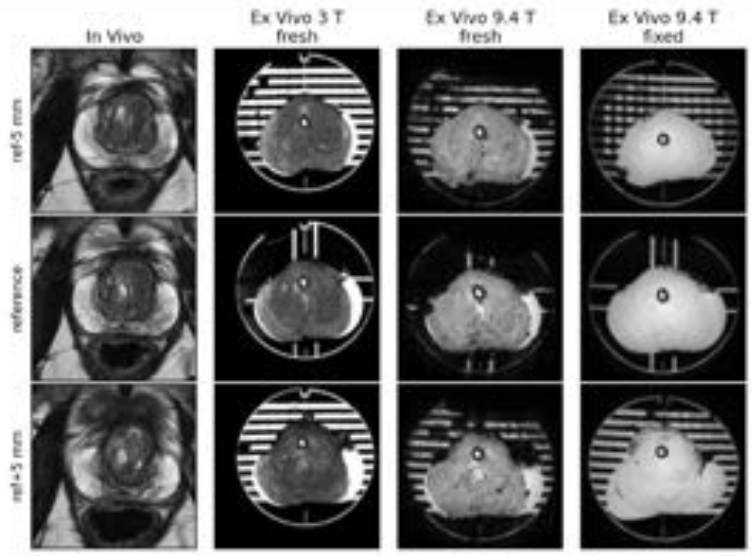

FIGURE 5 | Images from the reference slice and slices ±5 mm from the reference. Contours from the *in vivo* scan's reference slice were aligned with the reference plane of the mold. The 8 channels in the reference plane were used to locate the reference slice for fresh scans at 3 and 9.4 T, as well as after fixation.

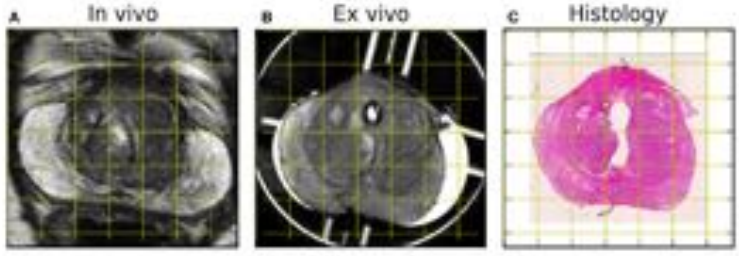

FIGURE 6 | Sample *in vivo* (A) and *ex vivo* (B) MR images after rigid registration to hematoxylin and eosin-stained histology (C). Note the collapse of the peripheral zone between *in vivo* and *ex vivo* scans, as well as the distortion around the urethra in the histological section.

with +10 and −10% adjustments to the axial plane scale and to fit the resected specimen to the mold that provides the best fit.

- ***In vivo–ex vivo* volume changes**. In our experience, there may be significant prostate volume reductions upon resection (see **Figure 5**) due to loss of luminal fluid. This may lead to a loose and unconstrained fit of the prostate in the mold and consequent misalignment of imaging planes and tissue sectioning planes. Inclusion of the urethral catheter reduces the likelihood of such misalignment, although introducing a small distortion of the tissue around the catheter. As the majority of tumors are not proximal to the urethra, the latter is a relatively minor issue.
- **Volume changes due to fixation**. The mold constrains prostate movement during fixation, but does not account for volume shrinkage. It is possible that the orientation of the prostate within the mold could change due to the less close fit after shrinkage. This issue could potentially be addressed by transferring the fixed prostate to a second mold with reduced prostate volume; however, we have not implemented this step that assumes a predictable and uniform shrinkage.
- **Inconsistent MRI and histology section thickness**. The apparatus described improves the reliability of imaging plane alignment with histology planes but does not specifically address the problem of sparse histology data in the direction orthogonal to the sectioning planes. This is primarily a tissue processing issue and if resources permit can be addressed by more comprehensive thin sectioning and processing of the tissue blocks.

AUTHOR CONTRIBUTIONS

Apparatus design: RB. Specimen preparation and handling: GS, AS, CB, SH, HP, and AF. Imaging: EJ, CB, and BS. Image registration: TM and CB. Project management: DA, DH, SP, and EP. Manuscript preparation: all.

FUNDING

RB received research funding from the Australian National Health and Medical Research Council (Grant 1026467). This project was funded by the EPSRC (EP/M020533/1). EP and CB are supported by the EPSRC (EP/N021967/1). HW is supported by Prostate Cancer UK grant PG14-014. HP and EJ by PG14-018-TR2. SH is funded by the Centre of Excellence (CEO13_2-002). The project also received funding from the National Institute for Health Research University College London Hospitals Biomedical Research Centre.

REFERENCES

1. Graham J, Kirkbride P, Cain K, Hasler E, Prettyjohns M. Prostate cancer: summary of updated NICE guidance. *BMJ* (2014) 348:f7524. doi:10.1136/bmj.f7524
2. Panagiotaki E, Chan RW, Dikaios N, Ahmed HU, O'Callaghan J, Freeman A, et al. Microstructural characterization of normal and malignant human prostate tissue with vascular, extracellular, and restricted diffusion for cytometry in tumours magnetic resonance imaging. *Invest Radiol* (2015) 50(4):218–27. doi:10.1097/RLI.0000000000000115
3. Wang S, Peng Y, Medved M, Yousuf AN, Ivancevic MK, Karademir I, et al. Hybrid multidimensional T2 and diffusion-weighted MRI for prostate cancer detection. *J Magn Reson Imaging* (2014) 39(4):781–8. doi:10.1002/jmri.24212
4. Meyer C, Ma B, Kuntz LP, Davenport M, Piert M. Challenges in accurate registration of 3-D medical imaging and histopathology in primary prostate cancer. *Eur J Nucl Med Mol Imaging* (2013) 40(1):72–8. doi:10.1007/s00259-013-2582-2
5. Orczyk C, Taneja SS, Rusinek H, Rosenkrantz AB. Assessment of change in prostate volume and shape following surgical resection through co-registration of in-vivo MRI and fresh specimen ex-vivo MRI. *Clin Radiol* (2014) 69(10):e398–403. doi:10.1016/j.crad.2014.06.012
6. Eiben A, Isebaert S, De Keyzer F, Himmelreich U, Joniau ST, Dresselaers T, et al. Validation and workflow of an improved patient-specific mold design for registration of in-vivo MRI and histology of the prostate. *Clinical Image-Based Procedures. Translational Research in Medical Imaging. 5th International Workshop, CLIP 2016, Held in Conjunction with MICCAI 2016, Athens, Greece, October 17, 2016 Proceedings*. Athens (2016). p. 36–43.
7. Orczyk C, Mikheev A, Rosenkrantz A, Melamed J, Taneja SS, Rusinek H. Imaging of prostate cancer: a platform for 3D co-registration of in-vivo MRI ex-vivo MRI and pathology. *SPIE Medical Imaging*. Orlando: International Society for Optics and Photonics (2012). 831625H p.

8. Bart S, Moser JI, Hemar P, Letourneau G, Comperat E, Renard-Penna R, et al. MRI-histology registration in prostate cancer. In: Mevlev P, Troccaz J, editors. *Proceedings of Surgetica*. Paris: Sauramps Medical (2005). p. 361–7.
9. Kalavagunta C, Zhou X, Schmechel SC, Metzger GJ. Registration of in vivo prostate MRI and pseudo whole mount histology using local affine transformations guided by internal structures (LATIS). *J Magn Reson Imaging* (2015) 41(4):1104–14. doi:10.1002/jmri.24629
10. Chappelow J, Bloch BN, Rofsky N, Genega E, Lenkinski R, DeWolf W, et al. Elastic *registration of multimodal prostate MRI and histology via multiattribute combined mutual information*. *Med Phys* (2011) 38(4):2005–18. doi:10.1118/1.3560879
11. Xiao G, Bloch BN, Chappelow J, Genega EM, Rofsky NM, Lenkinski RE, et al. Determining histology-MRI slice correspondences for defining MRI-based disease signatures of prostate cancer. *Comput Med Imaging Graph* (2011) 35(7):568–78. doi:10.1016/j.compmedimag.2010.12.003
12. Shah V, Pohida T, Turkbey B, Mani H, Merino M, Pinto PA, et al. A method for correlating in vivo prostate magnetic resonance imaging and histopathology using individualized magnetic resonance-based molds. *Rev Sci Instrum* (2009) 80(10):104301. doi:10.1063/1.3242697
13. Trivedi H, Turkbey B, Rastinehad AR, Benjamin CJ, Bernardo M, Pohida T, et al. *A step towards personalized medicine: use of a patient-specific MRI based prostate mold for validation of multi-parametric MRI in the localization of prostate cancer*. Urology (2012) 79(1):233. doi:10.1016/j.urology.2011.10.002
14. Priester A, Natarajan S, Le JD, Garritano J, Radosevcev B, Grundfest W, et al. *A system for evaluating magnetic resonance imaging of prostate cancer using patient-specific 3D printed molds*. *Am J Clin Exp Urol* (2014) 2(2):137.
15. Turkbey B, Mani H, Shah V, Rastinehad AR, Bernardo M, Pohida T, et al. *Multiparametric 3T prostate magnetic resonance imaging to detect cancer: histopathological correlation using prostatectomy specimens processed in customized magnetic resonance imaging based molds*. *J Urol* (2011) 186(5):1818–24. doi:10.1016/j.juro.2011.07.013
16. Xu J, Humphrey PA, Kibel AS, Snyder AZ, Narra VR, Ackerman JJ, et al. *Magnetic resonance diffusion characteristics of histologically defined prostate cancer in humans*. *Magn Reson Med* (2009) 61(4):842–50. doi:10.1002/mrm.21898
17. Jonmarker S, Valdman A, Lindberg A, Hellström M, Egevad L. *Tissue shrinkage after fixation with formalin injection of prostatectomy specimens*. *Virchows Arch* (2006) 449(3):297–301. doi:10.1007/s00428-006-0259-5
18. Bourne RM, Bongers A, Chatterjee A, Syed P, Watson G. Diffusion anisotropy in fresh and fixed prostate tissue ex vivo. *Magn Reson Med* (2013) 70(2):626–34. doi:10.1002/mrm.24808
19. Mertzanidou T, Hipwell J, Dalmis M, Platel B, van der Laak J, Mann R, et al. Towards spatial correspondence between specimen and in-vivo breast imaging. In: Fujita H, Hara T, Muramatsu C, editors. *Breast Imaging: 12th International Workshop, IWDM 2014, Gifu City, Japan, June 29–July 2, 2014: Proceedings*. Gifu: Springer International Publishing (2014). p. 674–80.
20. Ourselin S, Roche A, Subsol G, Pennec X, Ayache N. Reconstructing a 3D structure from serial histological sections. *Image Vis Comput* (2001) 19(1):25–31. doi:10.1016/S0262-8856(00)00052-4

Conflict of Interest Statement: The authors declare that the research was conducted in the absence of any commercial or financial relationships that could be construed as a potential conflict of interest.

Appendix F

Other work

Traditional poster presented at ISMRM 2017 regarding validation of MRI SI

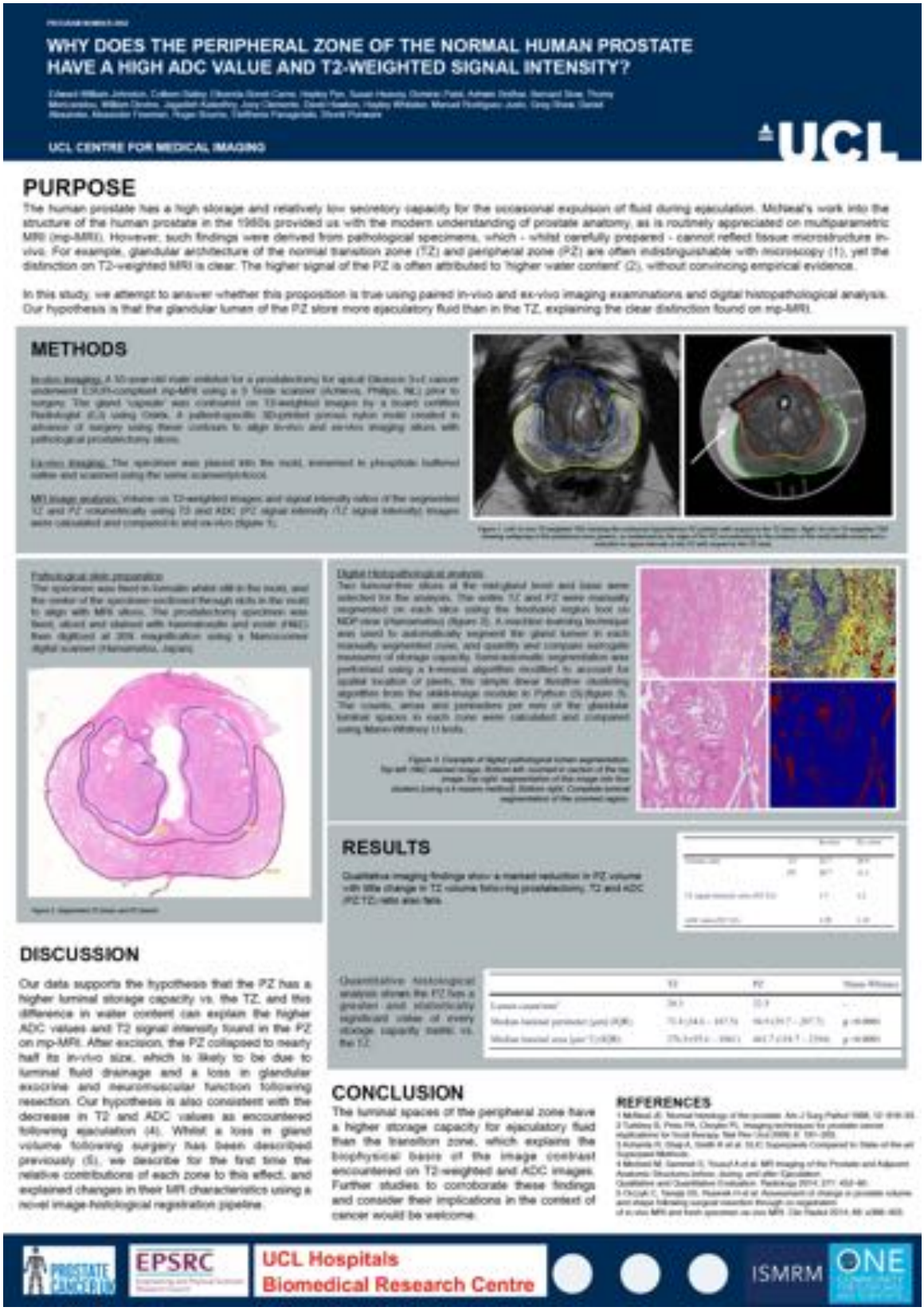

E-poster presented at ISMRM 2017: PROGENY (radiogenomic) study

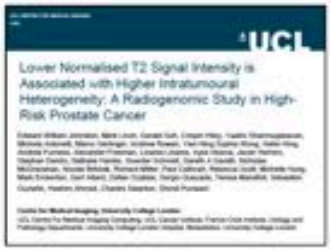

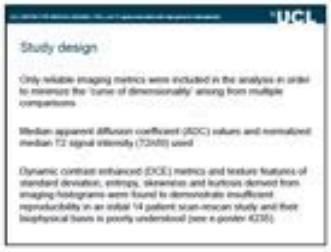

Acquisition

mp-MRI performed on a range of 5 machines at 1.5 and 3 Tesla (T) with 2 manufacturers (Philips, Best, the Netherlands and Siemens, Erlangen, Germany), using pelvic phased array coils.

European Society of Uroradiology (Barentsz, Eur Radiol 2012) and UK (Kirkham, Clin Radiol 2013) guidelines compliant

Scanning protocols

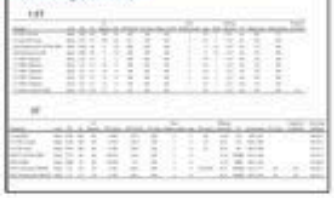

Quantitative mp-MRI analysis

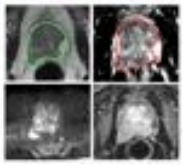

- MR datasets analysed using Osirix, version 7.0 (Pixmeo, Switzerland)
- A board certified Radiologist manually contoured the entire tumor volume on T2 and ADC images, using all sequences for further guidance
- The largest possible region of interest (ROI) was placed on a single slice of the bladder urine for T2 normalization purposes
- T2nSI was calculated by dividing the median signal intensity of the lesion by that of the bladder

Statistical analysis

- Data analysed using GraphPad Prism v6 (San Diego, California, USA)
- Data demonstrated linearity, normality and homoscedasticity
- Pearson's product moment correlation coefficient (r) was performed

RESULTS

%ITH vs. Normalised Median T2 SI

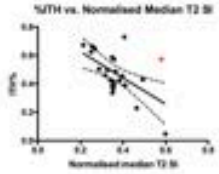

T2 and ADC vs. %ITH

Parameter	Pearson's r	p-value
Median T2nSI	-0.181 (-0.76 - 0.51)	0.5628 ns
Median T2nSI (within maverick)	-0.75 (-0.88 - -0.46)	<0.0001****
Median ADC	-0.62 (-0.35 - 0.43)	91.99%

RESULTS

No association between median T2nSI and degree of SNV heterogeneity or Gleason score and SNV heterogeneity

DISCUSSION

- Genetically diverse tumors tend to demonstrate lower T2nSI, with apparent independence from Gleason score
- The reason for decreased T2 relaxation times encountered in genetically heterogeneous tumors is uncertain, and presents an opportunity for further work
- Possible biophysical explanations could arise from changes in water compartmentalization (extracellular, cytoplasmic or nuclear) (Langer et al. Radiology. 2010) regional macromolecules, cell density (Gibbs et al. Invest Radiol 2009), blood vessels, hemoglobin content and pH (Vosberg AM, et al. Neuroradiology 2002)

CONCLUSIONS

- T2nSI may have value in predicting % mutational ITH in prostate cancer
- Larger prospective studies should be conducted to confirm this association and evaluate the prognostic ability of this the T2nSI metric

Acknowledgements

UCL Hospitals
Biomedical Research Centre
A partnership between UCL and University College London Hospitals NHS Foundation Trust

THE FRANCIS CRICK INSTITUTE

PROSTATE CANCER FOUNDATION

NHS
National Institute for Health Research

References

1. Morris LGT, Riaz N, Desrichard A, et al. Pan-cancer analysis of intratumor heterogeneity as a prognostic determinant of survival. Oncotarget. 2016; 7: 10051–63.

2. Kirkham a PS, Haslam P, Keanie JY, et al. Prostate MRI: who, when, and how? Report from a UK consensus meeting. Clin Radiol 2013; 68: 1016–23.

3. Barentsz JO, Richenberg J, Clements R, et al. ESUR prostate MR guidelines 2012. Eur Radiol 2012; 22: 746–57.

4. Gibbs P, Liney GP, Pickles MD, et al. Correlation of ADC and T2 measurements with cell density in prostate cancer at 3.0 Tesla. Invest Radiol 2009; 44: 572–6.

5. Langer DL, van der Kwast TH, Evans AJ, et al. Prostate tissue composition and MR measurements: investigating the relationships between ADC, T2, Ktrans, ve, and corresponding histologic features. Radiology. 2010; 255: 485–94.

6. Schilling AM, Blankenburg FB, Bernarding J, et al. Intracerebral pH affects the T2 relaxation time of brain tissue. Neuroradiology 2002; 44: 966–72.